Imperial College London

Studies of Magnetised and Non-local Transport in Laser-Plasma Interactions

Henry Charles Watkins

Department of Physics

The Blackett Laboratory
Imperial College London
SW7 2AZ

A thesis submitted for the degree of

Doctor of Philosophy of Imperial College London

July 2019

Abstract

The application of magnetic fields in inertial fusion experiments has led to renewed interest in fully understanding magnetised transport in laser-plasma regimes. This motivated the development of a new laser magnetohydrodynamic code PARAMAGNET, written to support investigations into classical magnetised transport phenomena and laser propagation in a plasma. This code was used to simulate laser-underdense plasma interactions such as the pre-heat stage of magneto-inertial fusion. Alongside these simulations, this thesis will present analytic focusing and filamentation models derived from magnetohydrodynamics extended with classical magnetised transport coefficients. These results showed the focal length and filamentation growth length shortened with magnetisation, a result of the magnetisation of the thermal conductivity.

Further investigation of the transport properties using the diffusion approximation kinetic code IMPACT showed significant deviation of the growth rate at intermediate values of magnetisation and non-locality, inexplicable using fluid models. The kinetic code result motivated exploring the influence of the high-order anisotropies of the distribution function (in terms of spherical harmonics), ignored in conventional approximations. By using a recursive matrix inverse method, corrections to the transport coefficients including all orders of the electron distribution expansion were found. Analysis of the conductivity ($\boldsymbol{\kappa}$), resistivity ($\boldsymbol{\alpha}$) and thermoelectric ($\boldsymbol{\beta}$) coefficients showed deviation by up to 50% from the classical form at intermediate magnetisation and non-locality. The diffusive approximation of the IMPACT simulations was insufficient to capture the transport behaviour present in the theoretical high order calculation.

Modern inertial fusion experiments work in regimes that are non-local and susceptible to significant focusing exacerbated by magnetisation. The resulting filamentation has detrimental implications to laser absorption and the modified non-local transport behaviour is a possible source of error in simulations. The complex interplay between non-locality and magnetisation in transport suggests using more terms of the spherical harmonic expansion in closures of plasma equations. Particular consideration is given to the implications to inertial fusion experiments. Together these results suggest the necessity of including non-local magnetised transport in the modelling of high-energy-density laser plasma experiments.

Contents

List of Figures

List of Tables

Role of the Author

The PARAMAGNET code was designed, written and used by the author. The author made use of the pre-existing simulation code IMPACT with the permission from its developers. The author also made use of the CX1 supercomputing cluster provided by the Imperial College London HPC serivce. The analysis of the output of these codes and its interpretation should be understood to be the work of the author.

Copyright

Declaration

I herewith certify that all material in this dissertation is my own and any that which is not my own work has been properly acknowledged and appropriately referenced.

Henry Charles Watkins

Acknowledgements

I would first like to thank my supervisor, Dr Robert Kingham for his guidance and insight in all aspects that led to this PhD. His patience and advice made this PhD go smoothly.

I count myself to be so lucky to have such a good research group, so to Emma, Jon, Ellias, Sam, Sav, Catalina, Meriame, Kris, Chris, Dom, Tim, Josh, Stefan and everyone else in the Imperial College plasma physics group thankyou for making my PhD so enjoyable.

Further thanks goes to the Imperial Taekwondo club for all the good times in training and competition that helped keep me sane. It has meant so much to me during my years at university and hopefully it will continue to do so beyond.

The years I have spent pursuing this PhD have been some of the best of my life, and this is in no small part thanks to all my friends at Goodenough College. My time at the college has no doubt changed me for the better and this is all thanks to the people there; so thanks go to Ross, Katherine, Zak, Gabrielle, Leah, Pei, James, Ben, Alex, James, Daniel, the fencing crew, the choir and the innumerable others who have made my time at the college so memorable and an experience unlike any other.

Finally I have to thank my supportive family for encouraging me in whatever I have pursued, it is no doubt this that has given me the confidence to make my own life's path.

And to Ruby, thankyou for all the time we have spent together, and your unfailing kind support.

All men dream: but not equally. Those who dream by night in the dusty recesses of their minds wake in the day to find that it was vanity: but the dreamers of the day are dangerous men, for they may act their dream with open eyes, to make it possible.

T.E. Lawrence, *Seven Pillars of Wisdom*

1

Introduction

Producing commercially available energy from nuclear fusion is one of the great scientific projects of our age. Fusion has the potential to safely produce all of Earth's energy needs without the burning of fossil fuels and without the production of large amounts of radioactive by-products; while doing so from abundant or breedable hydrogen isotope fuel. Today fusion experiments can be broadly classed into magnetic-confinement (MCF) schemes and inertial-confinement schemes (ICF) which achieve fusion-relevant conditions by very different confinement methods. While MCF lies outside the scope of this thesis, an overview of ICF will be described in depth shortly herein. While ICF devices have made great headway towards ignition, they have also provided an excellent experimental platform for fundamental discovery science and a platform for stockpile stewardship; all the while providing the context for the work in this thesis.

The core objective of this thesis is the theoretical and computational study of the effect of magnetisation on transport in laser-plasma interactions. The development of inertial fusion schemes instigated the thorough study of laser interactions and transport properties in plasmas. This in turn has led to the development of detailed thermal and magnetic transport models to understand and correctly simulate the results of fusion experiments.

In an attempt to further improve the performance of inertial fusion schemes, magnetic fields have been applied to long-pulse laser-plasma experiments, taking advantage of the known property of the reduction in thermal transport across the magnetic field. However, the high-frequency electromagnetic field of a laser and the slow, almost static applied magnetic field used in such experiments creates a complex system that has not been fully explored. It is the aim of this thesis to close the gap between theory and the parameter space of experiments that are beginning to probe plasmas with ever higher laser energies and magnetic field strengths.

This thesis introduces a new fluid plasma physics code with magnetised transport, written for the purpose of simulating these regimes of high magnetisation and low magnetic pressure. Given the importance of laser interactions, the code was extended with a laser solver to accurately simulate the long-pulse laser propagation present in current ex-

periments. In addition to simulations, this thesis presents analytic investigations of magnetised corrections to laser-plasma phenomena; the results of which motivated exploring kinetic effects using the kinetic code IMPACT. Kinetic theory provides a more accurate model of plasma dynamics, especially at high frequencies and small scales. This in turn motivated an analytic investigation the influence of higher-order terms on magnetised transport which are ignored in most kinetic simulations.

It is hoped insights presented herein provide a deeper understanding of laser-created collisional plasmas in the regime where magnetisation significantly affects the transport dynamics. This work will conclude with a discussion on the influence these results have in applications such as inertial fusion and laser-plasma experiments. Though the field of plasma physics has a long history, the accurate modelling of dynamics still proves challenging. The core problem of closure in non-equilibrium plasmas presents fertile ground for new physics and prompts the creation of new methods of simulation.

1.1 Inertial Confinement Fusion

The fusion of two nuclei occurs when they collide with the energy to overcome the Coulomb barrier between the particles, allowing the attractive strong nuclear force to bind a set of the constituent nucleons into a more energetically stable daughter product. The rate of this process is significantly increased by quantum tunnelling, whereby the incoming particles can tunnel through the Coulomb barrier, reducing the amount of energy required by each particle. Nuclear fusion in the sun is dominated by two processes, the proton-proton chain reaction and the carbon-nitrogen-oxygen cycle [1]. Unfortunately for physicists, the conditions in the core of the sun where these processes occur are not replicable in laboratories on Earth.

While the processes that power the sun are out of reach, other fusion processes have much higher cross-sections for conditions achievable on Earth. The reaction most amenable to laboratory fusion is the reaction of a deuterium and a tritium nucleus into an $\alpha-$particle and a neutron

$$ {}^{2}_{1}D + {}^{3}_{1}T \rightarrow {}^{4}_{2}He + n. \tag{1.1} $$

This reaction has a very high cross-section relative to other light nuclei and so is the chosen reaction in all potential fusion schemes. By considering the fusion energy gain versus energy losses in a hypothetical power plant, the requirements for a viable fusion plant is given by the Lawson Criterion [2]. It requires the product of fuel number density n and energy confinement time τ to be above a critical value,

$$ n\tau > \frac{12 k_b T}{\langle \sigma v \rangle E_\alpha}. \tag{1.2} $$

Here E_α is the energy of the alpha particle product, T is the fuel temperature and $\langle\sigma v\rangle$ comes from the D-T fusion reaction rate $W = n_t n_d \langle\sigma v\rangle$, with deuterium and tritium number densities n_d, n_t, respectively.

Inertial confinement fusion attempts to reach the density and confinement time requirements of the Lawson Criterion by confining a plasma with its own inertia, such that it converges to a central 'hotspot' surrounded by cooler, denser fuel with the density and temperature required for nuclear fusion to occur [3]. This confinement can be performed using several approaches including Z pinches and high-power lasers. Whilst numerous inertial fusion schemes exist, this thesis will remain in the context of direct-drive inertial confinement fusion, indirect-drive inertial confinement fusion and magnetised liner inertial fusion (MagLIF).

Inertial Fusion Schemes

In direct-drive inertial confinement fusion a fuel capsule filled with a mixture of deuterium and tritium is illuminated directly by an array of high-power $10^{15} W cm^{-2}$ nanosecond laser pulses [4, 5]. The energy is absorbed at the surface of the capsule, illustrated in figure 1.1, ablating material off the surface and forming a plasma corona. In order to conserve momentum, the inner material is compressed by a 'rocket effect', driving the fuel to a high temperature hotspot, surrounded by a cooler, denser region. When the fuel ignites in the centre, the subsequent production of alpha particles spread out, causing a 'burn-wave' through the rest of the fuel. In this scheme, lasers propagate directly through the corona, imprinting the laser heating profile onto the surface of the capsule. As such this method is susceptible to hydrodynamic instabilities such as the Rayleigh-Taylor instability, seeded by the non-uniform laser imprint and capsule surface roughness, which mix up the plasma and cause non-uniform compression. This degrades confinement and can lead to high-Z material from the shell mixing deep into the fuel, radiating away energy from the core.

Indirect drive inertial confinement fusion instead has the high-power lasers illuminate the interior of a gold 'hohlraum', shown in figure 1.1. This process creates soft X-rays that drive the compression of the fuel capsule held in the centre of the hohlraum [6, 7, 8]. The benefit of X-ray driven compression over direct-drive is the uniformity of the radiation incident on the capsule surface, reducing the impact of laser-seeded hydrodynamic instabilities. However by using a X-ray bath the energy coupling to the capsule is much lower than direct-drive since the conversion of laser energy to X-rays by the hohlraum is not perfectly efficient, with only a fraction (Lindl et al. cites a conversion efficiency of $\sim 15\%$ [8]) of the incident laser energy eventually driving the capsule compression. In addition, in this process the laser is propagating through a plasma within the hohlraum, a result of a gas-fill or from the ablation of the hohlraum wall. This means the laser can be further susceptible to laser-plasma interactions (LPIs), focusing and backscatter as the beam enters the hohlraum.

High-power lasers are not the only way to compress a fuel capsule however. A Z-

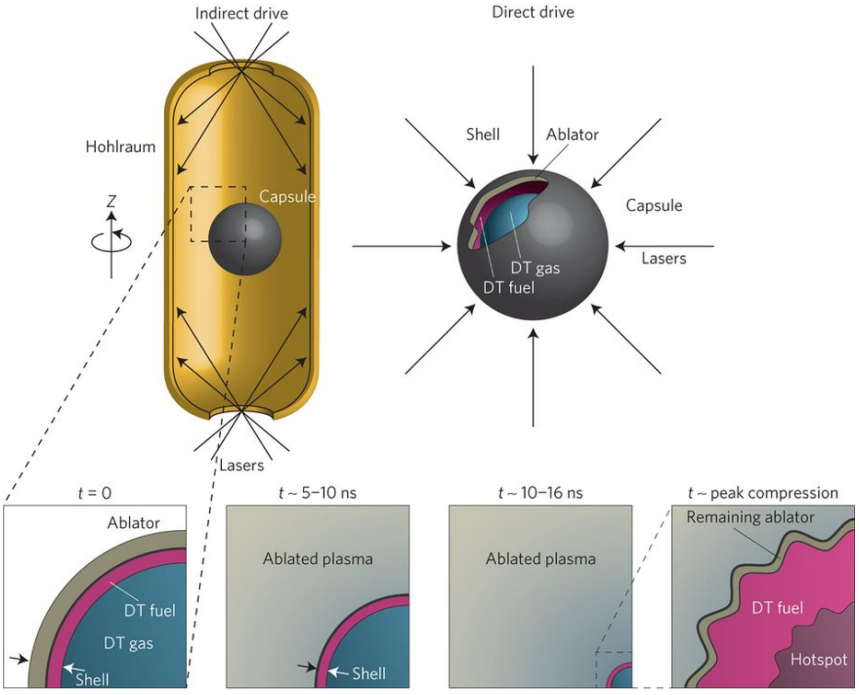

Figure 1.1: Illustration of indirect and direct drive ICF methods, taken from Betti *et al.* [6]. Indirect-drive (left) uses X-rays to compress a capsule, produced by laser-heating a gold hohlraum. Direct-drive (right) uses direct illumination of the capsule by high-power lasers. Reproduced from Betti *et al.* [6], with permission of Springer Nature.

pinch is a pulse power device that drives a very large current, with the Sandia National Laboratory - based Z accelerator producing peak drive currents of 18MA. When this current is passed through a cylindrical liner, it induces a very strong magnetic field. The magnetic pressure of this field implodes the liner, compressing the fuel within to fusion conditions (via PdV work). This convergence process lies at the heart of the MagLIF scheme [9, 10, 11, 12]. Unlike the laser-driven methods described above, the convergence is cylindrical, with a density that changes with $\sim (R_i/R_f)^2$; by comparison in spherical convergence the density changes as $\sim (R_i/R_f)^3$. To account for this less efficient compression, a pre-heat laser is used to heat the fuel in the capsule, pushing it onto a higher adiabat. This entails laser propagation through a 'window' into the fuel, exciting similar laser-plasma interactions and requiring a thorough understanding of thermal transport in the core.

Inertial fusion experiments were initially invented to create burning thermonuclear fuel, however these experimental setups have also found uses in creating exotic forms of matter such as warm dense matter [13], studying astrophysical analogues in laboratory astrophysics [14, 15] and testing equations of state [16, 17]. The understanding of the physics of high-energy-density plasmas goes beyond nuclear fusion.

Given the large and complex nature of these experiments - with a great deal of different physics operating at different time and length scales - theory and numerical simulation is paramount in understanding and designing such experiments [18]. The accurate simulation of high-energy-density physics on the world's largest supercomputers is a rich area

of science. With the advent of exascale computing, computational physics methods and the design of codes will only become more important in plasma physics.

1.2 Magnetic Fields in Laser Plasma Experiments

Thusfar the performance of fusion schemes has been found wanting, with the neutron production rate - the key sign that nuclear fusion has occurred - being lower than necessary. The pursuit of better performance in ICF experiments has led to proposing the use of applied magnetic fields [10, 12, 19, 20, 21].

Electrons in a magnetic field travel on circular Larmor orbits perpendicular to the direction of the magnetic field. If the field is strong enough, the electron mean free path can be effectively reduced to the radius of this orbit and the step-length of collisional transport processes are reduced to this Larmor radius perpendicular to the magnetic field. In this regime the plasma is magnetised and experiments can take advantage of the reduced thermal conductivity in order to better confine the thermal energy. In doing so these experiments aim to maintain higher temperatures, and hopefully overcome the Lawson criterion threshold.

This magnetisation is quantified in terms of the dimensionless Hall parameter, defined as the product of the electron cyclotron frequency ω_e and the electron-ion collision time τ_{ei}

$$\chi = \omega_e \tau_{ei}. \tag{1.3}$$

When this exceeds the order of 1-10, collisional transport in the plasma becomes magnetised. Following the formalism of Braginskii [22] this magnetisation causes the thermal conductivity in the plane perpendicular to the magnetic field direction, $\kappa_\perp$ to deviate from the classical isotropic form, κ by a factor that is a function of the Hall parameter,

$$\kappa_\perp \sim \frac{\kappa}{1+\chi^2}. \tag{1.4}$$

Aside from reducing the thermal conductivity, magnetisation of the plasma also induces new transport phenomena such as Righi-Leduc heat flow and thermoelectric effects such as the Nernst effect [16]. The Righ-Leduc heat flow is the flow of heat perpendicular to both the temperature gradient and the magnetic field, and it arises from the magnetic field rotating the heat flow vector as the electrons are deflected by the field. The Nersnt effect represents the advection of a magnetic field by temperature gradients, more information about these effects can be found in section 2.5. While the Nernst effect is inhibited for the regime $\chi >> 1$, it only requires a small value of magnetisation ($\chi << 1$) to be significant. These effects then feed into the dynamics of the plasma in ICF experiments through the generalised Ohm's law [23, 24].

In a magnetised plasma the transport becomes anisotropic, with the magnetic field breaking the spherical transport symmetry and providing a characteristic direction. This results in tensor transport coefficients and combined these transport phenomena can give rise to instabilities not present in unmagnetised plasmas, such as the magneto-thermal instability [25] and the Tidman-Shanny instability [26] (which only requires $\chi << 1$). These instabilities require the feedback of out of phase magnetised transport phenomena (such as the Nernst effect) that grow in the presence of large quasi-static plasma gradients. Magnetised instabilities like the magneto-thermal instability have been found to plague underdense laser-plasma simulations, growing to create steep non-linear profiles in temperature which cause the simulation code to fail [27].

Even in the absence of an applied fields, magnetic fields can be generated spontaneously in inertial fusion plasmas by numerous mechanisms such as the Biermann battery effect [28, 29, 30] and the electro-thermal instability [31]. They are observed in simulations using fluid models, such as Walsh *et al.* [32] who observed over 10^4T fields induced and driven into the core of ICF capsule implosions, where the Righi-Leduc effect cools the hotspot. Kinetic models also see self-generated fields, via a density gradient non-local mechanism not present in fluid models [33]. In these models magnetic fields can seed a Weibel-like instability and significantly impact transport [34].

Experimentally, fields up to 85T have been observed by Lancia *et al.* with proton deflectometry in the plasma corona of a long-pulse laser-foil experiment at the LULI facilty [35]. The thermal conductivity and magnetic field advection differed significantly from simulations without magnetised transport terms. Meanwhile Igumenshchev *et al.* observed fields up to 300T in nanosecond pulse direct-drive ICF experiments performed at the OMEGA facility (based at the Laboratory for Laser Energetics at the University of Rochester, USA). The ensuing magnetised transport was found to affect the growth of local perturbations [28]. Indirect-drive ICF is likewise susceptible, with Manuel *et al.* measuring Rayleigh-Taylor mixing that induced Biermann battery magnetic fields in regimes present in ICF hohlraums [36]. Magnetisation of the plasma in fusion conditions is inevitable and can lead to measurable changes in the plasma dynamics in simulations and experiments. Therefore incorporating magnetic field terms in simulations is necessary for accurate plasma physics models in inertial fusion regimes.

Key experimental platforms for investigating applied magnetic fields and transport are laser-gas-jet and laser-foil experiments. A simplified schematic for a laser-gas-jet can be found in figure 1.2. In these experiments a laser propagates through an underdense plasma, providing an analogy of the environment found in indirect-drive ICF hohlraums aswell as replicating astrophysical conditions.

Gregori *et al.* [37] used a gas-jet setup to study thermal transport in underdense long-pulse laser-plasmas, providing evidence for non-local transport that would map over to ICF experiments where plasma conditions are more difficult to measure. A > 10T applied magnetic field was found by Froula *et al.* [38] to quench the non-local transport in a gas-jet setup and Tang *et al.* used a magnetised laser-foil experiment to emulate the laser-hohlraum interaction [39]. They measured the ablation of material from a hohlraum-wall-

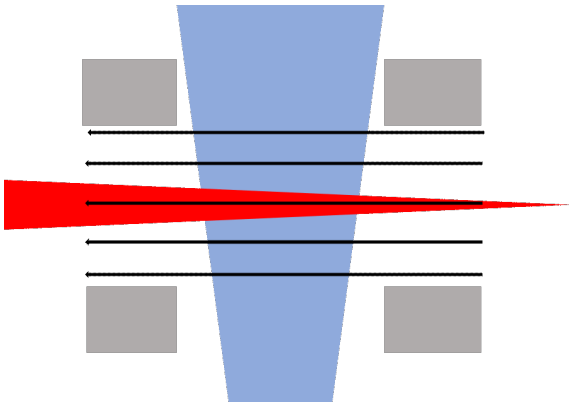

Figure 1.2: This diagram shows a simplified schematic of the magnetised laser-gas jet experiment. The laser (red) passes through a gas jet (blue) while a Helmholtz coil (grey) induces a magnetic field (black arrows) parallel to the laser.

like foil, and found a magnetic field confined the plasma bubble, potentially preventing the expansion of material into the ICF hohlraum.

Applying a magnetic field to a gas jet can also be performed using a capacitor coil, the simplified schematic for which can be found in figure 1.3. These devices can produce magnetic fields of strengths much higher than conventional Helmholtz coils, with Fujioka *et al.* [40] measuring fields on the order of kiloteslas. This provides another platform in which very strong magnetic fields influence plasma dynamics.

Magnetised Inertial Fusion Schemes

The application of magnetic fields to a direct-drive experiments follows the simplified schematic of figure 1.4, where a Helmhotz coil induces a field that is rapidly compressed as the fuel capsule implodes.

The role of magnetic fields in direct-drive ICF has been found by Chang *et al.* [20] and Hohenberger *et al.* [41] to increase fusion yields and increase the ion temperature by restricting the thermal conductivity. They performed direct-drive implosions at the OMEGA facility with a seeded magnetic field from a Helmhotz coil, illustrated in figure 1.5. As the fuel capsule converged, the magnetic flux was similarly compressed, magnetising the hotspot. The heat flow was suppressed, resulting in ion temperatures 15% higher and neutron yields 30% higher than unmagnetised shots. Even if no magnetic field is applied, the self-generated fields induced during the plasma evolution are strong enough to affect heat fluxes in the conduction zone and can be transported via the Nernst effect [28].

The benefits of applied magnetic fields have also been investigated in the context of indirect-drive ICF. In this case, the hohlraum of an indirect drive experiment is magnetised by an axial magnetic field from an external Helmholtz coil, a simplified schematic for this setup is shown in figure 1.6. Perkins *et al.* [19] performed magnetised hohlraum simulations that showed magnetisation with ~ 10T fields relaxed the conditions required for thermonuclear burn. Figure 1.7 illustrates the results of these simulations, it shows

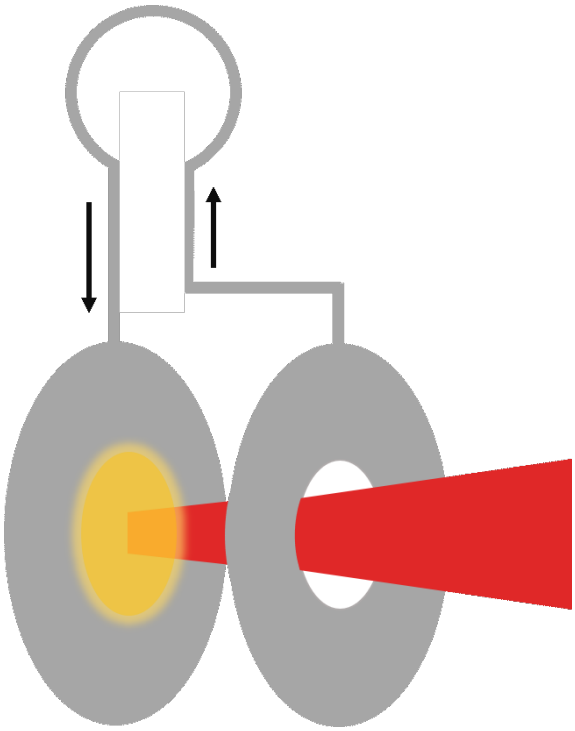

Figure 1.3: A simplified diagram of the capacitor coil setup used to magnetise a laser-gas experiment. The laser (red) passes through a washer (grey) through which a very large current pulse induces a strong magnetic field in a coil connecting the plates.

how the magnetisation of the hohlraum shifts the drop-off in yield so that implosions can achieve ignition with inflight conditions that would otherwise only result in low yields. The reduction in the perpendicular heat flow, localisation of alpha particle transport and stabilisation of the Rayleigh-Taylor instability for high modes improve the conditions for ignition.

Further experiments performed by Montgomery *et al.* [21] have found $\approx 7T$ fields applied axially with the hohlraum can improve the laser coupling with the hohlraum wall. The higher electron temperatures measured decreased the laser energy losses via inverse bremmsstrahlung. With greater coupling, the energy budget available to X-ray generation for fuel capsule compression is higher. Simulations of this setup performed by Strozzi *et al.* [42] corroborated the experimental result in the context of National Ignition Facility ICF regimes and saw 12 times higher energy deposition into the D-T fuel. Again the laser propagation through the intermediate plasma and its interaction with the wall 'blow-off' plasma is the deciding factor that determines the improvement to coupling under magnetic fields.

Like the laser methods described above, the MagLIF scheme [9, 10] relies on an axial magnetic field to reduce the perpendicular heat flow in the D-T fuel within the liner. In this concept, the D-T fuel lies in a capsule within a metal liner. A laser pulse pre-heats the fuel under the magnetic field before the Z-pinch liner implosion; figure 1.8 shows an idealised diagram of how the scheme works.

The concept has been tested at the Z-machine facility at Sandia National Laboratory by

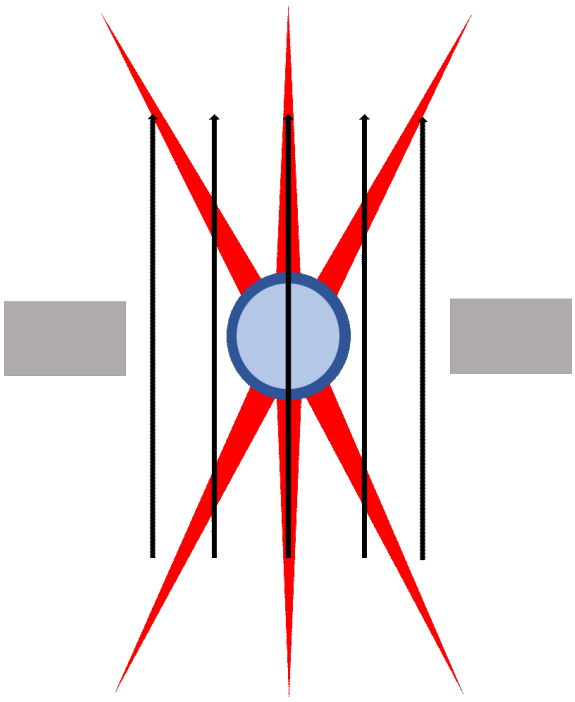

Figure 1.4: This is a diagram of the magnetised direct-drive inertial fusion scheme. The fuel capsule (blue) is directly irradiated by long-pulse lasers (red), ablating the surface and compressing the fuel inside. The coil (grey) induces a magnetic field (black arrows) parallel to the polar axis of the capsule.

Gomez *et al.* [12]. Experimental results found the scheme produced fusion-relevant conditions with an applied field of $\approx 10T$. However discrepancies between simulations and the laser-coupling results remained, with only a fraction of expected pre-heat laser energy coupling to the fuel. This was puported to be the result of unexpected backscatter from LPIs. Laser pre-heat experiments performed by Sefkow *et al.* [43] and Harvey-Thompson *et al.* [44] have found the magnetic field increases the laser energy coupling to the plasma, in addition to the reduction of perpendicular thermal transport. However these experiments also found discrepancy in laser propagation between simulations and experimental results.

Thusfar we have seen the use of several laser-based fusion schemes, but results from experiments lead to the question of the effect of the magnetic field on laser propagation through the plasma itself. Studies of laser propagation in fusion conditions have not commonly incorporated magnetised transport terms into the laser dynamics, as such there is a need to study the influence of magnetised transport on laser propagation.

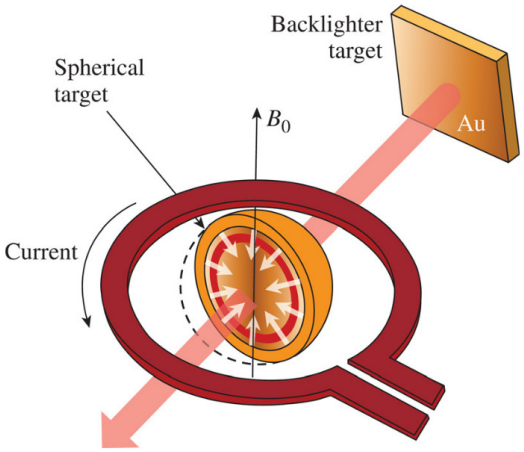

Figure 1.5: Schematic of a magnetised direct-drive ICF capsule experiment performed at the OMEGA facility. A magnetic field is seeded by the coil before being compressed as the capsule implodes. The implosion is diagnosed by an X-ray backlighter. Taken from Hohenberger *et al.* [41], reproduced with permission of AIP Publishing.

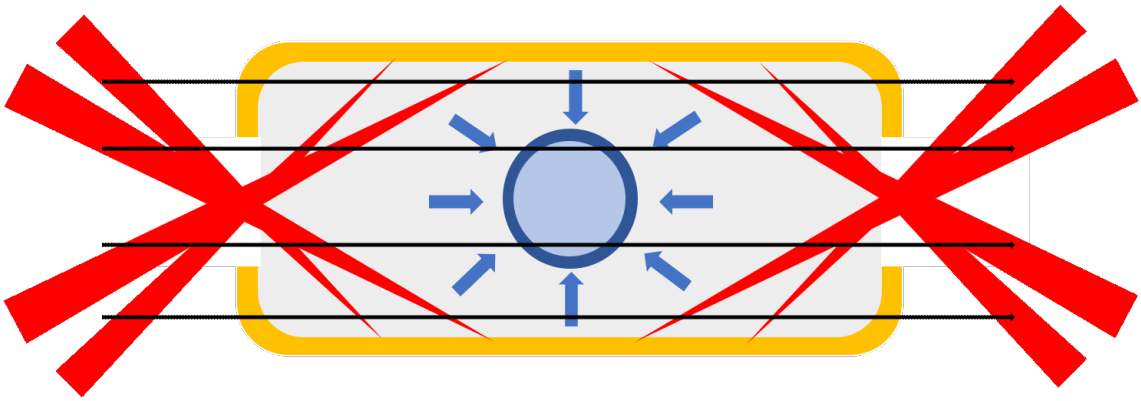

Figure 1.6: This diagram shows a simplified schematic of the magnetised hohlraum indirect-drive fusion scheme. The hohlraum (gold) is irradiated by an array of lasers (red), producing a bath of X-rays (blue arrows) which compress a fuel capsule (blue circle). A magnetic field (black arrows) can be applied externally to the hohlraum.

1.3 Modelling Lasers and Plasmas

Key to designing and understanding the outcomes of the experiments described above is the use of simulation codes. Plasmas exhibit a wide range of complex behaviour over an enormous parameter space. To tackle theoretical predictions with analytic methods alone limits one to idealised systems. As such numerical methods are an indispensable tool in laser-plasma physics. With a better understanding of the physics from fully non-linear simulations, one can gain valuable insights into the physics involved.

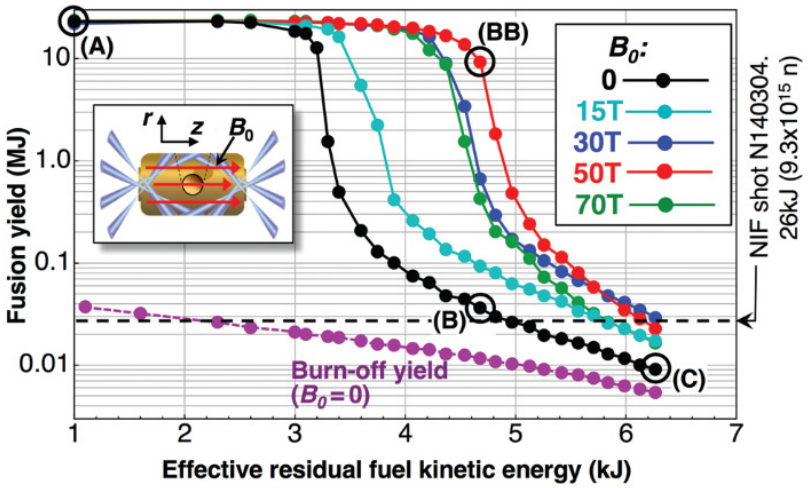

Figure 1.7: Fusion yield against residual fuel kinetic energy in 2D ICF simulations performed by Perkins *et al.* [19]. The 'ignition cliff' is shifted to the right as higher magnetic fields are applied, showing that magnetic fields allow the fuel to withstand larger perturbations while still producing a significant neutron yield. Reproduced from Perkins *et al.* [19], with permission of AIP Publishing.

Approaches to Simulating Plasmas

To simulate plasmas, two broad approaches are in common use. The first, the fluid model treats the plasma as a fluid [45]. In these numerical models the code solves the conservation equations for mass, momentum and energy. Fluid codes such as FLASH [46] are fundamentally important in the simulation of plasma physics experiments, providing explanations for observations. However for fluid models to be a closed set of partial differential equations they require a closure relation; this relation requires the distribution function for the species to be close to equilibrium. Furthermore for a single-fluid model like the one used in this thesis, the plasma must also be quasi-neutral. These requirements are often broken in real experiments.

The second approach are kinetic models, these models are classed into particle-in-cell (PIC) [47] and Vlasov-Fokker-Planck (VFP) codes [48]. PIC methods solve Hamilton's equations directly for macro-particles of the electrons and ions in the plasma. This allows the ions and electrons to diverge arbitrarily from equilibrium whilst also self-consistently including the electromagnetic field. Their downside is that they can be computationally very costly and fail to easily include Coulomb collisions and sub-Debye length physics.

VFP models solve the VFP equation directly for the particle distributions. As the distribution function is six-dimensional, this model is computationally very costly. However the dimensionality of the problem can be reduced by taking a spherical harmonic expansion of the distribution, this approach is used in codes such as OSHUN [49] and IMPACT [50]. These models are crucial to understanding the physics of ICF plasma physics because they can capture phenomena not present in fluid codes, such as non-local transport and the dynamics of non-thermal particle populations. Non-Maxwellian popula-

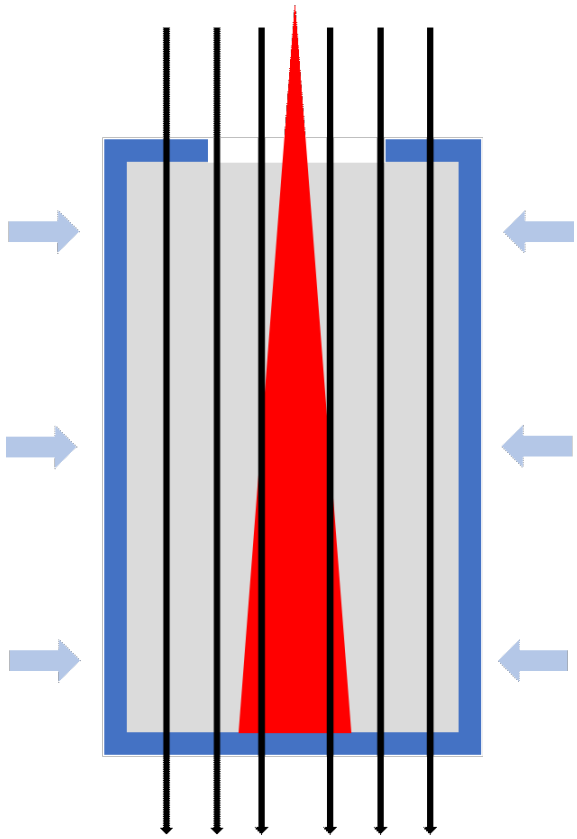

Figure 1.8: A simplified schematic of the MagLIF fusion scheme during the pre-heat stage. A long-pulse laser (red) pre-heats the fuel (grey) inside a cylindrical liner (blue). A magnetic field (black arrows) can be applied parallel to the laser during the pre-heat stage to aid thermal energy confinement. The liner then implodes, compressing the fuel.

tions arise naturally in ICF plasmas through LPIs and fusion reactions, while also being intrinsic to ICF schemes such as fast ignition. The very short timescales and lengthscales of shock fronts of an ICF experiment can also mean the inter-particle collision frequency may not be high enough to thermalise the plasma to local thermal equilibrium, producing regions where the plasma is far from a Maxwellian. In this case a kinetic model is necessary for an accurate simulation. While PIC models are used to simulate fast electron populations [42], VFP models can naturally incorporate collisions and are also free from the statistical distribution sampling noise present in PIC models.

The two most popular methods for simulating laser are ray-tracing and the paraxial approximation. The first, ray-tracing methods, are popular due to their simplicity. In a ray-tracing model the laser is modelled as a bundle of rays that represent paths normal to the wavefront, and relies on the theory of geometric optics. Refraction and reflection of the rays can be easily incorporated into a ray-tracing model by considering the local refractive index, but the diffraction and interference of light cannot be simulated because ray optics effectively assumes the wavelength $\rightarrow 0$.

The second laser simulation approach is the paraxial method [51]. This model solves a reduced Helmholtz equation for the laser's electric field, where the laser wavevector is assumed to be approximately unidirectional. The benefit of the paraxial method is that

is can provide the intensity of the laser field directly, rather than attributing an intensity profile to a bundle of rays. In doing so this model can simulate diffraction, interference and small-angle refraction. The downside however is this model is limited to underdense regimes where the electron density is much less than a value known as the critical density n_c (i.e. $n_e << n_c$). This critical density is the electron density at which the plasma frequency is equal to the laser frequency, further of which details can be found in section 2.1 and chapter 3. In recent years the work of Colaitis *et al.* has introduced a mixed-paraxial-geometric laser model that may combine the best of both worlds [52].

In fluid and VFP models the laser is coupled to the plasma via extra source terms whilst in PIC models the electric field of the laser is incorporated self-consistently into the solution of Maxwell's equations. Coupling mechanisms such as inverse bremmstrahlung, the ponderomotive force and resonance absorption must be included in fluid models by using extra individual source terms, while kinetic codes must add a source term whereby the laser can couple to the electron distribution [53]. In ICF schemes where laser-coupling is the driver for the plasma evolution, the accuracy of the coupling is of fundamental importance.

Each approach has its limitations, none being perfect for every laser-plasma system one might wish to investigate. Plasma physics in fusion experiments is inherently multi-scale [18] with different phenomena having characteristic time and spatial scales that range over a wide parameter space. This limits their predictive capacity and make full simulations computationally very costly.

The Simulation Regime

The lasers driving the plasmas of the aforementioned experiments and relevant to this thesis are *long-pulse*. This regime is typified by lasers with intensities approximately $\sim 10^{15} W cm^{-2}$ with a pulse duration on the order of $1ns$. This choice reflects the current status of high-power laser systems used in the field of high-energy-density physics. The lasers that make up the National Ignition Facility (NIF) (based at the Lawrence Livermore National Laboratory in the USA), currently the largest and most powerful ICF facility, generate nanosecond pulses of up to 1.8 MJ with a peak power of 500 TW with a wavelength of 351 nm [54]. The Laser Mega-Joule (LMJ), a similar facility dedicated to indirect-drive ICF, produces pulses of 1.5 MJ and a peak power of 400 TW at $1\mu m$ (frequency tripled to 351 nm) [55]. These facilities represent the upper limit of current experimental apparatus for high-energy-density physics, able to create matter at extremes of density and temperature.

The experiments mentioned in this section made use of Helmholtz coils to produce pulsed magnetic fields. These apparatus are however limited to field strengths in the range of tens of Tesla, which will be the region of interest to this thesis. Though much stronger magnetic fields have been produced with the aid of capacitor coils [40], they lie out of the scope of this thesis since the plasma beta, the ratio of thermal to magnetic pressure, is no longer very large. When the plasma beta is very small, magnetic pressure

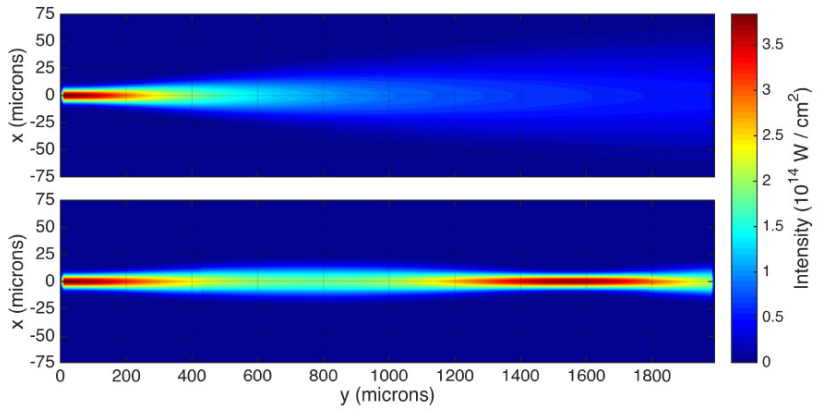

Figure 1.9: Magnetised laser self-focusing reported by Read [58] shows when the Nernst effect is included (above) the beam does not focus, but does when it is ignored (below). Reproduced from Read *et al.* [58], with permission of IOP Publishing

dominates the hydrodynamics, with the charged particles bound to guiding centres and the excitation of magnetic plasma wave modes [56].

Furthermore, the plasmas under consideration are all underdense. This is the regime where the electron number density n_e is much smaller than the plasma critical density n_c (up to $n_c/4$). This region of parameter space is of such interest because it lies in the intersection of current laser technology and its applicability to inertial fusion schemes. The corona of a direct-drive capsule [4], the 'blow-off' plasma and gas-fill plasma of an indirect-drive hohlraum [8] and the fuel during the pre-heat stage of a MagLIF shot [43] all have electron densities lower than the critical density. This underdense plasma allows the use of paraxial laser-modelling methods introduced in the previous section, and the relatively low density means the laser absorption is dominated by inverse bremmsstrahlung. This will simplify the modelling of the plasma in later chapters, where higher density, overdense laser-plasma interactions are left out of the scope of this thesis.

Simulations of Magnetised Laser Propagation

Given the fundamental importance of lasers in this field, the study of laser-plasma interactions has been the subject of a great of study and yielded a zoo of complex effects [57]. These complicate the problem of simulating long-pulse laser-plasma experiments and interpreting the outcome. One particular effect, self-focusing, will be explored in depth in this thesis and its influence on experiments will be analysed in the context of magnetisation in chapter 5. Read *et al.* [58] reported simulations using a coupled 2D laser-fluid-plasma code, highlighting the role of Nernst advection of the magnetic field on self-focusing, illustrated in figure 1.9. Furthermore, Perkins *et al.* showed the thermal mechanism is significant in self-focusing [59]. This leads to the question: if the magnetisation of a plasma can reduce the thermal conductivity, then it should follow through to the thermal focusing mechanism. This will be explored in much greater depth in chapter 5.

Like focusing, when the beam has small scale non-uniformity, the resulting filamentation may also show a magnetic field signature. Filamentation has been well studied [60, 61, 62] and its effect on the coupling of lasers and inertial fusion plasmas well characterised, however the work in magnetised plasmas remains wanting. Simulation methods have been developed, [52, 63] but lack the incorporation of the extra transport terms despite the recognition of their importance in hydrodynamics [23].

Small scale structures in the laser beam from speckles or seeded elsewhere can imprint on the capsule in direct-drive experiments [5, 64, 65, 66], providing a source of hydrodynamic instability. If the filamentation of lasers in the plasma corona are susceptible to magnetised transport corrections, then this could exacerbate imprint and be detrimental to compression stability. In an inertial fusion scenario, parametric instabilities plague fusion yield performance [67, 68, 69]. Indirect-drive hohlraums may also be susceptible to magnetised corrections to laser propagation that compound the production of these parametric instabilities. Performing simulations that can predict the behaviour of the aforementioned phenomena with the addition of magnetised transport terms would shed light on their effect on fusion experiments.

1.4 Non-Local Transport and Magnetisation

Problems with the aforementioned fusion schemes remain, one notable problem is in the difficulty of correctly calculating thermal transport in a laser-driven plasma. The non-Maxwellian deviation of thermal transport from the classical Spitzer-Härm approximation has been known for many years, with work by Bell [70, 71] and Albritton [72, 73] providing some of the first theoretical work. The electron distribution function is generally assumed be Maxwellian with only small deviations from local thermal equilibrium. This local approximation holds in the regime $L_T >> \lambda_{ei}$, where the electron-ion collision mean-free-path λ_{ei} is much smaller than the temperature scale length L_T defined as

$$\frac{1}{L_T} = \frac{1}{T}\frac{dT}{dx}. \tag{1.5}$$

More details on non-locality can be found in section 2.7.

In high-energy-density physics and ICF experiments this condition is broken [74], with evidence of non-Spitzer-Härm heat flux limitation dating back to the 1970's [75]. Experiments performed at the OMEGA facility found the non-local effect to be so significant as to require an extra simulation model package to replicate the results of measured non-Spitzer-Härm thermal conductivity [76, 77]. Gregori *et al.* provided direct experimental evidence of non-local transport in an ICF-like gas-jet experiment driven by a nanosecond $1.5 \times 10^{14} W cm^{-2}$ laser [37], the temperature and density profiles showed very good agreement with a VFP numerical model but replicated poorly by a flux-limited

fluid model. Altogether these results imply non-locality is of paramount importance in understanding long-pulse laser plasma interactions.

One approach to incorporate the a more accurate kinetic model into the analysis of transport is the so called *diffusion approximation*. This approximates the full kinetic problem by considering an expansion of the VFP equation in terms a Cartesian tensor expansion and truncating the expansion after only the first term.

$$f_e(\mathbf{x}, \mathbf{v}, t) = f_0(\mathbf{x}, v, t) + \mathbf{f}_1(\mathbf{x}, v, t) \cdot \frac{\mathbf{v}}{v} \tag{1.6}$$

In doing so the 6-dimensional partial differential equation becomes a simpler 4-dimensional pair of equations that model the evolution of the isotropic and anisotropic contributions to the electron distribution function. More details on this approximation can be found in section 2.7 and 6.3. The diffusion approximation is commonly used in the analysis of non-equilibrium plasmas because of the relative simplicity of the equation set.

Non-Local Transport Models

Simulations of plasmas in non-local regimes such as ICF hohlraums and Tokamak scrape-off layers cannot accurately predict the heat flow due to this non-local nature. While numerous models have been create to account for non-locality, advances in high-energy-density physics are required to better understand how to close the hydrodynamic equations in systems far from equilibrium. Kinetic simulation codes such as KALOS, OSHUN and IMPACT [49, 50, 78] can accurately reproduce this non-local transport, with and without the presence of a magnetic fields. Incorporating their calculations into the fluid codes that are the workhorses of experimental design and interpretation is difficult because of the large computational requirements of kinetic simulations.

Non-local models based on convolutions of the local thermal transport were the first attempt at avoiding solving the full VFP while reproducing thermal transport [79, 80, 81]. These models require convolution over a large domain and have been found difficult to generalise to 3D problems. Figure 1.10 shows the convolutional kernel used by Epperlein, derived as a correction factor to Spitzer-Härm conductivity. While simpler than a full VFP calculation, the convolutional kernel is chosen somewhat arbitrarily and there is little insight into the physical mechanism.

Transport models derived from the simplified VFP equation such as the SNB model [84, 85], the M1 model [86] and the CMB model [87, 88, 89] are more readily incorporated into fluid codes [76]. The SNB model has also been readily extended to include magnetic fields [90]. Comparisons of these models with fully kinetic codes, in both the magnetised and unmagnetised cases, have however found errors. Detailed comparisons performed by Sherlock *et al.* [91] and Marocchino *et al.* [92] found these reduced models could replicate the characteristic flux limitation but significantly over-estimated the precursor heating in front of the temperature gradient. Further tests performed by Brodrick *et al.* [93] showed the SNB model to be more accurate than the eigenvector integral closure (EIC) [94] and Landau fluid (NFLF) [95] models; however even when the heat flux is correctly calcu-

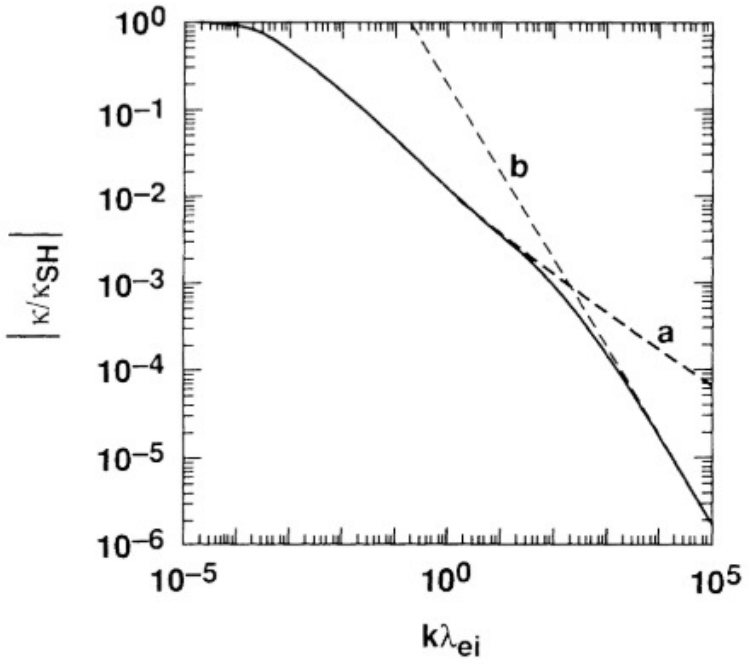

Figure 1.10: The non-local (encapsulated in the parameter $k\lambda_{ei}$) dependence of thermal conductivity calculated by Epperlein [82]. Note the gradient of the drop compared to previous models by Bell (dashed line a) [71] and Hammett and Perkins (dashed line b)[83]. Reproduced from Epperlein *et al.* [82], with permission of the American Physical Society.

lated, the underlying distribution function is far from accurate. These models are also all reliant on the diffusion approximation, the validity of which is questionable in the face of evidence found by Feugeas *et al.* [96]. In this work, 2D hotspot simulations showed the diffusion approximation breaks down, and more terms in the polynomial expansion are required to match an exact kinetic model.

Non-Locality and Laser Propagation

In laser propagation, the thermal mechanisms of self-focusing and filamentation of a laser are mediated by the thermal conductivity; as such we expect these processes to be modified by a mixture of non-locality and magnetisation. Kinetic theory applied to linearised filamentation models by Epperlein [97, 98] and corresponding simulations [99] show the thermal mechanism becoming dominant because of a non-local reduction in thermal conductivity. This can increase the growth rate of filamentation far above the local model, which is illustrated in figure 1.11. This figure compares the growth rates of filamentation against wavenumber of three mechanisms, the first is for the thermal mechanism derived from kinetic theory, the second is for the classical thermal mechanism derived from a fluid model, and the third is the growth rate for filamentation resulting from the ponderomotive force of the laser. Functional forms for these growth rates are discussed in greater detail in sections 5.4 and 6.2. Methods have been derived to go beyond the diffusive approximation; for linear waves in a plasma Epperlein defined a correction to the

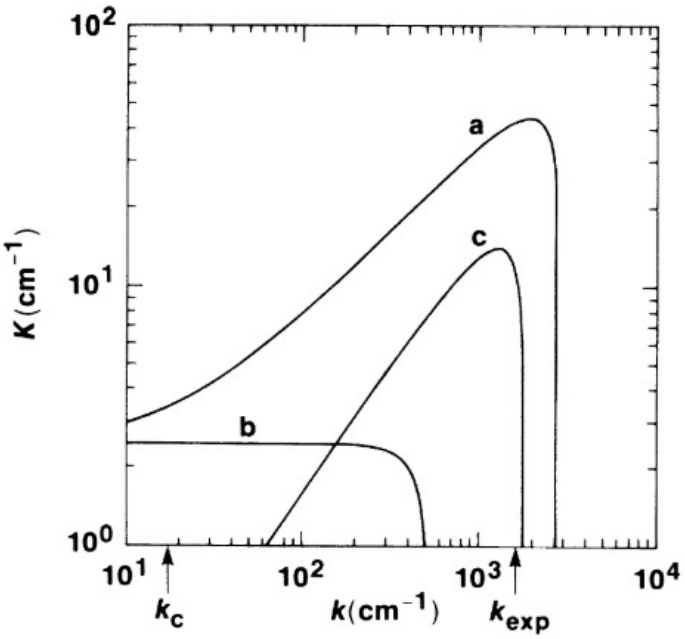

Figure 1.11: Non-local filamentation growth rates calculated by Epperlein [98] show the kinetic thermal mechanism growth rate (a) is much higher than the classical thermal mechanism rate (b) and ponderomotive mechanism (c) rates. Reproduced from Epperlein [98], with permission of AIP Publishing.

collision frequency that could go beyond the diffusion approximation and account for the the whole electron distribution expansion [82]. Bychenkov *et al.* then applied this method to the decay of waves, and derived transport coefficients that were exact in the regime of linear perturbations [100]. While useful for unmagnetised plasmas, this result has not been applied to magnetised focusing, or to the explanation of the interplay between magnetisation and non-locality.

Furthermore, energy deposition by a laser into a plasma is dominated by inverse bremsstrahlung, which has also been shown to skew the electron distribution away from a Maxwellian towards a flat-topped 'super-Gaussian' distribution [53, 101]. This is a Gaussian distribution

$$f(v) \propto \exp(-cv^m), \tag{1.7}$$

but with $m > 2$. This is caused by inverse bremmsstrahlung preferentially heating electrons close to the quiver speed of the laser field. This will also change the transport away from the classical calculation, adding yet another source of non-Maxwellian behaviour in laser-plasma experiments.

The Influence of Magnetic Fields

The Nernst effect and the Righi-Leduc heat flow in magnetised simulations are similarly affected by non-local transport. Kho and Haines saw significant deviation from classical coefficients in 1D VFP simulations, with the magnetic fields strongly coupled to the heat flow [102, 103]. The deviation extends to indirect-drive ICF simulations. Simulations

performed by Joglekar *et al.* of a pre-magnetised ICF hohlraum saw $3\times$ enhanced magnetic field from Nernst advection itself amplified $2\times$ as a result of non-locality [104]. The heat flow is also strongly non-local, driving higher temperatures at the hohlraum axis. Comparisons between simulated and experimental heat transport at NIF performed by Farmer *et al.* [105] saw much better agreement with the non-local numerical model and also found the Righi-Leduc heat flow was necessary to explain the results in this magnetised, non-local system.

The non-Maxwellian electron distribution results in the other magnetised transport coefficients similarly diverging from their classical Braginskii form. Kinetic simulations by Hill and Kingham [106] and Strozzi *et al.* [42] including magnetic fields imply the non-locality of these other magnetised transport effects significantly changes the dynamics in both direct-drive and indirect-drive respectively. As such there is a need for a model that can be used in codes that accurately reproduces the full range of magnetised transport that is present in VFP simulations without the computational overhead.

Exact non-local linear models have been developed by Brantov *et al.* [107] and Frolov *et al.* [108]. These do give transport coefficients but are limited to the linear regime of plasma wave decay. The results of Brantov *et al.* are illustrated in figure 1.12, where the position of the characteristic 'drop-off' of the thermal conductivity with non-locality changes with magnetisation. This result was obtained by considering the decay of linear perturbations with a wavevector at 45 degrees to a constant magnetic field in a uniform background plasma.

Another approach followed by Brodrick *et al.* uses the SNB thermal transport model, applying it to find a correction to the coefficient responsible for Nernst advection [109]. This method relies on the strong coupling between heat flow and magnetic fields, with the electron fluid 'dragging' around the magnetic fields. This relies on Haines approximation based on the similarity of the terms in Ohm's law [110]. These methods all however rely on the diffusive approximation, as such the electron distribution function must be close to an isotropic Maxwellian, despite the magnetic field introducing an inherently anisotropic term to the VFP equation. Magnetic fields complicate the creation of an accurate model of non-local transport, with the complex interplay between non-locality and magnetisation greatly influencing transport in plasmas.

1.5 Studies of Laser Propagation in a Magnetised Plasma

The over-arching theme of this thesis is how magnetic fields can influence the transport of thermal energy and magnetic fields in long-pulse laser-plasma experiments. The first result of this thesis will describe investigations into the laser propagation dynamics in experiments under magnetic fields. The motivation for this work is the result of the experiments described in the previous section where long-pulse lasers propagated through

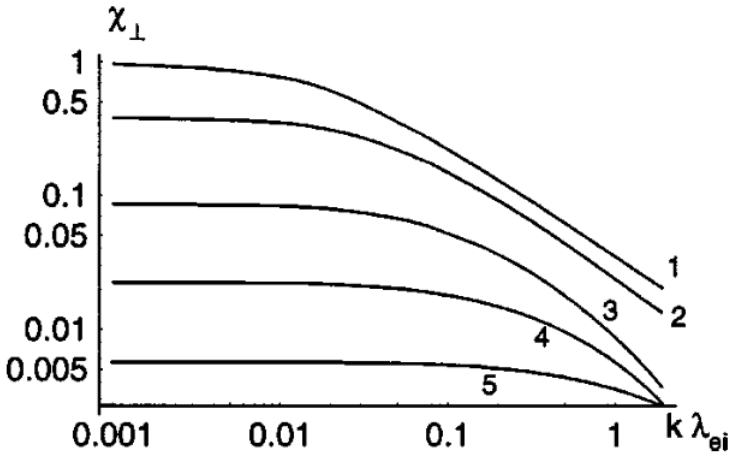

Figure 1.12: The normalised perpendicular thermal conductivity (with the symbol $\chi_\perp$) as a function of non-locality parameter ($k\lambda_{ei}$) for different values of magnetisation, as calculated by Brantov [107]. It shows the conductivity decreasing with both non-locality and magnetisation. Reproduced from Brantov *et al.* [107], with permission of AIP Publishing

ICF plasma conditions. The pre-heat stage of a MagLIF experiment, a hohlraum with a gas-fill in an indirect-drive experiment and a direct-drive coronal plasma all sit in the regime of a collisional magnetised plasma.

The theory of self-focusing [59] suggests the magnetic field present in these experiments should feed into the focusing dynamics via the thermal conductivity. The question to answer is how does this happen? How does this effect experiments? It follows from the theory of self-focusing that the similar phenomenon of laser filamentation should also be exacerbated by the magnetisation of the thermal conductivity. Ideally one would want a model of filamentation, supported by simulations that elucidated the influence of magnetisation.

The system of equations in this laser-plasma model is very complex and therefore accurate predictions require the construction of a numerical model. This code, PARAMAGNET (PARAllel MAGnetised Newton-method Electron Transport) is a 3D magneto-hydrodynamic code that incorporates full Braginskii electron transport with Epperlein and Haines coefficient corrections [111]. This magneto-hydrodynamic model is coupled to a paraxial laser model to allow the accurate simulation of long-pulse laser dynamics, the full description can be found in Chapter 4. By using a 3D code, inherently 3 dimensional effects such as Righi-Leduc heat flow can be simulated. Previous studies have neglected magnetic field effects, assuming them to be irrelevant due to the low plasma beta in such plasma regimes, however this thesis will present results suggesting this is not a good approximation.

Alongside the numerical model, a theoretical model has been developed that elucidates the effect of magnetised thermal conductivity on self-focusing and filamentation. Together the simulation and theoretical results demonstrate that applied magnetic fields can enhance the rate of growth in space of the filamentation instability as the laser propa-

gates across the domain; the theoretical model is shown to be in qualitatively good agreement with PARAMAGNET simulations. Figure 1.13 shows how the magnetic field effects the focal length in laser propagation. The full results can be found in chapter 5. In in the context of experiments, this result means the applied magnetic fields play a significant role in the behaviour of lasers in underdense plasmas, despite the low plasma beta.

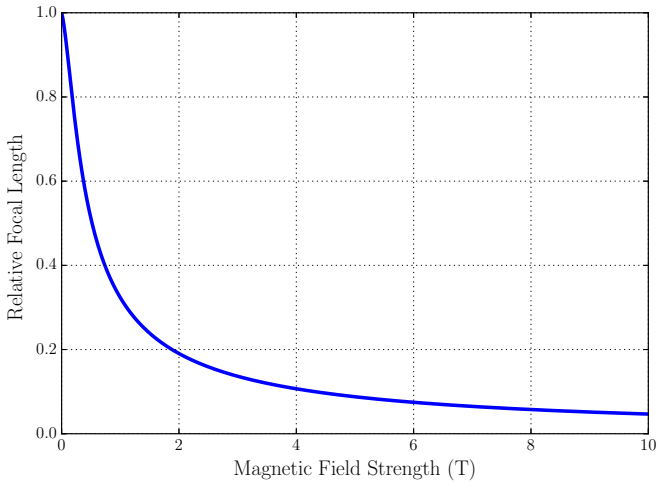

Figure 1.13: The application of a magnetic field is found to shorten the self-focal length of a laser propagating through a plasma. This plot is taken from chapter 5, where the full results are described in detail. Reproduced from Watkins and Kingham [112], with permission of AIP Publishing.

1.6 Studies of Non-Local Transport in Magnetised Plasmas

The second set of results presented herein will extend the thermal decay analysis to include non-local corrections, and so find a more accurate result for magnetised laser propagation. The first step would be to find a diffusive approximation correction using a kinetic code by performing the Epperlein-Short test [97]. Performing this test with the IMPACT code meant simulating the decay of linear thermal perturbations over a range of modes and comparing it to the local approximation. A phenomenological fit to the numerically-simulation data yielded a correction factor as a function of the magnetisation and non-locality parameter.

Past kinetic studies of laser filamentation such as Epperlein [98] neglected the influence of magnetic fields. With this correction, the dispersion relations and growth rates of filamentation were found to diverge from the local approximation. Chapter 6 will show these kinetic growth rates are higher in regions accessible to current laser-plasma experiments. The growth rate of filamentation is a key metric of stability as a laser propagates through a plasma. As such in the context of fusion experiments, these unaccounted-for

kinetic effects can be detrimental to laser-plasma energy coupling and propagation in experiments such as in MagLIF pre-heat and laser-gas-jets.

In previous studies of linear non-local corrections, Epperlein [82] only considered an unmagnetised plasma, and did not calculate transport coefficients. Bychenkov [100] calculated transport coefficients using Epperlein's correction factor, again it lacked a magnetic field. Brantov [107] extended the theory to include magnetic fields but the result relied on the diffusive approximation. Including both the magnetic field and the higher-polynomial terms considerably complicates the problem, but this leaves an important gap in the theory. Furthermore the resulting coefficients were calculated numerically, such that there was no closed-form expression that could be used in a simulation code. Though lineouts teased interesting results as to the combined non-local magnetised effect, the work lacked sufficient explanatory power.

The higher polynomial terms of the spherical harmonic expansion of the electron distribution are conventionally ignored in local fluid models. This thesis will also investigate how they influence magnetised transport. Non-local transport models such as the SNB model [84, 85, 90] also ignore the higher-order terms, sticking to the diffusion approximation. Chapter 6 will analyse the error that comes from ignoring these terms and how their absence from the closure effects the Nernst effect, perpendicular thermal transport and all the other transport coefficients.

Chapter 6 will show how the truncation of the distribution function expansion leads to errors in the corresponding transport coefficients. Comparison of the truncated and full expansion at intermediate non-locality values ($k\lambda_{ei} \approx 10 - 100$) will show significant deviation. This leads to transport coefficients varying significantly from expected behaviour as reported by Brantov [107]. This suggests a complex interplay between the localising effect of magnetic fields and the non-locality of non-Maxweillian distributions. As an example, figure 1.14 shows a map of the correction factor to the diffusive approximation. The interplay between non-locality and magnetisation requires a more complete treatment of transport for simulations to be accurate to experimental results.

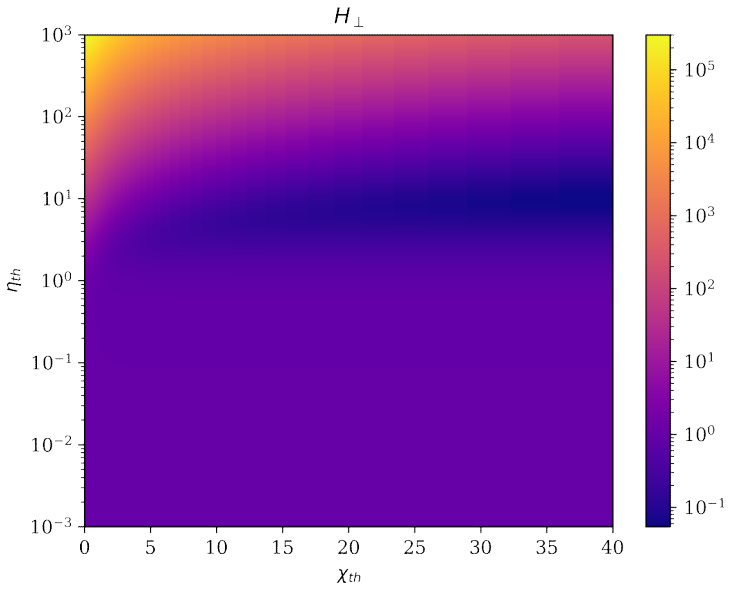

Figure 1.14: This 2D parameter map shows the correction factor for perpendicular transport. The dependence on magnetisation χ and non-locality parameter η is not simple, with a clear valley that widens as magnetisation increases. This plot is taken from the results from chapter 6

1.7 Thesis Outline

- **Plasma Physics Theory**

  This chapter will introduce the necessary plasma physics theory used in this thesis, including a description of kinetic theory in plasmas and the derivation of the MHD equations. The transport closures in a magnetised plasma will also be discussed.

- **Laser Propagation in a Plasma**

  Laser propagation in terms of the slowly-varying envelope approximation will be introduced and the paraxial equation derived from the Helmholtz model. The coupling with a fluid plasma via the ponderomotive force and inverse bremsstrahlung will be reviewed and their source terms in the fluid equation set introduced.

- **Code Architecture and Testing**

  After introducing the numerical methods employed by the PARAMAGNET code, the design and implementation of said methods will be described in detail. In this chapter the code will be tested against several standard numerical MHD and laser tests to examine the accuracy and capabilities of the code.

- **Magnetised Laser Self-Focusing and Filamentation**

  Theory and simulations are presented that analyse the influence of collisional magnetised effects on the phenomena of laser self-focusing in an underdense plasma. The related phenomena of filamentation is likewise investigated under a magnetic field using analytic theory and the simulation code.

- **Non-local Corrections to Filamentation and Magnetised Transport**

  The kinetic code IMPACT is used to find corrections to fluid approximations and delve deeper into the combined magnetisation and non-local physics. Kinetic theory is used to extend the ideas of the previous chapter to investigate the combined influence of non-locality and magnetisation beyond the diffusion approximation of IMPACT.

- **Conclusions**

  I conclude the thesis with a discussion of the major results and their meaning within a broader context of the field of plasma physics and fusion; ending with a discussion of future work and possible extensions.

1.8 List of Publications

- Watkins, H.C. and Kingham, R.J. "Magnetised thermal self-focusing and filamentation of long-pulse lasers in plasmas relevant to magnetised ICF experiments", Phys. Plasmas 25, 092701 (2018).
- Watkins, H.C. and Kingham, R.J. (2019). "Non-local Corrections to Collisional Transport in Magnetised Plasmas". arXiv:1904.05450. (submitted to Physical Review E)

2

Plasma Physics Theory

This chapter will introduce the important theoretical background and equations lying at the foundation of this thesis. The plasma state is characterised by being a macroscopically quasi-neutral ensemble of charged particles. As such the electromagnetic interactions between the charged particles lead to long-range electromagnetic forces, alongside the short range collisional forces.

Kinetic theory will be the framework used to describe the dynamics of this state of matter. The starting point of this chapter will be the Vlasov-Fokker-Planck equation and an introduction to the kinetic theory of plasmas, following with the derivation of the single fluid model of Magneto-Hydrodynamics. Alongside the basics of collisions and transport phenomena, this chapter will include an introduction to magnetised and non-local transport, focusing on the processes relevant to results of later chapters. This chapter will end with the closure of the Magneto-Hydrodynamic equation set used in this thesis.

2.1 The Kinetic Theory of Plasmas

A plasma is a statistical ensemble of ions and electrons that undergo long-range interactions via the Lorentz force

$$\mathbf{F} = q(\mathbf{E} + \mathbf{v} \times \mathbf{B}), \tag{2.1}$$

for some particle of charge q.

Though the electrostatic force of a single particle has an infinite range, the collective nature of an ensemble of charged particles means any charge imbalance will experience shielding from oppositely - charged particles. Considering the thermal motion of charged particles in the electric potential of a charge imbalance, this effect defines a characteristic

length scale over which shielding occurs known as the *Debye length*

$$\lambda_D = \left(\frac{\epsilon_0 k_b T_e}{n_e e^2} \right)^{1/2}, \tag{2.2}$$

where the electron number density n_e is in m^{-3} and the electron temperature T_e is expressed in units of Kelvin. Physically the Debye length can be considered the length scale of the screening of bare charges in plasma. Beyond a sphere of radius λ_D, the Debye sphere, the plasma can be considered quasi-neutral.

The electric fields of this ensemble self-consistently adapt to the charge environment of the collection of particles. As a result imbalances in charge excite plasma oscillations with a characteristic frequency that act to re-establish quasi-neutrality. This frequency is known as the *plasma frequency*

$$\omega_p = \left(\frac{n_e e^2}{m_e \epsilon_0} \right)^{1/2}. \tag{2.3}$$

The plasma frequency defines a timescale above which the plasma can be considered quasi-neutral.

These two parameters define the length and timescales above which we can define the collective statistical state called a plasma. The most accurate model to describe this N-particle system would be the Liouville equation under the action of a self-consistent electromagnetic field. However, the requirements to solve a system in $6N$ dimensional phase space is not necessary or possible. Instead this collective behaviour is best described in terms of the *distribution function*, $f(\mathbf{x}, \mathbf{v}, t)$, which represents the particle density in the 6-dimensional single-particle phase space. The evolution of distribution functions is the subject of kinetic theory. A plasma is described kinetically by the *Vlasov-Fokker-Planck* (VFP) equation

$$\frac{\partial f_\alpha}{\partial t} + \mathbf{v}_\alpha \cdot \nabla f_\alpha + \frac{q_\alpha}{m_\alpha}(\mathbf{E} + \mathbf{v}_\alpha \times \mathbf{B}) \cdot \nabla_v f_\alpha = \left(\frac{\partial f_\alpha}{\partial t} \right)_{coll} \tag{2.4}$$

for a species α. The collision operator on the right-hand-side is the Fokker-Planck operator which will be introduced in section 2.3. There is a VFP equation for each species present in the plasma, and represents the conservation of probability in phase space. The collision term on the right-hand-side takes the form of the Fokker-Planck operator, which determines how the Coulomb collisions between particles in the plasma influence the evolution of the distribution function. Intuitively while one would think the electric fields of every particle should influence the evolution of the plasma, Debye shielding allows the separation of the electromagnetic field into a microscopic, fluctuating component that forms part of the collision term, and macroscopic fields that sit in the left hand side of the VFP equation.

The most accurate approach would be to start straight from the VFP model of a plasma and solve for the electron and ion distribution functions. However one can start with a simpler hydrodynamic approximation. Very collisional plasmas can be assumed to have

a distribution function close to a Maxwell-Boltzmann distribution, which for electrons is

$$f_m = n_e \left(\frac{1}{2\pi v_{th}^2}\right)^{3/2} \exp\left(-\frac{v^2}{2v_{th}^2}\right), \tag{2.5}$$

with the standard deviation being the thermal speed defined as $v_{th} = \sqrt{k_b T_e/m_e}$. This allows the use of a fluid description which can be derived by considering a small deviation from equilibrium, this fluid model is known as Magneto-Hydrodynamics.

2.2 Magneto-Hydrodynamics

Deriving Magneto-Hydrodynamics (MHD) from kinetic theory consists of taking moments of the VFP equation. These moments are the macroscopic quantities found from taking averages over the distribution; in particular the conserved quantities or mass, momentum and energy. However in taking successive moments, each moment equation couples to the next. To create a closed system of equations, transport relations must be found that couple to a lower-order moment; in MHD this is achieved with the Fokker-Planck collision term.

Moments of the Vlasov-Fokker-Planck Equation

For a macroscopic fluid model the equations must describe the relationships between macroscopic quantities. The moments are found by multiplying the distribution function by successive velocity variables v_i and integrating over the whole of velocity space. The first few moments below are number density, fluid velocity, total energy density, heat and enthalpy flux and the stress tensor, respectively

$$n(\mathbf{r},t) = \int f(\mathbf{r},\mathbf{v},t)d^3v, \tag{2.6}$$

$$\mathbf{V}(\mathbf{r},t) = \langle \mathbf{v} \rangle = \frac{1}{n}\int \mathbf{v} f(\mathbf{r},\mathbf{v},t)d^3v, \tag{2.7}$$

$$\mathcal{E}(\mathbf{r},t) = \frac{1}{2}mn\langle v^2 \rangle = \frac{1}{2}m\int v^2 f(\mathbf{r},\mathbf{v},t)d^3v, \tag{2.8}$$

$$\mathbf{q}(\mathbf{r},t) = \frac{1}{2}mn\langle w^2\mathbf{v} \rangle = \frac{1}{2}m\int w^2\mathbf{v} f(\mathbf{r},\mathbf{v},t)d^3v, \tag{2.9}$$

$$\sigma_{ij} = mn\langle w_i w_j \rangle = m\int w_i w_j f(\mathbf{r},\mathbf{v},t)d^3v, \tag{2.10}$$

where w is the 'anomalous velocity', the deviation from the mean velocity, $\mathbf{w} = \mathbf{v} - \mathbf{V}$. In general the n^{th} moment of the distribution function is

$$\langle \mathbf{v}^n \rangle = \frac{1}{n}\int \mathbf{v}^n f(\mathbf{r},\mathbf{v},t)d^3v. \tag{2.11}$$

Taking the first moment of the VFP equation for species α yields the continuity equation

$$\frac{\partial n}{\partial t} + \nabla \cdot (n\mathbf{V}) = \int \left(\frac{\partial f_\alpha}{\partial t}\right)_{coll} d^3v. \tag{2.12}$$

If there are no collisions that lead to a change in particle number of the species in question i.e ionisation or recombination, then

$$\int \left(\frac{\partial f_\alpha}{\partial t}\right)_{coll} d^3v = 0. \tag{2.13}$$

The second moment can be found by multiplying the VFP equation by $m\mathbf{v}$ and following the same routine to give

$$\frac{\partial}{\partial t}(mnV_j) + \frac{\partial}{\partial x_i}(mn\langle v_i v_j\rangle) - qn(E_j + (\mathbf{V}\times\mathbf{B})_j) = \int mv_j \left(\frac{\partial f_\alpha}{\partial t}\right)_{coll} d^3v. \tag{2.14}$$

To put this equation into a more familiar form note that the velocity $\mathbf{V}$ is the sum of the average ($\mathbf{V}$) and 'anomalous' ($\mathbf{w}$) parts $\mathbf{v} = \mathbf{w} + \mathbf{V}$, therefore

$$\begin{aligned}\langle v_i v_j\rangle &= \langle (V_i + w_i)(V_j + w_j)\rangle \\ &= V_i V_j + \langle w_i w_j\rangle,\end{aligned}$$

remembering $\langle w_i\rangle = 0$ as it is an anomalous, random fluctuation. Putting this into the equation and invoking the continuity equation allows the equation to be written

$$mn\frac{\partial V_i}{\partial t} + mnV_j\frac{\partial V_i}{\partial x_j} - qn(E_i + (\mathbf{V}\times\mathbf{B})_i) = -\frac{\partial \sigma_{ij}}{\partial x_j} + \int mv_i \left(\frac{\partial f_\alpha}{\partial t}\right)_{coll} d^3v. \tag{2.15}$$

The stress tensor can be written in terms of the isotropic pressure p and anisotropic stress π_{ij},

$$\sigma_{ij} = p\delta_{ij} + \pi_{ij}. \tag{2.16}$$

If the plasma is inviscid the anisotropic part is ignored and what is left is the momentum equation,

$$mn\frac{\partial \mathbf{V}}{\partial t} + mn\mathbf{V}\cdot\nabla\mathbf{V} - qn(\mathbf{E} + \mathbf{V}\times\mathbf{B}) = -\nabla p + \mathbf{R}. \tag{2.17}$$

The collision term has been shortened to

$$\mathbf{R} = \int m\mathbf{v}\left(\frac{\partial f_\alpha}{\partial t}\right)_{coll} d^3v. \tag{2.18}$$

Which satisfies

$$\mathbf{R} = \sum_\beta \mathbf{R}_{\alpha\beta},$$

since there are collisions with all other species. Also note self-collisions conserve momen-

tum, hence $\mathbf{R}_{\alpha\alpha} = 0$.

The third equation to be derived is the energy equation. However for this thesis the energy equation will be transformed so that the subject is instead temperature. Since Boltzmann's constant k_b is always associated with the temperature T, we shall for the remainder of this thesis absorb it into the definition of T, which is thereby measured in units of energy rather than degrees (thus $k_bT \to T$ from here on). Using the following definitions of thermal energy density, kinetic energy density and thermal heat flow,

$$\mathcal{E}_\mathcal{T} = \frac{1}{2}mn\langle w^2\rangle = \frac{3}{2}nT, \tag{2.19}$$

$$\mathcal{E}_K = \frac{1}{2}nmV^2, \tag{2.20}$$

$$\mathbf{q}' = \frac{1}{2}mn\langle w^2\mathbf{w}\rangle = \frac{1}{2}m\int w^2\mathbf{w}f(\mathbf{r},\mathbf{v},t)d^3v, \tag{2.21}$$

and the ideal gas law

$$p = nT. \tag{2.22}$$

The temperature equation can be written

$$\frac{3}{2}n\left(\frac{\partial T}{\partial t} + \mathbf{V}\cdot\nabla T\right) + \nabla\cdot\mathbf{q}' + p\nabla\cdot\mathbf{V} = Q, \tag{2.23}$$

where the collision terms have been shortened to Q by using

$$Q = \frac{1}{2}m\int v^2\left(\frac{\partial f_\alpha}{\partial t}\right)_{coll} d^3v - \mathbf{R}\cdot\mathbf{V}. \tag{2.24}$$

If this analysis is done for both the electron and ion VFP equations the result is a set of six transport equations, three each for the electrons and ions.

$$\frac{\partial n_e}{\partial t} + \nabla\cdot(n_e\mathbf{V}_e) = 0, \tag{2.25}$$

$$m_en_e\frac{\partial \mathbf{V}_e}{\partial t} + m_en_e\mathbf{V}_e\cdot\nabla\mathbf{V}_e + en_e(\mathbf{E}+\mathbf{V}_e\times\mathbf{B}) = -\nabla p_e + \mathbf{R}_e, \tag{2.26}$$

$$\frac{3}{2}n_e\frac{\partial T_e}{\partial t} + \frac{3}{2}n_e\mathbf{V}_e\cdot\nabla T_e + \nabla\cdot\mathbf{q}_e' + p_e\nabla\cdot\mathbf{V}_e = Q_e, \tag{2.27}$$

$$\frac{\partial n_i}{\partial t} + \nabla\cdot(n_i\mathbf{V}_i) = 0, \tag{2.28}$$

$$m_in_i\frac{\partial \mathbf{V}_i}{\partial t} + m_in_i\mathbf{V}_i\cdot\nabla\mathbf{V}_i - Zen_i(\mathbf{E}+\mathbf{V}_i\times\mathbf{B}) = -\nabla p_i + \mathbf{R}_i, \tag{2.29}$$

$$\frac{3}{2}n_i\frac{\partial T_i}{\partial t} + \frac{3}{2}n_i\mathbf{V}_i\cdot\nabla T_i + \nabla\cdot\mathbf{q}_i' + p_i\nabla\cdot\mathbf{V}_i = Q_i. \tag{2.30}$$

The Single Fluid Model

Thusfar the plasma can be seen as two inter-penetrating fluids. Using the fact that the mass of the electron is much lower than that of a proton, it is justifiable to ignore the electron inertia and define a simpler single fluid model with fluid velocity **V** and density

ρ.

Since $m_i >> m_e$, the total plasma density is dominated by the ion density,

$$\rho = m_i n_i + m_e n_e \approx m_i n_i. \tag{2.31}$$

Likewise the total momentum then becomes the ion momentum, with the fluid velocity the ion velocity (henceforth the subscript on $\mathbf{V}_i$ will be dropped)

$$\rho \mathbf{V} = m_i n_i \mathbf{V}_i + m_e n_e \mathbf{V}_e \approx m_i n_i \mathbf{V}_i. \tag{2.32}$$

Quasi-neutrality implies the number density of electrons and ions follows the relationship

$$Z n_i = n_e, \tag{2.33}$$

where Z is the average ionisation of the plasma. If the two continuity equations are summed, the above approximations yield the total continuity equation

$$\frac{\partial \rho}{\partial t} + \nabla \cdot (\rho \mathbf{V}) = 0. \tag{2.34}$$

Considering charge continuity, one can define the charge density, current and relative velocity

$$\begin{aligned} \rho_c &= e(Z n_i - n_e), \\ \mathbf{U} &= \mathbf{V}_e - \mathbf{V}_i, \\ \mathbf{j} &= \rho_c \mathbf{V}_i - e n_e \mathbf{U}, \end{aligned}$$

which means the charge continuity equation is

$$\frac{\partial \rho_c}{\partial t} + \nabla \cdot \mathbf{j} = 0. \tag{2.35}$$

Since the plasma is quasi-neutral, $\rho_c << e n_e$ and so

$$\mathbf{j} = -e n_e \mathbf{U}, \tag{2.36}$$

which gives the quasi-neutrality condition

$$\nabla \cdot \mathbf{j} = 0. \tag{2.37}$$

The single fluid momentum equation is found by taking the sum of the fluid momentum equations. This equation can be simplified by first applying quasi-neutrality, which removes the electric field term. Momentum is conserved in collisions, and so the collision terms cancel because they satisfy

$$\mathbf{R}_e = -\mathbf{R}_i. \tag{2.38}$$

After neglecting electron inertia and defining total pressure $p = p_e + p_i$ and using the

definition of the current, the momentum equation is

$$\rho\frac{\partial \mathbf{V}}{\partial t} + \rho\mathbf{V}\cdot\nabla\mathbf{V} = -\nabla p + \mathbf{j}\times\mathbf{B}. \tag{2.39}$$

The Energy Equation

To find the appropriate energy equation one must begin with the electron energy equation eq. 2.27 and use the current definition, eq. 2.36, to remove the electron velocity. Then one uses the heat flow in the ion frame

$$\mathbf{q} = \mathbf{q}' - \frac{5}{2en_e}p_e\mathbf{j}. \tag{2.40}$$

To find a total energy equation for the plasma, the cold ion assumption will be employed where $T_i \approx 0$. The cold ion approximation is used throughout this thesis because in laser-plasma regimes the thermal energy is dominated by the electron temperature, and the heat flow dominated by the electron heat flow. While ions are also heated in the presence of shocks [16], the simulations presented in this thesis do not enter the shock regime. In this approximation the ion pressure can be ignored $p_i \approx 0$ and the ion energy equation is removed. In this case the total thermal energy of the plasma is held by the electron temperature. The energy equation is then

$$\frac{3}{2}n_e\left(\frac{\partial T_e}{\partial t} + \mathbf{V}\cdot\nabla T_e\right) + p\nabla\cdot\mathbf{V} + \nabla\cdot\mathbf{q} = \mathbf{R}_e\cdot\mathbf{j}/en_e. \tag{2.41}$$

Maxwell's Equations

The evolution of electromagnetic fields in the plasma is determined by Maxwell's equations

$$\nabla\cdot\mathbf{E} = \frac{\rho_c}{\epsilon_0}, \tag{2.42}$$

$$\nabla\cdot\mathbf{B} = 0, \tag{2.43}$$

$$\nabla\times\mathbf{E} = -\frac{\partial\mathbf{B}}{\partial t}, \tag{2.44}$$

$$\nabla\times\mathbf{B} = \mu_0\mathbf{j} + \mu_0\epsilon_0\frac{\partial\mathbf{E}}{\partial t}. \tag{2.45}$$

As the plasma is quasi-neutral, the charge density on a scale above that of the Debye length will be zero, $\rho_c = 0$. The temporal regime of interest in this thesis is that described by *low-frequency* phenomena, where the characteristic timescale is much longer than the plasma period, i.e $\partial_t << \omega_p$. The displacement field in the Ampere-Maxwell law can be ignored since the timescale of the plasma dynamics is far below the fast electron plasma

period $(1/\omega_p)$ timescale. This means Maxwell's equations in plasmas become

$$\nabla \cdot \mathbf{B} = 0, \tag{2.46}$$

$$\nabla \times \mathbf{E} = -\frac{\partial \mathbf{B}}{\partial t}, \tag{2.47}$$

$$\nabla \times \mathbf{B} = \mu_0 \mathbf{j}. \tag{2.48}$$

2.3 Closure and Collisions

So far the system of equations is not closed as there is no equation that could be used to eliminate heat flow $\mathbf{q}$ or the electric field $\mathbf{E}$ or the collision term $\mathbf{R}_e$ from the system. The conventional approach to close the system of equations is to use the Chapman-Enskog expansion [113]. In this approach the distribution function is assumed to be approximately Maxwellian with only a small deviation. This approximation holds very well in very collisional plasmas because collisions drive the distribution towards equilibrium. In calculating collision terms, closure relations will be found that complete the model.

Collisions in Plasmas

The collisions between charged particles in a plasma are **Coulomb collisions**, where a charged particle is scattered by the electrostatic field of another charged particle. Considering the single-particle motion of an electron in an electrostatic field, the collision frequency of an electron with speed v from ions in a plasma is [22, 114]

$$\nu_{ei}(v) = \frac{n_i \Gamma_{ei}}{v^3} = \frac{3\sqrt{\pi}}{4\tau_{ei}} \left(\frac{v_{th}}{v}\right)^3, \tag{2.49}$$

with the factor Γ_{ei}, collision time τ_{ei}, Coulomb logarithm $\ln \Lambda$ and thermal speed v_{th} defined as

$$\Gamma_{ei} = \frac{Z^2 e^4 \ln \Lambda}{4\pi \epsilon_0^2 m_e^2}, \tag{2.50}$$

$$\tau_{ei} = \frac{12\pi^{3/2}}{\sqrt{2}} \frac{\sqrt{m_e} T_e^{3/2} \epsilon_0^2}{n_i Z^2 e^4 \ln \Lambda}, \tag{2.51}$$

$$\ln \Lambda = \ln(4\pi n_e \lambda_D^3), \tag{2.52}$$

$$v_{th} = \sqrt{\frac{T_e}{m_e}}. \tag{2.53}$$

The velocity dependence of the collision frequency is of the order v^{-3} and so slow, low energy particles are highly collisional whereas fast particles are collisionless. At the thermal speed one can also see from this definition the temperature dependence of the collision frequency is of the order $T_e^{-3/2}$. One can also define the mean free path of e-i collisions

λ_{ei} to be

$$\lambda_{ei} = v_{th}\tau_{ei}. \tag{2.54}$$

Comparing the collision frequencies of ion-ion, electron-electron and ion-electron collisions one can find they approximately follow the scaling [114]

$$\nu_{ee} \sim \nu_{ei}/\sqrt{2} >> \nu_{ii} \sim \sqrt{\frac{m_e}{m_i}}\nu_{ei} >> \nu_{ie} \sim \frac{m_e}{m_i}\nu_{ei}. \tag{2.55}$$

Since i-i and i-e collisions have a frequency much lower than e-i collisions (by factors $\sqrt{m_e/m_i}$ and m_e/m_i respectively) it is possible to safely ignore them in approximations of transport and collisional effects on the distribution function. This argument cannot however be applied to electron-electron collisions and so the e-e operator must be included.

The Fokker-Planck Collision Operator

The starting point to derive collision terms is first to derive the form of the collision operator alluded to in eq. 2.4. For the plasmas in this thesis, Coulomb collisions are small-angle, glancing collisions and the operator that very accurately models such collisions in this regime is the Fokker-Planck operator

$$\left(\frac{\partial f}{\partial t}\right)_{coll} = -\frac{\partial}{\partial \mathbf{v}}\left(\frac{\langle \Delta \mathbf{v}\rangle f}{\Delta t}\right) + \frac{1}{2}\frac{\partial^2}{\partial \mathbf{v}\partial \mathbf{v}}\left(\frac{\langle \Delta \mathbf{v}\Delta \mathbf{v}\rangle f}{\Delta t}\right). \tag{2.56}$$

This operator is split into two terms that represent 'drift' and 'diffusion' of the distribution function through velocity space. To transform the Fokker-Planck operator into explicitly Coulomb-collision form, the Rosenbluth potentials H_β and G_β are used for species β. The expressions $\frac{\langle \Delta \mathbf{v}\Delta \mathbf{v}\rangle}{\Delta t}$ and $\frac{\langle \Delta \mathbf{v}\rangle}{\Delta t}$ are written in terms of these potentials thus

$$\frac{\langle \Delta v_i\rangle}{\Delta t} = \Gamma_{\alpha\beta}\frac{\partial H_\beta}{\partial v_i}, \tag{2.57}$$

$$\frac{\langle \Delta v_i \Delta v_j\rangle}{\Delta t} = \Gamma_{\alpha\beta}\frac{\partial G_\beta}{\partial v_i \partial v_j}, \tag{2.58}$$

$$G_\beta(\mathbf{v}) = \int |\mathbf{v} - \mathbf{v}_\beta| f_\beta(\mathbf{v}_\beta) d\mathbf{v}_\beta, \tag{2.59}$$

$$H_\beta(\mathbf{v}) = \frac{m + m_\beta}{m_\beta}\int \frac{f_\beta(\mathbf{v}_\beta)}{|\mathbf{v} - \mathbf{v}_\beta|} d\mathbf{v}_\beta, \tag{2.60}$$

for collisions between species α and β. By using these forms the Rosenbluth form of the Fokker-Planck equation becomes

$$\left(\frac{\partial f_\alpha}{\partial t}\right)_{coll} = \Gamma_{\alpha\beta}\left[-\frac{\partial}{\partial v_i}\left(f_\alpha \frac{\partial}{\partial v_j}H_\beta\right) + \frac{1}{2}\frac{\partial}{\partial v_i}\frac{\partial}{\partial v_j}\left(f_\alpha \frac{\partial}{\partial v_i}\frac{\partial}{\partial v_j}G_\beta\right)\right]. \tag{2.61}$$

Furthermore, the cold ion approximation means a Maxwellian ion distribution is taken to be a Dirac delta $f_i = n_i\delta(\mathbf{v}_i)$ because the variance of the ion distribution vanishes. The

Rosenbluth potentials reduce to

$$G_i(\mathbf{v}) = n_i v, \tag{2.62}$$

$$H_i(\mathbf{v}) = n_i / v. \tag{2.63}$$

The Fokker-Planck operator for electron-ion collisions reduces to the Lorentz scattering operator.

$$\left(\frac{\partial f_e}{\partial t}\right)_{coll} = \frac{n_i \Gamma_{ei}}{2} \frac{\partial}{\partial v_i} \left[\left(\frac{v^2 \delta_{ij} - v_i v_j}{v^3} \right) \frac{\partial f_e}{\partial v_j} \right]. \tag{2.64}$$

Closure using a near-Maxwellian distribution

Closure is achieved via the Chapman-Enskog method [114], whereby the distribution function is assumed to be approximately Maxwellian,

$$f_e(\mathbf{x}, \mathbf{v}, t) = f_m + \delta f. \tag{2.65}$$

Spherical harmonics can be used to take advantage of the form of the Lorentz scattering operator. This operator is linear and has spherical harmonic eigenfunctions and so expanding the distribution function in terms of spherical harmonics will simplify the collision term.

$$f_e(\mathbf{x}, \mathbf{v}, t) = \sum_{l=0}^{\infty} \sum_{m=-l}^{l} f_l^m(\mathbf{x}, v, t) P_l^m(\cos\theta) e^{im\phi}, \tag{2.66}$$

Of particular importance to this thesis will be the use of the *diffusive approximation*. In this approximation the expansion of the distribution function expansion is truncated after $l = 1$ such that the terms $l > 1$ are ignored. If f_0 is further assumed to be Maxwellian f_m, this becomes the *local approximation*. Using this local approximation in the VFP equation, the expressions for the collisional force terms $\mathbf{R}$ and the heat flow $\mathbf{q}$ are obtained from the moment definitions eq. 2.18 and 2.9 respectively.

The Collision Terms

The momentum exchange terms $\mathbf{R}_e$ can be split into thermal and friction components

$$\mathbf{R} = \mathbf{R}_T + \mathbf{R}_u. \tag{2.67}$$

Following Braginskii [22], these components are proportional to the temperature gradient and current respectively

$$\mathbf{R}_T = -n_e \underline{\underline{\boldsymbol{\beta}}} \cdot \nabla T, \tag{2.68}$$

$$\mathbf{R}_u = \underline{\underline{\boldsymbol{\alpha}}} \cdot \mathbf{j} \frac{1}{e n_e}. \tag{2.69}$$

The transport coefficients $\underline{\underline{\boldsymbol{\beta}}}$ and $\underline{\underline{\boldsymbol{\alpha}}}$ are the thermoelectric tensor and the resistivity tensor respectively. These coefficients are tensors because transport parallel and perpendicular

to a magnetic field is not equal and so the transport becomes anisotropic.

Ohm's Law

Ohm's law is derived from the momentum equation for the electrons eq. 2.26. Ignoring electron inertia and inputting the form of the collision term $\mathbf{R}_e$ above yields the full generalised Ohm's law

$$en_e(\mathbf{E} + \mathbf{V} \times \mathbf{B}) = -\nabla p_e + \mathbf{j} \times \mathbf{B} + \frac{1}{en_e}\underline{\underline{\boldsymbol{\alpha}}} \cdot \mathbf{j} - n_e \underline{\underline{\boldsymbol{\beta}}} \cdot \nabla T_e. \tag{2.70}$$

The Heat Flow Equation

The electron heat flux is found from the moment definition eq. 2.9 and considering the difference between intrinsic and extrinsic heat flow, eq. 2.40. Like the collision term $\mathbf{R}_e$ it is made up of two parts corresponding to thermal and frictional components

$$\mathbf{q}_e = \mathbf{q}_u + \mathbf{q}_T, \tag{2.71}$$

where

$$\mathbf{q}_u = -\underline{\underline{\beta}} \cdot \mathbf{j}\frac{T_e}{e}, \tag{2.72}$$

$$\mathbf{q}_T = -\underline{\underline{\kappa}} \cdot \nabla T_e. \tag{2.73}$$

These expressions close the system of equations, however the exact forms of the magnetised transport coefficients $\underline{\underline{\alpha}}, \underline{\underline{\beta}}, \underline{\underline{\kappa}}$ must now be specified. Alternative descriptions of the derivation of the transport terms can also be found in Helander and Sigmar [114] or Boyd and Sanderson [113].

2.4 Magnetised Transport

The Transport Coefficients

Electrons in a magnetised plasma travel on circular orbits in the plain perpendicular to the direction of the magnetic field $\hat{\mathbf{b}}$. These orbits have a radius $r_L(= v/\omega_c)$, the *Larmor radius* and orbit at the Larmor or *cyclotron frequency*, ω_c,

$$\omega_c = \frac{eB}{m_e}. \tag{2.74}$$

Electrons in a plasma are constantly performing Coulomb collisions with ions and other electrons. In classical plasma theory, transport is a collisional process and it is pos-

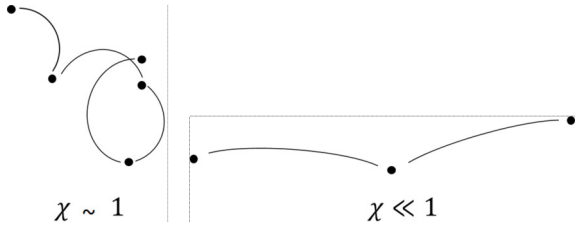

Figure 2.1: At low magnetisation (right), the electron mean free path changes little under a magnetic field. When the magnetisation is very large, (left) the collisional transport is 'constrained' into a smaller region.

sible to parameterise the influence of the magnetic field in terms of a dimensionless parameter known as the *Hall parameter*

$$\chi = \omega_c \tau_{ei}, \tag{2.75}$$

which is a product of the electron-ion collision time and the electron cyclotron frequency. This parameter is a measure of how magnetised the plasma is; when electrons undergo Coulomb collisions, they hop onto a different Larmor orbit. If the Hall parameter is low, (see figure 2.1) the magnetic field does not deflect the electron far from its path between collisions, if the Hall parameter is large the electron is effectively 'confined' to a small region, with the electron performing potentially many full orbits between collisions.

The deviation from isotropic, unmagnetised transport is encapsulated in the dimensionless tensors $\underline{\underline{\boldsymbol{\alpha}}}^c, \underline{\underline{\boldsymbol{\beta}}}^c, \underline{\underline{\boldsymbol{\kappa}}}^c$,

$$\begin{aligned}
\underline{\underline{\boldsymbol{\alpha}}} &= \frac{m_e n_e}{\tau_{ei}} \underline{\underline{\boldsymbol{\alpha}}}^c, \\
\underline{\underline{\boldsymbol{\beta}}} &= \underline{\underline{\boldsymbol{\beta}}}^c, \\
\underline{\underline{\boldsymbol{\kappa}}} &= \frac{n_e T_e \tau_{ei}}{m_e} \underline{\underline{\boldsymbol{\kappa}}}^c.
\end{aligned}$$

When the plasma is completely unmagnetised, such that $\chi \to 0$, the coefficients $\underline{\underline{\boldsymbol{\alpha}}}^c, \underline{\underline{\boldsymbol{\kappa}}}^c$ become diagonal and $\underline{\underline{\boldsymbol{\beta}}}^c$ vanishes.

To better understand the effect the anisotropic, off-diagonal terms have on transport, these coefficients can be written in a geometry where the basis is set by the direction of the magnetic field. When a magnetic field is applied to a plasma it defines a preferred direction, breaking the isotropy of transport processes in a plasma and turning the transport coefficients into tensors. The magnetic field direction is defined

$$\hat{\mathbf{b}} = \frac{\mathbf{B}}{|\mathbf{B}|}. \tag{2.76}$$

Given this geometry it is possible to write the contraction of a general transport coefficient $\underline{\underline{\eta}}$ with a driving gradient $\mathbf{s}$ as

$$\underline{\underline{\eta}} \cdot \mathbf{s} = \eta_{\parallel} \hat{\mathbf{b}} (\hat{\mathbf{b}} \cdot \mathbf{s}) + \eta_{\perp} \hat{\mathbf{b}} \times (\mathbf{s} \times \hat{\mathbf{b}}) + \eta_{\wedge} \hat{\mathbf{b}} \times \mathbf{s}. \tag{2.77}$$

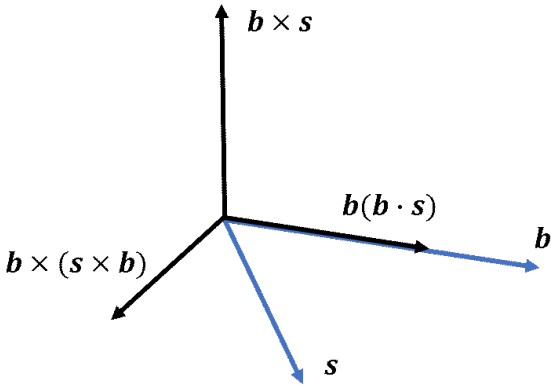

Figure 2.2: The three components have directions parallel, perpendicular and cross-perpendicular relative to the magnetic field. In this way one can define a perpendicular coordinate system based on the magnetic field direction **b** and the driving gradient direction **s**.

This splits the transport into three terms, parallel $\eta_\parallel$, perpendicular $\eta_\perp$ and cross-perpendicular $\eta_\wedge$ to the magnetic field. These directions are illustrated in figure 2.2.

A Cartesian tensor form for this contraction will be useful when transitioning to a numerical model,

$$\eta_{ij} = \eta_\parallel b_i b_j + \eta_\perp \left(\delta_{ij} - b_i b_j\right) + \eta_\wedge \epsilon_{ikj} b_k, \tag{2.78}$$

which in full matrix form is

$$\underline{\underline{\eta}} = \begin{pmatrix} \eta_\perp + (\eta_\parallel - \eta_\perp) b_x^2 & -\eta_\wedge b_z + (\eta_\parallel - \eta_\perp) b_x b_y & \eta_\wedge b_y + (\eta_\parallel - \eta_\perp) b_x b_z \\ \eta_\wedge b_z + (\eta_\parallel - \eta_\perp) b_x b_y & \eta_\perp + (\eta_\parallel - \eta_\perp) b_y^2 & -\eta_\wedge b_x + (\eta_\parallel - \eta_\perp) b_y b_z \\ -\eta_\wedge b_y + (\eta_\parallel - \eta_\perp) b_x b_z & \eta_\wedge b_x + (\eta_\parallel - \eta_\perp) b_y b_z & \eta_\perp + (\eta_\parallel - \eta_\perp) b_z^2 \end{pmatrix} \tag{2.79}$$

The closure equations of the previous section were derived without the electron-electron collision operator. While the assumption of no electron collisions applies for high-Z plasmas, the effect must be considered for low-Z plasmas. Calculating the magnetised transport coefficients with a full electron-electron Fokker-Planck collision operator is not analytically feasible. Epperlein and Haines [111] used a numerical scheme to solve the electron Vlaslov-Fokker-Planck equation with electron-electron collisions and fitted a polynomial expansion to the result to give expressions of the transport coefficients in terms of the dimensionless Hall parameter. These functional forms have explicit dependence on the Hall parameter and will be used later in the numerical model. The full coefficients can be found in Appendix A. As an example, figure 2.3 shows the Epperlein and Haines coefficients as functions of the Hall parameter for $Z = 1$.

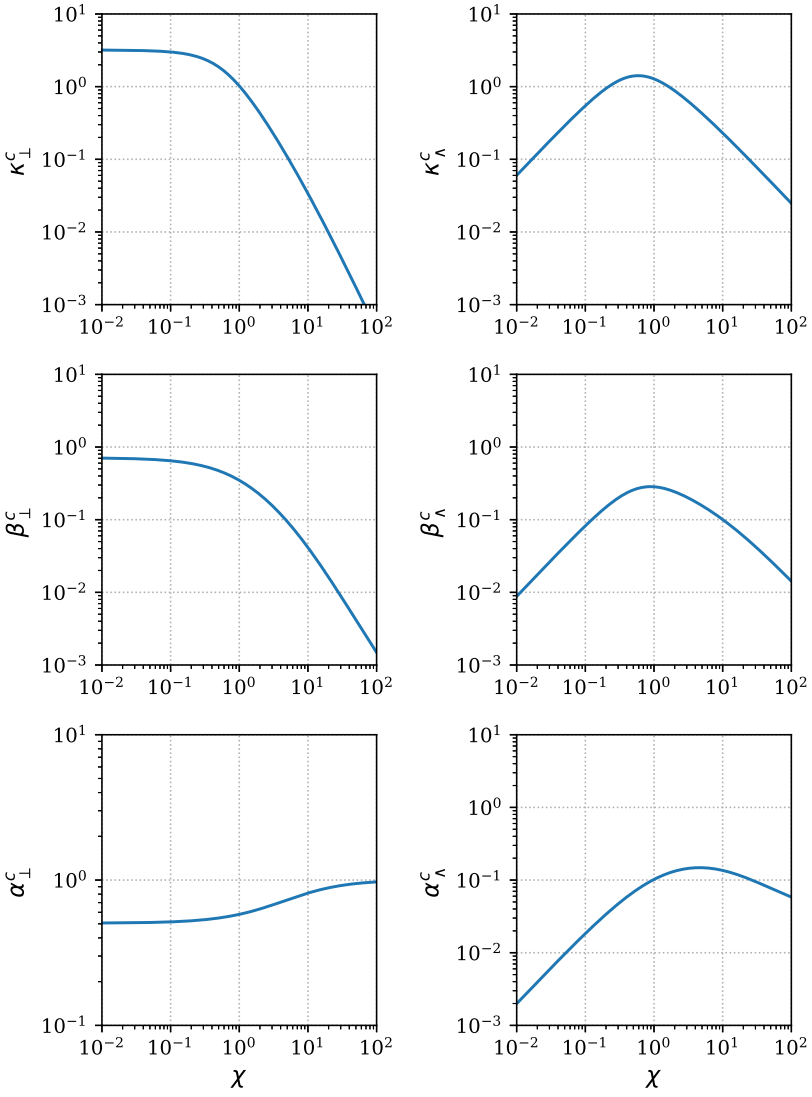

Figure 2.3: Shown here are the six magnetised transport coefficients plotted against the Hall parameter. These coefficients are for a hydrogen Z=1 plasma as calculated by Epperlein and Haines [111]. In the limit $\chi \to 0$, the $\wedge$ coefficients vanish and the perpendicular coefficients converge on a constant value.

2.5 Magnetised Transport Phenomena

The magnetised form of the transport coefficients greatly complicates the possible behaviour with more terms and the appearance of thermoelectric transport $\underline{\underline{\boldsymbol{\beta}}}$ in Ohm's law. This section will discuss the different phenomena that appear out of these tensor coefficients.

Diffusive and Righi-Leduc Heat Flow

Considering eqs. 2.74 and 2.78, the heat flow now splits into three parts

$$\mathbf{q}_T = -\kappa_\parallel \nabla_\parallel T_e - \kappa_\perp \nabla_\perp T_e - \kappa_\wedge \mathbf{b} \times \nabla T_e. \tag{2.80}$$

The first two terms are *diffusive heat flow* and the third term is the *Righi-Leduc heat flow*. The diffusive nature is made clear with eq. 2.41 and looking only at the time derivative and heat flow divergence terms. After substituting $\mathbf{q}$, the result is a diffusion equation

$$\frac{3}{2} n_e \frac{\partial T_e}{\partial t} = \nabla \cdot \left(\kappa_\parallel \nabla_\parallel T_e + \kappa_\perp \nabla_\perp T_e + \kappa_\wedge \mathbf{b} \times \nabla T_e \right). \tag{2.81}$$

Looking at the asymptotic forms of the perpendicular heat flow $\kappa_\perp$ as $\chi \to 0$ and $\chi \to \infty$, Helander [114] has (for a Lorentz plasma)

$$\kappa_\perp = \frac{n_e \lambda_{ei}^2}{\tau_{ei}} \frac{128}{3\pi}, \qquad \chi << 1 \tag{2.82}$$

$$\kappa_\perp = \frac{n_e \lambda_{ei}^2}{\tau_{ei}} \frac{13}{4\chi^2}, \qquad \chi >> 1 \tag{2.83}$$

$$= n_e \frac{r_L^2}{\tau_{ei}} \frac{13}{4}. \tag{2.84}$$

Using the length scale definition of the Hall parameter $\chi = \lambda_{ei}/r_L$, it is clear at very high magnetisation the characteristic diffusive 'step-length' switches from the electron-ion mean free path λ_{ei} to the Larmor radius r_L. The Righi-Leduc heat flow $\mathbf{q}_\wedge$ acts perpendicular to both the magnetic field and the temperature gradient. It 'deflects' the flow of thermal energy, rotating the temperature profile of the plasma in the plane perpendicular to the magnetic field. As noted by Bissell [27], the Righi-Leduc heat flow can dominate over the diffusive heat flow $\mathbf{q}_\perp$ when χ is very large. In the regime of $\chi >> 1$, the perpendicular thermal conductivity $\kappa_\perp \propto \kappa_\parallel / \chi^2$ and the Righi-Leduc conductivity $\kappa_\wedge \propto \kappa_\parallel / \chi$.

Ettingshausen Heat Flow

The *Ettingshausen heat flow* is a thermoelectric heat flow that results from the $\beta_\wedge$ term of eq. 2.72,

$$\mathbf{q}_E = -\beta_\wedge \frac{T_e}{e}\mathbf{b}\times\mathbf{j}. \tag{2.85}$$

This flow is associated with the advection of temperature down magnetic field gradients. As noted by Bissell [115] this is made clear when eq. 2.85 is substituted into eq. 2.41 and using Ampere's law to get

$$\frac{3}{2}n_e\frac{\partial T_e}{\partial t} + \nabla\cdot(\mathbf{v}_E T_e) = 0. \tag{2.86}$$

This is an advection equation for temperature with an advection velocity

$$\mathbf{v}_E = -\frac{\beta_\wedge}{e\mu_0}\nabla B. \tag{2.87}$$

However generally this term has found to play a relatively minor role.

The Nernst Effect

The *Nernst effect* likewise arises from the $\beta_\wedge$ term. However instead it represents an advection of magnetic fields down temperature gradients. This has been used to infer a relationship with diffusive heat flow, which has been used alongside non-local thermal transport models for non-local corrections to Nernst advection [109]. When the thermoelectric term of Ohm's law is substituted into Faraday's law, one finds an advection equation

$$\frac{\partial \mathbf{B}}{\partial t} = \nabla\times(\mathbf{v}_N\times\mathbf{B}), \tag{2.88}$$

with the characteristic velocity

$$\mathbf{v}_N = -\frac{\beta_\wedge\nabla T_e}{eB}. \tag{2.89}$$

Therefore the Nernst effect advects magnetic fields with velocity $\mathbf{v}_N$ down temperature gradients, concentrating the magnetic field in low temperature regions. Davies *et al.* [23] and Walsh *et al.* [32] showed the Nernst effect plays a significant role in compressing self-generated magnetic fields in ICF implosions, suggesting this once-neglected effect should play a greater role in plasma physics simulations.

Resistive Diffusion

In resistive MHD the term $\frac{1}{en_e}\underline{\underline{\boldsymbol{\alpha}}}\cdot\mathbf{j}$, in conjunction with Faraday's and Ampere's law (eqs. 2.47 and 2.48) can be combined to give an advection-diffusion equation

$$\frac{\partial \mathbf{B}}{\partial t} = \mathbf{v}_\alpha\times(\nabla\times\mathbf{B}) + \frac{\alpha_\perp}{e^2 n_e^2\mu_0}\nabla^2\mathbf{B}, \tag{2.90}$$

with the advection velocity

$$\mathbf{v}_\alpha = -\frac{1}{e^2\mu_0}\nabla\left(\frac{\alpha_\perp}{n_e^2}\right). \tag{2.91}$$

The second term on the right hand side of eq. 2.90 refers to the resistive diffusion of the magnetic field. The advective term with velocity $\mathbf{v}_\alpha$ corresponds to the resistive advection of the magnetic field in regions where the resistivity is non-uniform. While small in general, the resistive advection can grow to be as fast as the frozen in flow near shock fronts [23].

Biermann Battery Magnetic Field Generation

Though not a result of the collisional transport terms, the Biermann battery effect [116] is an important magnetic field generation mechanism arising from the electron pressure term in Ohm's law (eq. 2.70). Though first discovered in the context of interstellar magnetic fields, the Biermann battery effect is significant in the regimes of laser-plasma interactions and has been used as a means to induce $\sim 100T$ magnetic fields with nanosecond laser pulses [117].

Considering the electric field determined by the electron pressure gradient (also known as the *ambipolar electric field*) in Ohm's law

$$\mathbf{E} = -\frac{\nabla p_e}{e n_e}, \tag{2.92}$$

and using the ideal gas law $p_e = n_e T_e$ with Faraday's law (eq. 2.47), the Biermann magnetic field generation mechanism follows

$$\frac{\partial \mathbf{B}}{\partial t} = \frac{1}{e n_e}\nabla T_e \times \nabla n_e. \tag{2.93}$$

From this expression one can see if the electron density and electron temperature fields have non-parallel gradients, a magnetic field will be induced via the Biermann battery effect. In laser-generated plasmas, energy deposition via a laser heating mechanism will locally heat a region of the plasma. With a very non-uniform density profile - as is common in laser-plasma interactions - magnetic field generation via this mechanism is one of the most significant sources of magnetic fields in experiments. Even if a magnetic field has not been imposed externally, this mechanism can magnetise the plasma, leading to magnetised transport terms.

2.6 The Single-Fluid Model

Finally, bringing together the results of the previous sections together, the set of equations that describe a single-fluid magnetised plasma, and which will be used as the core set in this thesis is thus:

The Continuity Equation

$$\frac{\partial \rho}{\partial t} + \nabla \cdot (\rho \mathbf{V}) = 0 \tag{2.94}$$

The Momentum Equation

$$\rho \frac{\partial \mathbf{V}}{\partial t} + \rho \mathbf{V} \cdot \nabla \mathbf{V} = -\nabla p_e + \mathbf{j} \times \mathbf{B} \tag{2.95}$$

Ohm's Law

$$e n_e (\mathbf{E} + \mathbf{V} \times \mathbf{B}) = -\nabla p_e + \mathbf{j} \times \mathbf{B} + \frac{1}{e n_e} \underline{\underline{\alpha}} \cdot \mathbf{j} - n_e \underline{\underline{\beta}} \cdot \nabla T_e \tag{2.96}$$

Heat Flow Equation

$$\mathbf{q}_e = -\underline{\underline{\kappa}} \cdot \nabla T_e - \underline{\underline{\beta}} \cdot \mathbf{j} \frac{T_e}{e} \tag{2.97}$$

The Energy Equation

$$\frac{3}{2} n_e \left(\frac{\partial T_e}{\partial t} + \mathbf{V} \cdot \nabla T_e \right) + p_e \nabla \cdot \mathbf{V} + \nabla \cdot \mathbf{q} = \mathbf{E} \cdot \mathbf{j} \tag{2.98}$$

Maxwell's Equations

$$\nabla \times \mathbf{E} = -\frac{\partial \mathbf{B}}{\partial t} \tag{2.99}$$

$$\nabla \times \mathbf{B} = \mu_0 \mathbf{j} \tag{2.100}$$

2.7 Non-Local Transport

The conventional derivation of fluid theory relies on the truncation of the spherical harmonic expansion of the electron distribution function in velocity space and the assumption that the isotropic part f_0 is Maxwellian [118]. This local approximation holds in the regime $L_T >> \lambda_{ei}$, where the electron-ion collision mean-free-path $\lambda_{ei}(\propto T_e^2)$ is much smaller than the temperature scale length L_T, defined as

$$\frac{1}{L_T} = \frac{1}{T}\frac{dT}{dx}. \tag{2.101}$$

From this one can define the Knudsen number,

$$Kn = \frac{\lambda_{ei}}{L_T}. \tag{2.102}$$

This number quantifies the degree of 'non-locality', in the regime of $Kn << 1$ the electrons in the plasma experience sufficient Coulomb collisions such that the distribution function is approximately Maxwellian and therefore in local thermal equilibrium. This condition however is frequently violated in high-intensity laser-plasma interactions [70, 71], where the interaction can drive steep temperature gradients. Electrons with collisional mean-free paths greater than the scale length of the gradient (where $L_T << \lambda_{ei}$), stream down the temperature gradient without thermalising to the local distribution. As a result there is an increase in these hotter electrons (coming from the tail of the distribution in a high temperature region) and a depletion in another region, resulting in non-Maxwellian distribution functions and the break-down of classical transport. This depletion of hot electrons in the tail of the distribution from the region of the temperature gradient leads to a lower peak heat flux than expected from the Spitzer-Härm approximation $\mathbf{q}_{sh}$, [74],

$$\mathbf{q}_{sh} \propto -n_e \lambda_{ei} v_{th} \nabla T_e. \tag{2.103}$$

The familiar Fourier law-type heat flow should also break down at sharp temperature gradients such as shock fronts, as the heat flow would diverge. The heat flow should saturate at approximately the free streaming heat flow $\mathbf{q}_F$; the heat flow if all the electrons moved at the thermal speed in the direction of the temperature gradient

$$\mathbf{q}_F = \frac{1}{2} m_e n_e v_{th}^3 \frac{\nabla T_e}{|\nabla T_e|}. \tag{2.104}$$

A simple method of accounting for this reduction is to use a flux limiter f_l, where the

classical heat flow is reduced to some fraction of the free streaming heat flow [119],

$$\frac{1}{q(x)} = \frac{1}{q_{sh}(x)} + \frac{1}{f_l q_F}. \tag{2.105}$$

This however does not capture the effect of pre-heat, where heat flow is present even before the temperature gradient. Most of the heat flow is carried by fast electrons with speeds 3 to $5v_{th}$. Since the mean free path grows as $\lambda_{ei} \propto v^4$, the less collisional, non-local electrons are carrying the heat flow beyond the temperature gradient. An alternative non-local thermal transport model that can capture this effect is through a convolutional kernel [79]. In one dimension,

$$q(x) = \int_{-\infty}^{\infty} W(x, x') q_{sh}(x') dx'. \tag{2.106}$$

The difficulty in flux-limited or convolutional models is that the choice of limiter or kernel is arbitrary, with no real physical basis for commonly used models, and some choosing them to fit experimental data. While these models are simple, a VFP approach is necessary to get correct results.

The reduction in thermal conductivity can also be cast in Fourier space for a temperature perturbation mode with wavenumber k. This effectively recasts the peak thermal flux reduction as a reduction of thermal conductivity for small length scale structures. Epperlein and Short [81] found a non-local conductivity suppression factor relating the Spitzer-Härm thermal conductivity κ_{sh} to the non-local thermal conductivity $\kappa_{nonlocal}$ of the form

$$\frac{\kappa_{nonlocal}}{\kappa_{sh}} = \frac{1}{1 + a(\sqrt{Z} k \lambda_{ei})^b}, \tag{2.107}$$

with the parameters a, b obtained by fitting this function to a numerical VFP simulation. The result is a reduction in thermal conductivity for higher modes (high $k\lambda_{ei}$) meaning short-wavelength scale structures saw reduced conductivity.

When magnetic fields are present in a plasma, the Larmor radius can become comparable to the mean free path. In this highly magnetised regime the Larmor radius becomes the characteristic step-length of diffusive transport. Given that the Larmor radius grows as $r_L \propto v$ and $\lambda_{ei} \propto v^4$, the hotter electrons in the tail (with higher v) of the electron distribution can be relatively unmagnetised while the bulk electrons are magnetised.

Under a sufficiently strong magnetic field the transport is localised in the plane perpendicular to the field, no matter how large λ_{mfp}. This quenching of non-locality is borne out in a magnetised gas-jet experiment performed by Froula [38] and seen in kinetic simulations performed by Ridgers [101]. The regime where non-locality and magnetisation are both significant is poorly understood.

3

Laser Propagation in a Plasma

The results of successive chapters rely heavily on the theory of long-pulse laser propagation and coupling to the plasma. This chapter will introduce the primary assumptions that allows the analysis of laser propagation, before deriving the unidirectional - or paraxial - laser model. The plasma coupling mechanisms of inverse bremmsstrahlung and the ponderomotive force will then be introduced before concluding with a brief description of some of the important laser-plasma interactions that occur in the regimes of interest to this thesis.

3.1 The Helmholtz Equation

Laser light is a monochromatic coherent electromagnetic wave, and so the starting point will be Maxwell's electromagnetic wave equation.

$$c^2\nabla^2\mathbf{E} - c^2\nabla(\nabla\cdot\mathbf{E}) = \frac{1}{\epsilon_0}\frac{\partial\mathbf{j}}{\partial t} + \frac{\partial^2\mathbf{E}}{\partial t^2}. \tag{3.1}$$

Solving this equation exactly would be numerically too demanding because the spatial and temporal resolution requirements would be too great and are unnecessary for nanosecond pulse duration, high-power lasers used in laser-plasma physics experiments. Several simplifying assumptions can be made to reduce this equation into the paraxial laser equation.

The current in a plasma is determined by the flux of the electrons. The dielectric behaviour of the plasma can thus be found from the electron equation of motion. The simplified equation of motion required for the fast electron response to the laser field is

$$m_e\frac{\partial(n_e\mathbf{V}_e)}{\partial t} = -en_e\mathbf{E} - m_e\nu_{ei}n_e\mathbf{V}_e. \tag{3.2}$$

The high-frequency response of a plasma to the oscillating laser fields justifies dropping the pressure gradient term. The magnetic field term is ignored because unless the plasma is relativistic, it will be much smaller than the electric field contribution due to the factor $\sim v/c$. Using the definition of the current in terms of electron velocity this can be recast as

$$\frac{\partial \mathbf{j}}{\partial t} = \frac{e^2 n_e}{m_e}\mathbf{E} - \nu_{ei}\mathbf{j}. \tag{3.3}$$

Unfortunately, in order to have a closed set of equations the collision term must be rewritten in terms of the electric field. In order to do this the current in the collision term is approximated as

$$\mathbf{j} \approx -\frac{e n_e}{m_e \omega_l^2}\frac{\partial \mathbf{E}}{\partial t}, \tag{3.4}$$

which only holds in the regime where the collision frequency ν_{ei} is much less than the laser angular frequency ω_l. Therefore the wave equation can be written

$$c^2\nabla^2\mathbf{E} = \frac{e^2 n_e}{\epsilon_0 m_e}\left(\mathbf{E} + \frac{\nu_{ei}}{\omega_l^2}\frac{\partial \mathbf{E}}{\partial t}\right) + \frac{\partial^2 \mathbf{E}}{\partial t^2}. \tag{3.5}$$

Given this describes a laser field, the electric field can be considered a product of the fast temporal oscillation at the laser angular frequency ω_l and a slowly varying 'envelope' $\mathbf{E'}(\mathbf{r})$, where in total $\mathbf{E}(\mathbf{r}) = \mathbf{E'}(\mathbf{r})e^{-i\omega_l t}$. It is not necessary to resolve the fast oscillation of the wave because the ω_l timescale is much faster than the timescale of the plasma dynamics. It is possible to integrate out the fast motion, giving an equation for the envelope of the laser field. Time derivatives of $\mathbf{E'}$ are ignored as the envelope is assumed to be slowly varying.

It is here we make use of the paraxial approximation, whereby $\mathbf{k}\cdot\mathbf{E} = 0$. This limits the validity of this model to small angle refraction from the wavevector axis (to within ± 15 degrees). While large angle refraction does occur in plasmas, the setups within this thesis are securely within the small-angle regime. This approximation removes the $\nabla\cdot\mathbf{E}$ term in the wave equation. This leaves the Helmholtz equation

$$\nabla^2\mathbf{E'} + \frac{\omega_l^2}{c^2}\epsilon\mathbf{E'} = 0. \tag{3.6}$$

Where the dielectric function ϵ is defined as

$$\epsilon = 1 - \frac{\omega_p^2}{\omega_l^2} + i\frac{\omega_p^2}{\omega_l^3}\nu_{ei}, \tag{3.7}$$

when expressed in terms of the plasma frequency,

$$\omega_p = \frac{e^2 n_e}{\epsilon_0 m_e}. \tag{3.8}$$

3.2 The Paraxial Laser Model

The laser model relies on the slowly varying envelope approximation. It is possible to write the electric field of a linearly polarised wave $\mathbf{E'}$ in terms of the envelope ψ (the magnitude in the axis of polarisation) and the phase $\phi(z)$. Without loss of generality the direction of propagation is chosen to be along the z-axis which gives

$$E'(r,z) = \psi(r,z)\exp i\phi(z). \tag{3.9}$$

The field is linearly polarised so it can be expressed as a complex scalar field. The phase function ϕ is chosen such that

$$\phi(z) = \frac{\omega_l}{c}\sqrt{\epsilon_a}z. \tag{3.10}$$

The factor ϵ_a is the dielectric function at the axis (that is, $r = 0$). This expression is plugged into the Helmholtz equation and the envelope is assumed to be slowly varying such that

$$|\partial_{zz}| << |k\partial_z|. \tag{3.11}$$

This is equivalent to assuming the wavevector of the laser light is directed along z axis and any variation away from this direction is small. This yields the paraxial transport equation

$$2ik\sqrt{\epsilon_a}\partial_z\psi + \nabla_\perp^2\psi + k^2\left(\epsilon - \epsilon_a\right)\psi = 0, \tag{3.12}$$

where the vacuum wavenumber k is

$$k^2 = \frac{\omega_l^2}{c^2}. \tag{3.13}$$

The paraxial transport equation allows one to use the intensity I of the laser field directly, calculated from the laser envelope ψ

$$I = \frac{1}{2}c\epsilon_0\eta|\psi|^2, \tag{3.14}$$

with the speed of light c, the permitivity of a vaccum ϵ_0 and η is the refractive index, defined as

$$\eta = \sqrt{1 - \frac{\omega_p^2}{\omega_l^2}}. \tag{3.15}$$

3.3 Gaussian Optics

In a vacuum the paraxial equation has a cylindrically symmetric solution known as a Gaussian beam [120]. This solution will be important for the remainder of this thesis as the model of the field of a laser pulse before it enters a plasma. This solution is

$$\psi(r,z) = \psi_0 \frac{w_0}{w(z)} \exp\left(\frac{-r^2}{w(z)^2}\right) \exp\left(-ikz - \frac{ir^2}{2R} + i\phi(z)\right). \tag{3.16}$$

This solution is defined in terms of the following parameters, the beam waist size

$$w(z) = w_0\sqrt{1 + \frac{z^2}{z_r^2}}, \tag{3.17}$$

the beam radius of curvature

$$R(z) = z\left(1 + \frac{z_r^2}{z^2}\right), \tag{3.18}$$

the Rayleigh length,

$$z_r = \frac{kw_0^2}{2}, \tag{3.19}$$

and the Gouy phase

$$\phi(z) = \arctan(\frac{z}{z_r}). \tag{3.20}$$

A map of the real part of the laser envelope ψ can be found in figure 3.1.

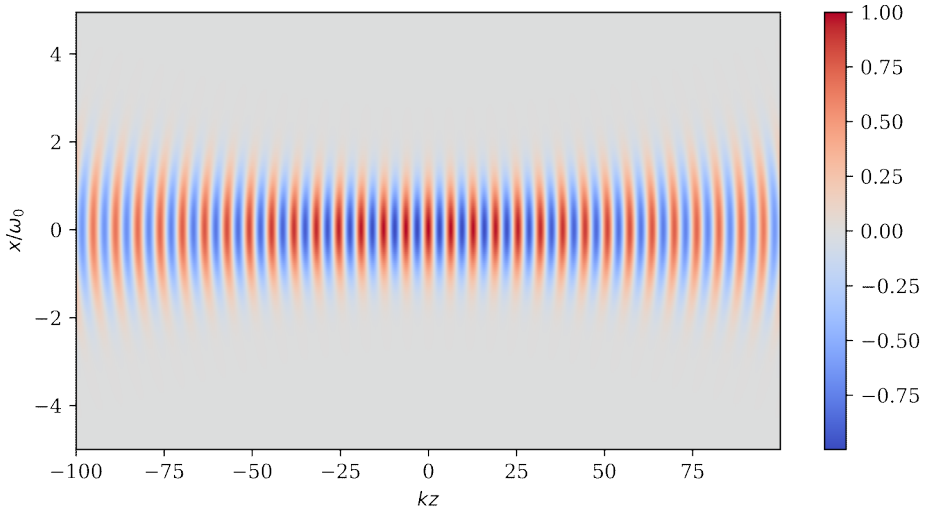

Figure 3.1: The real part of a Gaussian beam in a vacuum illustrated here shows how the beam focuses to a focal point in the centre of the plot. The width of the beam at the focal point defines the minimum beam waist ω_0.

3.4 Plasma-Laser Coupling

As the core of this thesis is an investigation of laser-plasma interactions, it is necessary to introduce the interaction processes. The plasmas of interest here are all produced by long pulse lasers with a laser wavelength of $\lambda_l = 1\mu m$. As such the laser intensity is moderate, with a peak intensity around $10^{15} W cm^{-2}$ and a laser-plasma coupling parameter $I\lambda_l^2$ in the region of $10^7 W$. To get a measure for the importance of special relativistic effects in laser-plasma coupling, one can consider the magnitude of the electron quiver speed v_{osc}, this is the speed of oscillation of an electron in the electric field of the laser. With intensities this low, relativistic effects can be ignored since the electron quiver speed relative to the speed of light

$$\frac{v_{osc}}{c} = \frac{eE}{m_e \omega_l c} = a_0, \tag{3.21}$$

is of the order $O(10^{-2})$ and so the electron motion is firmly non-relativistic. The term a_0 is known as the normalised vector potential, and is commonly used in the theory of laser-plasma interactions.

Chapter 2 introduced the concept of the plasma frequency ω_p, which is the characteristic frequency at which the electron fluid restores quasi-neutrality in a plasma. This provides a lower limit to the frequencies of electromagnetic radiation can propagate through a plasma. This is because when the laser frequency ω_l equals ω_p, the electron current in the plasma can cancel the displacement current in Ampere's law, effectively quenching the electric field of the laser. The length scale of this attenuation is called the *skin depth* and is defined

$$\delta = \frac{c}{\omega_p} \tag{3.22}$$

The limit on frequency also defines an important parameter of laser-plasma interactions, the critical density n_c. This is the cut-off electron density at which the plasma frequency equals the laser frequency. Using the definition of the plasma frequency, this density is defined

$$n_c = \frac{\epsilon_0 m_e \omega_l^2}{e^2}. \tag{3.23}$$

While there are other mechanisms by which lasers can couple to a plasma and exchange energy, the parameter space of interest in this thesis limits the coupling to the most significant processes in ICF regimes. In this thesis' model, the laser affects the plasma through two processes, the ponderomotive force [121] and inverse bremmstrahlung [2]. The ponderomotive force term appears in the plasma momentum equation and the inverse bremsstrahlung term in the energy equation.

The Ponderomotive Force

The ponderomotive force is the result of the collective oscillation of the electrons in the oscillating electric field of the laser. A spatially varying laser electric field envelope drives electrons from regions of high intensity to regions of lower intensity. The timescale of the laser oscillation period is so much higher than the timescale of the dynamics of the plasma, one can temporally integrate over this collective motion to obtain a ponderomotive potential. Gradients in this potential act as a force in the momentum equation.

The form of the ponderomotive force can be obtained from the second order terms of the electron fluid momentum equation

$$m_e n_e \frac{\partial \mathbf{V}_e}{\partial t} = -m_e n_e \mathbf{V}_e \cdot \nabla \mathbf{V}_e - e n_e (\mathbf{V}_e \times \mathbf{B}). \tag{3.24}$$

Using the magnetic vector potential $\mathbf{B} = \nabla \times \mathbf{A}$, and the first order oscillating field (quiver) approximation $\mathbf{V}_e = -\frac{e\mathbf{E}}{m_e \omega} = \frac{e\mathbf{A}}{m_e}$, the momentum equation becomes

$$m_e n_e \frac{\partial \mathbf{V}_e}{\partial t} = -\frac{1}{2} \frac{e^2 n_e}{m_e \omega_l^2} \nabla A^2. \tag{3.25}$$

By integrating out the fast oscillation, this expression yields the ponderomotive force density, which can be written in terms of the laser field envelope ψ,

$$\mathbf{F}_p = -\frac{\omega_p^2}{\omega_l^2} \nabla \langle \frac{1}{2} \epsilon_0 E^2 \rangle = -\frac{n_e}{n_c} \frac{1}{2} \epsilon_0 \nabla |\psi|^2. \tag{3.26}$$

This form shows the force as a negative gradient of a potential; on timescales much longer than the laser oscillation period, the ponderomotive force can be thought of as an electric field pressure on the electron fluid.

Inverse Bremsstrahlung

Inverse bremmsstrahlung (IB) is the inverse of the bremmstrahlung emission process. This is a collisional absorption process, whereby an electron-ion Coulomb collision is caused by the oscillating electric field of the laser forcing the electrons to quiver. In this process a photon of laser light is absorbed by an electron scattered in the field of an ion. IB acts as a source term in the plasma energy equation with energy from the laser light absorbed by the plasma. For underdense plasmas in the regimes of interest in this thesis, IB is the primary heating process.

To derive the form of the IB operator, consider the Langdon operator for the f_0 equation [53], defined as

$$\left(\frac{\partial f_0}{\partial t} \right)_{IB} = \frac{A v_{osc}^2}{3v^2} \frac{\partial}{\partial v} \left(\frac{g(v)}{v} \frac{\partial f_0}{\partial v} \right). \tag{3.27}$$

With $A = \frac{2\pi n_e Z e^4}{m_e^2}$ and $v_{osc} = \frac{eE_0}{m_e \omega_l}$, where E_0 is the laser field. In this model, the oscillating laser field acts as a source term for the isotropic part of electron distribution function.

The IB heating term in the energy equation can then be derived in the same way as

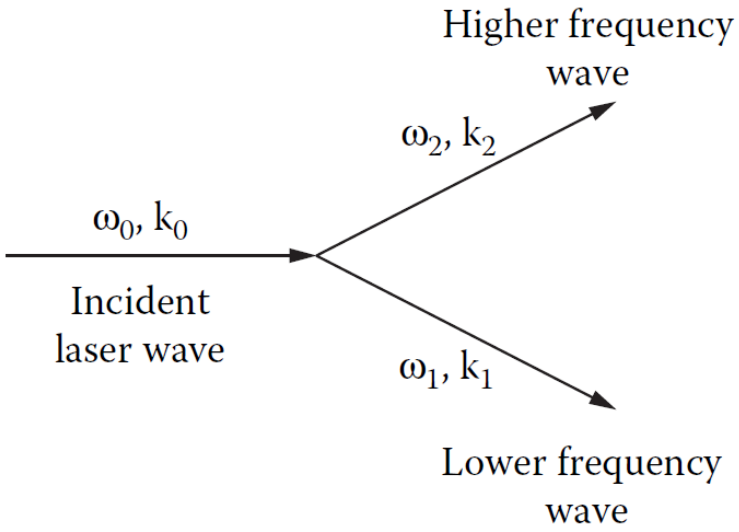

Figure 3.2: Diagram of a 3-wave parametric process, an intense laser photon decays into two new waves. Taken from Pfalzner [2].

the rest of the energy equation, by taking the correct moment of the Landgon IB operator and using a Maxwellian distribution for f_0. The factor $g(v)$ can be assumed to be 1 in the regime within which these equations are derived (where $v_{osc} << v_{th}$). Therefore, using the definition of the electron-ion collision time τ_{ei}, the laser heating term is

$$\left(\frac{\partial \mathcal{E}}{\partial t}\right)_{laser} = \frac{\omega_p^2}{\omega_l^2}\nu_{ei}\langle\frac{1}{2}\epsilon_0 E^2\rangle = \frac{n_e}{n_c}\frac{1}{2}\epsilon_0\nu_{ei}|\psi|^2, \tag{3.28}$$

where it has been put in terms of the laser field envelope ψ.

These two laser-plasma coupling terms allows the laser to deposit energy and momentum in the plasma, whilst other laser-plasma interactions do exist [121], on the long-pulse, $1ns$ timescales investigated in this thesis, they are negligible. The above forms also allow the direct use of the slowly-varying laser field envelope ψ - calculated from the paraxial equation - in the plasma coupling terms.

3.5 Parametric Laser-Plasma Instabilities

Parametric instabilities are caused by the non-linear interactions between intense laser light and the plasma [122]. The refractive index of a plasma is dependent on the electron number density, as such, light will refract in regions of inhomogeneous electron density. In particular laser light finds itself refracted into electron density channels [62]. Small density fluctuations scatter laser light, with the intense laser pump wave decaying into two new waves. Depending on the kind of waves that are excited, these instabilities can enhance laser absorption or enhance laser backscatter [123].

This three-wave decay process is illustrated in figure 3.2. Because energy and momentum must be conserved, the incident $(\omega_0, \mathbf{k}_0)$ and scattered $(\omega_1, \mathbf{k}_1), (\omega_2, \mathbf{k}_2)$ waves must satisfy the wavenumber and frequency matching relations

$$\omega_0 = \omega_1 + \omega_2, \tag{3.29}$$

$$\mathbf{k}_0 = \mathbf{k}_1 + \mathbf{k}_2. \tag{3.30}$$

The intensity of the incident wave (i.e the laser) has to exceed a certain threshold in order for the parametric instability to occur, because collisional or collisionless damping will act to damp the growth of an unstable mode. If the laser intensity is higher than this limit, the amplitude of the parametric decay mode grows exponentially with a characteristic growth rate.

A high-power pump laser in an ICF or laser-plasma experiment can decay via a number of different parametric instabilities. The processes of interest in the underdense moderate-intensity laser interactions described in this thesis, and most common in underdense ICF experiments are stimulated Raman scattering and stimulated Brillouin scattering.

Stimulated Raman Scattering

Stimulated Raman scattering (SRS) is the parametric process where the incident pump wave (with frequency ω_0) decays into an electron plasma wave (with frequency ω_p, the plasma frequency) and lower-energy scattered electromagnetic wave (with frequency ω_s). It is the parametric resonance between the incident laser light with the normal modes of the plasma. The frequency matching relation

$$\omega_0 = \omega_s + \omega_p \tag{3.31}$$

implies this instability can only occur if the initial pump frequency satisfies $\omega_0 > 2\omega_p$. The dependence on the local plasma density (via the plasma frequency) also limits this instability to the region in the plasma where $n_e \approx n_c/4$ and below.

SRS is unstable because it acts as a feedback loop; small changes in electron density δn_e oscillate, generating currents in the plasma which excite electromagnetic radiation with frequency $\omega_0 \pm \omega_p$. The combination of the incident and scattered electromagnetic wave reinforce the density fluctuations through the ponderomotive force, completing the loop. SRS can scatter light forward or backward, with backscattering the most important for laser-plasma experiments. SRS has a peak growth rate at

$$\gamma_{max} = \frac{\omega_0}{2\sqrt{2}} \frac{v_{osc}}{c} \frac{n_e}{n_c}. \tag{3.32}$$

This instability is problematic not only because it is detrimental to laser absorption, but also because it generates hot electrons which can cause pre-heat.

Stimulated Brillouin Scattering

Stimulated Brillouin scattering (SBS) is another resonant parametric instability where the pump wave decays into an ion-acoustic wave and lower energy electromagnetic wave [121] with the matching condition

$$\omega_0 = \omega_s + \omega_{ia}, \tag{3.33}$$

where the ion-acoustic frequency $\omega_{ia} = v_s k_{ia}$ is defined via the ion-acoustic sound speed v_s. In this mechanism the density fluctuation is associated with a low-frequency ion-acoustic wave. This scattering off ion-acoustic modes is limited to the region where $n_e \leq n_c$ and has a peak growth rate (for backscattering)

$$\gamma_{max} = \frac{1}{2\sqrt{2}} \frac{k_0 v_{osc} \omega_{ia}}{\sqrt{\omega_0 k_0 v_s}}. \tag{3.34}$$

For plasma conditions expected to be produced by high-power laser implosions at the National Ignition Facility, the backscatter from both SBS and SRS is large enough to reflect a significant portion of the laser light [8]. In both indirect and direct-drive ICF the coupling of energy into the target is significantly decreased, as such these LPIs must be avoided for good implosion performance.

4

Code Architecture and Testing

For all but the simplest systems, the equations of plasma and laser physics are non-linear and too complex to analytically calculate results. Therefore to examine the physical system at the core of this thesis, it was necessary to build a coupled laser plasma code that solves the complex set of equations. This chapter will introduce the numerical methods used to solve systems of partial differential equations and how they are applied to plasma and laser solving routines.

The equations in question are the extended-MHD equations alongside the paraxial equation, the full model can be found in Appendix B. The resulting algorithm is the PARAMAGNET (Parallel MAGnetised Newton method code for Electron Transport) code that will be used to simulate systems of lasers and plasmas in the remainder of this thesis.

Before the code can be used on physical problems, numerical tests must be performed to validate the accuracy of the model. This chapter will end with a description of numerical test cases applied to the two parts of the code and the isolation of issues specific to each module.

4.1 Numerical Methods

To solve a system of partial differential equations numerically, the fields subject to these equations are decomposed onto a discrete mesh. The values of these field variables at each point are evolved according to a solution algorithm that acts as the discrete equivalent of the partial differential equation which maps the field variables onto the solution of the equation. The result is a linear or non-linear algebra problem with a very large number of variables.

Finite Difference Methods

In finite difference methods, equations are transformed into the numerical form by converting derivatives to their finite-difference approximations. These rely on the Leibniz definition of a derivative as the difference between two mesh points over the displacement. In the limit of that displacement approaching zero, the difference converges towards the exact derivative. In this method, a continuous field variable, u, is discretised onto a mesh with a finite number of elements, u_{ijk} at mesh positions i, j, k.

There are a range of finite difference approximations, however the PARAMAGNET code uses central differencing for the spatial derivatives, whereby the derivative at a mesh point is approximated using the difference between two points either side of it,

$$\frac{\partial f}{\partial x} \Leftrightarrow \frac{f_{i+1} - f_{i-1}}{2\delta x}. \tag{4.1}$$

Distrete time-stepping in the model is achieved using the backward Euler step. This is an implicit method in which time derivatives are approximated using,

$$\frac{\partial f}{\partial t} = g \Leftrightarrow \frac{f^{n+1} - f^n}{\delta t} = g^{n+1}, \tag{4.2}$$

with spatial operators (such as g) taken at timestep $n + 1$. In the limit of $\delta t \to 0, \delta x \to 0$ the discrete equation, and the numerical solution obtained from a simulation, should converge to the continuous result.

The Newton Method For Non-linear Equations

If the finite-difference approximation is applied to non-linear systems such as MHD, the resulting discrete algebraic system is also non-linear. This requires an algorithm suitable to large sparse non-linear matrix equations. The Newton-Raphson method [124] iteratively converges onto a solution of a non-linear matrix equation from an initial guess. The univariate Newton-Raphson method is recognisable from school as a way of finding the roots of a function, but the multi-variable form can be used to solve the non-linear matrix equations found in computational physics.

If the field variables at timestep n are held in a solution vector $\mathbf{v}^n$ and an implicit time-stepping method used such as backward Euler step, the discrete form of the partial differential equation can be represented as a matrix equation.

$$\underline{\underline{\mathbf{A}}}(\mathbf{v}^{n+1})\mathbf{v}^{n+1} = \underline{\underline{\mathbf{B}}}(\mathbf{v}^{n+1})\mathbf{v}^n. \tag{4.3}$$

The matricies $\underline{\underline{\mathbf{A}}}$ and $\underline{\underline{\mathbf{B}}}$ hold the discrete structure of the partial differential equation. Because the equation may be non-linear, these matrices are functions of $\mathbf{v}^{n+1}$. The Newton method works by first defining a residual vector,

$$\mathbf{f}(\mathbf{v}^{n+1}) = \underline{\underline{\mathbf{A}}}(\mathbf{v}^{n+1})\mathbf{v}^{n+1} - \underline{\underline{\mathbf{B}}}(\mathbf{v}^{n+1})\mathbf{v}^n. \tag{4.4}$$

If the residual is Taylor expanded

$$\mathbf{f}(\mathbf{v}^{n+1} + \Delta\mathbf{v}^{n+1}) = \mathbf{f}(\mathbf{v}^{n+1}) + \frac{\partial \mathbf{f}(\mathbf{v}^{n+1})}{\partial \mathbf{v}^{n+1}} \Delta\mathbf{v}^{n+1} + O((\Delta\mathbf{v}^{n+1})^2), \tag{4.5}$$

the Jacobian matrix can be defined as

$$\underline{\underline{\mathbf{J}}} = \frac{\partial \mathbf{f}(\mathbf{v}^{n+1})}{\partial \mathbf{v}^{n+1}}. \tag{4.6}$$

To find the 'root' of this system of equations the terms in second order $O((\Delta\mathbf{v}^{n+1})^2)$, are ignored and

$$\mathbf{f}(\mathbf{v}^{n+1} + \Delta\mathbf{v}^{n+1}) = 0 \tag{4.7}$$

is sought as this means eq. 4.3 is solved. Since these equations are non-linear, the solution of the resulting linear matrix equation

$$\underline{\underline{\mathbf{J}}} \Delta\mathbf{v}_k^{n+1} = -\mathbf{f}, \tag{4.8}$$

will only be an approximation and so successive approximations, with an appropriate linear matrix solver, must be made until the system converges within the specified tolerance, therefore

$$\mathbf{v}_{k+1}^{n+1} = \mathbf{v}_k^{n+1} + \Delta\mathbf{v}_k^{n+1}. \tag{4.9}$$

is iterated over the index k until a satisfactory accuracy is reached. A common definition of accuracy is to set an error threshold E_0, and iterate until the error drops below this value. Error can be defined as the 2-norm of the residual vector $\mathbf{f}$ or the difference vector $\Delta\mathbf{v}^{n+1}$,

$$E = ||\Delta\mathbf{v}^{n+1}|| \text{ or } E = ||\mathbf{f}||. \tag{4.10}$$

The Jacobian-Free Newton Krylov Method

The PARAMAGNET code itself does not evaluate the Jacobian directly but rather makes use of the Jacobian-Free-Newton-Krylov (JFNK) method [125]. In this method the product of the Jacobian with a vector $\mathbf{v}$ can be approximated using a Taylor expansion as

$$\underline{\underline{\mathbf{J}}}\mathbf{u} \approx \frac{1}{\epsilon} \left(\mathbf{f}(\mathbf{v} + \epsilon\mathbf{u}) + \mathbf{f}(\mathbf{v}) \right), \tag{4.11}$$

with some specified small factor ϵ. Here the vector $\mathbf{v}$ comes from $\underline{\underline{\mathbf{J}}} = \frac{\partial \mathbf{f}(\mathbf{v})}{\partial \mathbf{v}}$.

This approximation allows one to use the Newton method without having to evaluate and store the Jacobian. This comes at a price of having to give up preconditioning during the linear solver stage and being limited to an unpreconditioned Krylov subspace method such as GMRES [124] for the linear solver. Without a stored Jacobian matrix, standard preconditioners cannot be calculated and so many more iterations may be needed before the linear solver converges below tolerance. GMRES and similar methods are ideal in this situation because they only require the residual vector and the Krylov subspace.

The Krylov subspace is the space of vectors formed from the repeated multiplication of the matrix A and the vector b from the linear system $Ax = b$. A full description of iterative linear solvers goes beyond the scope of this thesis, but a full in-depth introduction can be found in Press *et al.* [124].

Writing high-performance linear and non-linear solvers is no small task however there are several libraries available for such software that can easily be implemented into any code. PARAMAGENT makes use of the PETSc library [126] for its sparse iterative linear and nonl-linear solver routines. The library is compatible with MPI parallelisation and has a C API which made it a good choice for the problem at hand. In particular PARAMAGNET makes use of the GMRES iterative linear solver and the Newton iterative non-linear solver routines which are run in parallel using MPI.

The Alternating-Direction Implicit Method

The paraxial laser equation (eq. 3.12) takes the form of a linear three-dimensional complex parabolic equation. Being linear, the numerical solution can take advantage of simple sparse matrix algorithms. However the problem is complicated by the second spatial dimension. This second spatial dimension will, using the finite difference scheme described in this chapter, produce a pentadiagonal as opposed to tridiagonal matrix. It would be possible to use a general sparse linear matrix solver, however a simpler solution will be to use the alternating-direction implicit (or ADI) method.

In the ADI method, operator-splitting decomposes the pentadiagonal matrix problem into two separate tridiagonal problems, one for each spatial dimension [124]. The two tridiagonal problems are then solved separately, making this a two-step solution algorithm. Given a pentadiagonal matrix A_0 formed from the application of an implicit time-step method to a parabolic equation, the linear problem $A_0 x = b_0$ is split into two tridiagonal problems

$$A_1 x^{n+1/2} = b_1,$$
$$A_2 x^{n+1} = b_2.$$

The operators A_1, A_2 represent the operator A split into the two dimensions x, y respectively. The key point is to feed the result of the intermediate step ($x^{n+1/2}$) into the right-hand side of the second step.

4.2 The PARAMAGNET Code

Normalisation Scheme

The equations are first put into a dimensionless form by using a set of reference values. This will remove the need to include dimensional constants in the numerical procedure. n_0, T_0 and I_0 represent arbitrary reference values of the density, temperature and laser intensity. They are usually set to the initial values of density, temperature and peak laser intensity respectively.

The reference thermal speed v_{th0}, collision length λ_0 and collision time τ_0 are functions of the reference density and temperature and are defined through

$$v_{th0}^2 = \frac{T_0}{m_e} \qquad\qquad \lambda_0 = v_{th0}\tau_0$$

The normalisations can be found in table 4.1 and the full set of equations in dimensionless form can be found in Appendix B.

$\tilde{t} = \frac{t}{\tau_0}$	$\tilde{x} = \frac{x}{\lambda_0}$	$\tilde{v}_x = \frac{v_x}{v_{th0}}$	$\tilde{B}_x = \frac{eB_x\tau_0}{m_e}$	$\tilde{j}_x = \frac{j_x}{en_0v_{th0}}$
$\tilde{n} = \frac{n}{n_0}$	$\tilde{T} = \frac{T}{T_0}$	$\tilde{E}_x = \frac{eE_x\tau_0^2}{m_e\lambda_0}$	$\tilde{q}_x = \frac{q_x}{n_0m_ev_{th0}^3}$	$\tilde{\psi} = \sqrt{\frac{2I_0}{\epsilon_0 c}}\psi$

Table 4.1: Table of variable normalisations in the PARAMAGNET code

Variable Storage

When using the above methods for multi-dimensional problems one can apply a row indexing scheme to turn the three-dimensional array of mesh points into a a one-dimensional vector. The problem is turned into a matrix equation for which conventional matrix solution methods can be used. The purpose of a row indexing scheme is to take each row of a Cartesian mesh of cells and pack them under each other so that a $n_x \times n_y \times n_z$ array of cells becomes a 1D vector of length $n_xn_yn_z$. If the number of physical fields (such as temperature T, x-velocity V_x, density n etc.) in the system is n_v, the total length of this vector then becomes $n_vn_xn_yn_z$.

To extract a particular variable from a particular mesh cell when the data is packed in this 1D structure we define the index p of a field variable with field index $a \in [1, n_v]$ and mesh indicies $i \in [1, n_x], j \in [1, n_y], k \in [1, n_z]$ to be

$$p = a + n_v(i-1) + n_vn_x(j-1) + n_vn_xn_y(k-1). \tag{4.12}$$

Boundary Conditions

When solving the Cauchy problem for a system of partial differential equations, the solution requires both initial and boundary conditions. In the PARAMAGNET code periodic, reflective and outflow boundary conditions have been implemented.

A **periodic** boundary is an example of a Dirichlet condition. The value of a function at one end of the domain is the same as the opposite end. So for some field $u(x)$ in a one dimensional domain $x \in [0, L]$ then

$$u(0) = u(L).$$

A **reflective** boundary is a Neumann boundary condition where the derivative is equal to zero on the boundary. Physically this means any vector quantities that hit the boundary are reflected back. Using the same approach above, at the left boundary $x = 0$ this is

$$\left.\frac{\partial u(x)}{\partial x}\right|_{x=0} = 0.$$

An **outflow** boundary extrapolates the solution from the interior cell values. The simplest method is to set the boundary 'ghost' cell value by linearly extrapolating the values of the closest two interior cells. This condition allows flow to leave the domain, acting as an absorbing boundary to energy and momentum. If a 1D domain is discretised into N mesh points with field values u_i, these boundary conditions are implemented in the simplest finite difference approach by

$$u_0 = u_{N-1},$$
$$u_N = u_1,$$

for periodic,

$$u_0 = u_2,$$
$$u_N = u_{N-2},$$

for reflective, and

$$u_0 = 2u_1 - u_2,$$
$$u_N = 2u_{N-1} - u_{N-2},$$

for outflow conditions.

Parallelisation

In order to speed up the run time, the code PARAMAGNET utilises shared-memory parallelisation with the OpenMP library. In parallelisation the domain is split into blocks of equal size and each thread of a computational node computes the solution of the algo-

rithm in its own block. Because the memory is shared, cell values on the boundary of each block is accessible to every thread, so no communication between nodes is necessary.

This however limits use to a single node since the code requires all data to be stored in one memory location. This gives an upper limit to the memory requirements and thus an upper limit to the size of the simulation. Other methods such as distributed parallelisation with MPI could be used to avoid this memory issue, but since the laser solver relies on a direct linear matrix solver it requires access to the entire domain. Therefore distributed memory methods cannot be used without significantly more communication for the laser solver stage; the decision was made to keep to shared-memory parallelisation to keep the code simpler, with extensions to left for a later date.

4.3 The Plasma Solver

The Plasma Equations

The MHD equations are a non-linear coupled set of partial differential equations. The model begins with the fields distributed on a three-dimensional Cartesian mesh. The numerical scheme applied to the plasma equations is the backward Euler step method for time derivatives and central differences for the space dimensions. These methods convert the equations into discrete forms that can be found in full dimensionless form in Appendix B. In the discrete form the notation uses an upper index n for the timestep and i, j, k for the mesh positions. The terms α, β, γ encapsulate the cell sizes

$$\alpha = \frac{\Delta t}{2\Delta x}, \tag{4.13}$$

$$\beta = \frac{\Delta t}{2\Delta y}, \tag{4.14}$$

$$\gamma = \frac{\Delta t}{2\Delta z}. \tag{4.15}$$

To simplify the writing and reading of the equations the central difference operator will be used and is defined as

$$\delta_x f = f_{i+1jk} - f_{i-1jk} \tag{4.16}$$

for some general variable f. For the other dimensions x is replaced by y or z and the differences taken in j or k respectively. As an example the continuity equation, with variables density (n) and velocity (V_x, V_y, V_z), becomes

$$n^{n+1}\left(1 + \alpha\delta_x V_x^{n+1} + \beta\delta_y V_y^{n+1} + \gamma\delta_z V_z^{n+1}\right) + \left(\alpha V_x^{n+1}\delta_x n^{n+1} + \beta V_y^{n+1}\delta_y n^{n+1} + \gamma V_z^{n+1}\delta_z n^{n+1}\right) = n^n. \tag{4.17}$$

The Plasma Solver Stage

When the implicit finite difference methods described in section 4.1 are applied to the plasma equations, (the full discrete set of which can be found in Appendix B) the equations can be expressed as a large non-linear matrix equation

$$\underline{\underline{\mathbf{A}}}(\mathbf{v}^{n+1})\mathbf{v}^{n+1} = \underline{\underline{\mathbf{B}}}(\mathbf{v}^{n+1})\mathbf{v}^n. \tag{4.18}$$

The vector $\mathbf{v}^n$ holds the state of the system (the values of all the variables at each mesh point) at timestep n using the row indexing scheme described in section 4.2 and the vector $\mathbf{v}^{n+1}$ holds the state of the system at timestep $n+1$. For each timestep the vector $\mathbf{v}^n$ is

a known vector of constants and the aim is to solve for $\mathbf{v}^{n+1}$. This system is non-linear because the matrices $\underline{\underline{\mathbf{A}}}$ and $\underline{\underline{\mathbf{B}}}$ are functions of the vector $\mathbf{v}^{n+1}$ and so an iterative non-linear solution method is required; for this the PARAMAGNET code uses the JFNK method supplied by the PETSc library [126]. A further virtue of the JFNK method is that it only requires calculation of the residual vector $\mathbf{f}$. This can be calculated directly form the finite-difference equations of Appendix B without calculating the matrices $\underline{\underline{\mathbf{A}}}$ and $\underline{\underline{\mathbf{B}}}$.

The choice of an implicit time-integration algorithm for the plasma solver was heavily influenced by prior work by Bissell [115], who used an implicit time-integrator for simulations of a similar equations set. In general an implicit time-integrator is ill-suited to ideal MHD and hyperbolic problems and can suffer from numerical dissipation. While numerical dissipation can be avoided by using higher resolution meshes, this greatly increases the computational workload and the use of an explicit scheme is more appropriate.

The algorithm for the JFNK plasma solver can be found in Algorithm 1.

Algorithm 1 *Implicit plasma (MHD) solver algorithm utilising a JFNK method*

function JFNK($\mathbf{v}^{n+1}$, $\mathbf{v}^{n}$)
  while $E > E_{tol}$ **do** ▷ Check if the error has converged within tolerance
    $\Delta\mathbf{v} = 0$
    $\mathbf{f} = FORMF(\mathbf{v}^{n+1}, \mathbf{v}^{n})$ ▷ Calculate the RHS residual vector
    $\Delta\mathbf{v} = GMRES(\mathbf{f})$ ▷ Call the GMRES solver from the PETSc library
    $\mathbf{v}^{n+1} = \mathbf{v}^{n+1} + \Delta\mathbf{v}$ ▷ Update the solution vector
    $E = ||\Delta\mathbf{v}||$ ▷ Calculate the error, the 2-norm of the update
  end while
end function

4.4 The Paraxial Laser Solver

The Paraxial Equation

From chapter 3, the paraxial equation for a laser with wave number k is

$$2ik\sqrt{\epsilon_a}\partial_z\psi + \nabla_\perp^2\psi + k^2(\epsilon - \epsilon_a)\psi = 0. \tag{4.19}$$

The dielectric ϵ and axial dielectric ϵ_a terms are defined as

$$\epsilon = 1 - \frac{n}{n_c} + i\frac{n}{n_c}\frac{\nu_{ei}}{\omega_l} \tag{4.20}$$

$$\epsilon_a = 1 - \frac{n_0}{n_c} \tag{4.21}$$

where ω_l is the laser angular frequency, n_c is the plasma critical density and n_0 is the initial plasma electron density. This allows us to define the dielectric in terms of a change

in density relative to the reference value n_0,

$$\epsilon - \epsilon_a = \frac{\delta n}{n_c} = \frac{n_0}{n_c} - \frac{n}{n_c} + i\frac{n\nu_{ei}}{n_c\omega_l}. \tag{4.22}$$

The paraxial equation is a complex Schrödinger-type equation with the laser wavevector propagating parallel to the z-axis. Like the plasma equations, the paraxial equation is turned into discrete form using finite differences and the solution ψ represented by a mesh of complex variables ψ_{ij}^k, however unlike the plasma equations, the z-derivative in eq. 4.19 is taken implicitly with a backward Euler step. This is because for the laser field ψ to remain numerically stable as the solution algorithm 'sweeps' across the domain in the z-direction, an unconditionally stable numerical method such as the implicit backward Euler step is necessary for the z-derivative.

When central-differencing is used for the x, y dimensions and their derivatives, the problem is reduced to a complex, linear pentadiagonal matrix problem. Because the paraxial equation is 3-dimensional, we can use the ADI scheme to decompose this pentadiagonal matrix into a two-step method. For each z 'slice' of the domain at position k, two - much simpler - tridiagonal matrix equations are solved,

$$A_1\psi^{k+\frac{1}{2}} = b_1, \tag{4.23}$$
$$A_2\psi^{k+1} = b_2. \tag{4.24}$$

The index $k + \frac{1}{2}$ represents a 'half-step', an intermediate solution that provides input to the second equation. A_1 represents the implicit step in x while A_2 represents the implicit step in y. The full form of these matrix equations derived from the paraxial equation are

$$\alpha_1\psi_{ij}^{k+\frac{1}{2}} + \beta_1(\psi_{i+1,j}^{k+\frac{1}{2}} + \psi_{i-1,j}^{k+\frac{1}{2}}) = \gamma_1\psi_{ij}^k + \delta_1(\psi_{i,j+1}^k + \psi_{i,j-1}^k) \tag{4.25}$$
$$\alpha_2\psi_{ij}^{k+1} + \beta_2(\psi_{i+1,j}^{k+1} + \psi_{i-1,j}^{k+1}) = \gamma_2\psi_{ij}^{k+\frac{1}{2}} + \delta_2(\psi_{i,j+1}^{k+\frac{1}{2}} + \psi_{i,j-1}^{k+\frac{1}{2}}). \tag{4.26}$$

Where the constants are defined as

$$\alpha_1 = 4ik\sqrt{\epsilon_a} - 2\frac{\Delta z}{\Delta x^2} + k^2\delta n\frac{\Delta z}{2n_c},$$
$$\alpha_2 = 4ik\sqrt{\epsilon_a} - 2\frac{\Delta z}{\Delta y^2} + k^2\delta n\frac{\Delta z}{2n_c},$$
$$\beta_1 = \frac{\Delta z}{\Delta x^2},$$
$$\beta_2 = \frac{\Delta z}{\Delta y^2},$$

$$\gamma_1 = 4ik\sqrt{\epsilon_a} + 2\frac{\Delta z}{\Delta y^2} - k^2\delta n\frac{\Delta z}{2n_c},$$
$$\gamma_2 = 4ik\sqrt{\epsilon_a} + 2\frac{\Delta z}{\Delta x^2} - k^2\delta n\frac{\Delta z}{2n_c},$$
$$\delta_1 = -\frac{\Delta z}{\Delta y^2},$$
$$\delta_2 = -\frac{\Delta z}{\Delta x^2}.$$

The Paraxial Solver Stage

Given this is a complex tridiagonal matrix problem one should simply be able to apply the tridiagonal matrix algorithm [124]. However there is an added complication because of the presence of the boundary conditions $\partial\psi$, defined on the edges of the domain in x and y. For the laser field ψ, we choose periodic boundary conditions in the x, y directions. To account for this condition, the tridiagonal linear solver will need to be modified such that off diagonal terms - which represent the boundary values - are present in the matrix. This can be achieved using the Sherman Morrison formula [124].

Periodic boundary conditions put non-zero terms in the far corners of the matrix, the Sherman-Morrison formula treats these as a small change to a tridiagonal matrix. Given a matrix A and an outer product uv^T containing the corner values, the inverse of the sum is

$$(A - uv^T)^{-1} = A^{-1} - \frac{A^{-1}uv^TA^{-1}}{1 + v^TA^{-1}u}. \tag{4.27}$$

This can be combined with the tridiagonal matrix algorithm to solve the matrix equation quickly with small memory requirements. The Sherman-Morrison-Tridiagonal algorithm to solve a tridiagonal matrix problem $Ax = b$, with periodic conditions, is described in full in Algorithm 2.

Algorithm 2 *The Sherman-Morrison-Tridiagonal algorithm*

function SMT(A, b)
  $A_{11} = b_1 + A_{11}$
  $A_{NN} = A_{NN} + A_{21}A_{12}/b_0$
  $y = tridiag(A, b)$ ▷ Solve the intermediate equation $Ay = b$
  $u_1 = -b_1$
  $u_N = A_{12}$
  $q = tridiag(A, u)$ ▷ Solve intermediate equation $Aq = u$
  $v_0 = 1$
  $v_N = -A_{12}/b_0$
  $x = y - \left(\frac{v\cdot y}{1+v\cdot q}\right) q$ ▷ Apply the Sherman-Morrison formula
  $b = x$ ▷ Re-write the solution x into the RHS vector b
end function

The laser field is solved at each timestep by sweeping across the domain in the z-direction with a succession of linear solves at each value of the z with index k, using the

SMT algorithm above. The full paraxial equation solver, using the ADI method can be found in Algorithm 3.

Algorithm 3 *Paraxial laser solver algorithm using the ADI method*

function PARAXIAL(ψ, $\mathbf{v}$)
  for $k = 1 : N_z$ **do**
    for $i = 1 : N_x$ **do** ▷ Begin $x-$axis sweep
      $A_1 = A_1(\mathbf{v})$ ▷ Calculate matrix A_1 (eq. 4.22) using the plasma density
      $b_1 = b_1(\psi^k)$ ▷ Calculate RHS vector b_1 (eq. 4.22)
      $\psi^{k+\frac{1}{2}} = SMT(A_1, b_1)$ ▷ Solve the intermediate matrix problem
    end for
    for $j = 1 : N_y$ **do** ▷ Begin $y-$axis sweep
      $A_2 = A_2(\mathbf{v})$ ▷ Calculate matrix A_2 (eq. 4.23) using the plasma density
      $b_2 = b_2(\psi^{k+\frac{1}{2}})$ ▷ Calculate RHS vector b_2 (eq. 4.23)
      $\psi^{k+1} = SMT(A_2, b_2)$ ▷ Solve the second matrix problem
    end for
  end for
end function

4.5 The Solution Algorithm

It is now possible to put all the previous algorithms together into the whole PARAMAGNET solver. The code begins by setting the initial conditions for the plasma $\mathbf{v}^0$ and the laser field ψ. The boundary conditions for the plasma are then set with *SetBoundary*. Within a time loop the laser field is updated first with the PARAXIAL solver, before calling the JFNK plasma solver, which updates the plasma state. It is specified in the code when and how frequently to output data and which variables to output. The output is in both raw ASCII format and VTK format; this VTK format allows the user to view the output using Paraview. See Algorithm 4 below for details.

Algorithm 4 *PARAMAGNET solution algorithm*

$\mathbf{v}^0 = InitialiseV(\mathbf{v}^0)$
$\psi = InitialiseLaser(\psi)$
$\partial\mathbf{v}^0 = SetBoundary()$ ▷ Set initial and boundary conditions
for $n = 1 : M$ **do**
  $PARAXIAL(\psi, \mathbf{v}^n)$ ▷ Update laser field
  $JFNK(\mathbf{v}^{n+1}, \mathbf{v}^n, \psi)$ ▷ Update the plasma state
  if $n = n_{output}$ **then** ▷ Check if the code should output on this step
    $OutputVTK(\mathbf{v}^n, \psi)$
    $OutputTXT(\mathbf{v}^n, \psi)$
  else
    Continue
  end if
end for

4.6 PARAMAGNET and Other Codes

The code described herein is by no means the first MHD code. While other MHD codes exist for the simulation of laser-plasma interactions, PARAMAGNET was written to fill a niche and quickly explore certain physics while applying a different numerical approach to conventional MHD codes.

Mature MHD codes such as FLASH [46] (maintained at the University of Chicago) are the product of many years of development and a large team. Though PARAMAGNET cannot compare in terms of performance or overall features, FLASH lacks a paraxial laser solver, opting instead for a ray-tracing model. At the time of writing FLASH also only incorporates the resistivty, Biermann and Hall terms in the generalised Ohm's law, while PARAMAGNET includes the full Ohm's law. The numerical solution methods employed by FLASH are more advanced and accurate than those employed by PARAMAGNET, but the small scale of this code allowed experimentation with the JFNK method. Implicit methods like JFNK are common in the treatment of parabolic terms and are commonly implemented with operator splitting, but the simplicity of the JFNK implementation does make it attractive over some of the conventional implicit approaches used by FLASH.

Another code MHD code called CHIMERA [127] (maintained by Imperial College London) was written specifically to simulate inertial confinement fusion experiments. During the time of this PhD, CHIMERA was extended to include radiation transport and the full Ohm's law, including the Nernst effect and the Righ-Leduc heat flow. While there is cross-over in the physics capability of this code and PARAMAGNET, CHIMERA again still lacks the paraxial solver that was required for the investigations detailed in chapter 5.

While performance of PARAMAGNET lags behind these codes, the smaller scale al-

lows a sole developer to experiment more and try out methods with a more focused objective. In this regard the PARAMAGNET code has performed very well, being a modern C++ code with a small codebase (~ 5000 lines) and without integration issues that can plague large projects.

4.7 Code Testing: The Plasma Solver

Before applying the PARAMAGNET code to physical problems, just like all other numerical software, it must be tested for accuracy. Errors in the algorithm or numerical scheme can lead to incorrect results in final simulations. Physical simulation codes are tested by standardised tests that attempt to replicate known results. An analytic comparison test is the most common form of numerical test.

In an analytic comparison test, an exact analytic result is derived from a simplified version of the Cauchy problem for the equation set. The code then simulates the system with the same boundary and initial conditions and the result is compared to the analytic expression from which one can calculate the error.

The plasma physics module solves the single-fluid MHD system with the extension of Braginskii transport coefficients. Being MHD, this system is not just a fluid solver but also an electromagnetic solver. Ampere's law and Faraday's law mix together electromagnetic fields with the fluid fields of density, velocity and temperature; in turn the module must also satisfy the property of a divergence-less magnetic field, as stipulated by Gauss' law for magnetism.

The MHD equations are a mixed system with hyperbolic and parabolic terms with 5 independent fields. The plasma module therefore must robustly calculate the solution despite terms with very different numerical behaviour. The plasma module tests described below include a circular-polarised Alfvén wave test, the Orszag-Tang vortex test and a temperature and magnetic field relaxation test.

Circular Polarised Alfvén Waves

An Alfvén wave is a cold plasma wave where the ions oscillate transversely under the application of a magnetic field (B) parallel to the direction of the wave [128]. These waves have the dispersion relation

$$\omega^2 = k^2 v_a^2, \tag{4.28}$$

with the Alfvén speed

$$v_a = \frac{B}{\sqrt{\mu_0 m_i n_i}}. \tag{4.29}$$

Circular polarised Alfvén waves have the useful property of being exact non-linear solutions to the ideal MHD system of equations. The circular polarised waves were also chosen because the analytic solution is non-zero for more of the terms in the ideal MHD set. They also do not transfer energy into thermal energy so the temperature should remain constant and provided the solution algorithm works, they should not decay into other modes via numerical errors.

To perform this ideal MHD test, all diffusive and transport terms were turned off, as were all laser coupling terms and the Biermann battery term. The wave is initialised propagating diagonally with the grid to capture any grid imprint that may be missed when using a wavevector parallel to the Cartesian grid axes. The domain itself is the unit square $x, y \in [0, 1]$, with the number of cells equal to $(n_x, n_y, n_z) = (128, 128, 1)$. The simulation was chosen to evolve over a period of $T = 1$ with $n_t = 1000$ timesteps. Periodic boundary conditions were used on all dimensions and the full initial condition for this test can be found in table 4.2.

$\rho = 1$	$V_x = -0.1\frac{\sqrt{2}}{2}\cos(k_\parallel x_\parallel)$	$B_x = \frac{\sqrt{2}}{2}(1 + 0.1\cos(k_\parallel x_\parallel))$
$p = 0.1$	$V_y = -0.1\frac{\sqrt{2}}{2}\cos(k_\parallel x_\parallel)$	$B_y = \frac{\sqrt{2}}{2}(-1 + 0.1\cos(k_\parallel x_\parallel))$
$k_\parallel x_\parallel = 2\pi(2x - 2y)$	$V_z = -0.1\sin(k_\parallel x_\parallel)$	$B_z = 0.1\sin(k_\parallel x_\parallel)$

Table 4.2: Initial condition of the Alfvén wave simulations, these are normalised values for the fields.

The results of this test are illustrated in figure 4.1, the 2D map shows a wave propagating diagonally across the domain at time $t = 0.5$. Lineouts of the wave are shown in figure 4.2 and one can see these waves maintain the required sinusoidal form as they propagate across the domain, however the amplitude does drop by approximately 5% over the whole simulation time (in this simulation $T_{max} = 1$), this comes from numerical errors (specifically numerical dissipation) leading to losses in energy. The simulation time was set to correspond to 5 wave propagation times, that is, the time taken for one wavelength to propagate across the whole domain.

The equation set described in the previous chapters and solved by the plasma module is not in conservative form, and the particular choice of finite-difference scheme employed by the PARAMAGNET code is not inherently conservative. As such there is the potential for mass, energy and momentum to be lost during a simulation. To see how well the code fares in this regard, the Alfvén wave test results will also be used to investigate the conservation properties of the plasma module.

The relative change in mass, momentum and total energy over the lifetime of the simulation gives a measure of how well the code conserves these quantities. Following the

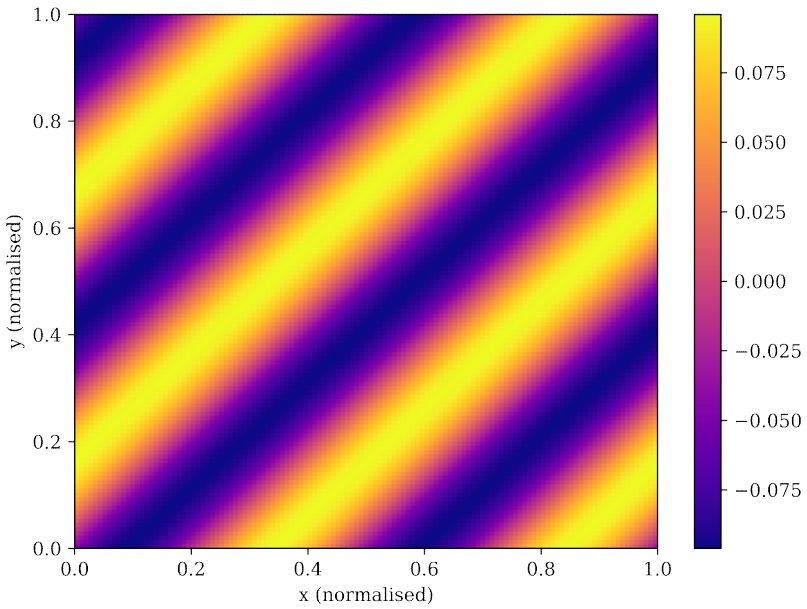

Figure 4.1: The total (normalised) magnetic field magnitude ($|\mathbf{B}|$) of a circular polarised Alfvén wave travelling diagonally in a two dimensional domain.

test used by Bissell [115], one can define the quantities

$$\Delta Q(t) = \frac{Q(t) - Q(0)}{Q(0)}, \tag{4.30}$$

$$Q(t) = \sum_{i,j,k} \frac{Q_{ijk}(t)}{n_x n_y n_z}, \tag{4.31}$$

where $Q_{ijk}(t)$ represents the quantity at cell position i, j, k at time t. Plotting ΔQ for mass, momentum and energy in figure 4.3, one can see the largest drop is in momentum. Whilst there is minimal change in the total mass and energy during the simulation, the momentum drops by approximately 7.5%. This can be attributed to the choice of implicit time-integration method, which is known to produce numerical dissipation. While the momentum losses in this advection test are larger than reported in other fluid codes such as FLASH [46], the losses in energy and density are within acceptable ($< 0.5\%$) limits for the diffusion-dominated simulations of this thesis.

The Orzsag-Tang Vortex

A second common test for plasma physics codes is the Orzag-Tang vortex [129]. This problem is useful for testing the shock-capturing capability of a plasma simulation. As the system evolves sharp shock fronts form in density, velocity and magnetic field, eventually leading to a very turbulent plasma.

Like the Alfvén wave test, this is an ideal MHD problem but does not have an analytic solution. This value of this test is to assess the code's performance in very non-linear and turbulent situations. The system is initialised in 2D with periodic boundary conditions

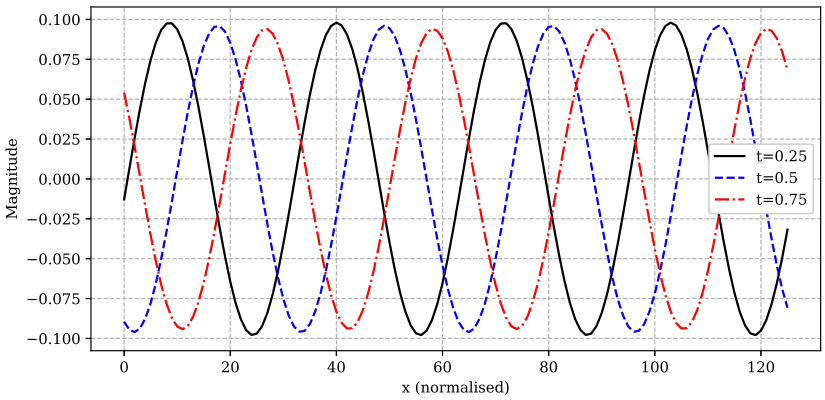

Figure 4.2: Diagonal lineouts of the total (normalised) magnetic field magnitude ($|\mathbf{B}|$) for three time points show the wave travelling to the right, maintaining its sinusoidal form.

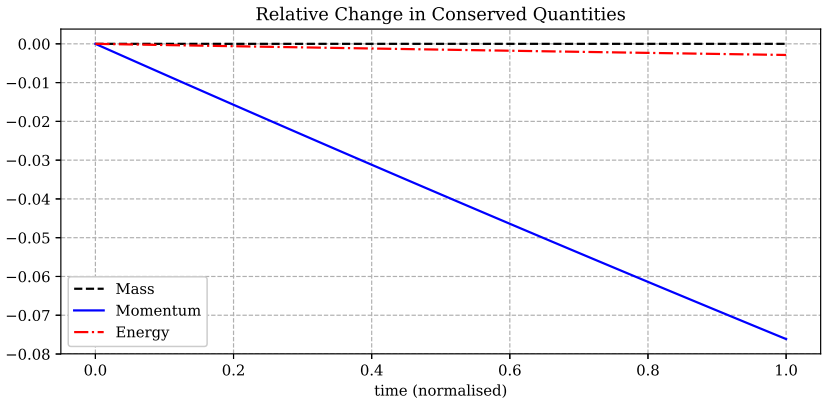

Figure 4.3: Lineouts of the total mass, momentum and energy of the plasma during the Alfvén wave test show the code conserves mass and energy well, with some loss in momentum.

and a unit square domain $x, y \in [0, 1]$ with mesh sizes $(n_x, n_y, n_z) = (256, 256, 1)$. The initial conditions for the fields can be found in table 4.3.

$\rho = \frac{25}{36\pi}$	$V_x = -\sin(2\pi y)$	$B_x = -\frac{1}{\sqrt{4\pi}}\sin(2\pi y)$
$p = \frac{5}{12\pi}$	$V_y = \sin(2\pi x)$	$B_y = \frac{1}{\sqrt{4\pi}}\sin(2\pi x)$

Table 4.3: Initial condition for the Orszag-Tang vortex, these values apply to the normalised variables

Figure 4.4 shows the results of the Orszag-Tang vortex test. By $t = 0.5$ the density, velocity magnitude and magnetic field magnitude have wrapped up into very non-linear profiles with the appearance of shock-like regions. The simulation of the Orszag-Tang vortex stalled at $t = 0.56$ after the formation of the first few strong shock fronts.

In the later stages, a highly resolved simulation of this problem should produce two-dimensional MHD turbulence. At later times strong shock waves should have formed and passed through each other, creating turbulent flow features at different spatial scales. For

comparison, compare the PARAMAGNET simulation of fig. 4.4 with the FLASH simulation [46] of the same test (both show the simulation at t=0.5) in fig. 4.5. The PARAMAGNET code clearly has lost the fine-scaled shock fronts. This is troubling for the accuracy of advective phenomena, especially in the regime of strong shocks. However given the performance of the advection in the Alfven wave test above, the code is accurate if the shock and turbulent regime is avoided.

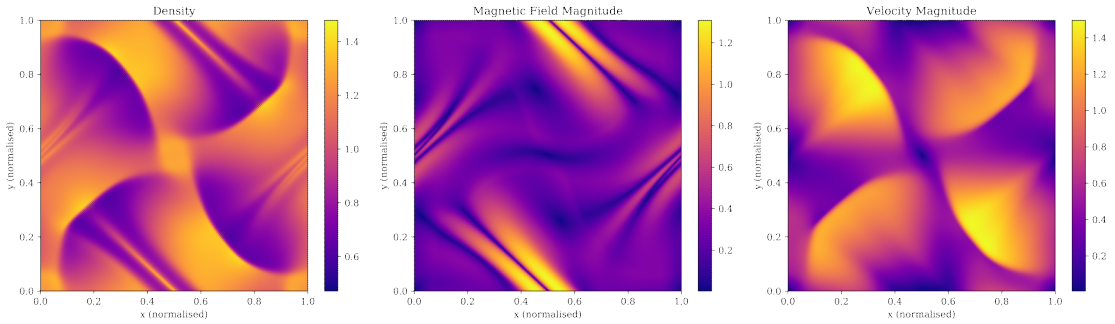

Figure 4.4: These maps show the density, velocity magnitude and magnetic field magnitude during the Orzsag-Tang Vortex test at $t = 0.5$. Shock fronts have begun to form in this very non-linear stage of the evolution. These variables are normalised according to the scheme in table 4.1.

The hydrodynamic algorithm used by PARAMAGNET is not adequate to capture such strong shock conditions. Figure 4.6 gives lineouts through the centre of the domain at $t = 0.5$, and the characteristic peaks and troughs of the early-stage Orszag-Tang vortex are clear.

Temperature and Magnetic field Relaxation

The third plasma solver test will verify the diffusive terms in the PARAMAGNET equations. Using a method introduced by Bissell [115], this test compares the decay of one-dimensional linear perturbations in the temperature and magnetic fields. It has the advantage of testing the thermal diffusion, resistive diffusion, Nernst advection and Ettingshausen effects simultaneously.

The system is initialised with a small perturbation on a uniform background under a unidirectional magnetic field, such that $B_z = B_0 + \delta B(x)$ and $T = T_0 + \delta T(x)$. Once laser-coupling, hydrodynamics, Biermann battery and Ohmic heating terms are turned off, the equation set solved by PARAMAGNET reduce to the parabolic system

$$\frac{\partial \delta B}{\partial t} = d_b \nabla^2 \delta B + a_E \nabla^2 \delta T, \tag{4.32}$$

$$\frac{\partial \delta T}{\partial t} = d_T \nabla^2 \delta T + a_N \nabla^2 \delta B, \tag{4.33}$$

with the coefficients are defined as

$$d_b = \frac{\alpha_\perp}{\mu_0 e^2 n_0^2}, \quad a_E = \frac{\beta_\wedge}{e}, \quad d_T = \frac{2\kappa_\perp}{3n_0}, \quad a_N = \frac{2T_0\beta_\wedge}{3e\mu_0 n_0}.$$

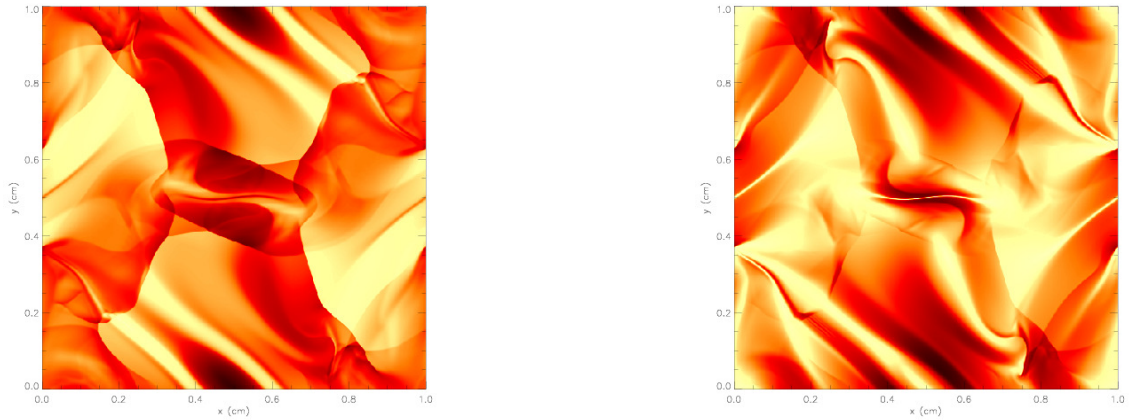

(a) Density map

(b) Magnetic field magnitude map

Figure 4.5: Density (a) and magnetic field magnitude (b) maps produced by the FLASH code during the Orszag-Tang test. These maps are taken at $t = 0.5$ when turbulence has already begun to form, and small scale shocks are present in the density and magnetic field profiles.

These are constants, the transport coefficients being functions of the uniform background T_0, B_0, n_0. If the system is Fourier transformed, the dispersion relation is found to be

$$\omega_{\pm} = \frac{k^2}{2}\left[-i(d_T + d_b) \pm \sqrt{-4a_E a_N - (d_b - d_T)^2}\right]. \tag{4.34}$$

This equation system can be solved analytically, in this case a sinusoidal initial condition is used. For the purposes of this test, the positive root of the dispersion relation is taken and the result is an exponentially decaying sinusoidal perturbation with a decay rate of $\gamma = \Im[\omega_+]$. The temperature and magnetic field perturbations are out of phase. Were the negative root taken the fields would be in phase and the advection affects would enhance the perturbations rather than contribute to their decay.

$$\delta T(t) = \delta T(0)\exp^{-\gamma t}, \quad \delta B(t) = \delta B(0)\exp^{-\gamma t}.$$

The simulation domain was chosen to be $200\mu m$ with a mesh of $(n_x, n_y, n_z) = (512, 1, 1)$ and periodic boundary conditions; the simulation time proceeded for $1ns$. The background plasma and initial conditions for the fields can be found in table 4.4.

$T = T_0(1 + \delta\sin(2\pi x/L_x))$	$B_z = B_0(1 + \delta\sin(2\pi x/L_x + \pi))$	$L_x = 200\mu m$
$B_0 = 5T$	$T_0 = 20eV$	$n_0 = 1 \times 10^{25} m^{-3}$

Table 4.4: Physical parameters used in the mode decay test

The results of this test can be found in figure 4.7. The code reproduced the decay of the linear mode in both the temperature and magnetic field successfully.

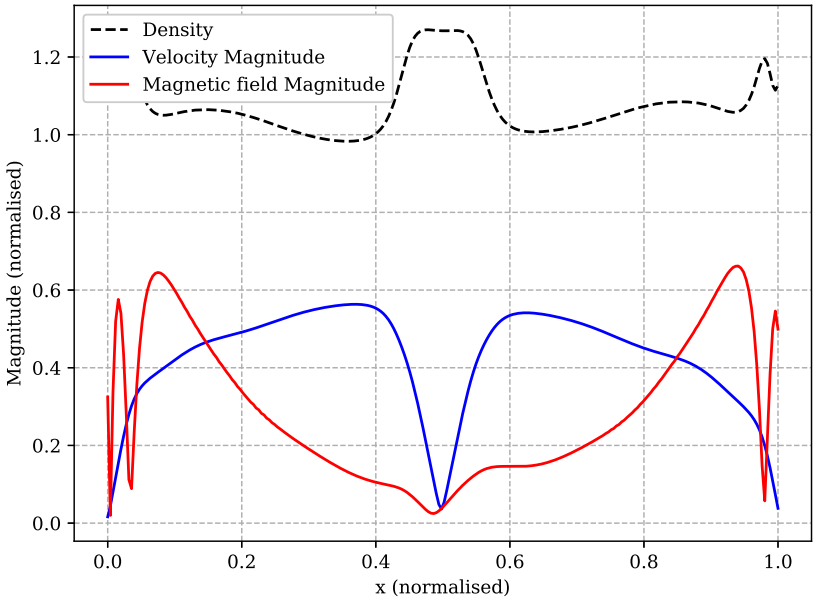

Figure 4.6: These lineouts show the values of the normalised density, velocity magnitude and magnetic field magnitude for the central slice of the domain at time point $t = 0.5$. While shock fronts have formed, the numerical dissipation has smoothed out the small-scale turbulence characteristic of the late-stage Orszag-Tang vortex.

4.8 Code Testing: The Laser Solver

To test the accuracy of the laser solver, two analytically solvable problems will be compared with the code output. The first of these is to reproduce the propagation of a Gaussian beam in a vacuum. The envelope of the electric field of a laser with a radial Gaussian profile can be derived exactly from the paraxial equation. The second test will be using a parabolic density profile to compare the laser propagation in the presence of a plasma. Like the Gaussian beam test this has an analytic solution when the electron number density (and thus the dielectric function) has a radial parabolic form.

Gaussian Beam

The functional form of a Gaussian beam can be found in the Laser Theory chapter §3.3. It is an exact cylindrically symmetric solution to the vacuum paraxial equation. For this test an initial condition is defined on the $z = 0$ boundary. The laser solver sweeps across the domain in the z-direction. The boundary condition was chosen so that the focal point of the Gaussian beam coincides with the centre of the domain.

By using the expression of a Gaussian beam defined in eqs. 3.14-3.18, the domain is chosen to be four Rayleigh lengths z_r in total, so that the left side of the domain ($z = 0$)

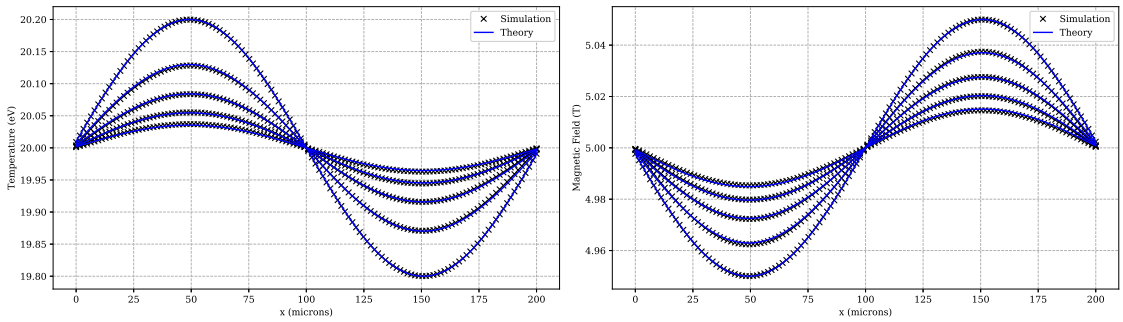

Figure 4.7: The decay of a linear perturbation in the magnetic field and temperature shows clear agreement with the theoretical result derived from a linearised model.

corresponds to the boundary condition

$$\partial\psi = \psi(-2z_r). \tag{4.35}$$

Since this test models a laser in a vacuum, laser-plasma coupling is turned off. It is also time-independent so only one time-step is required. A 3D domain is used for this simulation with mesh size $(n_x, n_y, n_z) = (256, 256, 1024)$. Figure 4.8 shows a 2D slice through the domain, in comparison with the analytic calculation. The intensity matches the theoretical result, including the position of the focal point and the beam divergence. An axial lineout of the intensity can be found in figure 4.9, and the code simulates the intensity profile of the theoretical calculation well, with some small under-prediction at the peak.

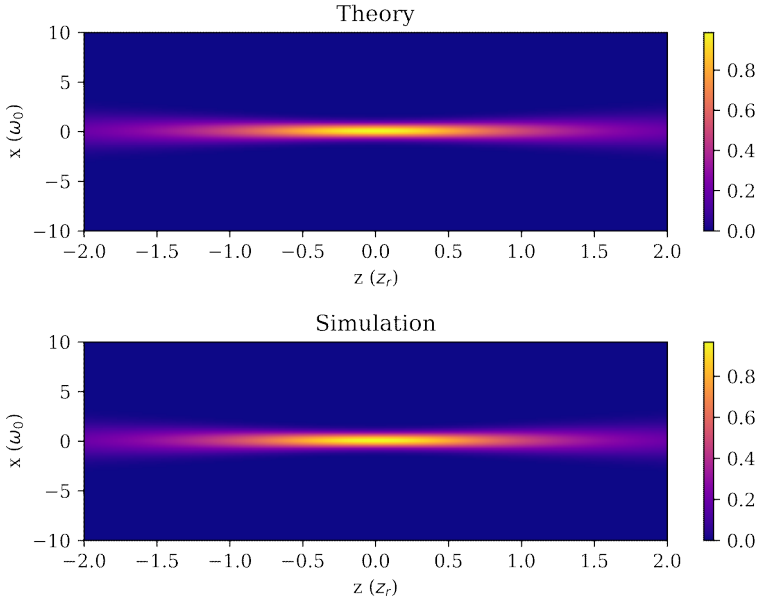

Figure 4.8: The laser intensity of a Gaussian beam compared with the output from the paraxial laser solver. The intensity map matches the theoretical result, including the focal point width (normalised in terms of the vacuum beam waist ω_0) and beam divergence.

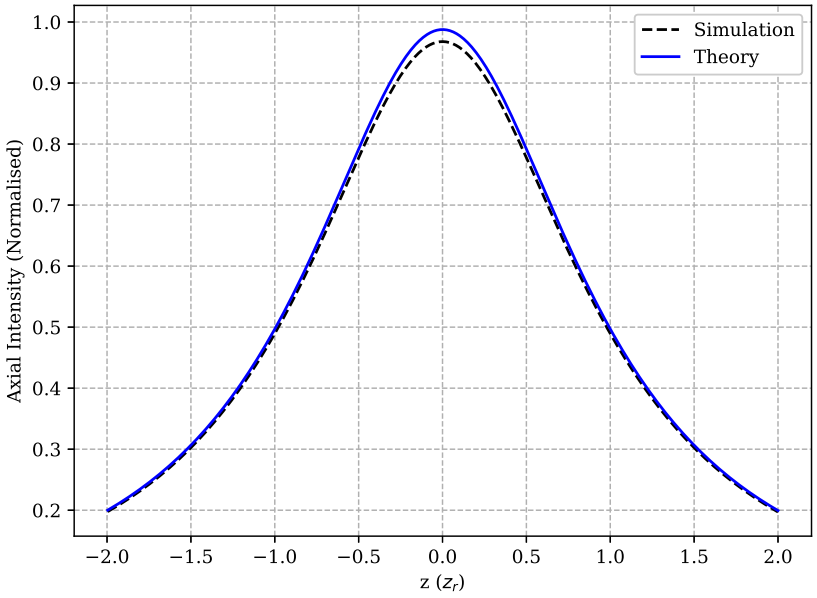

Figure 4.9: The axial intensity of a Gaussian beam compared to the paraxial laser solver output shows some under-approximation at the focal point.

Parabolic Density Profile

It is possible to construct an analytic expression for the density profile for which a Gaussian beam will neither focus or defocus [120]. This will test the laser-plasma coupling via the refractive index by reproducing a zero-focusing or defocusing Gaussian beam. Looking at the definition of the paraxial equation, eq. 3.12. this implies $\nabla^2\psi = -k_0^2(\epsilon - \epsilon_0)$. Using this condition one can derive a density profile that should prevent any focusing

$$n(r) = n_0\left(1 + \frac{n_c^2}{n_0^2 k^2 \omega_l^2} r^2\right) \quad \forall z \tag{4.36}$$

This test uses the same setup as the previous Gaussian beam test above, however this time the domain is no longer a vacuum and so the refractive index term is now turned on (and can deviate from 1). The boundary condition for $z = 0$ is now set to be the focal spot of a Gaussian beam of the form of eq. 3.14, such that the boundary condition $\partial\psi$ is

$$\partial\psi = \psi(0). \tag{4.37}$$

The result of the test is illustrated in figure 4.10 where the uniform-density solution is compared with the parabolic-density solution. With the presence of the non-uniform density, the beam divergence has been cancelled exactly by the refractive index. Figure 4.11 shows a lineout of the axial intensity in both simulations. The simulation with a parabolic profile, the axial intensity is a constant, whilst in the uniform density simulation, the axial intensity drops as the beam diverges. This test shows the laser solver has successfully replicated the expected theoretical result when the refractive index term is

included in the paraxial equation.

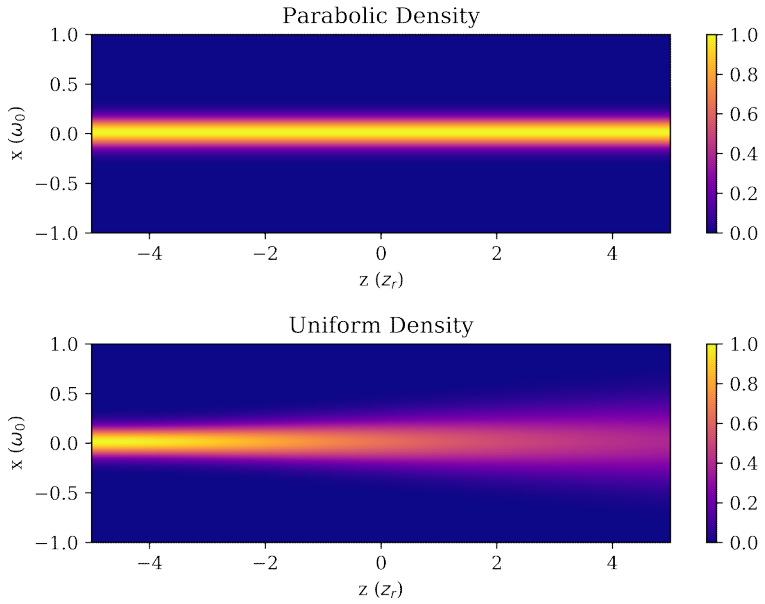

Figure 4.10: Comparing the laser intensity of a Gaussian beam in a plasma with a parabolic density profile and in a vacuum shows how the density profile exactly cancels the beam divergence.

4.9 Summary

The PARAMAGNET code is a brand new C++, single-fluid plasma physics code coupled to a paraxial laser solver. By using a JFNK method to solve the core plasma equations the computational complexity was kept to a minimum and allowed a fully-implicit algorithm. The lack of preconditioners for the non-linear matrix problem however restricts the convergence rate of the nonlinear solver. In future, physics-based preconditioners could be used to improve the convergence properties and the overall speed of the plasma solver. When restricted to diffusion-dominated systems, such as described in chapter 5, the implicit choice can be justified because of the stiffness of these systems. As a fully JFNK plasma physics code, PARAMAGNET could also be used as a testbed for the JFNK method in future simulation codes for terms with different mathematical properties.

The 3D paraxial solver utilising an ADI method allows the direct calculation of the laser field, rather than inferring the field present by using Gaussian beam approximations as is the case in ray-tracing methods. The direct matrix solver based on the tridiagonal algorithm allows the very fast calculation of the laser field and is successfully parallelised with the OpenMP shared-memory parallel library.

The PARAMANGET code was tested on a set of plasma and laser physics tests that

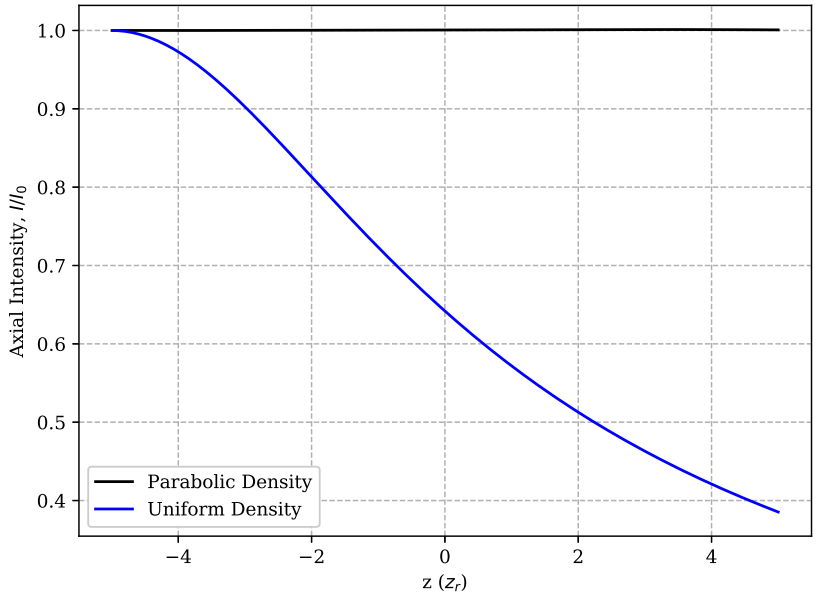

Figure 4.11: Looking at the axial intensity, we see the parabolic density profile prevents the beam diverging. In a vacuum the intensity drops as the beam diverges.

have been used as standard in other plasma physics applications. The Orszag-Tang vortex, an Alfvén wave, the diffusive relaxation of a perturbation, a Gaussian beam and a beam in a parabolic density profile were all simulated to validate the accuracy of the code's solution. In all tests the code has performed well and converges to the expected analytic results, thus providing the confidence to proceed with simulations of physical phenomena.

Though accurate in reproducing the theoretical results, the code struggled with the strong shock fronts present in the Orzag-Tang vortex. Whilst this for now limits the applicability to less extreme conditions, this could be solved with the use of a more robust advection scheme in the plasma equations. The limitations in advection are the result of the use of implicit time-integration scheme for the whole set of equations. Implicit time-integration is beneficial for parabolic and diffusive-dominant problems because the unconditionally stable character of implicit methods allows longer timesteps for stiff problems. While this is useful, these methods are numerically dissipative and fail for advection problems like the Orszag-tang vortex test. A better approach would be the use of operator splitting to allow implicit time-integration for parabolic terms and explicit time-integration methods for the rest of the problem.

In future, optimisation of the code to improve the speed and robustness would allow its use in more general plasma physics applications. With this code completed, it is now possible to bring fully 3D Braginskii-MHD simulations to bear on problems driven by long-pulse lasers.

5

Magnetised Laser Filamentation and Self-Focusing

This chapter concerns the influence of the magnetised thermal conductivity on the propagation of a nanosecond $10^{14} W cm^{-2}$ laser in an underdense plasma. These values were chosen to replicate long-pulse experimental campaigns mentioned in the introductions such as those of Froula *et al.* [130] and Gregori *et al.* [37].

This chapter will begin by deriving an analytic laser focusing model from the paraxial equation introduced in chapter 3, using both the thermal and ponderomotive mechanisms and will show the existence of a bifurcation of focusing behaviour in this mixed-mechanism system. The analytic model shows the influence of the magnetic field arising through the thermal conductivity. Given the model itself makes some approximations, the use of the PARAMAGNET code is required to confirm the results in the non-linear regime.

After studying focusing, the related phenomenon of filamentation will be introduced and the dispersion relation calculated from an MHD model. By using a modified theory to include collisional magnetisation, a similar magnetised thermal effect in the filamentation dispersion relation is found. The thermal mechanism is found to have an increased spatial growth rate in a magnetised plasma, a result of the magnetisation of the thermal conductivity. This chapter ends with a discussion on the effect of these results on recent magnetised inertial fusion experiments. Some of the work in this chapter has been published, and the results reproduced from Watkins and Kingham [112] with the permission of AIP publishing.

5.1 Self-Focusing

Laser self-focusing in a plasma is the effect in which the laser causes the local plasma refractive index to change. The beam then refracts into this channel in a process that feeds back and becomes unstable and forms laser filaments [60, 131]. This process can occur via thermal and ponderomotive mechanisms where the laser digs a channel in electron density, changing the refractive index. It can also occur by a relativistic mechanism where the relative mass increase of the electron results in a local refractive index change. This process can be detrimental to the performance of ICF experiments as the non-uniformity of the beam can seed hydrodynamic instabilities in direct drive[4] and the high-intensity laser fields in the filaments can make the experiment more susceptible to parametric instabilities [132].

The presence of laser propagation through a magnetised plasma in these experiments leads to the question of the effect of the magnetic field on the laser propagation through the plasma itself. The thermal mechanisms of self-focusing and filamentation of a laser are mediated by the thermal conductivity [97]; as such one expects these processes to be modified by the plasma magnetisation and importantly the factor $\kappa_\perp^c$ introduced in the magnetised transport theory section of chapter 2. There has been limited consideration of the influence of magnetised transport effects in existing theoretical and simulation studies of self-focusing, which will be considered in this chapter.

The model equations used for the following analysis come from a simplified set of the MHD equations along with the paraxial equation. Given a laser with vacuum wavenumber k_0 and a plasma with critical density n_c, the momentum, energy and paraxial Helmholtz equations become

$$\frac{m_i n}{Z}\frac{\partial \mathbf{V}}{\partial t} = -n\nabla_\perp T - T\nabla_\perp n - \frac{1}{2}\varepsilon_0 \frac{n}{n_c}\nabla_\perp |\psi|^2, \tag{5.1}$$

$$\frac{3}{2}n\frac{\partial T}{\partial t} = -\nabla_\perp \cdot \mathbf{q} + \frac{1}{2}\varepsilon_0 \frac{n}{n_c}\nu_{ei}|\psi|^2, \tag{5.2}$$

$$2ik_0\sqrt{\epsilon_a}\partial_z\psi + \nabla_\perp^2\psi + k_0^2\delta\epsilon\psi = 0, \tag{5.3}$$

$$\mathbf{q} = -\boldsymbol{\kappa}\cdot\nabla_\perp T. \tag{5.4}$$

The plasma coupling along the beam is minimal and so the gradient along the beam can be ignored, this approximation is valid when gradients along the z direction are much smaller than perpendicular to the z axis. The thermoelectric term in the the heat flow has also been ignored given that it is proportional to the current, and in this magnetised laser-plasma system the curl of the magnetic field is small.

The quantity $\delta\epsilon$ is the dielectric change and represents the plasma response to the laser and ϵ_a is the dielectric function of the uniform initial density. Note the symbol ε_0 is the

vacuum permittivity.

Steady State Model

The propagation time of the laser through the plasma is effectively instantaneous and the inertia terms of the plasma are small, therefore one can use a steady state model

$$n\nabla_\perp T + T\nabla_\perp n = -\frac{1}{2}\varepsilon_0\frac{n}{n_c}\nabla \perp |\psi|^2, \tag{5.5}$$

$$-\nabla_\perp \cdot (\boldsymbol{\kappa}\cdot\nabla_\perp T) = \frac{1}{2}\varepsilon_0\frac{n}{n_c}\nu_{ei}|\psi|^2, \tag{5.6}$$

$$2ik_0\sqrt{\epsilon_a}\partial_z\psi + \nabla_\perp^2\psi + k_0^2\delta\epsilon\psi = 0. \tag{5.7}$$

In the following analysis, the plasma and beam are cylindrically symmetric and the aim is to find an expression for the self-focal length. The theory of self-focusing here follows from the approach described by He [120] for neutral media. The aim is to determine the plasma response to the laser in terms of the density change δn.

Starting from the steady-state set of equations (5.5-5.7) but with the cylindrically symmetric approximation, the laser envelope ψ has the form

$$\psi = A(r,z)e^{ik_0 S(r,z)}, \tag{5.8}$$

$$|\psi|^2 = A^2 = \frac{A_0^2}{\alpha(z)^2}e^{-\frac{r^2}{a_0^2\alpha^2}}, \tag{5.9}$$

$$S = \beta(z)\frac{r^2}{2} + \phi(z). \tag{5.10}$$

The focal spot of the beam is the point at which the normalised Gaussian variance α^2 is a minimum. This minimum beam waist is a_0. The functions in these expressions satisfy the boundary conditions

$$\alpha(0) = 1, \tag{5.11}$$

$$\phi(0) = 0, \tag{5.12}$$

$$\beta(0) = \frac{1}{R}, \tag{5.13}$$

$$A^2(r,0) = A_0^2 e^{-\frac{r^2}{a_0^2}}. \tag{5.14}$$

This approximation means the beam has a beam waist of size a_0 positioned at $z = 0$ and a radius of curvature of the phase front of R. Using eq. 5.8 the paraxial equation (eq. 5.7) becomes the coupled pair

$$2\partial_z S + \left(\frac{\partial S}{\partial r}\right)^2 = \frac{1}{k_0^2 A}\left(\frac{\partial^2 A}{\partial r^2} + \frac{1}{r}\frac{\partial A}{\partial r}\right) + \delta\epsilon, \tag{5.15}$$

$$\partial_z A^2 + A^2\left(\frac{\partial^2 S}{\partial r^2} + \frac{1}{r}\frac{\partial S}{\partial r}\right) + \frac{\partial S}{\partial r}\frac{\partial A^2}{\partial r} = 0. \tag{5.16}$$

The dielectric variation $\delta\epsilon$ can be represented by an expansion in terms of orders of r,

$$\delta\epsilon(z,r) = \delta\epsilon_0(z) + \delta\epsilon_1(z)r + \delta\epsilon_2(z)r^2 + O(r^3). \tag{5.17}$$

By putting the expressions eqs. 5.10 and 5.09 into the first of eq. 5.15, one finds an algebraic expression in powers of r. Equating the terms proportional to the orders of r yields the following expressions

$$\alpha' = \beta\alpha, \tag{5.18}$$

$$\beta' + \beta^2 = \frac{1}{k_0^2 a_0^4 \alpha^4} + \delta\epsilon_2, \tag{5.19}$$

$$2\phi' = -\frac{2}{k_0^2 a_0^2 \alpha^2} + \delta\epsilon_0. \tag{5.20}$$

The primes represent derivatives with respect to z. Furthermore, by taking the derivative of eq. 5.18 and using eq. 5.19,

$$\alpha'' = \left(\beta' + \beta^2\right)\alpha = \left(\frac{1}{k_0^2 a_0^4 \alpha^4} + \delta\epsilon_2\right)\alpha. \tag{5.21}$$

The Isothermal Model

It is useful to analyse a simplified case with which to compare [120]. For this purpose this section will consider an isothermal plasma, with only the ponderomotive force as the laser-plasma coupling. The momentum equation is then

$$T\frac{\partial n}{\partial r} = \varepsilon_0 \frac{n}{n_c} r \frac{|\psi|^2}{a_0^2\alpha^2}. \tag{5.22}$$

which can be solved for the density

$$n = n_0 \exp\left(-\frac{\varepsilon_0|\psi|^2}{2Tn_c}\right). \tag{5.23}$$

This result, taken from He [120]. When the exponent is expanded, this gives a dielectric change

$$\delta\epsilon = -\frac{\delta n}{n_c} = \delta\epsilon_0 + \delta\epsilon_2 = \frac{n_0\varepsilon_0 A_0^2}{n_c^2 2T\alpha^2}\left(1 - \frac{r^2}{a_0^2\alpha^2}\right). \tag{5.24}$$

It is possible now to put this expression into eq. 5.21 and find an equation for the focal width α,

$$\frac{\alpha''}{\alpha} = \frac{1}{k_0^2 a_0^4 \alpha^4} - \frac{n_0\varepsilon_0 A_0^2}{n_c^2 2T a_0^2 \alpha^4}. \tag{5.25}$$

This equation can be solved by multiplying by $2\alpha'$ and integrating to get α^2. After using the equations 5.18 - 5.20 and the boundary conditions to find the constants this is

$$\alpha^2 = \left(\frac{1}{R^2} + \frac{1}{k_0^2 a_0^4} - \frac{n_0\varepsilon_0 A_0^2}{n_c^2 2T a_0^2}\right) z^2 + \frac{2}{R} z + 1. \tag{5.26}$$

Which yields the focal length by finding the minimum of α^2

$$z_f = \left(\frac{-1}{R} \pm \sqrt{\frac{n_0 \varepsilon_0 A_0^2}{n_c^2 2T a_0^2} - \frac{1}{k_0^2 a_0^4}} \right) \left(\frac{1}{R^2} + \frac{1}{k_0^2 a_0^4} - \frac{n_0 \varepsilon_0 A_0^2}{n_c^2 2T a_0^2} \right)^{-1}. \tag{5.27}$$

The Thermal Focusing Mechanism

Moving now to the thermal mechanism, the temperature equation is included and now there is both ponderomotive and IB coupling to the plasma. This model was first introduced by Perkins [59] but will be extended to analyse the influence of magnetic fields. In the formalism of Braginskii [22] the electron heat flow driven by a temperature gradient splits the familiar Fourier law into the parallel ($\kappa_\parallel$), perpendicular ($\kappa_\perp$) and Righi-Leduc ($\kappa_\wedge$) terms relative to the direction of the magnetic field **b**,

$$\mathbf{q} = -\kappa_\parallel \mathbf{b}(\mathbf{b} \cdot \nabla T) - \kappa_\perp \mathbf{b} \times (\nabla T \times \mathbf{b}) - \kappa_\wedge \mathbf{b} \times \nabla T. \tag{5.28}$$

We now introduce the the coordinate system, which is made up of the angle θ between the magnetic field **b** and the plane perpendicular (**r**) to the laser wavevector **k**, which satisfies the relations (illustrated in figure 5.1)

$$\sin\theta \mathbf{n} = \mathbf{r} \times \mathbf{b},$$
$$\cos\theta = \mathbf{r} \cdot \mathbf{b}.$$

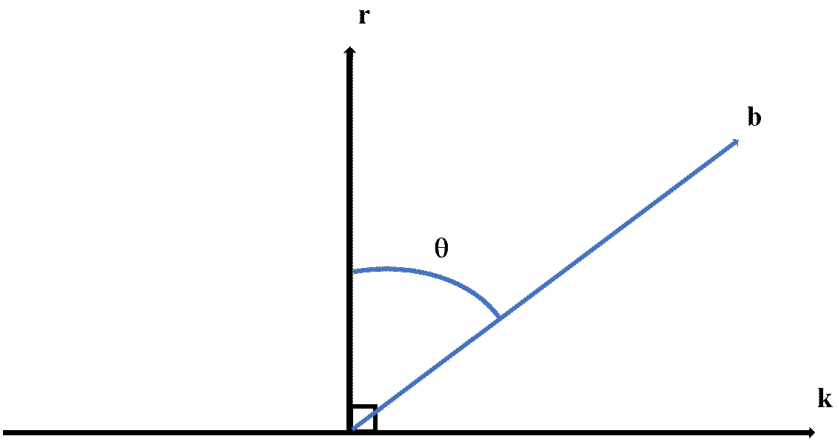

Figure 5.1: Geometry of the self-focusing calculation, with the laser wavevector **k**, the magnetic field direction **b** and the angle θ between the magnetic field and the plane perpendicular to **k**

The heat flow in these coordinates also takes advantage of the slowly varying envelope approximation, whereby plasma gradients (induced by the laser field) parallel to the wavevector can be ignored as they are very small relative to gradients in the plane

perpendicular to the wavevector. The heat flow becomes

$$\mathbf{q} = -\left(\kappa_{\parallel}\mathbf{b}\cos\theta + \kappa_{\perp}\mathbf{b}\times\mathbf{n}\sin\theta + \kappa_{\wedge}\mathbf{n}\sin\theta\right)\frac{\partial T}{\partial r}. \tag{5.29}$$

The radial divergence of the heat flow gives the energy balance equation

$$-\frac{1}{r}\frac{\partial}{\partial r}\left(r\{\kappa_{\parallel}\cos^2\theta + \kappa_{\perp}\sin^2\theta\}\frac{\partial T}{\partial r}\right) = \varepsilon_0\frac{n}{2n_c}\nu_{ei}|\psi|^2. \tag{5.30}$$

When the applied magnetic field is parallel with the direction of the laser wavevector (i.e $\cos^2\theta = 0$), the problem becomes cylindrically symmetric, so the energy balance equation becomes

$$-\frac{1}{r}\frac{\partial}{\partial r}\left(r\kappa_{\perp}\frac{\partial T}{\partial r}\right) = \varepsilon_0\frac{n}{2n_c}\nu_{ei}|\psi|^2. \tag{5.31}$$

This equation and the momentum equation are nonlinear, therefore to find an analytic solution the momentum and energy equations are linearised with small perturbations about a background constant density and temperature

$$T = T_0 + \delta T, \tag{5.32}$$

$$n = n_0 + \delta n, \tag{5.33}$$

with these approximations the energy and momentum equations become

$$n_0\frac{\partial\delta T}{\partial r} + T_0\frac{\partial\delta n}{\partial r} = -\varepsilon_0\frac{n_0}{2n_c}\frac{\partial|\psi|^2}{\partial r}, \tag{5.34}$$

$$-\frac{1}{r}\frac{\partial}{\partial r}\left(r\kappa_{\perp}^0\frac{\partial\delta T}{\partial r}\right) = \varepsilon_0\frac{n_0}{2n_c}\nu_{ei}^0|\psi|^2. \tag{5.35}$$

$\kappa_{\perp}^0$, and ν_{ei}^0 are the constant thermal conductivity and collision frequency, as functions of the background density and temperature.

Following the analysis of the last section, these equations are used to find a dielectric change which can be plugged into eq. 5.15. After substituting the linearised momentum equation into the linearised energy equation, the equation for the density change is

$$\frac{1}{r}\frac{\partial}{\partial r}\left(r\frac{\partial\delta n}{\partial r}\right) = \frac{1}{2}\frac{n_0}{T_0 n_c}\varepsilon_0|\psi|^2\left(\frac{n_0\nu_{ei}^0}{\kappa_0} + \frac{4}{a_0^2\alpha^2}\left(1 - \frac{r^2}{a_0^2\alpha^2}\right)\right). \tag{5.36}$$

In order to solve this equation the close-to-axis approximation is required

$$|\psi|^2 \approx \frac{A_0^2}{\alpha^2}\left(1 - \frac{r^2}{a_0^2\alpha^2}\right). \tag{5.37}$$

eq. 5.36 is then integrated twice to find δn and the second order dielectric variation required to find the equation for the beam variance is then

$$\delta\epsilon_2 = -\frac{1}{8}\left(\frac{n_0}{n_c}\right)^2\frac{\varepsilon_0 A_0^2}{n_0 T_0\alpha^2}\left(\frac{n_0\nu_{ei}^0}{\kappa^0} + \frac{4}{a_0^2\alpha^2}\right). \tag{5.38}$$

This is then used with eq. 5.21

$$\alpha'' = \frac{c_1}{\alpha^3} - \frac{c_2}{\alpha}, \tag{5.39}$$

with the constants defined as

$$c_1 = \frac{1}{k_0^2 a_0^4} - \frac{1}{2}\left(\frac{n_0}{n_c}\right)^2 \frac{\varepsilon_0 A_0^2}{T_0 a_0^2}, \tag{5.40}$$

$$c_2 = \frac{1}{8}\left(\frac{n_0}{n_c}\right)^2 \frac{\varepsilon_0 A_0^2}{n_0 T_0} \frac{n_0 \nu_{ei}^0}{\kappa_\perp^0}. \tag{5.41}$$

This can be written

$$\left(\frac{d\alpha^2}{dz}\right)^2 = -c_2 \alpha^2 \ln \alpha^2 + c_3 \alpha^2 - c_1. \tag{5.42}$$

In order to find an analytic result, the natural log is approximated to be

$$\alpha^2 \ln \alpha^2 \approx \alpha^2(\alpha^2 - 1), \tag{5.43}$$

which holds in the region $\alpha \in [0, 1]$ and yields

$$\left(\frac{d\alpha^2}{dz}\right)^2 = -c_2 \alpha^4 + (c_3 + c_2)\alpha^2 - c_1, \tag{5.44}$$

and the solution is found to be

$$\alpha^2 = d_1 + d_2 \sin(d_3 z + d_4), \tag{5.45}$$

with constants $d_1 - d_4$ defined as

$$d_1 = \frac{\frac{1}{R^2} + c_1 + c_2}{2c_2}, \tag{5.46}$$

$$d_2 = \sqrt{d_1^2 - \frac{c_1}{c_2}}, \tag{5.47}$$

$$d_3 = \sqrt{c_2}, \tag{5.48}$$

$$d_4 = \arcsin\left(\frac{1 - d_1}{d_2}\right). \tag{5.49}$$

In the case of a long geometric focus, such that the Rayleigh length is very long relative to the propagation distance ($R \to \infty$), these expressions are reduced to

$$d_1 = \frac{1}{2}(1 + \frac{c_1}{c_2}), \tag{5.50}$$

$$d_2 = \frac{1}{2}(1 - \frac{c_1}{c_2}), \tag{5.51}$$

$$d_3 = \sqrt{c_2}, \tag{5.52}$$

$$d_4 = \frac{\pi}{2}. \tag{5.53}$$

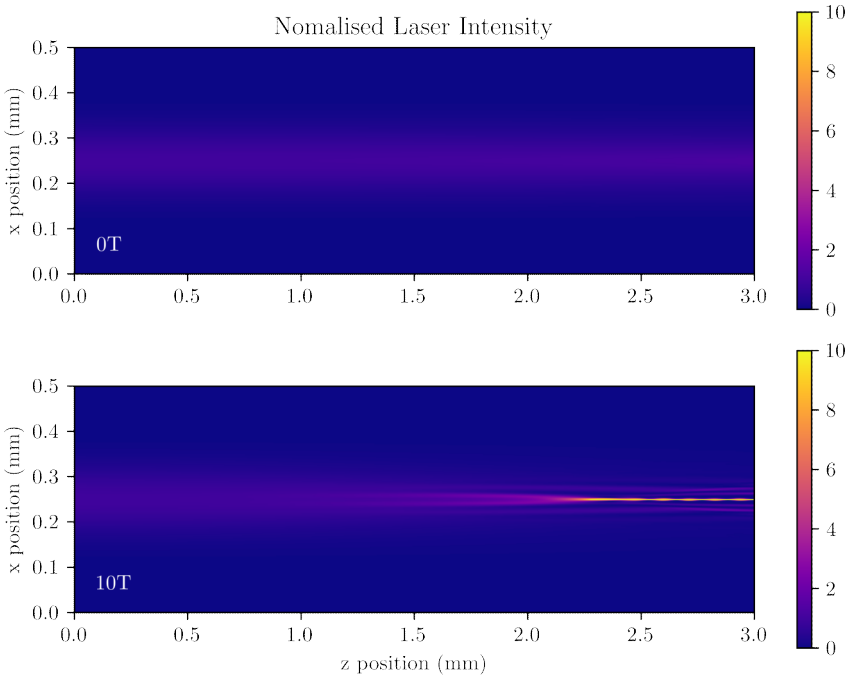

Figure 5.2: From this PARAMAGNET laser-plasma simulation, one can see that as the laser propagates through the plasma it undergoes self-focusing. This laser intensity map shows how a magnetic field influences the self-focal point. The 10T plot shows the focal point pulled far back, with a peak intensity at $\approx 2.5mm$

The result of the derivation is

$$\alpha^2(z) = \frac{1}{2}\left(1 + \frac{c_1}{c_2}\right) + \frac{1}{2}\left(1 - \frac{c_1}{c_2}\right)\cos(\sqrt{c_2}z). \tag{5.54}$$

This expression gives the variance (α^2) of the beam along the propagation direction, the focal point z_f of the beam being the z position where the variance is a minimum

$$z_f = \frac{\pi}{2\sqrt{c_2}}. \tag{5.55}$$

To put this result in context, eq. 5.54 gives the variance of the Gaussian beam. This shows that the width of the beam focuses then defocuses periodically leading to the laser profile of fig. 5.2 . The constant c_2 defined in eq. 5.41 determines the wavelength of the periodic shape and given that it is a function of the thermal conductivity, the magnetic field lengthens and shortens the wavelength via this conductivity.

5.2 Magnetised Thermal Self-Focusing

The constants in the equation 5.54 contained the thermal conductivity. Since the self-focal length is dependent on the thermal conductivity, a magnetic field will change the position of the self-focal spot by reducing the conductivity. For a particular choice of density and temperature the focal length decreases as the magnetic field increases with the dependence $\sim \sqrt{\kappa}$. Following the formalism of Braginskii [22] this magnetisation causes thermal transport to deviate from the classical isotropic form,

$$\kappa_{clas} = \frac{128}{3\pi}\zeta(Z) n_e v_{th} \lambda_{ei}. \tag{5.56}$$

This is the product of the electron number density n_e, the electron thermal speed v_{th}, the electron-ion collision length λ_{ei} and the function $\zeta(Z)$ which is

$$\zeta(Z) = \frac{Z + 0.24}{Z + 4.2}. \tag{5.57}$$

Along with the factor $128/3\pi$, this is taken from Epperlein [81] and accounts for an electron - electron collisional correction to the conductivity; henceforth this constant will be $\kappa^{(1)} = \frac{128}{3\pi}\zeta(Z)$. The thermal conductivity becomes anisotropic to a degree dependent on the Hall parameter. The functional form of the magnetised perpendicular thermal conductivity is

$$\kappa_\perp = \kappa_{clas}\kappa^c_\perp(\chi, Z). \tag{5.58}$$

The factor $\kappa^c_\perp(\chi, Z)$ corresponds to a normalised Hall parameter dependent correction to account for the magnetisation. In the analysis and the numerical simulations that follow the explicit expression of this term is the Epperlein and Haines form [111] obtained via a polynomial fit to a numerical solution of the electron Vlasov-Fokker-Planck equation. However, unlike in the Epperlein-Haines expression, it will be taken to be the normalised form such that $\kappa^c_\perp(0, Z) = 1$.

If the thermal conductivity in the expression for the focal length (eq. 5.55) is replaced with this magnetised form, the focal length becomes a function of magnetisation. When written in more intuitive form in terms of the peak laser intensity I_0 and the electron-ion collision length λ_{ei}, it is

$$z_f = \pi\frac{n_c}{n_0}\lambda_{ei}\sqrt{\frac{cn_0T_0}{I_0}}\sqrt{\kappa^{(1)}}\sqrt{\kappa^c_\perp}. \tag{5.59}$$

The factor $\kappa^c_\perp$ appears in the expression for the focal length, therefore as the thermal conductivity decreases with increasing magnetisation, the focal length will shorten. With a greatly reduced heat flow, gradients in the temperature profile are maintained. This leads to a higher pressure gradient and deeper electron density channel formation. The

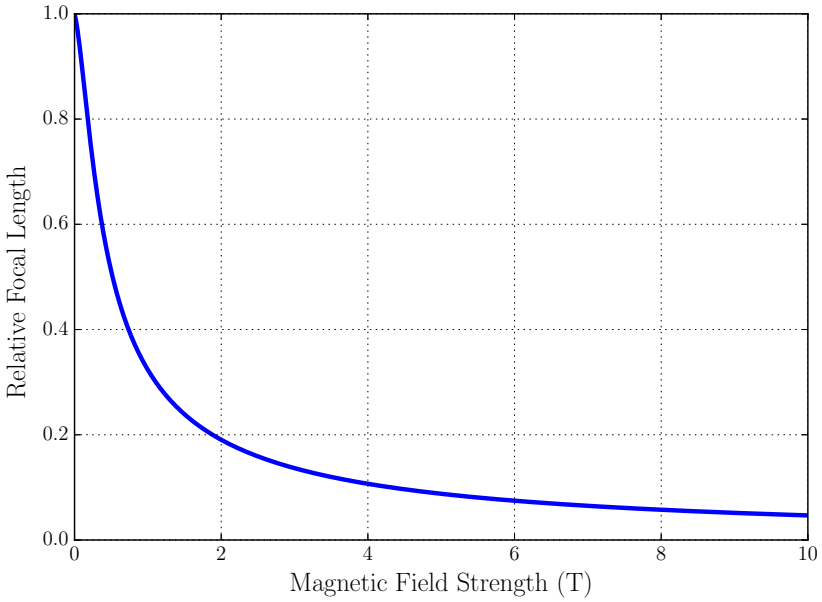

Figure 5.3: The focal length of the beam relative to the unmagnetised case shows the focal length decreases with an increasing magnetic field strength. In a plasma with 1 keV electron temperature and density of $1 \times 10^{20}\mathrm{cm}^{-3}$ the length drops sharply, at lower temperatures the gradient becomes shallower. Reproduced from [112], with permission of AIP publishing.

refractive index changes more and the beam refracts with a shorter focal length.

This is illustrated in fig. 5.3. According to eq. 5.59, for a $Z = 1$, 1 keV temperature, $1{\times}10^{20}\mathrm{cm}^{-3}$ number density plasma the focal length of a 1 μm wavelength, $1{\times}10^{14}\mathrm{Wcm}^{-2}$ Gaussian beam under a 2 Tesla axial field (magnetising the plasma to a Hall parameter of $\chi = 4.8$) is 0.2 of the unmagnetised focal length. In the highly magnetised regime corresponding to $\chi >> 1$, $\kappa_\perp \propto \frac{1}{\chi^2}$ and so the relative focal length is inversely proportional to the applied field strength B.

Looking at the intensity of the laser as it undergoes self focusing also shows significant impact of the magnetic field. The axial intensity of a Gaussian beam normalised to the initial peak intensity follows the expression

$$\frac{I(z, r = 0)}{I_0} = \frac{1}{\alpha(z)^2}. \tag{5.60}$$

Therefore the axial intensity can be found from eq. 5.60 and this is plotted in fig. 5.4 for a 0,5 and 10 Tesla applied field with the same parameters as fig. 5.3. Comparing the three curves, the axial intensity grows to multiple times the initial intensity over a much shorter length scale as the applied magnetic field increases.

Simulations of the Self-Focusing of a Gaussian Beam in a Magnetised Plasma

To compare this theory with the non-linear regime a simulation was performed with the PARAMAGNET Eulerian magnetised laser-plasma code. The PARAMAGNET code is a

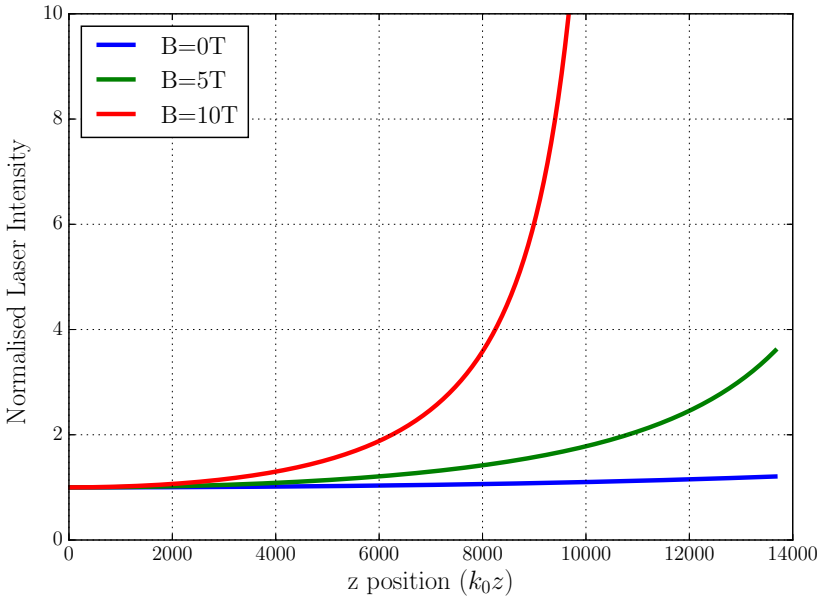

Figure 5.4: The normalised axial laser intensity from the analytic model shows the focusing of the beam when an axial magnetic field is applied with a field strength of 0T, 5T and 10T. The beam focuses over a shorter distance when the magnetic field strength increases. Reproduced from [112], with permission of AIP publishing.

fluid plasma - paraxial laser simulation code and is described in detail in chapter 3. The parameters for the simulations can be found in table 5.1.

Domain	Plasma	Laser
$L_x = 1\text{mm}$	$n_0 = 1 \times 10^{20}\text{cm}^{-3}$	$I_0 = 1 \times 10^{14}\text{Wcm}^{-2}$
$L_z = 3\text{mm}$	$T_0 = 20\text{eV}$	$\lambda_l = 1\mu\text{m}$
$t_{max} = 1\text{ns}$	$Z = 1$	$\omega_{waist}(0) = 100\mu\text{m}$
	$B_z = 0, 5, 10\text{T}$	

Table 5.1: Physical parameters used in self-focusing simulations

A 1 μm wavelength laser with a cylindrical Gaussian profile and peak intensity of $1 \times 10^{14}\text{Wcm}^{-2}$ is incident on a pre-ionised $Z = 1$, 20 eV plasma with an initially uniform electron density of $1 \times 10^{20}\text{cm}^{-3}$. The beam has an initial waist size of 100 μm at the edge of the simulation domain and propagates through the 3 mm plasma under an applied magnetic field of 0,5 and 10T orientated parallel to the beam wavevector. Fig. 5.5 shows the comparison between the axial laser intensity extracted from the simulation after 100ps and the analytic model given by eq. 5.60. Two cases are compared, one with a 10T field applied axially with the beam and the other without a magnetic field. In the magnetised simulation the position of the focal point matches closely with the model but the model breaks down when it hits a singularity (an artefact of the approximations eq. 5.37 and eq.5.43) which comes from a pole in eq. 5.60. At this point the simulation begins to see

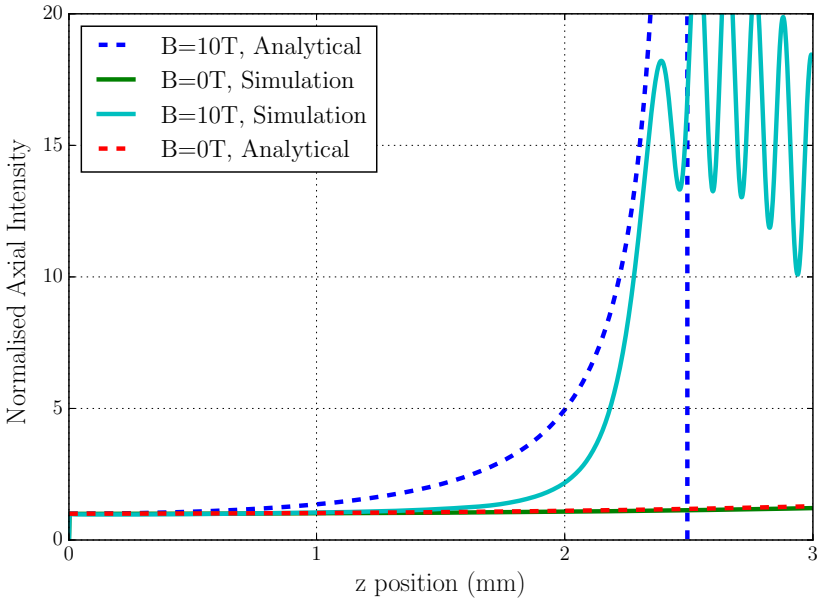

Figure 5.5: The normalised axial laser intensity is compared for the simulated and analytic models for an unmagnetised laser focusing over 3 mm and for a laser-plasma magnetised with a 10T axial field. The analytic model shows good agreement with the simulation up to the first focal point where the analytic model breaks down. The simulated axial intensity starts to oscillate as the bean focuses into and defocuses out of the density channel. Reproduced from [112], with permission of AIP publishing.

oscillating behaviour where the beam focuses and defocuses in and out of the density channel. The switch from the rising to oscillating behaviour that the simulation exhibits at $z \approx 2.3$ cannot be captured with such a simple analytic model. The unmagnetised cases match closely, with a minor rise in axial intensity as the beam focuses.

Despite the approximations made in the derivation of eq. 5.54 the fully nonlinear PARAMAGNET simulation shows Eq. 6.55 reproduces the correct focal point position but underestimates the gradient of the intensity increase leading up to the focal point. This is a result of the approximation made in eq. 5.43. As with the analytic model the intensity grows significantly over the spatial scale of the simulation to multiple times the initial intensity. The simulation domain was chosen as 3 mm to be similar to laser-underdense plasma experimental conditions such as the preheating stage of MagLIF [43]. This implies the laser propagating in such an experiment will focus significantly over the length of several millimetres in a way not present without consideration of the magnetisation of the thermal conductivity.

5.3 Focusing Bifurcation

Looking more closely at the equations of the previous section shows more nuanced behaviour when one adds the extra terms for the thermal mechanism. The equation describing the spatial evolution of the beam waist in the mixed-mechanism system,

$$\alpha'' = \frac{c_1}{\alpha^3} - \frac{c_2}{\alpha}, \tag{5.61}$$

can be decomposed into two first order equations. In Hamiltonian form this is the pair

$$\alpha' = p, \tag{5.62}$$
$$p' = \frac{c_1}{\alpha^3} - \frac{c_2}{\alpha}. \tag{5.63}$$

Where the constants c_1, c_2 are those defined in eqs. 5.40 and 5.41. This pair of non-linear ODEs exhibits a bifurcation at a critical value of the parameter c_1. The phase portraits of this equation system in the subcritical and supercritical regimes are shown in figure 5.6. Physically, the subcritical case (when $c_1 < 0$) represents a stable saddle point in the phase portrait, with the beam diverging. When $c_1 > 0$ the beam ocillates and the phase portrait exhibits centres. This can be written in the form $\mathbf{x} = \begin{bmatrix} p \\ \alpha \end{bmatrix}$. The fixed points $\mathbf{x}_f$ of this system are at

$$\mathbf{x}_f = \begin{bmatrix} 0 \\ \pm\frac{\sqrt{c_1}}{c_2} \end{bmatrix}$$

Linearising around the fixed points, the corresponding coefficient matrix $G_{\mathbf{x}_f}$ is

$$G_{\mathbf{x}_f} = \begin{bmatrix} 0 & 1 \\ \pm\frac{2c_2^2}{c_1} & 0 \end{bmatrix}$$

The nature of the solution around these fixed points is found by the trace and determinant of this matrix.

$$Tr(G_{\mathbf{x}_f}) = 0,$$
$$Det(G_{\mathbf{x}_f}) = \frac{2c_2^2}{c_1}.$$

Therefore the fixed points are *centres* for $c_1 > 0$ or *saddle points* for $c_1 < 0$. This change of behaviour across this critical value means there is a *Hopf bifurcation*. The phase portrait for this system is shown in figure 5.6.

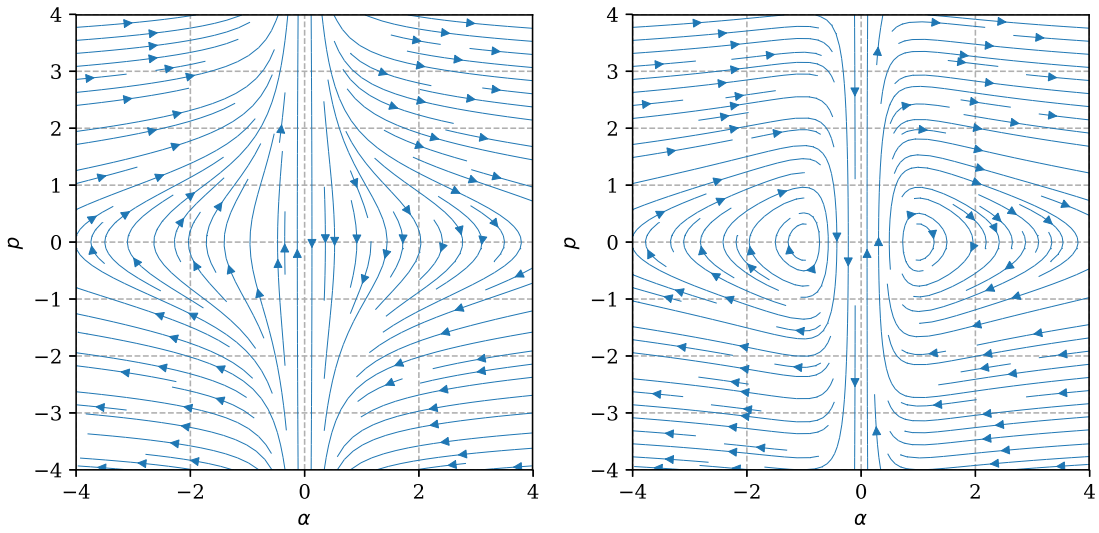

Figure 5.6: On the left, the phase portrait shows saddle points when $c_1 = -1$. The system undergoes a Hopf bifurcation as c_1 crosses 0, whereupon the phase portrait shows centres (right).

Physical interpretation

The physical interpretation of this Hopf bifurcation is a qualitative change in behaviour. When the parameter $c_1 < 0$ the laser is in a subcritical region that represents a diverging beam. When this parameter crosses the critical value and enters the supercritical regime ($c_1 > 1$), the laser beam shows oscillating behaviour. This oscillation shows itself as centres in the phase portrait. This appearance of oscillating behaviour can be seen in the PARAMAGNET simulation of fig. 5.5.

The parameter c_1 represents the strength of the ponderomotive coupling between the plasma and laser, indeed it also appears in the purely ponderomotive focusing mechanism introduced in the isothermal model of eq. 5.25. As such the transition from diverging to oscillating behaviour can be viewed as one driven by ponderomotive coupling. The parameter c_2 by comparison, represents the relative importance of the thermal mechanism on the focusing behaviour of the laser (the collision frequency only shows up in the definition of c_2 in eq. 5.41). Interestingly, the bifurcation from a diverging beam to an oscillation one does not depend on c_2, and so the critical value at which the laser bifurcation occurs is not affected by thermal effects.

For practical purposes, the parameter c_1 could be used as a means of deciding what laser and plasma parameters would best serve an experiment, either to obtain the oscillation and laser trapping in a channel, or to obtain a purely diverging beam.

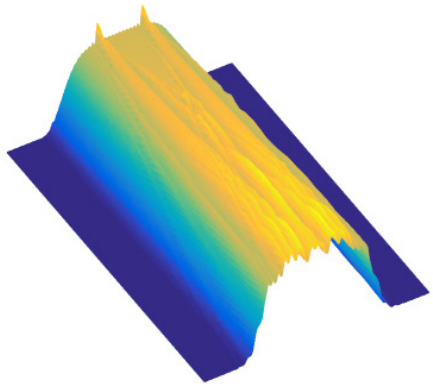

Figure 5.7: This surface plot of the laser intensity shows small perturbations growing as the laser propagates, eventually the laser intensity splits into filaments.

5.4 Filamentation

The phenomenon of self-focusing is closely related to the filamentation of a laser. As with focusing, filamentation proceeds by the laser digging a density channel and so changing the local refractive index. However instead of a single Gaussian beamlet or macroscopic profile, filamentation considers small perturbations in the laser field and how they grow. An example can be found in figure 5.7, where a small perturbation causes the large beam to break up into smaller laser filaments.

As in the previous chapter, the analysis of filamentation will start with a steady state model. The dielectric change $\delta\epsilon$ will again take centre stage as the plasma response to the laser, within which the effect of the magnetic field should be present.

A Steady State Model

The starting point is the steady state model of the previous sections

$$n\nabla_\perp T + T\nabla_\perp n = -\frac{1}{2}\varepsilon_0\frac{n}{n_c}\nabla_\perp|\psi|^2 \tag{5.64}$$

$$-\nabla_\perp\cdot(\kappa\cdot\nabla_\perp T) = \frac{1}{2}\varepsilon_0\frac{n}{n_c}\nu_{ei}|\psi|^2 \tag{5.65}$$

$$2ik_0\sqrt{\epsilon_a}\partial_z\psi + \nabla_\perp^2\psi + k_0^2\delta\epsilon\psi = 0 \tag{5.66}$$

The aim is to find the plasma response $\delta\epsilon$ in terms of the laser envelope ψ. In the case of filamentation the density n, temperature T and laser envelope ψ are perturbed by the inhomogeneous beam profile. The dielectric change $\delta\epsilon$ follows from the definition of the dielectric function in a plasma

$$\delta\epsilon = -\frac{\delta n}{n_c}. \tag{5.67}$$

To derive the spatial growth rate γ of the filamentation of a perturbation mode $\mathbf{k}_\perp$ perpendicular to the laser with wavenumber k_0, we follow the approach taken by Epperlein [81, 98]. In this case the steady-state equations are linearised with

$$T = T_0 + \delta T e^{(i\mathbf{k}_\perp\cdot\mathbf{x}-\gamma z)}, \tag{5.68}$$

$$n = n_0 + \delta n e^{(i\mathbf{k}_\perp\cdot\mathbf{x}-\gamma z)}, \tag{5.69}$$

$$\psi = \psi_0 + (\delta\psi_1 + i\delta\psi_2)e^{(i\mathbf{k}_\perp\cdot\mathbf{x}-\gamma z)}, \tag{5.70}$$

where the 'background' envelope ψ_0 is real. These lead to a set of linear equations

$$2k_0\gamma\delta\psi_2 - k_\perp^2\delta\psi_1 - k_0^2\frac{\delta n}{n_c}\psi_0 = 0, \tag{5.71}$$

$$2k_0\gamma\delta\psi_1 + k_\perp^2\delta\psi_2 = 0, \tag{5.72}$$

$$n_0\delta T + T_0\delta n = -\varepsilon_0\frac{n_0}{n_c}\psi_0\delta\psi_1, \tag{5.73}$$

$$\underline{\underline{\kappa}}^0 : \mathbf{k}_\perp\mathbf{k}_\perp\delta T = \varepsilon_0\frac{n_0}{n_c}\nu_{ei}^0\psi_0\delta\psi_1. \tag{5.74}$$

These equations are then used to derive the filamentation dispersion relation with spatial growth rate γ,

$$4k_0^2\gamma^2 = k_0^2k_\perp^2\left(\frac{n_0}{n_c}\right)^2\frac{\varepsilon_0|\psi_0|^2}{n_0T_0}\left(1 + \frac{n_0\nu_{ei}^0}{\underline{\underline{\kappa}}^0 : \mathbf{k}_\perp\mathbf{k}_\perp}\right) - k_\perp^4. \tag{5.75}$$

Here the thermal mechanism is represented by the term including the collision frequency ν_{ei}^0 and ponderomotive mechanism is represented by the term unity. From this relation one can see the ponderomotive mechanism will dominate when $n_0\nu_{ei}^0/\underline{\underline{\kappa}}^0 : \mathbf{k}_\perp\mathbf{k}_\perp << 1$ and the thermal mechanism will dominate in regimes where this term is $>> 1$.

What we shall see in the next section however, is that the appearance of a magnetic field can modify the magnitude of the term $n_0\nu_{ei}^0/\underline{\underline{\kappa}}^0 : \mathbf{k}_\perp\mathbf{k}_\perp$. Thus in regions where the ponderomotive force might normally be dominant, the thermal mechanism can acquire a correction that makes it far larger.

5.5 Magnetised Thermal Filamentation

The effect of the magnetic field appears through the thermal conductivity $\underline{\underline{\kappa}}_0$. Since the electrons in a magnetic field travel in orbits the collisional transport perpendicular to the magnetic field is reduced. This in turn means temperature gradients are steeper since the thermal dissipative mechanism is reduced. With steeper pressure gradients the change in density is faster, and so too the filamentation rate. The degree to which the magnetic field affects filamentation is dependent on the magnitude of the field and the angle between the field and the perturbation wavevector $\mathbf{k}_\perp$.

This expression can be simplified by defining the angle θ between the magnetic field direction and the perturbation vector $\mathbf{k}_\perp$, such that

$$\underline{\underline{\kappa}}^0 : \mathbf{k}_\perp \mathbf{k}_\perp = k_\perp^2 \kappa_{clas} (\kappa_\parallel^c \cos^2\theta + \kappa_\perp^c \sin^2\theta). \tag{5.76}$$

Considering now only the magnetic fields parallel with the laser wavevector (when the angle $\theta = \pi/2$) the dispersion relation can be written

$$4k_0^2\gamma^2 = k_0^2 k_\perp^2 \left(\frac{n_0}{n_c}\right)^2 \frac{2I_0}{cn_0T_0} \left(1 + \frac{1}{\lambda_{ei}^2 \kappa^{(1)} \kappa_\perp^c k_\perp^2}\right) - k_\perp^4. \tag{5.77}$$

Where the vacuum intensity definition has been used,

$$I = \frac{1}{2} c\varepsilon_0 |\psi|^2. \tag{5.78}$$

This dispersion relation includes both the ponderomotive and thermal mechanisms, with the latter modified by the normalised magnetised thermal conductivity $\kappa_\perp^c$.

Fig. 5.8 shows the spatial growth rate of a $1 \times 10^{14}\mathrm{Wcm}^{-2}$ laser undergoing filamentation due to the thermal mechanism alone under a 0, 5 and 10T applied axial field. With an electron density of $1 \times 10^{20}\mathrm{cm}^{-3}$ and a temperature of 1 keV this corresponds to Hall parameters of $\chi = 0$, 11.9 and 23.9. It is plotted against the perturbation wavelength, defined as $\lambda_\perp = \frac{2\pi}{k_\perp}$, normalised with the laser wavenumber k_0. The thermal mechanism dispersion relation is obtained by ignoring the factor of unity in eq. 5.77. As the term $\kappa_\perp^c$ is reduced through magnetisation the maximum growth rate will increase and the growth rate will cutoff at higher perturbation wavenumbers. Indeed the maximum spatial growth rate under a 10 Tesla field is ~ 1.3 orders of magnitude greater than the unmagnetised plasma.

In the highly magnetised case where approximately $\kappa_\perp^c \sim 1/\chi^2$ the maximum thermal growth rate is

$$\gamma_{max} \approx \frac{n_0}{n_c} \sqrt{\frac{I_0}{2cn_0T_0}} \frac{\chi}{\sqrt{\kappa^{(1)}}\lambda_{ei}}. \tag{5.79}$$

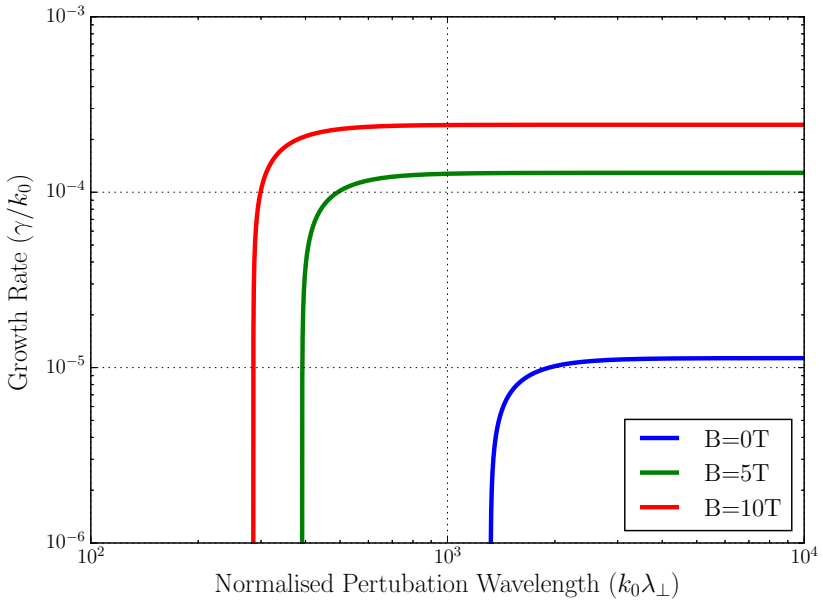

Figure 5.8: The filamentation growth rate of the thermal mechanism plotted against the perturbation wavelength shows that as the applied magnetic field increases, the peak growth rate increases and the cutoff is shifted to shorter wavelengths. Reproduced from [112], with permission of AIP publishing.

It is instructive to look at the combined effect of both the ponderomotive and thermal mechanisms and their influence on the growth e-folding length, defined as

$$L_g = (2\gamma)^{-1}. \tag{5.80}$$

This parameter allows the comparison of the susceptibility of experimental parameters to this instability. We define an experiment to be susceptible to filamentation if the length scale of the plasma through which the laser propagates is smaller than a couple of e-folding lengths $(1/\gamma)$. This is because if the length scale of the plasma is very short $(<< L_g)$, the instability will not grow sufficiently large over the experimental domain. However if the domain is $> L_g$ the initial perturbation grows to multiple times its original amplitude over the domain, possibly transitioning to the nonlinear regime and significantly changing the plasma profile in the process.

Fig. 5.9 shows the growth length against perturbation wavelength for an applied axial magnetic field with a strength of 0, 5 and 10T. Superimposed onto the plot is a line representing 2mm. This has been chosen as this is a characteristic experimental scale length in laser plasma experiments with magnetic fields [38, 41, 104]. Therefore the region of the plot above this line is stable to this instability since the length is too short for the instability to grow significantly over the length scale.

As can be seen in fig. 5.9 a significant proportion of the growth length curve dips into the unstable region. The effect of the magnetic field appears as a lowering of the instability growth length at longer perturbation wavelengths whereas the combined ponderomotive-

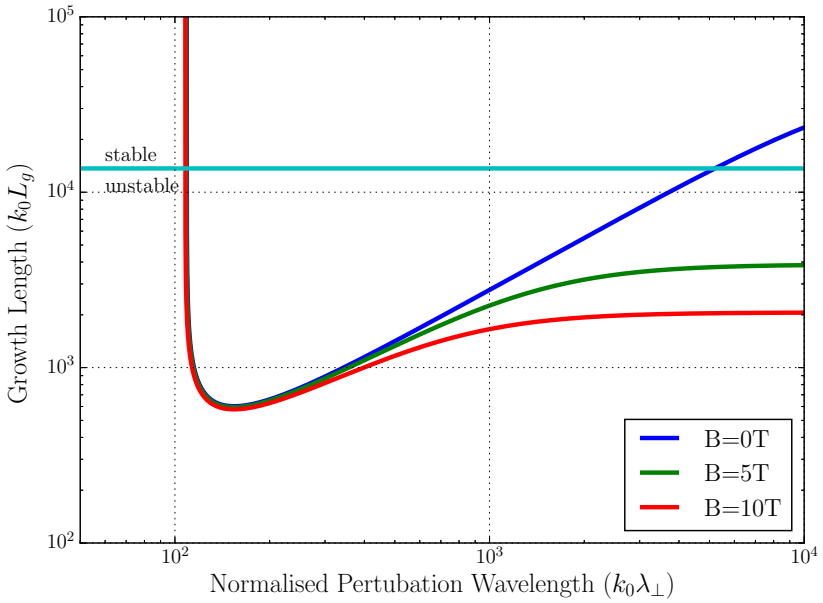

Figure 5.9: The dispersion relation shows the relationship between the growth length and perturbation wavelength for combined ponderomotive and thermal mechanisms. As the magnetic field is increased, the longer wavelength modes have a shorter growth length, meaning magnetised experiments are more susceptible to long perturbation wavelength filamentation. Reproduced from [112], with permission of AIP publishing.

thermal mechanism cutoff (where the combined mechanism growth rate equals zero) provides a lower limit to the influence of the magnetic field. This means that under a magnetic field the longer wavelength perturbation modes will grow faster and an experiment in which these modes are present will be more susceptible to filamentation.

Simulations of Filamentation in a Magnetised Plasma

To verify the linear analysis of this magnetised effect, the PARAMAGENT code was used to simulate a uniformly irradiated plasma. The full parameters of this simulation can be found in table 5.2.

Domain	Plasma	Laser
$L_x = 0.2\text{mm}$	$n_0 = 1 \times 10^{20}\text{cm}^{-3}$	$I_0 = 1 \times 10^{15}\text{Wcm}^{-2}$
$L_z = 0.4\text{mm}$	$T_0 = 20\text{eV}$	$\lambda_l = 1\mu\text{m}$
$t_{max} = 100\text{ps}$	$Z = 1$	$k_\perp = 10\pi/L_x$
	$B_z = 0, 5, 10\text{T}$	

Table 5.2: Physical parameters used in filamentation simulations

A uniform 1 μm laser field of intensity $1 \times 10^{15}\text{Wcm}^{-2}$ with small (0.1%) harmonic perturbations heated the plasma with initial uniform electron density $1 \times 10^{20}\text{cm}^{-3}$ under a magnetic field parallel to the laser wavevector. The initial perturbation wavelength has

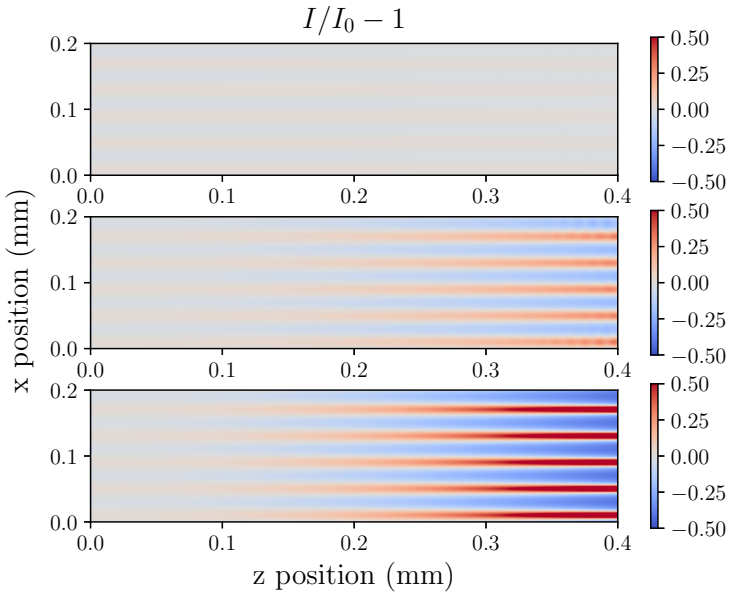

Figure 5.10: PARAMAGNET filamentation simulation (linear regime). This plot shows output from a PARAMAGNET simulation of the deviation of the laser intensity away from the uniform background. Evident is the filamentation of a uniform laser with 0.1% perturbations for the unmagnetised (top), 5T (middle) and 10T (bottom) cases show the laser filaments with a shorter growth length as the magnetic field increases. Reproduced from [112], with permission of AIP publishing.

been chosen as representative of longer-wavelength laser inhomogeneity such as those seeded by the disintegration of the target window in MagLIF [44]. The use of local Braginskii transport in the theory and simulations presented above is justified in the regime where the electron mean free path or Larmor radius is smaller than the perpendicular wavelength. In the simulation above the parameters $k_\perp \lambda_{ei}$, $k_\perp r_L$ (with r_L the Larmor radius) are 0.022 and 0.15 respectively. As such the use of Braginskii transport in the fluid simulations is justified.

Fig. 5.10 shows the output from the PARAMAGNET simulation after 100ps, It shows the difference between the normalised laser intensity and the initial background under three different field strengths. The 10T field has caused the beam perturbations to grow to 50% of the uniform background intensity over a length of only 0.4 mm; whilst the unmagnetised case sees little variation over the same length. Using the output of the simulation at 100ps, where the background temperature had reached an average value of $\approx$ 730 eV, eqs. 5.79 and 5.80 yield a growth length of 0.35 mm of the unmagnetised case, 0.09 mm for 5T and 0.05 mm for 10T.

The Effect of Magnetised Filamentation on Experiments

Parametric instabilities such as Stimulated Raman Scattering (SRS) and Stimulated Brillouin Scattering (SBS) have an intensity threshold. The choice of laser intensity in the pre-heat stage is partially to undercut this threshold and mitigate the influence of SRS

and SBS backscatter. This backscatter can reduce the absorption of the laser light into the MagLIF fuel cell by scattering it out of the fuel and also reducing the depth of the penetration of the laser into the fuel cell.

Therefore the magnetisation can lead to more backscatter as the local filament intensity exceeds the parametric instability threshold; as such the laser penetration will shorten and the absorption less effective compared to the unmagnetised case.

In a hohlraum environment the effect of magnetic fields can likewise influence laser propagation and absorption. In such experiments the magnetic field can be applied externally [20, 41] or self-generated [29]; the orientation of the magnetic field will not be exactly parallel to the laser wavevector as investigated in this work, however the influence of the magnetised thermal conductivity will similarly drive down the instability threshold for thermal regime filamentation, attenuated by a trigonometric factor to account for orientation. Taking as example the parameters of the magnetised helium gas-fill hohlraum simulations performed by Strozzi [42], the maximum thermal filamentation growth length is 0.82 mm, relative to the hohlraum length of 1 cm.

Furthermore, in direct drive experiments the laser uniformity is important for ensuring the reduction of laser-imprint seeded hydrodynamical instabilities[4]. The phenomenon of laser filamentation can cause small scale non-uniformity to grow in the underdense coronal plasma.The magnetisation increases the spatial growth rate of filamentation thus putting greater constraints of laser uniformity in the case of an experiment with an applied magnetic field.

5.6 Summary

In summary, this chapter investigated how the effect of a magnetised thermal conductivity influences the propagation of a laser through an underdense plasma in regimes common in magnetised high energy density physics experiments. By using an analytic model of the self-focal point of a Gaussian beam derived from a steady-state fluid-plasma paraxial-laser model, the focal point is shown to shorten by a factor proportional to the square root of the perpendicular thermal conductivity of the magnetised plasma; this is a direct result of the anisotropic magnetised transport of Braginskii. This in turn means for a highly magnetised plasma, the focal length relative to the unmagnetised case is approximately inversely proportional to the magnetic field strength parallel to the wavevector of the laser.

Using the PARAMAGNET laser-plasma transport code, simulations of this self focusing effect were performed with a Gaussian laser in a plasma with a range of magnetic field strengths. In these simulations, the self-focal point from the analytic model is retrieved whilst showing nonlinear behaviour such as repeated defocusing and refocusing not present in the analytic model. The quantitative difference in focusing behaviour resulting from magnetisation of the thermal conductivity is manifest.

In recent years the use of magnetic fields has been suggested as a means to improve the performance of inertial confinement fusion experiments. Of particular interest is the pre-heat stage of the MagLIF scheme [9]. The MagLIF scheme necessarily has the laser pre-pulse propagating through a low Z plasma with a coaxial 10T magnetic field. The purpose is to pre-heat the fuel and as such uniform and deep penetration is required for effective heating. In such experiments the plasma is strongly magnetised and given the laser wavelength and intensity sits well within the unstable region of thermal regime filamentation. In the filament the local intensity can reach multiples of the initial intensity.

Taking as example the parameters of pre-heat experiments performed on the OMEGA-EP laser [44], a $1.3 \times 10^{14}\mathrm{Wcm}^{-2}$ intensity laser propagating through a plasma with $n_e = 2.5 \times 10^{20}\mathrm{cm}^{-3}(0.025n_c)$ under an axial magnetic field of 7.5T. When a temperature of 400 eV is used, the maximum thermal growth length calculated using eq. 5.79 is 1.01 mm, much smaller than the scale length of the 8mm D_2-gas filled tube used in the experiment. This means the pre-heat stage is susceptible to significant self-focusing due to the magnetisation of the thermal conductivity.

The second half of this chapter derived a linear model of thermal filamentation of a laser. The resulting dispersion relation follows the same asymptotic dependence of the normalised thermal conductivity. This leads to an increase in the thermal mechanism growth rate as electrons are increasingly magnetised. When combined with the ponderomotive mechanism and the effect of magnetisation, the filamentation of long-wavelength perturbations is particularly significant. Simulations performed with the PARAMAGNET code of the linear regime of filamentation yields an order of magnitude shortening of the e-folding length for even low values of the Hall parameter in the range of 0.1-1.

When considering these effects in the context of magnetised laser fusion experiments, it is found they sit in regimes susceptible to significant laser focusing exacerbated by magnetisation. The resulting filamentation produces localised intensities much higher than the threshold for parametric instabilities. These instabilities are detrimental to laser absorption and penetration by the laser by backscattering the laser light out of the fuel or hohlraum. As such it is important in the modelling of high-energy-density laser plasma experiments to include the influence of full thermal magnetised transport, not just on the plasma but also on the laser propagation.

6

Non-local Corrections to Filamentation and Magnetised Transport

The theoretical and simulation results thus far have been predicated on the MHD model, however the very high order modes present in filamentation simulations and experiments are known to drive the electron distribution function significantly far from a Maxwell-Boltzmann distribution. This non-locality of the electron species introduces the possibility of significant errors in understanding the dynamics of laser-plasma interactions.

This chapter will introduce non-locality and the diffusive-approximation kinetic code IMPACT. This code is then used to simulate thermal decay in such a way as to capture the kinetic effects on filamentation described in the previous chapter. This code however is limited to the diffusion approximation, as such it ignores all terms in the expansion of the distribution function above the first. This chapter will then investigate the influence of the higher order terms on magnetised transport.

Beginning with a linear problem, a continued matrix inverse method is used to calculate corrections to the collision frequency in a magnetised plasma. By re-summing up all the higher order terms into these corrections, it will be possible to measure their effect on magnetised transport. This chapter ends with the calculation of the full set of transport coefficients and explores the deviation they have compared to classical local approximations. The results of the IMPACT simulations and their interpretation in the regimes of plasma experiments has been reproduced from Watkins and Kingham [112] with the permission of AIP publishing.

6.1 Kinetic Effects in Filamentation

Kinetic effects on thermal transport are important in laser-produced plasmas [93, 101, 104]. Small scale structures in laser filamentation in the thermal regime mean the corresponding temperature profile will have characteristic length scales of the same magnitude as the electron-ion collision length. In unmagnetised plasmas this kinetic correction has been found to significantly alter filamentation [98, 99]. In this regime heat flow becomes non-local and the kinetic modification to the thermal conductivity must be included. Therefore a useful question to ask is the influence of non-local transport effects on the magnetised thermal mechanism filamentation.

The non-locality of thermal transport in the absence of magnetic fields is encapsulated in the dimensionless non-locality parameter $k\lambda_{mfp}$, defined as the product of the wavenumber of a perturbation in the plasma temperature k and the electron delocalisation mean free path $\lambda_{mfp} = \sqrt{\lambda_{ee}\lambda_{ei}} = \sqrt{Z}\lambda_{ei}$. This can also be called the Fourier-space Knudsen number. For higher values of this parameter the thermal conductivity drops off relative to the Spitzer-Härm result according to an expression introduced by Epperlein [97], where a plasma heated by inverse bremsstrahlung showed a deviation that followed the form,

$$\frac{\kappa_{nl}}{\kappa_{sh}} = \frac{1}{1 + (30\sqrt{Z}k\lambda_{ei})^{4/3}}. \tag{6.1}$$

However, when a plasma is magnetised the heat flow of the plasma is localised [33, 85]. These two effects, the reduction of the heat flow via non-locality and via magnetisation combine and the dual influence on filamentation must be considered. Kinetic, magnetised thermal transport has been considered by Brantov[107] however only a simplified phenomenological form is required. Consider a phenomenological function for the thermal conductivity perpendicular to the magnetic field relative to the local, unmagnetised conductivity

$$\frac{\kappa_{\perp nl}}{\kappa_{clas}} = \frac{a}{1 + b(\sqrt{Z}k\lambda_{ei})^c + d\chi^e}. \tag{6.2}$$

This model includes the combined effect of the reduction from the magnetisation (χ) and non-locality $(k\lambda_{ei})$. The assumption taken here is that magnetisation acts to reduce conductivity (perpendicular to the magnetic field) in the same way as non-locality, in that they both represent the characteristic length scale of diffusive process. The phenomenological form is found as the result of combining eq. 6.1 and eq. 2.84.

6.2 IMPACT simulations

In order to find the parameters a, b, c, d, e the Epperlein-Short test [97] is performed. The Epperlein-Short test aims to find the non-local thermal evolution of a 1D plasma using a numerical VFP model. Given the requirements for a magnetised plasma, we use the IMPACT VFP code[50]. IMPACT solves the electron VFP equation in the diffusion approximation alongside the full Maxwell's equations allowing the inclusion of magnetic field phenomena.

We use Brodrick's [93] approach, in which a 1D hydrogen (Z=1) plasma is initialised with a small (0.1%) sinusoidal temperature perturbation and is allowed to decay over multiple collision times. The parameters of the simulation are listed in table 6.1.

Domain	Plasma
$k_\perp \lambda_{ei} = 0.01, 0.1, 1, 10, 100$	$n_0 = 1 \times 10^{20} \mathrm{cm}^{-3}$
$L_x = \frac{10\pi}{k_\perp \lambda_{ei}} \lambda_{ei}$	$T_0 = 100 \mathrm{eV}$
$t_{max} = \frac{5\tau_{ei}}{(k_\perp \lambda_{ei})^2}$	$Z = 1$
	$\chi = 0, 0.1, 1, 2, 10$

Table 6.1: Physical parameters used in IMPACT simulations

A static and uniform magnetic field of varying strengths is applied perpendicular to the temperature perturbation. The decay rate of the sinusoidal perturbation is proportional to the thermal conductivity of the plasma via

$$\frac{\kappa_{\perp nl}}{\kappa_{clas}} = \frac{\gamma_{nl}}{\gamma_{clas}}. \tag{6.3}$$

The local unmagnetised decay rate for a sinusoid with wavenumber k is defined as

$$\gamma_{clas} = \frac{2}{3} k^2 \frac{128}{3\pi} \zeta(Z) v_{th} \lambda_{ei}. \tag{6.4}$$

The thermal speed v_{th} and the electron-ion mean-free-path are defined in chapter 2, while the correction factor $\zeta(Z)$ is defined in eq. 5.57.

The non-local decay rate γ_{nl} is found by fitting (with a least-squares fit) a decaying sinusoid to the output of the IMPACT simulations. The output from the IMPACT simulations are shown in Fig. 6.1. The function eq. 6.2 is fitted to the data and the values are found to be $a = 1.12, b = 2.73, c = 1, d = 3.72, e = 1.4$. The result is overlaid on fig. 6.1. The use of the diffusion approximation on the IMPACT code limits the accuracy of the decay in the high $k\lambda_{ei}$ regime, as such the data is fitted to runs up to values of $k\lambda_{ei} = 10$. An interesting feature of figure 6.1 is the data points rise as $k\lambda_{ei}$ before dropping off to the

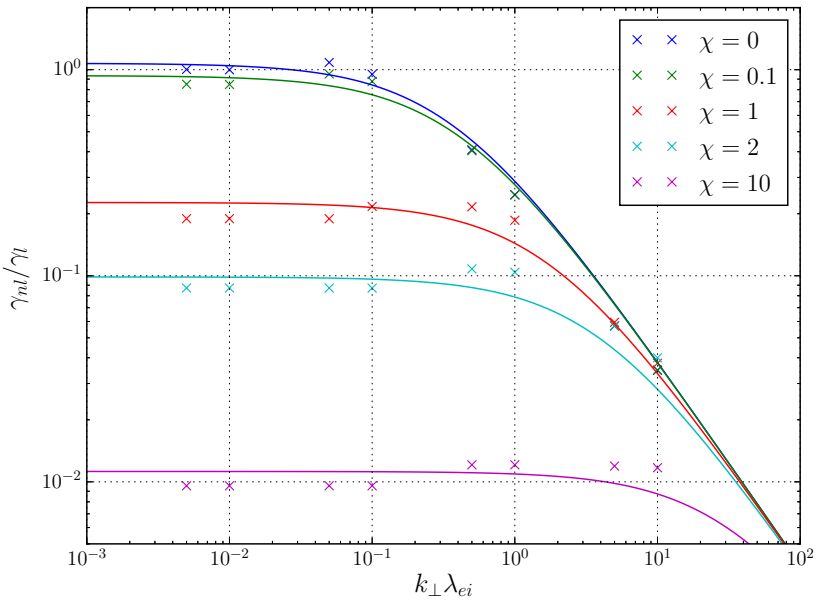

Figure 6.1: The kinetic decay rate of a small (perpendicular, $k_\perp$) temperature perturbation relative to the local analytic result against the non-locality parameter. Data for IMPACT simulations with five different Hall parameters, 0, 0.1,1,2 and 10. The fit is overlaid on the data. The magnetisation localises and reduces the thermal conductivity, the non-local drop off of the conductivity is shifted down and to the right. Reproduced from [112], with permission of AIP publishing.

asymptotic value in the limit $k\lambda_{ei} \to \infty$. This feature is not captured exactly by the simple monotonic phenomenological form used to fit the data (eq. 6.1). It does however anticipate non-monotonic results that will be presented later in section 6.6, where the inclusion of higher-orders in the distribution expansion provide a explanation.

The thermal filamentation dispersion relation using this non-local expression now has both a magnetisation and non-locality parameter dependence and the growth rate is plotted in fig. 6.2. In the local limit ($k\lambda_{ei} << 1$) the curves all plateau with a value determined by the magnetisation. As the non-locality parameter increases the curve drops off, the point where the curve begins to drop off is shifted to the right at higher magnetisation values. This is the result of the magnetisation localising the thermal conductivity.

Looking now at the plot of the dispersion relation of thermal filamentation in isolation in fig. 6.2 , the most obvious difference as compared to the local thermal mechanism is the much higher peak growth rate. Also unlike the local case in fig. 5.8 where the curve flattened to a constant at long wavelengths, the kinetic growth rate converges towards the local rate at longer wavelengths. Whilst this is subdued in the magnetised curves, the influence is still noticeable. In the absence of a magnetic field the dispersion curve cutoff is shifted far to the left and has a higher peak growth rate.

If we now compare the mixed ponderomotive and thermal growth length curves between fig. 5.9 and fig. 6.3 the differences compared with the local case are most evident at longer perturbation wavelengths. The curve shows some deviation from the local curve

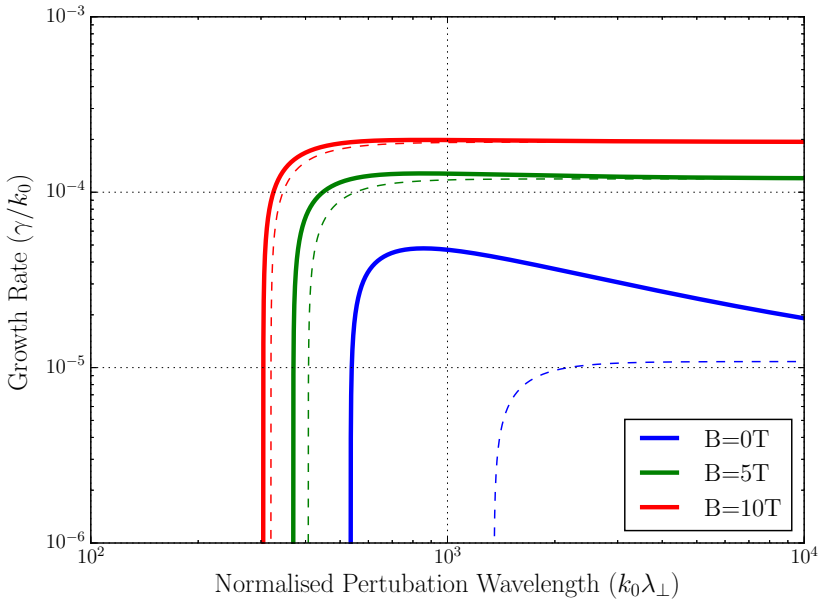

Figure 6.2: The filamentation growth rate of the kinetic thermal mechanism (solid lines) plotted against the perturbation wavelength shows that in the unmagnetised case, the peak growth rate is greater relative to the local case (dashed lines) and the cutoff is shifted to shorter wavelengths. This nonlocal effect is suppressed in the magnetised curves. Reproduced from [112], with permission of AIP publishing.

in the long wavelength region whilst the low wavelength cutoff is unchanged.

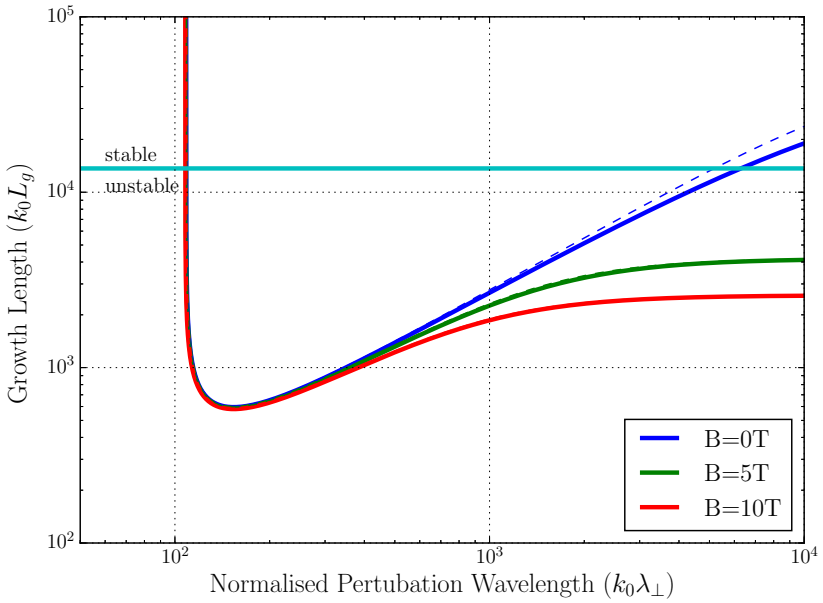

Figure 6.3: The combined ponderomotive and thermal filamentation dispersion relation with the kinetic corrections (solid lines) shows some deviation from the classical case (dashed lines) in the longer wavelength region. Reproduced from [112], with permission of AIP publishing.

6.3 Non-local Magnetised Transport Corrections

Calculating plasma behaviour directly by solving the VFP equation, though accurate, is too computational demanding because of the 6-dimensional phase space occupied by the distribution function f_e. As such methods such as the diffusive approximation have been popular, computationally tractable kinetic models that are more accurate than fluid approaches. The deviation from an isotropic Maxwellian motivates the use of a Cartesian tensor expansion of the distribution function,

$$f_e(\mathbf{x}, \mathbf{v}, t) = f_0 + \mathbf{f}_1 \cdot \frac{\mathbf{v}}{v} + \mathbf{f}_2 : \frac{\mathbf{vv}}{v^2} + ... \tag{6.5}$$

The anisotropy in the distribution is contained in the terms $\mathbf{f}_1$ and higher. The *diffusion approximation* truncates this expansion at so that all terms above $\mathbf{f}_1$ are ignored, i.e

$$f_e = f_0 + \mathbf{f}_1 \cdot \frac{\mathbf{v}}{v}.$$

This significantly simplifies the problem and is far more amenable to computational models. While this approximation is more accurate than fluid models, the inherently anisotropic nature of magnetic fields means their influence on the $f_n, n > 1$ terms may be significant.

The second part of this chapter will analyse the influence of the higher-order terms

$(n > 1)$ of the expansion on magnetised transport. These terms are ignored in local fluid models but also in conventional non-local transport models such as the SNB model [84, 90]. This chapter will examine whether ignoring higher terms in the expansion introduces error in magnetised transport effects such as the Nernst effect and perpendicular thermal transport. To incorporate the higher order terms, this analysis will consider the linearised electron VFP model with a magnetic field. This will enable the use of a continued fraction method introduced by Epperlein [82], used previously in local linear theories without a magnetic field [100, 133].

The inclusion of a magnetic field acts as a localisation mechanism [38], and thus complicates the creation of an accurate model to simulate non-local transport by adding an anisotropic effective mean free path. One can follow Epperlein [134] and start with the non-locality parameter of the last section,

$$\eta = k\lambda_{ei}(v). \tag{6.6}$$

It has been defined with the symbol η for brevity in the rest of the chapter. The thermal value is $\eta_{th} = k\lambda_{ei}(v_{th})$. Modes with high values of η will be less collisional and the electrons unable to relax to be locally Maxwellian.

Magnetised Form of the Electron VFP

In the diffusion approximation the electron VFP equation becomes the two equations

$$\frac{\partial f_0}{\partial t} + \frac{v}{3}\nabla\cdot\mathbf{f}_1 + \frac{1}{3v^2}\frac{\partial}{\partial v}\left(v^2\mathbf{a}\cdot\mathbf{f}_1\right) = C_{e0}, \tag{6.7}$$

$$\frac{\partial \mathbf{f}_1}{\partial t} + v\nabla f_0 + \mathbf{a}\frac{\partial f_0}{\partial v} + \boldsymbol{\omega}\times\mathbf{f}_1 = -\nu_{ei}\mathbf{f}_1 + \mathbf{C}_{e1}, \tag{6.8}$$

where the electromagnetic fields are defined as

$$\mathbf{a} = -\frac{e}{m_e}\mathbf{E}, \tag{6.9}$$

$$\boldsymbol{\omega} = -\frac{e}{m_e}\mathbf{B}. \tag{6.10}$$

From the f_1 equation (eq. 6.8), if the time dependence is ignored, such that f_1 is instantaneously calculated from f_0, it can be shown that

$$\mathbf{f}_1 = -\frac{1}{\nu_{ei}(v)}\underline{\mathbf{M}}\left(v\nabla f_0 + \mathbf{a}\frac{\partial f_0}{\partial v}\right). \tag{6.11}$$

Given this definition of $\mathbf{f}_1$, it is possible to calculate the fluxes of charge (current, $\mathbf{j}$) and thermal energy (the intrinsic heat flow, $\mathbf{q}'$), and in turn the transport coefficients using

the moment expressions [135],

$$\mathbf{j} = -e\frac{4\pi}{3}\int_0^\infty \mathbf{f}_1 v^3 dv, \tag{6.12}$$

$$\mathbf{q} = \frac{4\pi}{3}\frac{m_e}{2}\int_0^\infty \mathbf{f}_1 v^5 dv, \tag{6.13}$$

$$\mathbf{q'} = \mathbf{q} + \frac{5T_e}{4e}\mathbf{j}. \tag{6.14}$$

The magnetic field has been incorporated into a 'magnetisation matrix' $\underline{\mathbf{M}}$ defined as

$$M_{ij} = \frac{\chi_i\chi_j}{\chi^2} + \left(\delta_{ij} - \frac{\chi_i\chi_j}{\chi^2}\right)\frac{1}{1+\chi^2} - \frac{\epsilon_{ikj}\chi_k}{1+\chi^2}, \tag{6.15}$$

in terms of the components of the Hall vector $\boldsymbol{\chi}$, defined earlier in terms of the Larmor frequency vector $\boldsymbol{\omega}$ and the collision frequency ν_{ei} as

$$\boldsymbol{\chi} = \frac{\boldsymbol{\omega}}{\nu_{ei}(v)}. \tag{6.16}$$

Where one can similarly define the thermal value $\chi_{th} = \chi(v_{th})$. The three terms of this matrix represent the fluxes parallel, perpendicular and cross-perpendicular to the magnetic field respectively, and follow the magnetised transport terms of chapter 2.

Considering the influence on linear perturbations to the electron fluid, this analysis follows the derivation used by Epperlein [111, 136]. After linearising the isotropic part f_0 about a Maxwellian distribution i.e

$$f_0 = f_m + \delta f_0,$$

and performing a Fourier transform, the $\mathbf{f}_1$ equation is

$$\hat{\mathbf{f}}_1 = -\frac{1}{\nu_{ei}(v)}\mathbf{M}\left[i\mathbf{k}v\delta\hat{f}_0 + \hat{\mathbf{a}}\frac{\partial f_m}{\partial v}\right]. \tag{6.17}$$

Where the Maxwellian f_m is defined in terms of the uniform background density and temperature n_0, T_0, with $v_{th} = \sqrt{T_0/m_e}$. A useful qualitative parameter with which one can approximate the magnetised non-local effect is

$$\eta_\perp = \frac{k\lambda_{ei}(v)}{1+\chi(v)^2}. \tag{6.18}$$

This parameter, defined in the plane perpendicular to the magnetic field, combines both dimensionless parameters that control the degree of locality. Looking at the velocity dependence, one can see $\chi \propto v^3$ and $\eta \propto v^4$ and so the mixed-timescale localisation parameter $\eta_\perp$ has a velocity dependence that is not a simple power-law.

6.4 Calculating the Local Transport Coefficients

The transport coefficients are recovered by forming the Onsager transport relations from moments defined by eqs. 6.12-6.14. The Onsager form is then transformed into the classical transport coefficient form, which will be recognisable from eqs. 2.97-2.98. By working with a linearised model, where there is a uniform background with sinusoidal pertubations of size δ, the electric field that corresponds to the electron pressure gradient can be separated out of the $\delta\hat{f}_0$ term by considering the form of Ohm's law. Denoting this field by $en_e\mathbf{E}' = -\nabla p_e$ and using the ideal gas equation of state, in Fourier space it becomes

$$\hat{\mathbf{E}}' = i\mathbf{k}\frac{T_0}{e}\left(\frac{\delta\hat{T}}{T_0} + \frac{\delta\hat{n}}{n_0}\right), \tag{6.19}$$

from which one can define

$$\hat{\mathbf{a}}' = -\frac{e\hat{\mathbf{E}}'}{m_e} = -i\mathbf{k}\frac{T_0}{m_e}\left(\frac{\delta\hat{T}}{T_0} + \frac{\delta\hat{n}}{n_0}\right). \tag{6.20}$$

The total electric field is now $\mathbf{a}^* = \mathbf{a}' + \mathbf{a}$. To simplify the analysis, the velocity is reparameterised such that $\tilde{v} = v/v_{th}$ and the equation becomes,

$$\hat{\mathbf{f}}_1 = -\frac{\tilde{v}^4}{\nu_T v_{th}}\mathbf{M}\left[i\mathbf{k}\frac{\delta\hat{T}}{m_e}\frac{1}{2}(\tilde{v}^2 - 5) - \mathbf{a}^*\right] f_m, \tag{6.21}$$

where $\nu_T = \nu_{ei}(v_{th})$. In order to simplify the integration procedure whilst taking moments of this equation, the following integral be used

$$\frac{n_0}{v_{th}^3}\langle\mathbf{M}\tilde{v}^n\rangle = 4\pi\int_0^\infty \mathbf{M}\tilde{v}^n f_m d\tilde{v}. \tag{6.22}$$

If this expression is now used alongside the moment definitions of heat flow and current, eqs. 6.12 and 6.13, these fluxes can be written,

$$\hat{\mathbf{j}}\left(-\frac{3}{ev_{th}^4}\right) = \frac{n_0}{\nu_T v_{th}^4}\left[\langle\mathbf{M}\tilde{v}^7\rangle\mathbf{a}^* - i\mathbf{k}\frac{\delta\hat{T}}{m_e}\frac{1}{2}\left(\langle\mathbf{M}\tilde{v}^9\rangle - 5\langle\mathbf{M}\tilde{v}^7\rangle\right)\right] \tag{6.23}$$

$$\hat{\mathbf{q}}\left(\frac{6}{m_e v_{th}^6}\right) = \frac{n_0}{\nu_T v_{th}^4}\left[\langle\mathbf{M}\tilde{v}^9\rangle\mathbf{a}^* - i\mathbf{k}\frac{\delta\hat{T}}{m_e}\frac{1}{2}\left(\langle\mathbf{M}\tilde{v}^{11}\rangle - 5\langle\mathbf{M}\tilde{v}^9\rangle\right)\right]. \tag{6.24}$$

This transport pair can now be put into the Onsager [114] form,

$$\hat{\mathbf{j}} = \boldsymbol{\sigma}\mathbf{E}^* + i\boldsymbol{\rho}\mathbf{k}\delta\hat{T} \tag{6.25}$$

$$\hat{\mathbf{q}} = i\boldsymbol{\zeta}\mathbf{k}\delta\hat{T} + \boldsymbol{\mu}\mathbf{E}^*. \tag{6.26}$$

In this form each thermodynamic flux $(\mathbf{j}, \mathbf{q})$ is driven by thermodynamic forces $(\mathbf{E}, \delta T)$ that are mediated by matrix-valued transport coefficients $\boldsymbol{\sigma}, \boldsymbol{\rho}, \boldsymbol{\mu}, \boldsymbol{\zeta}$. It will however be of more use to use the classical transport forms common in the literature. Inverting the current equation eq. 6.25 and re-expressing the heat flow equation in terms of the intrinsic heat flow $\mathbf{q}'$, Bychenkov [100] derives

$$en_0\mathbf{E}^* = \boldsymbol{\alpha}\mathbf{j} - n_0 i\boldsymbol{\beta}\mathbf{k}\delta\hat{T}, \tag{6.27}$$

$$\hat{\mathbf{q}}' = -i\boldsymbol{\kappa}\mathbf{k}\delta\hat{T} - \boldsymbol{\beta}\mathbf{j}\frac{T_0}{e}. \tag{6.28}$$

The classical forms for the thermal conductivity $\boldsymbol{\kappa}$, the resistivity $\boldsymbol{\alpha}$ and the thermoelectric coefficient $\boldsymbol{\beta}$ are put in terms of the Onsager coefficients,

$$\boldsymbol{\alpha} = en_0\boldsymbol{\sigma}^{-1} \tag{6.29}$$

$$\boldsymbol{\kappa} = -(\boldsymbol{\zeta} + \boldsymbol{\mu}\boldsymbol{\sigma}^{-1}\boldsymbol{\rho}) \tag{6.30}$$

$$\boldsymbol{\beta} = -e\boldsymbol{\sigma}^{-1}\boldsymbol{\rho}. \tag{6.31}$$

By collecting the terms of the above equations, one can see the coefficients have the form,

$$\boldsymbol{\alpha} = \frac{3m_e\nu_T}{e}\langle\mathbf{M}\tilde{v}^7\rangle^{-1}, \tag{6.32}$$

$$\boldsymbol{\kappa} = \frac{n_0 v_{th}^2}{\nu_T 12}\left[\langle\mathbf{M}\tilde{v}^{11}\rangle - \langle\mathbf{M}\tilde{v}^9\rangle\langle\mathbf{M}\tilde{v}^7\rangle^{-1}\langle\mathbf{M}\tilde{v}^9\rangle\right], \tag{6.33}$$

$$\boldsymbol{\beta} = \frac{1}{2}\left[\right]\langle\mathbf{M}\tilde{v}^7\rangle^{-1}\langle\mathbf{M}\tilde{v}^9\rangle - 5\mathbf{I}\right], \tag{6.34}$$

Without loss of generality, the magnetic field can be considered to lie along the z-axis, in which case the magnetisation matrix moment integral $\langle\mathbf{M}\tilde{v}^n\rangle$ can be more simply written as,

$$\langle\mathbf{M}\tilde{v}^n\rangle = \begin{bmatrix} \langle\tilde{v}^n\rangle_\perp & -\langle\tilde{v}^n\rangle_\wedge & 0 \\ \langle\tilde{v}^n\rangle_\wedge & \langle\tilde{v}^n\rangle_\perp & 0 \\ 0 & 0 & \langle\tilde{v}^n\rangle_\parallel \end{bmatrix}$$

The individual elements are integrals over a Maxwellian with the form,

$$\langle\tilde{v}^n\rangle_\parallel = 4\pi\int_0^\infty \tilde{v}^n\tilde{f}_m d\tilde{v}, \tag{6.35}$$

$$\langle\tilde{v}^n\rangle_\perp = 4\pi\int_0^\infty \frac{\tilde{v}^n}{(1+\chi_{th}^2\tilde{v}^6)}\tilde{f}_m d\tilde{v}, \tag{6.36}$$

$$\langle\tilde{v}^n\rangle_\wedge = 4\pi\int_0^\infty \frac{\chi_{th}\tilde{v}^{n+3}}{(1+\chi_{th}^2\tilde{v}^6)}\tilde{f}_m, d\tilde{v} \tag{6.37}$$

with $\tilde{f}_m = (2\pi)^{3/2}\exp -\tilde{v}^2/2$ and $\chi_{th} = \chi(v_{th})$.

When the correction factors are included, the corrected transport coefficients are cal-

culated by using the modified forms,

$$\langle \tilde{v}^n \rangle_\parallel = 4\pi \int_0^\infty \frac{\tilde{v}^n}{H_\parallel} \tilde{f}_m d\tilde{v}, \tag{6.38}$$

$$\langle \tilde{v}^n \rangle_\perp = 4\pi \int_0^\infty \frac{\tilde{v}^n}{H_\perp (1+\chi_{th}^2 \tilde{v}^6)} \tilde{f}_m d\tilde{v}, \tag{6.39}$$

$$\langle \tilde{v}^n \rangle_\wedge = 4\pi \int_0^\infty \frac{\chi_{th} \tilde{v}^{n+3}}{H_\wedge (1+\chi_{th}^2 \tilde{v}^6)} \tilde{f}_m, d\tilde{v} \tag{6.40}$$

Finally, using these expressions for each individual coefficient parallel, perpendicular and cross-perpendicular to the field, the normalised coefficients are

$$\alpha_\parallel^c = \frac{3}{\langle \tilde{v}^7 \rangle_\parallel} \tag{6.41}$$

$$\alpha_\perp^c = \frac{3\langle \tilde{v}^7 \rangle_\perp}{\langle \tilde{v}^7 \rangle_\perp^2 + \langle \tilde{v}^7 \rangle_\wedge^2} \tag{6.42}$$

$$\alpha_\wedge^c = \frac{3\langle \tilde{v}^7 \rangle_\wedge}{\langle \tilde{v}^7 \rangle_\perp^2 + \langle \tilde{v}^7 \rangle_\wedge^2} \tag{6.43}$$

$$\kappa_\parallel^c = \frac{1}{12}\left[\langle \tilde{v}^{11} \rangle_\parallel - \frac{\langle \tilde{v}^9 \rangle_\parallel^2}{\langle \tilde{v}^7 \rangle_\parallel} \right] \tag{6.44}$$

$$\kappa_\perp^c = \frac{1}{12}\left[\langle \tilde{v}^{11} \rangle_\perp - \left(\frac{\langle \tilde{v}^9 \rangle_\perp^2 \langle \tilde{v}^7 \rangle_\perp + 2\langle \tilde{v}^9 \rangle_\perp \langle \tilde{v}^9 \rangle_\wedge \langle \tilde{v}^7 \rangle_\wedge - \langle \tilde{v}^9 \rangle_\wedge^2 \langle \tilde{v}^7 \rangle_\perp}{\langle \tilde{v}^7 \rangle_\perp^2 + \langle \tilde{v}^7 \rangle_\wedge^2} \right) \right] \tag{6.45}$$

$$\kappa_\wedge^c = \frac{1}{12}\left[\langle \tilde{v}^{11} \rangle_\wedge - \left(\frac{\langle \tilde{v}^9 \rangle_\wedge^2 \langle \tilde{v}^7 \rangle_\wedge - \langle \tilde{v}^9 \rangle_\perp^2 \langle \tilde{v}^7 \rangle_\wedge + 2\langle \tilde{v}^9 \rangle_\wedge \langle \tilde{v}^7 \rangle_\perp \langle \tilde{v}^9 \rangle_\perp}{\langle \tilde{v}^7 \rangle_\perp^2 + \langle \tilde{v}^7 \rangle_\wedge^2} \right) \right] \tag{6.46}$$

$$\beta_\parallel^c = \frac{1}{2}\frac{\langle \tilde{v}^9 \rangle_\parallel}{\langle \tilde{v}^7 \rangle_\parallel} - \frac{5}{2} \tag{6.47}$$

$$\beta_\perp^c = \frac{1}{2}\left[\frac{\langle \tilde{v}^9 \rangle_\perp \langle \tilde{v}^7 \rangle_\perp + \langle \tilde{v}^9 \rangle_\wedge \langle \tilde{v}^7 \rangle_\wedge}{\langle \tilde{v}^7 \rangle_\perp^2 + \langle \tilde{v}^7 \rangle_\wedge^2} \right] - \frac{5}{2} \tag{6.48}$$

$$\beta_\wedge^c = -\frac{1}{2}\left[\frac{\langle \tilde{v}^9 \rangle_\perp \langle \tilde{v}^7 \rangle_\wedge - \langle \tilde{v}^7 \rangle_\perp \langle \tilde{v}^9 \rangle_\wedge}{\langle \tilde{v}^7 \rangle_\perp^2 + \langle \tilde{v}^7 \rangle_\wedge^2} \right] \tag{6.49}$$

6.5 Calculating the High-Polynomial Corrections

The methodology described above can be extended to incorporate the higher-order terms by finding a correction factor that sits in the matrix **M**. Finding this correction will first require a review of continued fractions, before delving into their generalisation to matrices.

Continued Fractions

In the linear regime the Vlasov-Fokker-Planck equation can, using the SH expansion, be represented as an infinite set of coupled linear equations. The system can written in the form of a recurrence relation [82],

$$f_{l+1} + a_l f_l + b_l f_{l-1} = 0. \tag{6.50}$$

In the unmagnetised case, this recurrence relation has the corresponding continued fraction

$$\frac{f_l}{f_{l-1}} = \cfrac{-a_l}{b_l + \cfrac{-a_{l+1}}{b_{l+1} + \cfrac{-a_{l+2}}{b_{l+2} + \ldots}}}. \tag{6.51}$$

Each successive equation in the hierarchy contributes to the fraction, which can be shown to converge at infinity. This form is used by Epperlein [82] to calculate a correction factor $H(\eta)$ to the collision frequency that 'sums up' the contributions of the entire infinite hierarchy of linear equations, and finds it to be approximately

$$H(\eta) = \sqrt{1 + \left(\frac{\pi\eta}{6}\right)^2}. \tag{6.52}$$

By analogy with this unmagnetised result, the aim will be to define a trio of modified collision frequencies $H_\parallel(\eta,\chi), H_\perp(\eta,\chi), H_\wedge(\eta,\chi)$, that encapsulate the effect of the higher-order terms. The magnetisation matrix would then become

$$M_{ij} = \frac{1}{H_\parallel}\frac{\chi_i\chi_j}{\chi^2} + \frac{1}{H_\perp}\left(\delta_{ij} - \frac{\chi_i\chi_j}{\chi^2}\right)\frac{1}{1+\chi^2} - \frac{\epsilon_{ikj}\chi_k}{1+\chi^2}\frac{1}{H_\wedge}. \tag{6.53}$$

The H functions would then follow through to the calculation of the coefficients via the moment integrals (eqs. 6.38-6.40). The question is how to calculate these H functions from the infinite hierarchy of linear equations that come out of the SH expansion of the magnetised VFP.

Spherical Harmonics and the KALOS Formalism

Constructing a recurrence relation that will apply to a magnetised plasma will require the KALOS formalism. The KALOS formalism [78] solves the electron Vlasov-Fokker-Planck equation by decomposing the distribution function into spherical harmonics,

$$f_e(\mathbf{x},\mathbf{v},t) = \sum_{l=0}^{\infty}\sum_{m=-l}^{l} f_l^m(\mathbf{x},v,t)P_l^m(\cos\theta)e^{im\phi}, \tag{6.54}$$

and solving the resulting non-linear system of equations numerically to an arbitrary choice of order of harmonic. After linearising, the KALOS system of equations become, for $l \geq 1$,

$$\frac{\partial f_l^m}{\partial t} = A_l^m + B_l^m + C_l^m + E_l^m, \tag{6.55}$$

$$C_l^m = -\frac{l(l+1)}{2}\nu_{ei}(v)f_l^m, \tag{6.56}$$

$$A_l^m = -\left(\frac{l-m}{2l-1}\right)v\frac{\partial f_{l-1}^m}{\partial x} - \left(\frac{l+m+1}{2l+3}\right)v\frac{\partial f_{l+1}^m}{\partial x}, \tag{6.57}$$

$$E_l^m = \frac{eE_x}{m_e}\frac{\partial f_m}{\partial v}. \tag{6.58}$$

Following the analysis of Epperlein, the electric field term E_l^m will only appear in the $l = 0$ equation. The collision term C_l^m only contains contributions from e-i collisions, under the assumption the e-e collisions only contribute weakly to terms $l > 0$. For the magnetic field term, there are two forms depending on the value of m, for $m = 0$,

$$Re(B_l^0) = -\frac{e}{m_e}l(l+1)(B_z Re(f_l^1) + B_y Im(f_l^1)), \tag{6.59}$$

and for $m > 0$,

$$B_l^m = -i\frac{eB_x}{m_e}mf_l^m - \frac{e}{2m_e}\left[(l-m)(l+m+1)(B_z - iB_y)f_l^{m+1} - (B_z + iB_y)f_l^{m-1}\right]. \tag{6.60}$$

Using a Fourier transform this set becomes an algebraic recurrence relation where each f_l^m is coupled to f_l^{m+1}, f_l^{m-1}, f_{l+1}^m and f_{l-1}^m. This problem is simplified by considering a uniform magnetic field directed along the z-axis, B_z; if this analysis is limited to low-frequency waves one can assume the Fourier transform of the time derivative term in eq. 6.55 is ignorable. Then at each order of $l > 1$ there is the 5-point recursion relation of the form,

$$\frac{l(l+1)}{2}f_l^m + i\eta\left[\frac{l-m}{2l-1}f_{l-1}^m + \frac{l+m+1}{2l+3}f_{l+1}^m\right] - \frac{\chi}{2}\left[(l-m)(l+m+1)f_l^{m+1} - f_l^{m-1}\right] = 0. \tag{6.61}$$

The Matrix Recursion Relation

This problem can be recast as a matrix recursion relation, with a vector $\mathbf{f}_l$ of length $l+1$ with elements $f_l^0, f_l^1, f_l^2, ...$ This recursion relation will have matrix coefficients of size $(l+1)\times(l+1)$. The objective, in analogy with the continued fraction method above, is to close the recursion relation with a matrix that contains contributions from all orders of f_l where $l > l_{max}$. This will entail finding a recursion relation closure of the form,

$$\mathbf{f}_{l+1} = S_{l+1}\mathbf{f}_l, \tag{6.62}$$

such that only the $l = 1$ equation is necessary and all the information from the higher modes is contained in the matrix S_{l+1}. In this way the influence of the entire infinite set can be included in only the first two orders.

For each order of l, eq. 6.61 has the matrix form,

$$M_l\mathbf{f}_l + i\eta N_l\mathbf{f}_{l-1} + i\eta P_l\mathbf{f}_{l+1} = 0. \tag{6.63}$$

The matrix M_l is tridiagonal with size $(l+1)\times(l+1)$ and defined as

$$M_l = \begin{bmatrix} & \cdots & \\ \frac{\chi}{2}, & \frac{l(l+1)}{2}, & -\frac{\chi}{2}(l-m)(l+m+1) \\ & \cdots & \end{bmatrix}$$

The matrices N_l and P_l are diagonal, with the diagonal elements (with $m \in [0, l]$)

$$N_l^m = \frac{l-m}{2l-1} \tag{6.64}$$

$$P_l^m = \frac{l+m+1}{2l+3} \tag{6.65}$$

Using the closure relation it is possible to convert the recurrence relation to the form,

$$\left(M_l + i\eta P_l S_{l+1}\right)\mathbf{f}_l = -iN_l\mathbf{f}_{l-1}, \tag{6.66}$$

and by comparison with the above equation from this one can find the matrix S_{l+1} defined in terms of a matrix continued fraction,

$$S_l = -\left(M_l + i\eta P_l S_{l+1}\right)^{-1} i\eta N_l. \tag{6.67}$$

However it will be useful to introduce a secondary form using the matrix G, defined as

$$G_l = M_l + i\eta P_l S_{l+1}, \tag{6.68}$$

which follows the matrix recursive definition

$$G_l = M_l + \eta^2 P_l G_{l+1}^{-1} N_{l+1}. \tag{6.69}$$

Comparing this equation to eq. 6.50, one can see the analogy with a continued fraction of the form of eq. 6.51

$$G_l = M_l + \eta^2 P_l \left(M_{l+1} + \eta^2 P_{l+1} G_{l+2}^{-1} N_{l+2}\right)^{-1} N_{l+1}.$$

One can see from this definition that if the plasma is perfectly local, i.e $\eta = 0$, the matrix G_l is equal to M_l and there is no need for a recursive definition as there is no coupling to successive orders of l. The following KALOS relations are used to close the system at the first order ($l = 1$),

$$f_l^x = f_l^0, \tag{6.70}$$

$$f_l^y = 2Re(f_l^1), \tag{6.71}$$

$$f_l^z = -2Im(f_l^1), \tag{6.72}$$

and map the elements of G_1 to the Cartesian coordinate system. It must be emphasised now that the matrix G represents the *deviation* from the diffusive approximation, so that if the maximum number of harmonics was one, i.e $l_{max} = 1$, then G would be the identity matrix.

Incorporating the f_0 Equation

So far, there has been no mention of the f_0 equation and the influence it will have on the correction factors. f_0 is assumed to be a local Maxwellian in fluid and simple non-local models [136], however the non-local deviation from a Maxwellian must be included and as such the f_0 equation must form part of the equation set. The linearised f_0 equation in Fourier space is

$$\frac{\partial \delta \hat{f}_0}{\partial t} + i\frac{v}{3}\mathbf{k}\cdot\hat{\mathbf{f}}_1 = C_{ee}[\delta \hat{f}_0]. \tag{6.73}$$

Assuming a BGK e-e collision operator, the Laplace transform of the above equation yields

$$s\delta \hat{f}_0 - \delta \hat{f}_m(0) + i\frac{v}{3}\mathbf{k}\cdot\hat{\mathbf{f}}_1 = -\nu_{ee}\delta \hat{f}_{nl}. \tag{6.74}$$

Where $\delta \hat{f}_{nl}$ represents the non-local contribution to the deviations from global equilibrium. The initial condition is represented by a perturbed, sinusoidal Maxwellian

$$\delta \hat{f}_m(0) = \delta \hat{m}(0) f_m = \left[\frac{\delta \hat{n}(0)}{n_0} + \frac{\delta \hat{T}(0)}{T_0}\frac{1}{2}\left(\frac{v^2}{v_{th}^2} - 3\right)\right] f_m. \tag{6.75}$$

The linearised $\mathbf{f}_1$ equation similarly is

$$i\mathbf{k}v\delta \hat{f}_0 - \hat{\mathbf{a}}\frac{v}{v_{th}^2} f_m = -\nu_{ei}\mathbf{M}^{-1}\hat{\mathbf{f}}_1. \tag{6.76}$$

If the deviation from the global f_0 is taken as the sum of local Maxwellian and non-local

parts, $\delta f_0 = \delta f_m + \delta f_{nl}$, and δf_0 is eliminated, this leaves

$$-\nu_{ei}\left[\mathbf{K} + \mathbf{M}^{-1}\right]\hat{\mathbf{f}}_1 = \left[i\mathbf{k}v\delta\hat{Q} - \hat{\mathbf{a}}\frac{v}{v_{th}^2}\right] f_m, \tag{6.77}$$

the factor $\delta\tilde{Q}$ is defined as

$$\delta\hat{Q} = \frac{\delta\hat{m}(0) + \nu_{ee}\delta\hat{m}}{s + \nu_{ee}}, \tag{6.78}$$

and the matrix $\mathbf{K}$ is defined as

$$K_{ij} = \frac{k_i k_j v^2}{3\nu_{ei}(s + \nu_{ee})}. \tag{6.79}$$

It is possible to use the quasi-static approximation for f_0 in which one can assume $\delta\hat{Q} = \delta\hat{m}$. Whilst the value of s is large at high frequency, for a quasi-collisional plasma $s << \nu_{ee}$ and s can be dropped without detrimentally effecting the values of the coefficients [137]. In this case the matrix $\mathbf{K}$ becomes $k_i k_j \lambda_{ei}\lambda_{ee}/3 = k_i k_j Z\lambda_{ei}^2/3$. In this case, the non-local influence of the f_0 equation on $\mathbf{f}_1$ is held within the matrix $\mathbf{K}$. It is possible to invert $\mathbf{K} + \mathbf{M}^{-1}$ such that the elements of $\mathbf{K}$ are held within the H functions.

Calculating the Correction Factors

By comparing the magnetisation matrix $\mathbf{M}$ defined in eq. 6.53 and modifying it to included the influence of the matrix $\mathbf{K}$, the form of the H functions are

$$H_{\parallel} = G_{zz} + \frac{Z\eta^2}{3}, \tag{6.80}$$

$$H_{\perp} = \frac{G_{xy}^2 + (G_{xx} + \frac{Z\eta^2}{3})^2}{(G_{xx} + \frac{Z\eta^2}{3})(1 + \chi^2)}, \tag{6.81}$$

$$H_{\wedge} = -\frac{(G_{xy}^2 + (G_{xx} + \frac{Z\eta^2}{3})^2)\chi}{G_{xy}(1 + \chi^2)}. \tag{6.82}$$

The matrix elements G_{ij} correspond to the Cartesian elements of the matrix G_1 calculated recursively from eq. 6.69. Therefore the terms G_{ij} correspond to the corrections from $l > 1$ and the matrix $\mathbf{K}$ corresponds to the corrections from the f_0 equation. These functions can then be used in eq. 6.53 to define a new magnetisation matrix for the $\mathbf{f}_1$ equation.

The H functions are evaluated by calculating the recursive definition of G_l (eq. 6.69) as a function of η, v, χ up to an arbitrarily large value of l. A numerical calculation is performed up to $l = 200$, for a mesh of values of these parameters across a wide range of scales. The result of the H functions are plotted in figures 6.4, 6.5a and 6.6a and lineouts for the magnetised coefficients are shown in figures 6.5b and 6.6b.

For $H_{\parallel}$, as shown in figure 6.4 there is no dependence on χ. This is to be expected given the magnetic field has no effect on the component parallel to the field. Reassuringly the functional form of $H_{\parallel}$ matches exactly the result of Epperlein, where the value of $H_{\parallel}$ rises monotonically as the non-locality parameter increases.

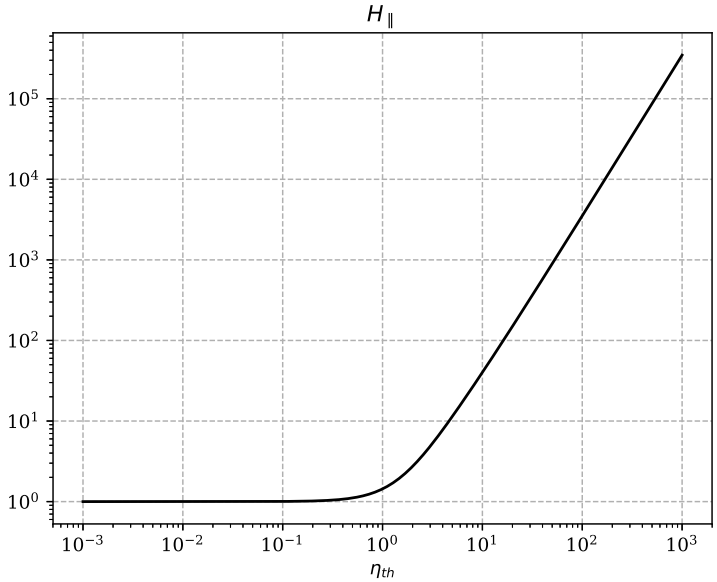

Figure 6.4: The dependence of $H_\parallel$ against non-locality parameter η. This logarithmic scale show that as the plasma becomes more non-local, at very high values of η the correction factor rises linearly.

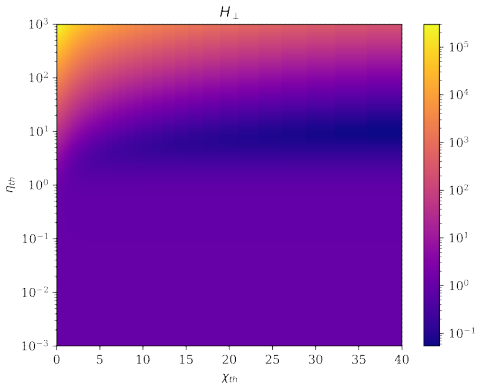

(a) Dependence of $H_\perp$ on magnetisation χ and non-locality η. This 2D map shows the emergence of a valley at approximately $\eta = 10$, and deepens as magnetisation increases.

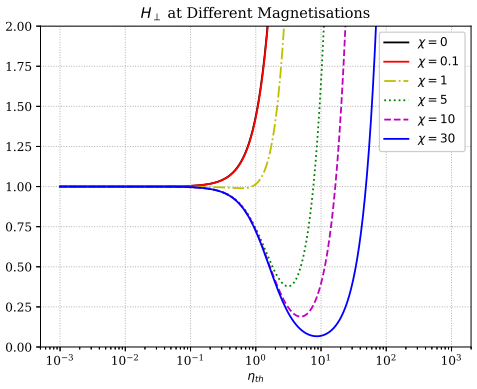

(b) Lineouts of $H_\perp$ for different magnetisation values against non-locality. For $\chi = 30$ the curve is non-monotonic, with a clear shift to higher η as magnetisation increases

Figure 6.5: The perpendicular correction factor $H_\perp$ as a function of non-locality η and magnetisation χ.

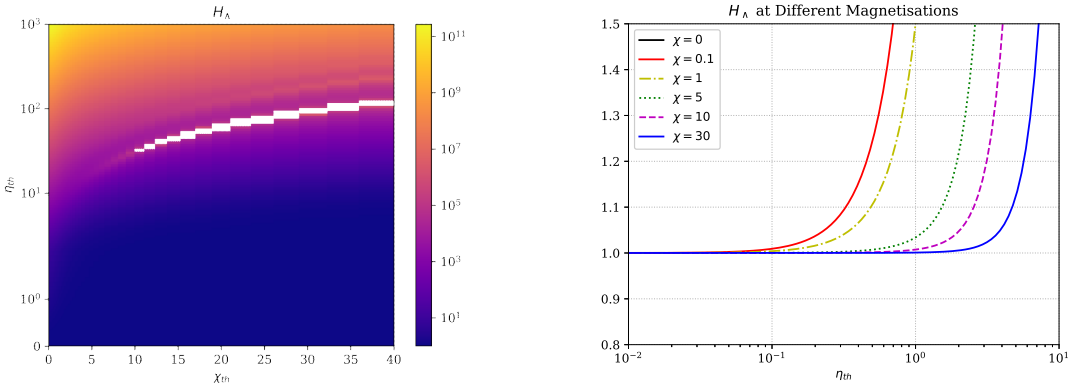

(a) Dependence of $H_\wedge$ on magnetisation χ and non-locality η. $H_\wedge$ similarly shows troughs beginning at $\chi = 5$ that again only appear at values of $\eta > 10$

(b) Lineouts of $H_\wedge$ for different magnetisation values against non-locality. $H_\wedge$ shows a clear shift to higher η as the magnetisation χ increases.

Figure 6.6: The cross-perpendicular correction factor $H_\wedge$ as a function of non-locality η and magnetisation χ.

The $H_\perp$ and $H_\wedge$ functions however show a very different picture, as functions of χ they show much more complex behaviour. In figure 6.5a, $H_\perp$ shows a clear 'valley' along a strip as χ increases. If we look at lineouts of this function in figure 6.5b, in the absence of a magnetic field it resembles $H_\parallel$ but as the magnetisation increases, it shifts to the right and forms a minimum where its value is lower than the local $(\eta = 0)$ value.

The functional form of $H_\wedge$ in figure 6.6b shows a similar 'shift' to higher non-locality η, as magnetisation χ, increases. This is clearer in the plot of $1/H_\wedge$ in fig. 6.7 where the drop-off value of η_{th} shifts to the right. This means magnetisation maintains the value of the transport perpendicular to both the magnetic field and the driving gradient, countering the non-local quenching.

Convergence of the Correction Factors

Given the diffusive approximation corresponds to ignoring all terms with $l > 1$, an important question is how the infinite continued fraction differs from this truncated version. How do the correction factors change as higher orders are included and does the result converge? The convergence of $H_\parallel$, shown in figure 6.8, shows that even including up to $l = 3$ still results in significant under-prediction for non-locality parameters $\eta_{th} > 10$. It is clear there is significant deviation at intermediate values of non-locality, entirely the result of missing higher-order modes that are ignored in almost all closures and transport models.

Similar plots for the $H_\perp$ and $H_\wedge$ factors are shown in figures 6.9 and 6.10. Again one can see that there is significant deviation away from unity in the region $\eta_{th} > 10$, with more terms in the expansion converging in the limit $l \to \infty$. This shows that the diffusive approximation for the perpendicular factors (where $l = 1$) also suffers from errors when compared to a calculation where terms $l > 1$ are included.

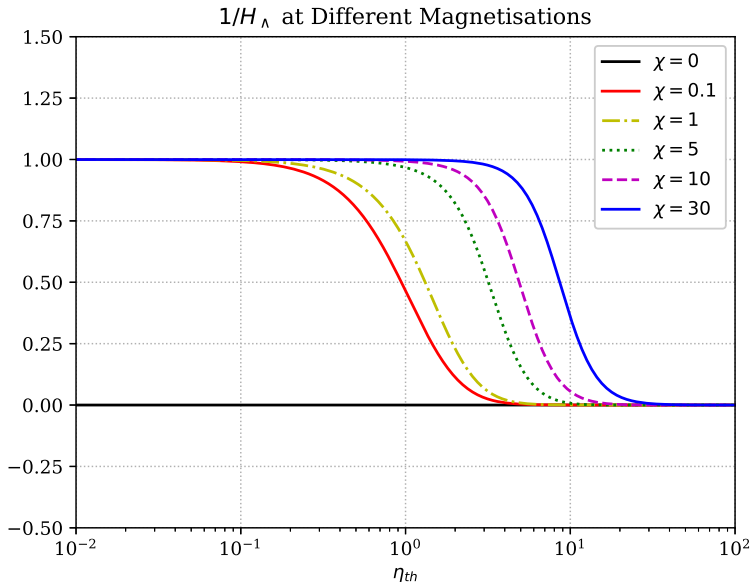

Figure 6.7: Lineouts of $1/H_{\wedge}$ for different magnetisation values against non-locality. The inverse of $H_{\wedge}$ more clearly shows how the cross perpendicular term $\wedge$ disappears at high values of η_{th}, with magnetisation shifting the drop-off to higher values of η_{th}

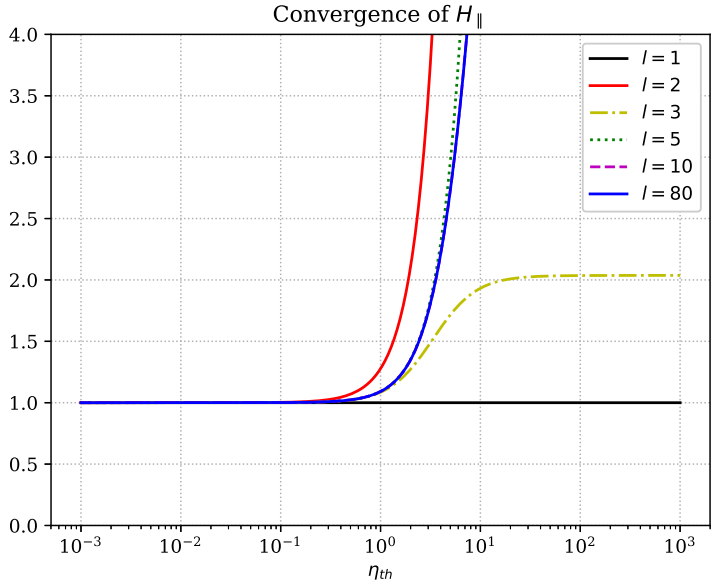

Figure 6.8: Convergence of $H_{\|}$ as more terms are included. Notice the $l = 3$ curve plateaus to a finite value at high η_{th}, truncating the expansion at $l = 3$ would result in significant errors.

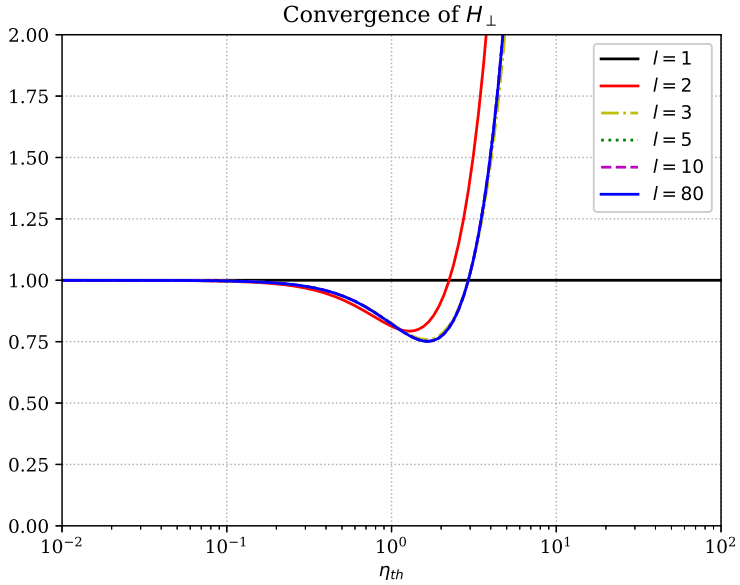

Figure 6.9: Convergence of $H_\perp$ for the value $\chi = 10$ as more terms are included. Though this factor converges faster than $H_\parallel$, adding extra terms does still show how more than $l = 1$ is necessary.

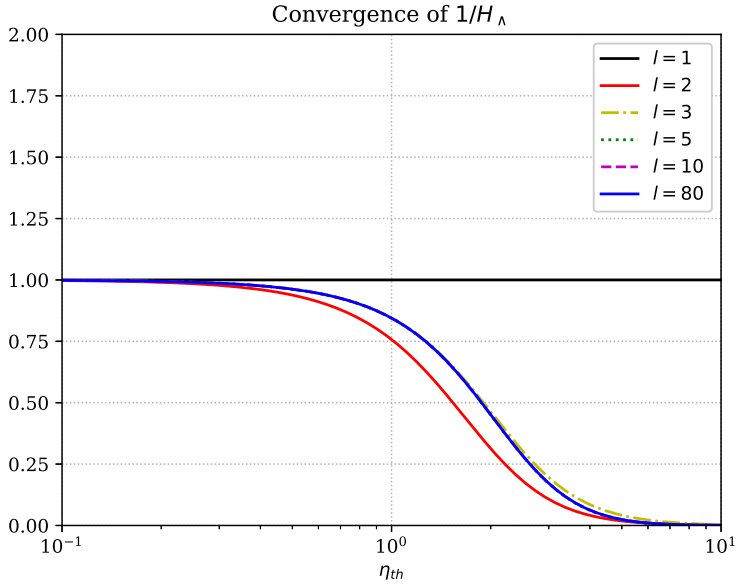

Figure 6.10: Convergence of $1/H_\wedge$ for $\chi = 0$ as more terms are included. The inverse is plotted here for clarity, and it shows significant deviation compared to the diffusive approximation for values $\eta_{th} > 1$.

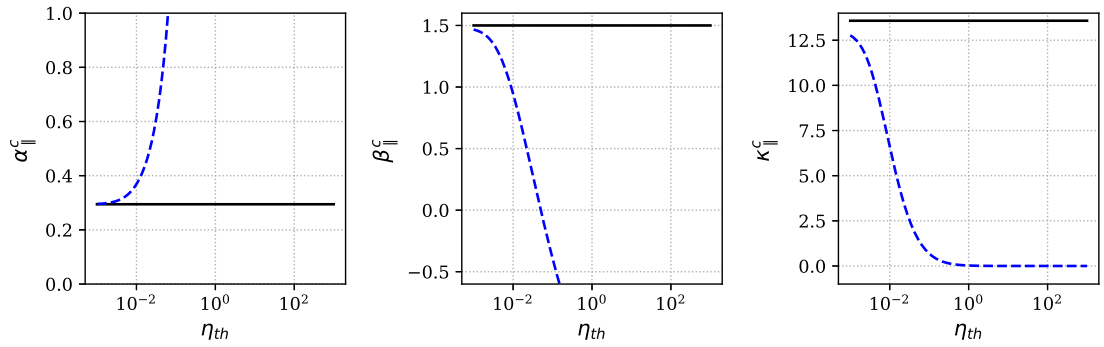

Figure 6.11: The black lines show the local parallel transport coefficients calculated by Epperlein and Haines in the Lorentz approximation. The non-local results presented in this paper are shown with dashed blue lines. The non-local correction has led to resistivity growing with η and thermal conductivity and the thermoelectric term dropping off to zero as η increases.

6.6 The Corrected Transport Coefficients

With these H functions, the transport coefficients in the linear regime can be recalculated using the expressions eqs. 6.41-6.49 and the modified moments eqs. 6.38-6.40. The first step will be to compare them to the coefficients calculated by Epperlein and Haines [111]. This will show how non-locality and the expansion truncation changes thermal conductivity, resistivity and the thermoelectric effect.

Figures 6.11 and 6.12 show the comparison between the Epperlein and Haines coefficients [111] and the new corrected forms. Figure 6.11 plots the normalised parallel coefficients against non-locality and reassuringly as the non-locality parameter $\eta \to 0$ the new coefficients converge on the Epperlein and Haines values in the Lorentz limit ($Z \to \infty$). Figure 6.12 focuses on the perpendicular and cross-perpendicular coefficients in the local approximation and again show a reassuring equivalence with the Epperlein and Haines dependence on the thermal Hall parameter $\chi_{th} = \chi(v_{th})$. This is apart from the highly magnetised cross-perpendicular resistivity $\alpha_\wedge$ where it peaks at a much higher value. This divergence from the result of Epperlein and Haines was also seen in previous work [136]. While the values converge asymptotically, the intermediate deviation corresponds not to non-locality but to the difference between the fitted form of [111] and the calculation in [136].

Figure 6.13 plots the parallel coefficients against non-locality parameter. Given there is no dependence on magnetisation for the parallel terms, the dependence on $\eta_{th} = \eta(v_{th})$ is monotonic. The parallel thermal conductivity and thermoelectric coefficient decrease, with $\beta_\parallel$ dropping sharply at $\eta_{th} \approx 0.05$. The resistivity mirrors the thermal conductivity with a steady increase with increasing non-locality.

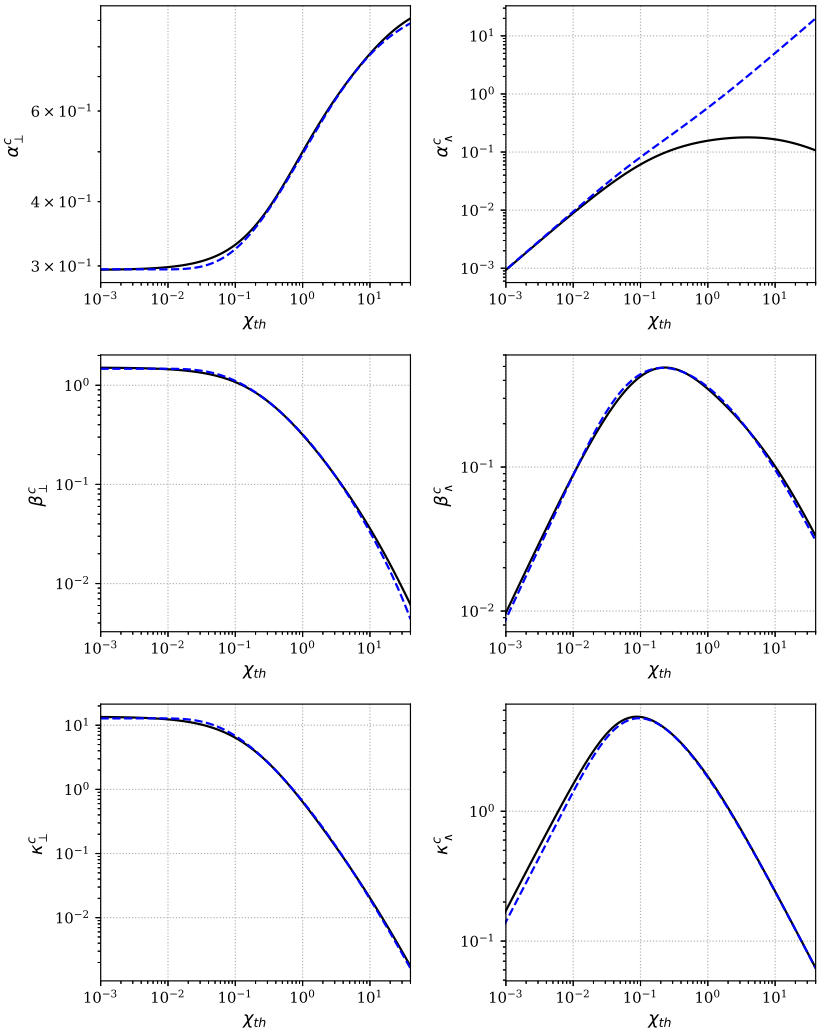

Figure 6.12: Comparison of the perpendicular and cross-perpendicular transport coefficients (blue dashed lines) presented in this paper, with the Epperlein and Haines results (solid black lines) in the Lorentz limit.

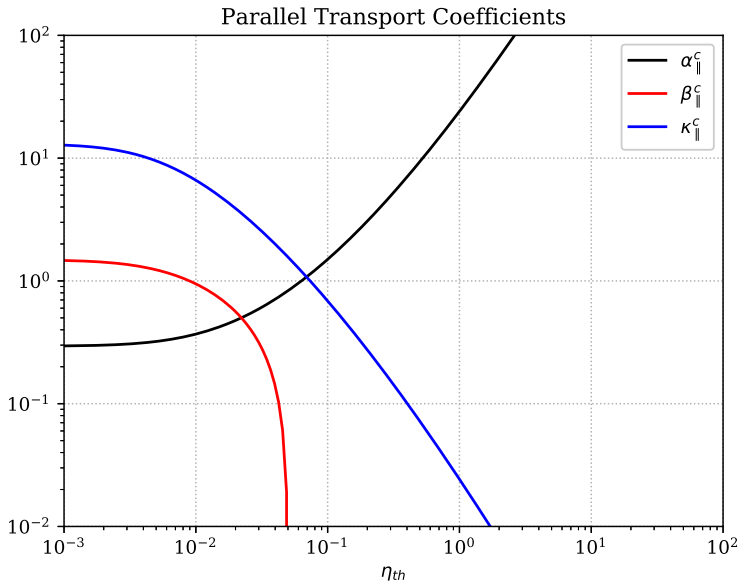

Figure 6.13: The parallel transport coefficients as a function of non-locality η_{th}. $\beta_\parallel$ drops quickly with η_{th} before changing sign, while $\alpha_\parallel$ and $\kappa_\parallel$ asymptotically have a linear depenence on η_{th}

The perpendicular and cross-perpendicular resistivity, shown in figures 6.14a and 6.14b, reveal the signs of the complex interplay between magnetisation and non-locality. The most significant feature of the magnetised non-local coefficients in this linear regime is shared by both the thermal conductivity and thermoelectric coefficients. All four show a peak, with a value greater than the local ($\eta_{th} = 0$) value, which appears and grows as χ_{th} increases, illustrated in lineouts figures 6.14c, 6.14d,6.14e and 6.14f. This in turn shifts the curves to higher values of η. This non-monotonic dependence appears as magnetisation grows. Plots of the functional dependence can be found in figs. 6.15a, 6.15b, 6.15c, 6.15d, 6.15e, 6.15f. In particular the sign-changing behaviour of the β coefficients in 6.15c and 6.15d shows how the switch appears. The value of η_{th} at which this happens remains approximately the same.

6.7 Implications For Laser-Plasma Experiments

The explanation for these effects lies in the coupling between different directions in a magnetised plasma. The magnetic field term in the VFP is skew-symmetric, coupling together different Cartesian components. When this is repeated in the recursion relation there is a coupling in the plane perpendicular to the magnetic field and back again *ad infinitum*. The localising nature of magnetisation perpendicular to the direction of the magnetic field leads to a minimum in $H_\perp$ and the corresponding non-monotonic behaviour with non-

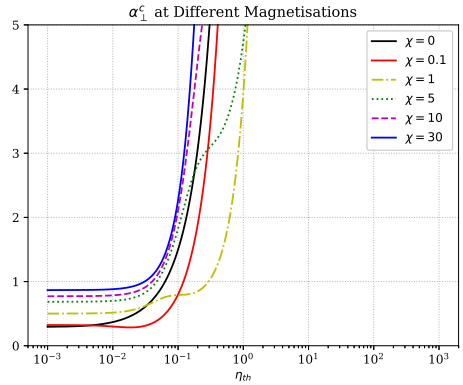

(a) These lineouts of $\alpha_\perp$ for different magnetisation values show an inflection point at $\eta_{th} \approx 0.1$ when $\chi_{th} > 15$

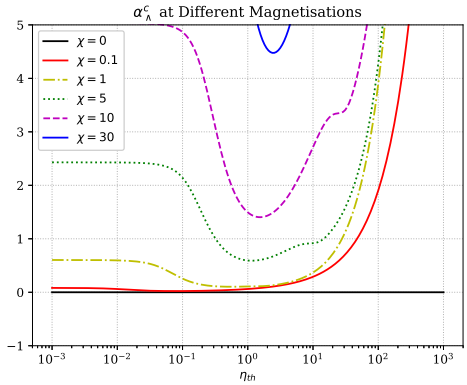

(b) When $\alpha_\wedge$ is magnetised, a drop appears at $\eta_{th} \approx 0.05$, with the depth of the valley larger at higher values of χ_{th}

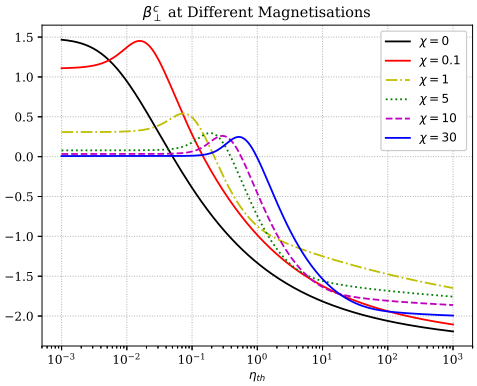

(c) Peaks in $\beta_\perp$ appear when $\chi_{th} > 0$, before eventually changing sign at a value of η_{th} that depends on the value of χ_{th}

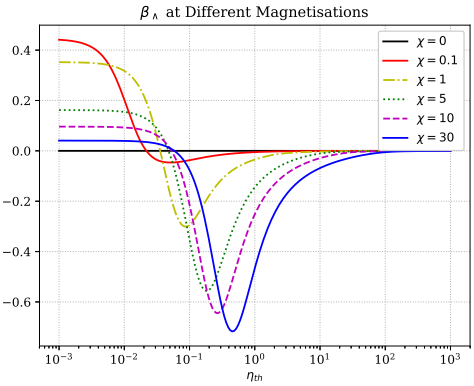

(d) Lineouts of $\beta_\wedge$ tend to zero at very high η_{th} at all values of χ_{th}. The swing from positive to negative is more extreme at higher χ_{th}.

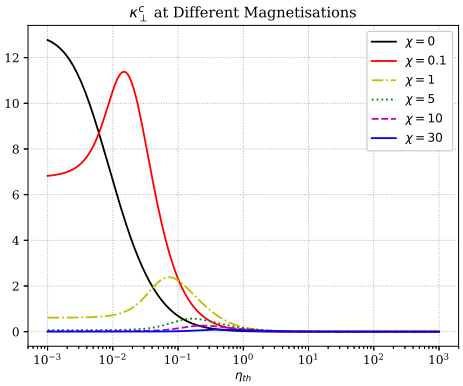

(e) Lineouts of $\kappa_\perp$ show a peak with a value up to twice the local value, with a position that shifts to the right as magnetisation increases.

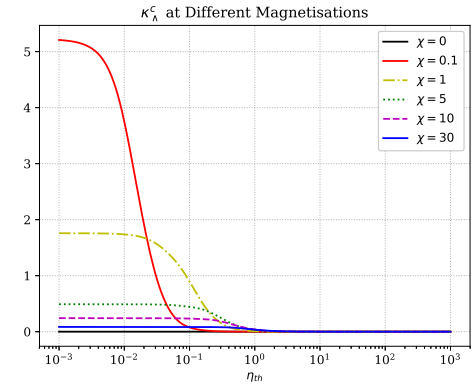

(f) Though $\kappa_\wedge$ vanishes at high η_{th} for all magnetisation values, the drop off shifts to the right as magnetisation increases.

Figure 6.14: Lineouts of the non-local magnetised transport coefficients under different magnetisations

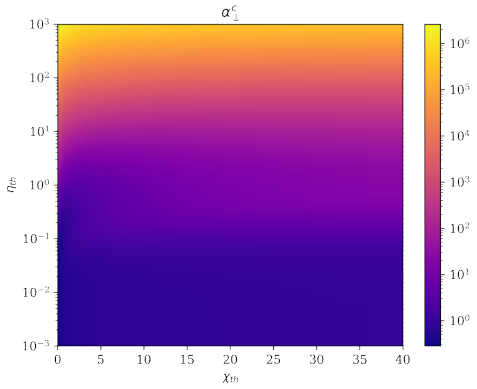

(a) $\alpha_\perp$ grows quickly with η_{th} but with an inflection point at $\eta_{th} \sim 0.1$

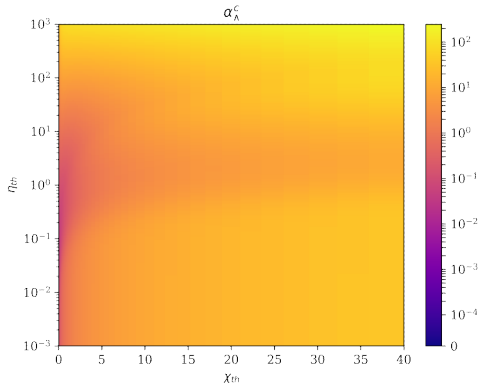

(b) $\alpha_\wedge$ shows a valley around $\eta_{th} \sim 1$ but note how its minimum rises with χ_{th}

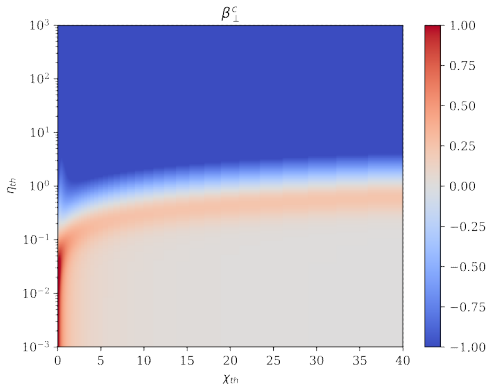

(c) $\beta_\perp$ quickly changes sign at around $\eta_{th} \sim 1$, note how this value changes in $0 < \chi_{th} < 5$.

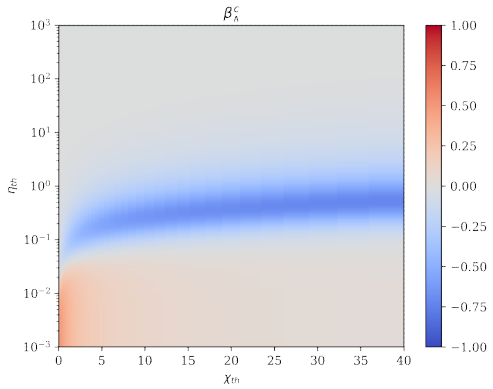

(d) $\beta_\wedge$ shows a valley at $\eta_{th} \sim 0.2$ that emerges as the plasma is magnetised

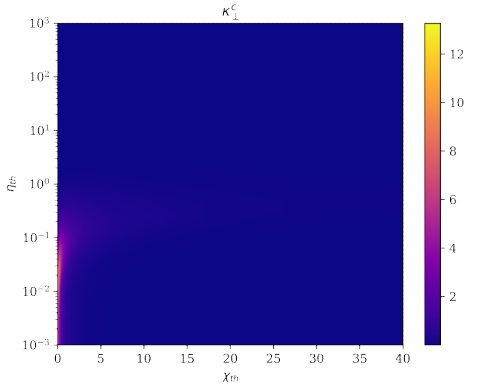

(e) It is difficult to see the features of $\kappa_\perp$ on this log-linear scale, however the moving peaks are still clear

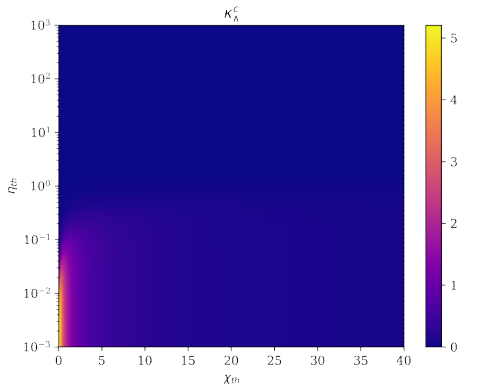

(f) $\kappa_\wedge$ has a wider drop-off with χ_{th} than $\kappa_\perp$ for $\eta_{th} < 0.1$.

Figure 6.15: 2D colourmaps of the dependence of the magnetised transport coefficients on non-locality η_{th} and magnetisation χ_{th}

locality in the transport coefficients. In particular, the reversal of the β coefficients corresponds to the value of η_{th} where $\langle \mathbf{M}\tilde{v}^9 \rangle = 5\langle \mathbf{M}\tilde{v}^7 \rangle$ in eq. 6.22. As the moments $\langle \tilde{v}^n \rangle$ are functions of the non-locality parameter η_{th}, there is a point where the thermoelectric term in the Onsager forms cancels out. Whilst the reversal of the β sign has been reported before in unmagnetised plasmas [138], it has not been seen for the full magnetised transport coefficients.

This also implies the Nernst effect switches direction at high values of η_{th}, since the thermal conductivity κ does not reverse in a similar manner, there is advection against heat flow. As an example, consider the Nernst effect acting on a single temperature mode δT; as the wavenumber of the mode increases, we can see from figure 6.15d that at some point - dependent on the value of magnetisation - the Nernst effect will act in anti-phase to the thermal diffusion.

In the context of laser-plasma experiments, experiments have been performed in both ICF-like [130] and MagLIF schemes [11] where the magnetisation parameter χ is of the order > 10. Comparing the temperature and density scales and the expected non-locality, magnetised plasma physics experiments frequently enter regimes where the transport coefficients differ by up to a factor of 2 because of the effects described above. If in addition the Nernst (driven by $\beta_\wedge$) and Cross-Nernst (driven by $\beta_\perp$) are as significant as recent simulations suggest [32, 106], their reversal of direction will further change the dynamics away from what conventional simulations suggest.

6.8 Summary

The small-scale structures that appear in filamentation suggests a kinetic treatment to accurately predict growth rates. The theory of the fluid approximation was very sensitive to the wavenumber of the perturbation and unmagnetised investigations by previous authors have shown using kinetic corrections is required. The natural extension to the results of the previous chapter necessitate using a kinetic code to explore the corrections that may appear when entering non-local regimes. The requirements for simulating collisional-timescale decay phenomena under magnetic fields led to the use of the IMPACT code.

Using the IMPACT code, the Epperlein-Short test was used to simulate the deviation of thermal decay from the expected classical magnetised value. These are diffusive approximation simulations of the thermal decay of sinusoidal temperature perturbations in a plasma. They show the combined effect of a decreased thermal conductivity, characteristic of both magnetisation and non-locality, but also see a small peak before dropping-off at high Knudsen numbers. When the simulation results are fitted to an phenomenological extension of the perpendicular thermal conductivity, this provides a phenomenological model that extends previous non-local work to include magnetic effects. When this fit is used in the filamentation dispersion relation it shows even shorter e-folding lengths in

the long-wavelength limit compared to the local dispersion relation. These results demonstrate the necessity of kinetic models for accurate transport results, despite the localising effect of magnetisation.

The question of the diffusive approximation remains. For electron distributions close to an isotropic Maxwellian, the diffusive approximation is accurate and justifiable. However, when applying inherently anisotropic magnetic fields, and when the perturbation modes go to very large non-locality values, the reliability of the diffusive approximation fails. Indeed, the fitted functional form used in this chapter showed unsatisfactory deviation from the ad-hoc expectation and motivated going to extra terms in the distribution function expansion.

To summarise the effect of the extra polynomial terms, in the linear regime the influence of magnetised non-locality can be aggregated into three correction functions $H_{\parallel}, H_{\perp}, H_{\wedge}$. This is performed using a matrix recursion method to all orders of the spherical harmonic expansion.thereby extending the work of Brantov [107]. These corrections represent the non-locality parallel, perpendicular and cross-perpendicular to the applied magnetic field respectively and can be considered modified collision frequencies. Using these to derive the corrected transport coefficients, one can show they differ from the classical approximation. The unexpected non-monotonic dependence on non-locality as these coefficients become increasingly magnetised has not been seen before in the literature. This does however resemble the results of the IMPACT simulations where a peak was seen in the thermal conductivity curves against non-locality. While the IMPACT results are limited to the diffusion approximation, this non-monotonicity provides an explanation to the IMPACT simulations. The transport coefficients in turn show significant, non-monotonic, deviation of up to 50% from the diffusive approximation at intermediate non-locality values ($k\lambda_{ei} \approx 10 - 100$) and would lead to as-yet unseen transport phenomena in the linear regime.

Though this chapter looked only at the case of a magnetic field perpendicular to the wavevector of a perturbation, these results could be extended to an arbitrarily-directed magnetic field. In this case, the recurrence relation would include more terms and the H function corrections would include contributions from all elements of the matrix G. Furthermore, this work could be improved by using a more accurate e-e collision term in the f_0 equation. The BGK e-e operator used in the analysis of section 6.5, though simple to use, is not as accurate as a Fokker-Planck operator so a comparison of the results under the different e-e operators is necessary.

By incorporating the higher-order modes into transport calculations, these results present a possible source of error in simulations of plasmas under magnetic fields. While only working in the linear regime, these results can be used directly in the analysis of damping of waves in plasmas. Overall, this result provides motivation for the closer study of the terms ignored in most fluid closures. The primary conclusion from this chapter is that it is necessary to use higher-order terms of the spherical harmonic expansion when constructing a closure in magnetised plasmas. Inertial fusion experiments today work in regimes where the transport in the plasma is non-local. With the use of very strong magnetic

fields, a better understanding of the interplay between non-locality and magnetisation is required.

7

Conclusions

In long-pulse laser-plasma experiments, the accurate simulation and prediction of transport phenomena is of utmost importance. They are fundamental to the design of experiments and interpretation of their results. With the introduction of magnetic fields into experiments, more complex models of transport phenomena are required. In order to answer these questions, the core of this thesis has been the simulation of magnetisation phenomena and laser propagation.These led to an investigation into the interplay of magnetic fields and non-locality in transport.

Results of a new laser-plasma simulation code, described in this thesis delivered insights into how magnetisation can be detrimental to laser propagation in plasmas. Further study using a kinetic code supported the hypothesis there is a non-local influence even in magnetised transport. An analytic study utilising higher terms of a spherical harmonic expansion demonstrated the inadequacy of the diffusive approximation in magnetised plasma experiments. These results show the importance of including magnetisation phenomena in simulation codes and the necessity of greater study of non-local magnetised transport in fusion plasmas.

7.1 A Simulation Code For Magnetised Transport

The first step in this thesis was the construction of a 3D laser-plasma simulation code. This code, PARAMAGNET, used a single-fluid MHD plasma solver with full Braginskii electron transport coupled to a paraxial laser solver via the ponderomotive force and inverse bremsstrahlung. This code enabled the simulation of three-dimensional long-pulse laser-plasma interactions in the underdense regime. Using a paraxial laser field allowed the direct calculation of laser-plasma coupling terms, as such the laser intensity can be retrieved directly from the magnitude of the laser field, making the intensity calculation

trivial relative to other laser simulation methods. This however limited the laser physics to approximately unidirectional laser problems. The alternating-direction-implicit method was chosen as the algorithm for the laser solver because it reduced the 3D evolution to a simple linear tridiagonal complex-valued matrix problem. The direct solution of this matrix method however prevented the use of distributed-memory parallelism with MPI because the domain decomposition method used in the laser solver would require access to the whole domain.

The MHD solver's fully implicit model struggled with strong shock areas where fine resolution was required to prevent the solver crashing unpredictably. The Jacobian-Free-Newton-Krylov method employed as the nonlinear solver was simple to write however without a preconditioner many more steps were required for convergence of the non-linear solve step. In general, the JFNK method was not suited to hyperbolic problems. Otherwise for strongly parabolic problems the MHD solver was robust and provided an all-in-one solver for the entire extended MHD equation set. The laser solver by comparison would be ideal for complex laser dynamics such as vortex beams because the laser field is solved directly and the resolution requirements are less stringent than a Helmholtz solver or Maxwell solver.

This code, despite the numerical flaws mentioned above, enabled the accurate study of laser propagation presented in this thesis, inclusive of the flux-limited magnetised transport effects. In future the paraxial solver could be made more powerful if coupled with a grid refinement method such as adaptive mesh refinement to better simulate small scale laser physics. The inclusion of non-local models discussed in this thesis into the transport terms would also extend the capability of this code to simulate arbitrary laser-plasma physics problems of interest to the laser-plasma community.

7.2 Long-Pulse Laser Propagation in Magnetised Plasmas

The first application of the new PARAMAGNET code was to simulate the laser propagation physics in the regimes of a MagLIF pre-heat scenario. This was done by simulating the propagation of a Gaussian long pulse beam in a magnetised underdense fuel capsule. An associated analytic model based on a simplified equation set produced a focusing Gaussian beam solution that provided an explanation for the mechanism responsible.

Initial simulations with the PARAMAGNET code showed a clear signature of the effects first observed by Read [27] where Nernst advection increased beam focusing. However the magnetisation of the thermal conductivity was found to have a more significant effect on reducing the self-focal length. When an axial field was applied this shortening followed an approximately linear relationship with the field strength B. With a reduced perpendicular thermal conductivity, the pressure gradient produced by the laser heating was maintained. As a result a deeper density channel was formed, earlier leading to

stronger focusing. The analytic model replicated the simulations before the breakdown of the linear approximations, that is a linear perturbation to a uniform background.

Following the focusing simulations, filamentation simulations were performed by initialising small harmonic perturbations over a wide range of wavenumbers on a uniform laser background. These were to represent modes of inhomogeneity present in all real laser pulses. With a magnetic field applied parallel with the laser wavevector, magnetised transport terms contributed to the evolution of the plasma, and by extension the laser field. The magnetised thermal conductivity reduced the transport of thermal energy, and the Nernst effect advected the magnetic field into lower-temperature regions, reducing the local magnetic field strength.

The initial harmonic perturbations grew into laser filaments, the magnitude of their peak laser field grew with a greater spatial growth rate under a magnetic field. The physical mechanism for this result was obtained from a linearised paraxial-MHD model and showed good agreement with PARAMAGNET simulations. The source of this filamentation growth was for the same as self-focusing, with the same approximately linear relationship with parallel field strength. As such, the filamentation e-folding length shortened as the magnetic field strength increased. The instability spectrum showed long-wavelength perturbations affected most, with micron-scale non-uniformity growing at multiple times the unmagnetised rate.

In the context of inertial fusion experiments like MagLIF, they have a configuration where the magnetic field applied to the fuel is parallel to the pre-heat laser, and so magnetisation of the fuel is detrimental to effective laser-coupling. The faster growth rates of filamentation increases backscatter by pushing the local laser intensity towards the parametric instability threshold. For direct-drive, uniform heating is necessary to avoid seeding hydrodynamic instabilities. If magnetisation increases focusing in the underdense corona during a direct-drive laser pulse, the uniformity of laser intensity will be detrimentally effected. Non-uniform structures will grow to sizes that can seed hydrodynamic instabilities in the fuel capsule.

In the introduction, this thesis described a need for an investigation into the 3D laser-plasma coupling under magnetic field. In response, these simulations and theoretical results identified unexplored effects in laser-plasma coupling necessary for explaining highly-magnetised experiments. These results support the need for inclusion of magnetised transport terms in simulations of long pulse laser-plasma experiments.

In future, further development of the results described in this thesis would require the inclusion of a parametric laser-plasma instability model that can calculate the growth and loss of laser energy from SRS, SBS and CBET. This is necessary to support the hypothesis that magnetised filamentation leads to increased parameteric instability backscatter and would provide a more accurate model for laser-plasma coupling. In addition, performing direct-drive laser imprint simulations would shed light on the degree that magnetisation can unintentionally increase inhomogenous laser imprint on the fuel capsule surface, and by extension its role in seeding the surface Rayleigh-Taylor instability. In terms of the simulation model, additions to the laser solver to deal with propagation near the critical

surface and terms to deal with reflection would increase the capability of the code.

7.3 Non-local Corrections to Magnetised Transport

The thermal transport results of the laser propagation section indicated investigating non-local effects with the kinetic code IMPACT. The small scale filament simulations implied the importance of non-local transport in their evolution, this is because of the relatively large Knudsen number of such filament structures. To explore this further, the IMPACT diffusive-approximation code was used to simulate the thermal decay of linear harmonic perturbations under a magnetic field and the results compared with the local approximation via the Epperlein-Short non-locality test. The numerically-derived result was fitted to an phenomenological extension of the perpendicular thermal conductivity.

The IMPACT simulations found an even shorter thermal e-folding length, the result of the combined reduction from both magnetisation and non-local transport suppression. In plasmas where the thermal focusing mechanism is dominant and for longer filamentation perturbation wavelengths, the kinetic thermal e-folding length is reduced up to a factor of 2. These regimes are regularly accessed in long-pulse laser-plasmas and so susceptible to such kinetic, magnetised effects.

For electron distributions close to an isotropic Maxwellian, the diffusive approximation is accurate and justifiable. However when applying inherently anisotropic magnetic fields and with perturbation modes that go to very large values of non-locality ($k\lambda_{ei}$), the reliability of the diffusive approximation fails. By using the spherical harmonic expansion of the electron VFP used in the KALOs formalism of Bell [78], one can derive a recursively-defined correction to the collision frequencies parallel, perpendicular and cross-perpendicular to the magnetic field. Analogous to a continued fraction used by Epperlein [82], this method 're-summed' the contributions to a linear magnetised kinetic model, thus encapsulating the magnetised non-local behaviour from all higher-order terms into a correction factor. This factor was in turn used to calculate corrected transport coefficients in the linear regime following the formalism introduced by Bychenkov [100].

The corrected transport coefficients showed significant deviation of up to 50% from the expected results at intermediate values of the non-locality parameter. They showed non-monotonic dependence on non-locality, deviating from any other previously reported results while also providing an explanation for peaks observed in the magnetised thermal conductivity seen in the above IMPACT simulations. The deviation from classical transport greatly modifies the expected transport of charge, heat and magnetic fields in a plasma, therefore for simulations to accurately reproduce experimental results transport models must be developed that incorporate these effects.

Inertial fusion experiments today work in regimes where the transport in the plasma is non-local. With the use of very strong magnetic fields, a better understanding of the in-

terplay between non-locality and magnetisation is required. As an example, if the Nernst-effect reversal observed in chapter 6 is considered in terms of a MagLIF implosion, the flux of magnetic field out of the hot fuel core will be slower than expected. What's more, if the thermal filamentation are reconsidered with the thermal conductivity result of chapter 6, the peak in magnetised thermal conductivity could decrease the peak filamentation e-folding length over and above what is presented in chapter 5.

Despite the localising effect of magnetisation, these unexpected results demonstrate the necessity to use kinetic models to look at non-Maxwellian behaviour; thus justifying the need defined in the introduction. Questions however remain, such as can a more analytic expression be derived for the non-local correction? Is it possible extend this method to non-linear variations? Even in the face of many years of study, the field of plasma physics still provides a rich world of stones unturned.

A

The Transport Coefficients

This appendix covers the form of the dimensionless transport coefficients used in the PARAMAGNET code of chapter 3. The functional form the transport coefficients used in this thesis were determined by Epperlein and Haines [111] by solving the Vlaslov-Fokker-Planck equation numerically then fitting a polynomial expression in terms of the dimensionless Hall parameter to the results. They used the expansion

$$\epsilon = \sum_{j=0}^{n} \alpha_j \chi^{j+s} \left(\sum_{j=0}^{d} a_j \chi^j \right)^{-r} \tag{A.1}$$

and found the values of n, d, r and s that best fit the numerical result. The Hall parameter is dimensionless and defined as

$$\chi = \omega_c \tau_{ei} \tag{A.2}$$

The functional dependence on the Hall parameter can be found in table A.1 and the values of the parameters are tabulated in table A.2.

A.1 The Transport Coefficients as Functions of the Hall Parameter

$$\alpha_{\parallel}^c = \alpha_0 \qquad \alpha_{\perp}^c = 1 - \frac{\alpha_1'\chi + \alpha_0'}{\chi^2 + a_1'\chi + a_0'} \qquad \alpha_{\wedge}^c = \frac{\chi(\alpha_1''\chi + \alpha_0'')}{(\chi^3 + a_2''\chi^2 + a_1''\chi + a_0'')^{8/9}} \tag{A.3}$$

$$\beta_{\parallel}^c = \beta_0 \quad \beta_{\perp}^c = \frac{\beta_1'\chi + \beta_0'}{(\chi^3 + b_2'\chi^2 + b_1'\chi + b_0')^{8/9}} \qquad \beta_{\wedge}^c = \frac{\chi(\beta_1''\chi + \beta_0'')}{\chi^3 + b_2''\chi^2 + b_1''\chi + b_0''} \tag{A.4}$$

$$\kappa_{\parallel}^c = \gamma_0 \qquad \kappa_{\perp}^c = \frac{\gamma_1'\chi + \gamma_0'}{\chi^3 + c_2'\chi^2 + c_1'\chi + c_0'} \qquad \kappa_{\wedge}^c = \frac{\chi(\gamma_1''\chi + \gamma_0'')}{\chi^3 + c_2''\chi^2 + c_1''\chi + c_0''} \tag{A.5}$$

A.2 Numerical Values

The functions have a set of numerical coefficients that are tabulated below. The primes refer to the the coefficient type, no prime is the parallel component; one prime is the perpendicular component and two primes is the third 'wedge' component. These values were calculated for several values of the ionization Z. The PARAMAGNET code only includes ionization values of Z=1 to 8.

	Z=1	2	3	4	5	6	7	8
α_0	0.5061	0.4295	0.395	0.3750	0.3618	0.3524	0.3454	0.3399
α_0'	1.37	1.58	1.68	1.74	1.78	1.80	1.82	1.84
α_1'	3.03	3.21	3.17	3.15	3.14	3.13	3.12	3.11
a_0'	2.77	2.78	2.78	2.78	2.78	2.79	2.79	2.79
a_1'	6.72	6.70	6.47	6.37	6.33	6.29	6.26	6.23
α_0''	2.66×10^2	4.91×10^2	6.30×10^2	7.06×10^2	7.23×10^2	7.57×10^2	7.94×10^2	8.17×10^2
α_1''	2.53	2.53	2.53	2.53	2.53	2.53	2.53	2.53
a_0''	3.28×10^3	3.72×10^3	3.79×10^3	3.67×10^3	3.37×10^3	3.28×10^3	3.25×10^3	3.20×10^3
a_1''	3.46×10^3	6.69×10^3	8.99×10^3	1.02×10^4	1.06×10^4	1.11×10^4	1.17×10^4	1.22×10^4
a_2''	3.66×10^2	5.54×10^2	6.75×10^2	7.35×10^2	7.44×10^2	7.69×10^2	7.93×10^2	8.25×10^2
β_0	0.7029	0.9054	1.018	1.092	1.146	1.186	1.218	1.244
β_0'	1.05×10^3	1.38×10^3	1.55×10^3	1.64×10^3	1.71×10^3	1.74×10^3	1.73×10^3	1.79×10^3
β_1'	6.33	6.33	6.33	6.33	6.33	6.33	6.33	6.33
b_0'	3.71×10^3	3.80×10^3	3.80×10^3	3.74×10^3	3.72×10^3	3.64×10^3	3.53×10^3	3.57×10^3
b_1'	4.11×10^3	7.05×10^3	8.75×10^3	9.73×10^3	1.07×10^4	1.11×10^4	1.13×10^4	1.17×10^4
b_2'	5.15×10^2	6.42×10^2	6.90×10^2	7.07×10^2	7.31×10^2	7.35×10^2	7.29×10^2	7.34×10^2
β_0''	2.54	4.40	3.37	3.43	3.20	3.05	2.92	2.82
β_1''	1.5	1.5	1.5	1.5	1.5	1.5	1.5	1.5
b_0''	2.87	2.43	1.46	1.06	0.848	0.718	0.629	0.565
b_1''	3.27	5.18	4.34	3.92	3.66	3.48	3.33	3.21
b_2''	7.09	9.34	8.65	8.27	8.02	7.83	7.68	7.55
γ_0	3.203	4.931	6.115	6.995	7.68	8.231	8.685	9.067
γ_0'	6.18	9.30	10.02	9.14	8.60	8.57	8.8.4	7.93
γ_1'	4.66	3.96	3.72	3.60	3.53	3.49	3.49	3.43
c_0'	1.93	1.89	1.66	1.31	1.12	1.04	1.02	0.875
c_1'	2.31	3.78	4.76	4.63	4.62	4.83	5.19	4.74
c_2'	5.35	7.78	8.88	8.80	8.80	8.96	9.24	8.84
γ_0''	4.01	2.46	1.13	0.628	0.418	0.319	0.268	0.238
γ_1''	2.5	2.5	2.5	2.5	2.5	2.5	2.5	2.5
c_0''	0.661	0.156	0.0442	0.018	9.63×10^{-3}	6.25×10^{-3}	4.61×10^{-3}	3.71×10^{-3}
c_1''	0.931	0.398	0.175	0.101	7.02×10^{-2}	5.51×10^{-2}	4.65×10^{-2}	4.10×10^{-2}
c_2''	2.50	1.71	1.05	0.775	0.646	0.578	0.539	0.515

Table A.1: The numerical values of the constants used in the transport coefficients

B

Finite Differenced Equations

This appendix covers the normalised system of equations of the coupled plasma-laser model solved by the PARAMAGNET code. They are presented in dimensionless form, using the normalisation scheme described in table 4.1. All together, the equations of the model are:

The Continuity Equation

$$\frac{\partial n}{\partial t} + \nabla \cdot (n\mathbf{V}) = 0 \tag{B.1}$$

The Momentum Equation

$$Rn\left(\frac{\partial \mathbf{V}}{\partial t} + \mathbf{V} \cdot \nabla \mathbf{V}\right) = -\frac{1}{2}\nabla nT + \mathbf{j} \times \mathbf{B} - \frac{1}{2}S_l n \nabla |\psi|^2 \tag{B.2}$$

The Energy Equation

$$\frac{3}{2}n\left(\frac{\partial T}{\partial t} + \mathbf{V} \cdot \nabla T\right) + nT\nabla \cdot \mathbf{V} + 2\nabla \cdot \mathbf{q} = 2\left(\mathbf{E} + \mathbf{V} \times \mathbf{B}\right) \cdot \mathbf{j} + S_l \frac{n^2}{T^{3/2}}|\psi|^2 \tag{B.3}$$

Ohm's Law

$$n\left(\mathbf{E} + \mathbf{V} \times \mathbf{B}\right) = -\frac{1}{2}\nabla nT + \mathbf{j} \times \mathbf{B} + \frac{n}{T^{3/2}}\underline{\underline{\alpha^c}} \cdot \mathbf{j} - \frac{1}{2}\underline{\underline{\beta}} \cdot \nabla T \tag{B.4}$$

Heat Flow

$$\mathbf{q} = -\frac{1}{4}T^{5/2}\underline{\underline{\kappa^c}} \cdot \nabla T - \frac{1}{2}\underline{\underline{\beta}} \cdot \mathbf{j}T \tag{B.5}$$

Maxwell's Equations

$$\nabla \times \mathbf{B} = \tilde{\mu}\mathbf{j} \tag{B.6}$$

$$\frac{\partial \mathbf{B}}{\partial t} = -\nabla \times \mathbf{E} \tag{B.7}$$

The constants that appear in the equations above are defined

$$R = \frac{m_i}{Zm_e} \qquad \tilde{\mu} = \frac{e^2 n_0}{m_e}\mu_0 \qquad S_l = \frac{I_0}{cn_c T_0}$$

With a dimensionless set of equations, it is now possible to transform them into a discrete form suitable to numerical solution. The numerical methods are described in detail in chapter 4. The finite difference scheme with backward-Euler time discretisation and central differences for spatial derivatives leads to the discrete form of the equations on a Eulerian Cartesian mesh. For vector equations, only the x-component is show for the sake of brevity. The finite difference equations can be simplified with the three cell-size constants, α, β, γ, defined as

$$\alpha = \frac{\Delta t}{2\Delta x}, \tag{B.8}$$

$$\beta = \frac{\Delta t}{2\Delta y}, \tag{B.9}$$

$$\gamma = \frac{\Delta t}{2\Delta z}, \tag{B.10}$$

with the central difference operator,

$$\delta_x f = f_{i+1jk} - f_{i-1jk}. \tag{B.11}$$

The Continuity Equation

$$n^{n+1}\left(1 + \alpha\delta_x V_x^{n+1} + \beta\delta_y V_y^{n+1} + \gamma\delta_z V_z^{n+1}\right) + \left(\alpha V_x^{n+1}\delta_x n^{n+1} + \beta V_y^{n+1}\delta_y n^{n+1} + \gamma V_z^{n+1}\delta_z n^{n+1}\right) = n^n \tag{B.12}$$

The Momentum Equation

$$Rn^{n+1}\left(V_x^{n+1} - V_x^n + \alpha V_x^{n+1}\delta_x V_x^{n+1} + \beta V_y^{n+1}\delta_y V_x^{n+1} + \gamma V_z^{n+1}\delta_z V_x^{n+1}\right) = -\frac{1}{2}\left(\alpha n^{n+1}\delta_x T^{n+1} + \alpha T^{n+1}\delta_x n^{n+1}\right) + \Delta t j_y^{n+1} B_z^{n+1} - \Delta t j_z^{n+1} B_y^{n+1} - \frac{1}{2} S_l n^n \alpha \delta_x |\psi|^2 \tag{B.13}$$

The Energy Equation

$$\frac{3n^{n+1}}{2}\left(T^{n+1}-T^{n}+\alpha V_x^{n+1}\delta_x T^{n+1}+\beta V_y^{n+1}\delta_y T^{n+1}+\gamma V_z^{n+1}\delta_z T^{n+1}\right)+$$
$$2\left(\alpha\delta_x q_x^{n+1}+\beta\delta_y q_y^{n+1}+\gamma\delta_z q_z^{n+1}\right)+n^{n+1}T^{n+1}\left(\alpha\delta_x V_x^{n+1}+\beta\delta_y V_y^{n+1}+\gamma\delta_z V_z^{n+1}\right)$$
$$-2\left(E_x^{n+1}+V_y^{n+1}B_z^{n+1}-V_z^{n+1}B_y^{n+1}\right)j_x^{n+1}-2\left(E_y^{n+1}+V_z^{n+1}B_x^{n+1}-V_x^{n+1}B_z^{n+1}\right)j_y^{n+1}-$$
$$2\left(E_z^{n+1}+V_x^{n+1}B_y^{n+1}-V_y^{n+1}B_x^{n+1}\right)j_z^{n+1}=S_l\frac{n^n}{T^{3/2}}|\psi|^2 \quad \text{(B.14)}$$

Ampere's Law

$$\beta\delta_y B_z^{n+1}-\gamma\delta_z B_y^{n+1}=\Delta t\tilde{\mu}j_x^{n+1} \quad \text{(B.15)}$$

Faraday's Law

$$B_x^{n+1}+\beta\delta_y E_z^{n+1}-\gamma\delta_z E_y^{n+1}=B_x^n \quad \text{(B.16)}$$

Ohm's law

$$n^{n+1}\left(E_x^{n+1}+V_y^{n+1}B_z^{n+1}-V_z^{n+1}B_y^{n+1}\right)+\frac{n^{n+1}\alpha}{2\Delta t}\delta_x T^{n+1}+\frac{T^{n+1}\alpha}{2\Delta t}\delta_x n^{n+1}-$$
$$j_y^{n+1}B_z^{n+1}+j_z^{n+1}B_y^{n+1}-\frac{n^{n+1}}{(T^{n+1})^{3/2}}\left(\alpha_{xx}^n j_x^{n+1}+\alpha_{xy}^n j_y^{n+1}+\alpha_{xz}^n j_z^{n+1}\right)+$$
$$\frac{n^{n+1}}{3\Delta t}\left(\alpha\beta_{xx}^n\delta_x T^{n+1}+\beta\beta_{xy}^n\delta_y T^{n+1}+\gamma\beta_{xz}^n\delta_z T^{n+1}\right)=0 \quad \text{(B.17)}$$

The Heat Flow Equation

$$q_x^{n+1}=-\frac{(T^{n+1})^{5/2}}{4\Delta t}\left(\kappa_{xx}^n\alpha\delta_x T^{n+1}+\kappa_{xy}^n\beta\delta_y T^{n+1}+\kappa_{xz}^n\gamma\delta_z T^{n+1}\right)$$
$$-\frac{T^{n+1}}{4}\left(\beta_{xx}^n j_x^{n+1}+\beta_{xy}^n j_y^{n+1}+\beta_{xz}^n j_z^{n+1}\right) \quad \text{(B.18)}$$

References

[1] Maurizio Salaris and Santi Cassisi. *Evolution of stars and stellar populations*. John Wiley & Sons, 2005. 12

[2] Susanne Pfalzner. *An introduction to inertial confinement fusion*. CRC Press, 2006. 12, 61, 63

[3] Stefano Atzeni and Jurgen Meyer-ter Vehn. *The Physics of Inertial Fusion : Beam Plasma Interaction, Hydrodynamics, Hot Dense Matter*. Oxford University, Oxford, 2004. 13

[4] R. S. Craxton, K. S. Anderson, T. R. Boehly, V. N. Goncharov, D. R. Harding, J. P. Knauer, R. L. McCrory, P. W. McKenty, D. D. Meyerhofer, J. F. Myatt, A. J. Schmitt, J. D. Sethian, R. W. Short, S. Skupsky, W. Theobald, W. L. Kruer, K. Tanaka, R. Betti, T. J.B. Collins, J. A. Delettrez, S. X. Hu, J. A. Marozas, A. V. Maximov, D. T. Michel, P. B. Radha, S. P. Regan, T. C. Sangster, W. Seka, A. A. Solodov, J. M. Soures, C. Stoeckl, and J. D. Zuegel. Direct-drive inertial confinement fusion: A review. *Physics of Plasmas*, 22(11):110501, 2015. 13, 24, 92, 111

[5] S. X. Hu, D. T. Michel, A. K. Davis, R. Betti, P. B. Radha, E. M. Campbell, D. H. Froula, and C. Stoeckl. Understanding the effects of laser imprint on plastic-target implosions on OMEGA. *Physics of Plasmas*, 23(10), 2016. 13, 25

[6] R. Betti and O. A. Hurricane. Inertial-confinement fusion with lasers. *Nature Physics*, pages 435–448, 2016. 13, 14

[7] Keith A. Brueckner and Siebe Jorna. Laser-driven fusion. *Reviews of Modern Physics*, 46(2):325–367, 4 1974. 13

[8] John D. Lindl, Peter Amendt, Richard L. Berger, S. Gail Glendinning, Siegfried H. Glenzer, Steven W. Haan, Robert L. Kauffman, Otto L. Landen, and Laurence J. Suter. The physics basis for ignition using indirect-drive targets on the National Ignition Facility. *Physics of Plasmas*, 11(2):339–491, 2 2004. 13, 24, 65

[9] S. A. Slutz, M. C. Herrmann, R. A. Vesey, A. B. Sefkow, D. B. Sinars, D. C. Rovang, K. J. Peterson, and M. E. Cuneo. Pulsed-power-driven cylindrical liner implo-

sions of laser preheated fuel magnetized with an axial field. *Physics of Plasmas*, 17(5):056303, 2010. 14, 18, 112

[10] Stephen A. Slutz and Roger A. Vesey. High-gain magnetized inertial fusion. *Physical Review Letters*, 108(2), 2012. 14, 15, 18

[11] S. A. Slutz, W. A. Stygar, M. R. Gomez, K. J. Peterson, A. B. Sefkow, D. B. Sinars, R. A. Vesey, E. M. Campbell, and R. Betti. Scaling magnetized liner inertial fusion on Z and future pulsed-power accelerators. *Physics of Plasmas*, 23(2):022702, 2 2016. 14, 138

[12] M. R. Gomez, S. A. Slutz, A. B. Sefkow, D. B. Sinars, K. D. Hahn, S. B. Hansen, E. C. Harding, P. F. Knapp, P. F. Schmit, C. A. Jennings, T. J. Awe, M. Geissel, D. C. Rovang, G. A. Chandler, G. W. Cooper, M. E. Cuneo, A. J. Harvey-Thompson, M. C. Herrmann, M. H. Hess, O. Johns, D. C. Lamppa, M. R. Martin, R. D. McBride, K. J. Peterson, J. L. Porter, G. K. Robertson, G. A. Rochau, C. L. Ruiz, M. E. Savage, I. C. Smith, W. A. Stygar, and R. A. Vesey. Experimental demonstration of fusion-relevant conditions in magnetized liner inertial fusion. *Physical Review Letters*, 113(15):1–5, 2014. 14, 15, 19

[13] Shuai Zhang, Kevin P Driver, François Soubiran, and Burkhard Militzer. First-principles equation of state and shock compression predictions of warm dense hydrocarbons. *Physical Review E*, 96(1):13204, 2017. 14

[14] Bruce A. Remington, R. Paul Drake, and Dmitri D. Ryutov. Experimental astrophysics with high power lasers and Z pinches. *Reviews of Modern Physics*, 78(3):755–807, 2006. 14

[15] G. Gregori, A. Ravasio, C. D. Murphy, K. Schaar, A. Baird, A. R. Bell, A. Benuzzi-Mounaix, R. Bingham, C. Constantin, R. P. Drake, M. Edwards, E. T. Everson, C. D. Gregory, Y. Kuramitsu, W. Lau, J. Mithen, C. Niemann, H.-S. Park, B. A. Remington, B. Reville, A. P. L. Robinson, D. D. Ryutov, Y. Sakawa, S. Yang, N. C. Woolsey, M. Koenig, and F. Miniati. Generation of scaled protogalactic seed magnetic fields in laser-produced shock waves. *Nature*, 481(7382):480–483, 1 2012. 14

[16] R Paul Drake. Introduction to High-Energy-Density Physics. In *High-Energy-Density Physics*, pages 1–17. Springer, 2006. 14, 15, 43

[17] Seth Root, Luke Shulenburger, Raymond W Lemke, Daniel H Dolan, Thomas R Mattsson, and Michael P Desjarlais. Shock Response and Phase Transitions of MgO at Planetary Impact Conditions. *Phys. Rev. Lett.*, 115(19):198501, 11 2015. 14

[18] S. H. Glenzer, D. H. Froula, L. Divol, M. Dorr, R. L. Berger, S. Dixit, B. A. Hammel, C. Haynam, J. A. Hittinger, J. P. Holder, O. S. Jones, D. H. Kalantar, O. L. Landen, A. B. Langdon, S. Langer, B. J. MacGowan, A. J. Mackinnon, N. Meezan, E. I. Moses, C. Niemann, C. H. Still, L. J. Suter, R. J. Wallace, E. A. Williams, and B. K. F. Young.

Experiments and multiscale simulations of laser propagation through ignition-scale plasmas. *Nature Physics*, 3(10):716–719, 10 2007. 14, 23

[19] L. J. Perkins, D. D.M. Ho, B. G. Logan, G. B. Zimmerman, M. A. Rhodes, D. J. Strozzi, D. T. Blackfield, and S. A. Hawkins. The potential of imposed magnetic fields for enhancing ignition probability and fusion energy yield in indirect-drive inertial confinement fusion. *Physics of Plasmas*, 24:062708, 2017. 15, 17, 21

[20] P. Y. Chang, G. Fiksel, M. Hohenberger, J. P. Knauer, R. Betti, F. J. Marshall, D. D. Meyerhofer, F. H. Séguin, and R. D. Petrasso. Fusion yield enhancement in magnetized laser-driven implosions. *Physical Review Letters*, 107:035006, 2011. 15, 17, 111

[21] D. S. Montgomery, B. J. Albright, D. H. Barnak, P. Y. Chang, J. R. Davies, G. Fiksel, D. H. Froula, J. L. Kline, M. J. MacDonald, A. B. Sefkow, L. Yin, and R. Betti. Use of external magnetic fields in hohlraum plasmas to improve laser-coupling. *Physics of Plasmas*, 22(1):010703, 1 2015. 15, 18

[22] S. I. Braginskii. Transport Processes in a Plasma. *Reviews of plasma physics*, 1:205, 1965. 15, 44, 46, 95, 99

[23] J R Davies, R Betti, P.-Y Chang, and G Fiksel. The importance of electrothermal terms in Ohm's law for magnetized spherical implosions. *Physics of Plasmas*, 22:112703, 2015. 15, 25, 52, 53

[24] A. Nishiguchi, T. Yabe, M. G. Haines, M. Psimopoulos, and H. Takewaki. Convective Amplification of Magnetic Fields in Laser-Produced Plasmas by the Nernst Effect. *Physical Review Letters*, 53(3):262–265, 7 1984. 15

[25] J. J. Bissell, C. P. Ridgers, and R. J. Kingham. Field Compressing Magnetothermal Instability in Laser Plasmas. *Physical Review Letters*, 105(17):175001, 10 2010. 16

[26] D A Tidman and R A Shanny. Field generating thermal instability in laser heated plasmas. *The Physics of Fluids*, 17(6):1207–1210, 1974. 16

[27] Martin Read. *Computational Studies of High Power Nanosecond Laser Propagation in Magnetised Plasmas*. PhD thesis, Imperial College London, 2016. 16, 51, 142

[28] I. V. Igumenshchev, A. B. Zylstra, C. K. Li, P. M. Nilson, V. N. Goncharov, and R. D. Petrasso. Self-generated magnetic fields in direct-drive implosion experiments. *Physics of Plasmas*, 21(6):062707, 6 2014. 16, 17

[29] W. A. Farmer, J. M. Koning, D. J. Strozzi, D. E. Hinkel, L. F. Berzak Hopkins, O. S. Jones, and M. D. Rosen. Simulation of self-generated magnetic fields in an inertial fusion hohlraum environment. *Physics of Plasmas*, 24(5):052703, 2017. 16, 111

[30] J. A. Stamper, K. Papadopoulos, R. N. Sudan, S. O. Dean, E. A. McLean, and J. M. Dawson. Spontaneous Magnetic Fields in Laser-Produced Plasmas. *Physical Review Letters*, 26(17):1012–1015, 4 1971. 16

[31] M. G. Haines. Thermal instability and magnetic field generated by large heat flow in a plasma, especially under laser-fusion conditions. *Physical Review Letters*, 47(13):917–920, 1981. 16

[32] C. A. Walsh, J. P. Chittenden, K. McGlinchey, N. P. L. Niasse, and B. D. Appelbe. Self-Generated Magnetic Fields in the Stagnation Phase of Indirect-Drive Implosions on the National Ignition Facility. *Physical Review Letters*, 118(15):155001, 4 2017. 16, 52, 138

[33] R. J. Kingham and A. R. Bell. Nonlocal Magnetic-Field Generation in Plasmas without Density Gradients. *Physical Review Letters*, 88(4):045004, 1 2002. 16, 114

[34] A. G R Thomas, R. J. Kingham, and C. P. Ridgers. Rapid self-magnetization of laser speckles in plasmas by nonlinear anisotropic instability. *New Journal of Physics*, 11, 2009. 16

[35] L. Lancia, C. Fourment, M. Nakatsutsumi, S. Hulin, S. Bastiani-Ceccotti, J. J. Santos, M. Gauthier, M. Rabec Le Gloahec, J. L. Feugeas, Ph Nicolaï, G. Schurtz, P. Audebert, J. Fuchs, and M. Migliorati. Measurements of self-generated magnetic fields influence on electron heat conduction in dense plasmas. *AIP Conference Proceedings*, 1209:55–58, 2010. 16

[36] M. J.-E. Manuel, C. K. Li, F. H. Séguin, J. Frenje, D. T. Casey, R. D. Petrasso, S. X. Hu, R. Betti, J. D. Hager, D. D. Meyerhofer, and V. A. Smalyuk. First Measurements of Rayleigh-Taylor-Induced Magnetic Fields in Laser-Produced Plasmas. *Physical Review Letters*, 108(25):255006, 6 2012. 16

[37] G. Gregori, S. H. Glenzer, J. Knight, C. Niemann, D. Price, D. H. Froula, M. J. Edwards, R. P. J. Town, A. Brantov, W. Rozmus, and V. Yu. Bychenkov. Effect of Nonlocal Transport on Heat-Wave Propagation. *Physical Review Letters*, 92(20):205006, 5 2004. 16, 25, 91

[38] D H Froula, L Divol, N B Meezan, S Dixit, P Neumayer, J D Moody, B B Pollock, J S Ross, L Suter, and S H Glenzer. Laser beam propagation through inertial confinement fusion hohlraum plasmas. *Physics of Plasmas*, 14(5):055705, 2007. 16, 56, 108, 119

[39] Hui-bo Tang, Guang-yue Hu, Yi-han Liang, Tao Tao, Yu-lin Wang, Peng Hu, Bin Zhao, and Jian Zheng. Confinement of laser plasma expansion with strong external magnetic field. *Plasma Physics and Controlled Fusion*, 60(5):055005, 5 2018. 16

[40] Shinsuke Fujioka, Zhe Zhang, Kazuhiro Ishihara, Keisuke Shigemori, Youichiro Hironaka, Tomoyuki Johzaki, Atsushi Sunahara, Naoji Yamamoto, Hideki

Nakashima, Tsuguhiro Watanabe, Hiroyuki Shiraga, Hiroaki Nishimura, and Hiroshi Azechi. Kilotesla Magnetic Field due to a Capacitor-Coil Target Driven by High Power Laser. *Scientific Reports*, 3(1):1170, 12 2013. 17, 23

[41] M. Hohenberger, P. Y. Chang, G. Fiksel, J. P. Knauer, R. Betti, F. J. Marshall, D. D. Meyerhofer, F. H. Séguin, and R. D. Petrasso. Inertial confinement fusion implosions with imposed magnetic field compression using the OMEGA Laser. *Physics of Plasmas*, 19(5):056306, 2012. 17, 20, 108, 111

[42] David J. Strozzi, L. J. Perkins, M. M. Marinak, D. J. Larson, J. M. Koning, and B. G. Logan. Imposed magnetic field and hot electron propagation in inertial fusion hohlraums. *Journal of Plasma Physics*, 81(06):475810603, 12 2015. 18, 22, 29, 111

[43] A B Sefkow, M S Wei, T Nagayama, E M Campbell, B E Blue, R F Heeter, J M Koning, K J Peterson, and A Schmitt. Laser propagation measurements in long-scale-length underdense plasmas relevant to magnetized liner inertial fusion. *Physical Review E*, 94(5):051201, 2016. 19, 24, 102

[44] A. J. Harvey-Thompson, A. B. Sefkow, T. N. Nagayama, M. S. Wei, E. M. Campbell, G. Fiksel, P. Y. Chang, J. R. Davies, D. H. Barnak, V. Y. Glebov, P. Fitzsimmons, J. Fooks, and B. E. Blue. Diagnosing laser-preheated magnetized plasmas relevant to magnetized liner inertial fusion. *Physics of Plasmas*, 22(12):122708, 2015. 19, 110, 112

[45] Stephen Jardin. *Computational Methods in Plasma Physics*. CRC Press, 2010. 21

[46] B. Fryxell, K. Olson, P. Ricker, F. X. Timmes, M. Zingale, D. Q. Lamb, P. MacNeice, R. Rosner, J. W. Truran, and H. Tufo. FLASH: An Adaptive Mesh Hydrodynamics Code for Modeling Astrophysical Thermonuclear Flashes. *The Astrophysical Journal Supplement Series*, 131(1):273–334, 11 2000. 21, 79, 82, 84

[47] Charles K Birdsall and A Bruce Langdon. *Plasma physics via computer simulation*. CRC press, 2004. 21

[48] A.G.R. Thomas, M. Tzoufras, A.P.L. Robinson, R.J. Kingham, C.P. Ridgers, M. Sherlock, and A.R. Bell. A review of Vlasov-Fokker-Planck numerical modeling of inertial confinement fusion plasma. *Journal of Computational Physics*, 231(3):1051–1079, 2 2012. 21

[49] M. Tzoufras, A.R. Bell, P.A. Norreys, and F.S. Tsung. A Vlasov–Fokker–Planck code for high energy density physics. *Journal of Computational Physics*, 230(17):6475–6494, 7 2011. 21, 26

[50] R. J. Kingham and A. R. Bell. An implicit Vlasov-Fokker-Planck code to model nonlocal electron transport in 2-D with magnetic fields. *Journal of Computational Physics*, 194:1, 2004. 21, 26, 115

[51] R. Sentis. Mathematical models for laser-plasma interaction. *ESAIM: Mathematical Modelling and Numerical Analysis*, 39(2):275–318, 2005. 22

[52] A. Colaïtis, G. Duchateau, P. Nicolaï, and V. Tikhonchuk. Towards modeling of nonlinear laser-plasma interactions with hydrocodes: The thick-ray approach. *Physical Review E - Statistical, Nonlinear, and Soft Matter Physics*, 89(3), 2014. 23, 25

[53] A. Bruce Langdon. Nonlinear Inverse Bremsstrahlung and Heated-Electron Distributions. *Physical Review Letters*, 44(9):575–579, 3 1980. 23, 28, 62

[54] J M Di Nicola, T Bond, M Bowers, L Chang, M Hermann, R House, T Lewis, K Manes, G Mennerat, B MacGowan, R Negres, B Olejniczak, C Orth, T Parham, S Rana, B Raymond, M Rever, S Schrauth, M Shaw, M Spaeth, B Van Wonterghem, W Williams, C Widmayer, S Yang, P Whitman, and P Wegner. The national ignition facility: laser performance status and performance quad results at elevated energy. *Nuclear Fusion*, 59(3):32004, 12 2018. 23

[55] J-L Miquel, C Lion, and P Vivini. The Laser Mega-Joule : {LMJ} & {PETAL} status and Program Overview. *Journal of Physics: Conference Series*, 688:12067, 3 2016. 23

[56] Dieter Biskamp. *Nonlinear magnetohydrodynamics*, volume 1. Cambridge University Press, 1997. 24

[57] William L. Kruer. *The physics of laser plasma interactions*. CRC Press, 2018. 24

[58] Martin Read, Robert Kingham, and John Bissell. The influence of magnetised electron transport on thermal self-focusing and channelling of nanosecond laser beams. In *Journal of Physics: Conference Series*, volume 717, page 12111. IOP Publishing, 2016. 24

[59] F. W. Perkins and E. J. Valeo. Thermal Self-Focusing of Electromagnetic Waves in Plasmas. *Physical Review Letters*, 32(22):1234–1237, 6 1974. 24, 30, 95

[60] P Kaw, G Schmidt, and T Wilcox. Filamentation and trapping of electromagnetic radiation in plasmas. *Physics of Fluids*, 16:1522, 1973. 25, 92

[61] Andrew J. Schmitt. The effects of optical smoothing techniques on filamentation in laser plasmas. *Physics of Fluids*, 31(10):3079–3101, 1988. 25

[62] R L Berger, B F Lasinski, T B Kaiser, E A Williams, and A B Langdon. Theory and three-dimensional in laser-produced plasma simulation of light filamentation. *Physics of Fluids B: Plasma Physics*, 5(7):2243–2258, 1993. 25, 63

[63] Milo R Dorr, F Xabier Garaizar, and Jeffrey A F Hittinger. Simulation of Laser Plasma Filamentation Using Adaptive Mesh Refinement. *Journal of Computational Physics*, 177:233–263, 2002. 25

[64] N.N. Demchenko, I.YA. Doskoch, S.YU. Gus'kov, P.A. Kuchugov, V.B. Rozanov, R.V. Stepanov, G.A. Vergunova, R.A. Yakhin, and N.V. Zmitrenko. Irradiation asymmetry effects on the direct drive targets compression for the megajoule laser facility. *Laser and Particle Beams*, 33(04):655–666, 2015. 25

[65] I. V. Igumenshchev, V. N. Goncharov, F. J. Marshall, J. P. Knauer, E. M. Campbell, C. J. Forrest, D. H. Froula, V. Yu Glebov, R. L. McCrory, S. P. Regan, T. C. Sangster, S. Skupsky, and C. Stoeckl. Three-dimensional modeling of direct-drive cryogenic implosions on OMEGA. *Physics of Plasmas*, 23(5), 2016. 25

[66] I. V. Igumenshchev, D. T. Michel, R. C. Shah, E. M. Campbell, R. Epstein, C. J. Forrest, V. Yu. Glebov, V. N. Goncharov, J. P. Knauer, F. J. Marshall, R. L. McCrory, S. P. Regan, T. C. Sangster, C. Stoeckl, A. J. Schmitt, and S. Obenschain. Three-dimensional hydrodynamic simulations of OMEGA implosions. *Physics of Plasmas*, 24(5):056307, 5 2017. 25

[67] C H Still, D E Hinkel, A B Langdon, J P Palastro, and E A Williams. Simulating NIF laser-plasma interaction with multiple SRS frequencies. *Journal of Physics: Conference Series*, 244(2):022025, 8 2010. 25

[68] Steven Langer, David Strozzi, Peter Amendt, Thomas Chapman, Laura Hopkins, Andrea Kritcher, and Scott Sepke. pF3D Simulations of SBS and SRS in NIF Hohlraum Experiments. In *APS Division of Plasma Physics Meeting*, 2016. 25

[69] D J Strozzi, D S Bailey, P Michel, L Divol, S M Sepke, G D Kerbel, C A Thomas, J E Ralph, J D Moody, and M B Schneider. Interplay of Laser-Plasma Interactions and Inertial Fusion Hydrodynamics. *Physical Review Letters*, 118(2):025002, 2017. 25

[70] A. R. Bell, R. G. Evans, and D. J. Nicholas. Elecron Energy Transport in Steep Temperature Gradients in Laser-Produced Plasmas. *Physical Review Letters*, 46(4):243–246, 1 1981. 25, 55

[71] A. R. Bell. Electron energy transport in ion waves and its relevance to laser-produced plasmas. *Physics of Fluids*, 26(1):279, 9 1983. 25, 27, 55

[72] J. R. Albritton. Laser Absorption and Heat Transport by Non-Maxwell-Boltzmann Electron Distributions. *Physical Review Letters*, 50(26):2078–2081, 6 1983. 25

[73] J. R. Albritton, E. A. Williams, I. B. Bernstein, and K. P. Swartz. Nonlocal Electron Heat Transport by Not Quite Maxwell-Boltzmann Distributions. *Physical Review Letters*, 57(15):1887–1890, 10 1986. 25

[74] A. R. Bell. Non-Spitzer heat flow in a steadily ablating laser-produced plasma. *Physics of Fluids*, 28(6):2007, 9 1985. 25, 55

[75] R. C. Malone, R. L. McCrory, and R. L. Morse. Indications of Strongly Flux-Limited Electron Thermal Conduction in Laser-Target Experiments. *Physical Review Letters*, 34(12):721–724, 3 1975. 25

[76] S. X. Hu, V. A. Smalyuk, V. N. Goncharov, S. Skupsky, T. C. Sangster, D. D. Meyerhofer, and D. Shvarts. Validation of Thermal-Transport Modeling with Direct-Drive, Planar-Foil Acceleration Experiments on OMEGA. *Physical Review Letters*, 101(5):055002, 7 2008. 25, 26

[77] D. T. Michel, A. K. Davis, V. N. Goncharov, T. C. Sangster, S. X. Hu, I. V. Igumenshchev, D. D. Meyerhofer, W. Seka, and D. H. Froula. Measurements of the Conduction-Zone Length and Mass Ablation Rate in Cryogenic Direct-Drive Implosions on OMEGA. *Physical Review Letters*, 114(15):155002, 4 2015. 25

[78] A R Bell, A P L Robinson, M Sherlock, R J Kingham, and W Rozmus. Fast electron transport in laser-produced plasmas and the KALOS code for solution of the Vlasov–Fokker–Planck equation. *Plasma Physics and Controlled Fusion*, 48(3):R37–R57, 3 2006. 26, 125, 144

[79] J. F. Luciani, P. Mora, and R. Pellat. Quasistatic heat front and delocalized heat flux. *Physics of Fluids*, 28(3):835, 6 1985. 26, 56

[80] E. M. Epperlein, G. J. Rickard, and A. R. Bell. Two-Dimensional Nonlocal Electron Transport in Laser-Produced Plasmas. *Physical Review Letters*, 61(21):2453–2456, 11 1988. 26

[81] E M Epperlein and R W Short. A practical nonlocal model for electron heat transport in laser plasmas. *Physics of Fluids B: Plasma Physics*, 3(3092), 1991. 26, 56, 99, 106

[82] E. M. Epperlein, R. W. Short, and A. Simon. Damping of ion-acoustic waves in the presence of electron-ion collisions. *Physical Review Letters*, 69(12):1765–1768, 9 1992. 27, 28, 32, 119, 124, 144

[83] Gregory W Hammett and Francis W Perkins. Fluid moment models for Landau damping with application to the ion-temperature-gradient instability. *Phys. Rev. Lett.*, 64(25):3019–3022, 6 1990. 27

[84] G. P. Schurtz, Ph. D. Nicolaï, and M. Busquet. A nonlocal electron conduction model for multidimensional radiation hydrodynamics codes. *Physics of Plasmas*, 7(10):4238, 9 2000. 26, 32, 119

[85] G. Schurtz, S. Gary, S. Hulin, C. Chenais-Popovics, J.-C. Gauthier, F. Thais, J. Breil, F. Durut, J.-L. Feugeas, P.-H. Maire, P. Nicolaï, O. Peyrusse, C. Reverdin, G. Soullié, V. Tikhonchuk, B. Villette, and C. Fourment. Revisiting Nonlocal Electron-Energy Transport in Inertial-Fusion Conditions. *Physical Review Letters*, 98(9):095002, 2 2007. 26, 32, 114

[86] D. Del Sorbo, J.-L. Feugeas, Ph. Nicolaï, M. Olazabal-Loumé, B. Dubroca, and V. Tikhonchuk. Extension of a reduced entropic model of electron transport to

magnetized nonlocal regimes of high-energy-density plasmas. *Laser and Particle Beams*, 34(03):412–425, 9 2016. 26

[87] Wallace Manheimer and Denis Colombant. Fokker Planck and Krook theory of energetic electron transport in a laser produced plasma. *Physics of Plasmas*, 22(9):092708, 9 2015. 26

[88] Wallace Manheimer, Denis Colombant, and Valeri Goncharov. The development of a Krook model for nonlocal transport in laser produced plasmas. I. Basic theory. *Physics of Plasmas*, 2008. 26

[89] Wallace Manheimer, Denis Colombant, and Valeri Goncharov. The development of a Krook model for nonlocal transport in laser produced plasmas. I. Basic theory. *Physics of Plasmas*, 15(8):083103, 8 2008. 26

[90] Ph. D. Nicolaï, J.-L. A. Feugeas, and G. P. Schurtz. A practical nonlocal model for heat transport in magnetized laser plasmas. *Physics of Plasmas*, 13(3):032701, 3 2006. 26, 32, 119

[91] M. Sherlock, J. P. Brodrick, and C. P. Ridgers. A comparison of non-local electron transport models for laser-plasmas relevant to inertial confinement fusion. *Physics of Plasmas*, 24(8):082706, 8 2017. 26

[92] A. Marocchino, M. Tzoufras, S. Atzeni, A. Schiavi, Ph. D. Nicolaï, J. Mallet, V. Tikhonchuk, and J.-L. Feugeas. Comparison for non-local hydrodynamic thermal conduction models. *Physics of Plasmas*, 20(2):022702, 2 2013. 26

[93] J. P. Brodrick, R. J. Kingham, M. M. Marinak, M. V. Patel, A. V. Chankin, J. T. Omotani, M. V. Umansky, D. Del Sorbo, B. Dudson, J. T. Parker, G. D. Kerbel, M. Sherlock, and C. P. Ridgers. Testing nonlocal models of electron thermal conduction for magnetic and inertial confinement fusion applications. *Physics of Plasmas*, 24(9):092309, 9 2017. 26, 114, 115

[94] Jeong-Young Ji, Eric D. Held, and Carl R. Sovinec. Moment approach to deriving parallel heat flow for general collisionality. *Physics of Plasmas*, 16(2):022312, 2 2009. 26

[95] A. M. Dimits, I. Joseph, and M. V. Umansky. A fast non-Fourier method for Landau-fluid operators. *Physics of Plasmas*, 21(5):055907, 5 2014. 26

[96] J.-L. Feugeas, Ph. Nicolaï, X. Ribeyre, G. Schurtz, V. Tikhonchuk, and M. Grech. Modeling of two-dimensional effects in hot spot relaxation in laser-produced plasmas. *Physics of Plasmas*, 15(6):062701, 6 2008. 27

[97] E. M. Epperlein and R. W. Short. Nonlocal heat transport effects on the filamentation of light in plasmas. *Physics of Fluids B: Plasma Physics*, 4(7):2211–2216, 3 1992. 27, 31, 92, 114, 115

[98] E. M. Epperlein. Kinetic theory of laser filamentation in plasmas. *Physical Review Letters*, 65(17):2145–2148, 10 1990. 27, 28, 31, 106, 114

[99] E. M. Epperlein. Kinetic simulations of laser filamentation in plasmas. *Physics of Fluids B: Plasma Physics*, 3(11):3082–3086, 11 1991. 27, 114

[100] V. Yu. Bychenkov, W. Rozmus, V. T. Tikhonchuk, and A. V. Brantov. Nonlocal Electron Transport in a Plasma. *Physical Review Letters*, 75(24):4405–4408, 12 1995. 28, 32, 119, 122, 144

[101] C. P. Ridgers, R. J. Kingham, and A. G. R. Thomas. Magnetic Cavitation and the Reemergence of Nonlocal Transport in Laser Plasmas. *Physical Review Letters*, 100(7):075003, 2 2008. 28, 56, 114

[102] T. H. Kho and M. G. Haines. Nonlinear Kinetic Transport of Electrons and Magnetic Field in Laser-Produced Plasmas. *Physical Review Letters*, 55(8):825–828, 8 1985. 28

[103] T. H. Kho and M. G. Haines. Nonlinear electron transport in magnetized laser plasmas. *Physics of Fluids*, 29(8):2665, 9 1986. 28

[104] A. S. Joglekar, C. P. Ridgers, R. J. Kingham, and A. G.R. Thomas. Kinetic modeling of Nernst effect in magnetized hohlraums. *Physical Review E*, 93(4):043206, 2016. 29, 108, 114

[105] W. A. Farmer, O. S. Jones, M. A. Barrios, D. J. Strozzi, J. M. Koning, G. D. Kerbel, D. E. Hinkel, J. D. Moody, L. J. Suter, D. A. Liedahl, N. Lemos, D. C. Eder, R. L. Kauffman, O. L. Landen, A. S. Moore, and M. B. Schneider. Heat transport modeling of the dot spectroscopy platform on NIF. *Plasma Physics and Controlled Fusion*, 60(4):044009, 4 2018. 29

[106] D W Hill and R J Kingham. Enhancement of pressure perturbations in ablation due to kinetic magnetized transport effects under direct-drive inertial confinement fusion relevant conditions. *Phys. Rev. E*, 98(2):21201(R), 8 2018. 29, 138

[107] A. V. Brantov, V. Yu Bychenkov, W. Rozmus, C. E. Capjack, and R. Sydora. Linear theory of nonlocal transport in a magnetized plasma. *Physics of Plasmas*, 10(12):4633, 2003. 29, 30, 32, 114, 139

[108] B. K. Frolov, S. I. Krasheninnikov, R. J. Kingham, and J. Edwards. Heat flux calculation in the semi-collisionless regime for substantial temperature variations including magnetic field. *New Journal of Physics*, 2006. 29

[109] J P Brodrick, M Sherlock, W A Farmer, A S Joglekar, R Barrois, J Wengraf, J J Bissell, R J Kingham, Del Sorbo, M P Read, and C P Ridgers. Incorporating kinetic effects on Nernst advection in inertial fusion simulations. *Plasma Physics and Controlled Fusion*, 60(15):084009, 2018. 29, 52

[110] M G Haines. Heat flux effects in Ohm's law. *Plasma Physics and Controlled Fusion*, 28(11):1705–1716, 11 1986. 29

[111] E M Epperlein and M G Haines. Plasma transport coefficients in a magnetic field by direct numerical solution of the Fokker – Planck equation. *Physics of Fluids*, 29:1029, 1986. 30, 49, 50, 99, 120, 133, 147

[112] H. C. Watkins and R. J. Kingham. Magnetised thermal self-focusing and filamentation of long-pulse lasers in plasmas relevant to magnetised ICF experiments. *Physics of Plasmas*, 25(9):092701, 9 2018. 31, 91, 100, 101, 102, 108, 109, 110, 113, 116, 117, 118

[113] Thomas James Morrow Boyd and Jeffrey John Sanderson. *The physics of plasmas*. Cambridge University Press, 2003. 44, 47

[114] Per Helander and Dieter J Sigmar. *Collisional transport in magnetized plasmas*, volume 4. Cambridge University Press, 2005. 44, 45, 46, 47, 51, 121

[115] J. J. Bissell, C. P. Ridgers, and R. J. Kingham. Super-Gaussian transport theory and the field-generating thermal instability in laser-plasmas. *New Journal of Physics*, 2013. 52, 75, 82, 84

[116] A Schlüter. Über den Ursprung der Magnetfelder auf Sternen und im interstellaren Raum. *Zeitschrift für Naturforschung A*, 5(2):65–71, 1950. 53

[117] P M Nilson, Louise Willingale, M C Kaluza, C Kamperidis, S Minardi, M S Wei, P Fernandes, M Notley, S Bandyopadhyay, and M Sherlock. Magnetic reconnection and plasma dynamics in two-beam laser-solid interactions. *Physical review letters*, 97(25):255001, 2006. 53

[118] Issie Peter Shkarofsky, Tudor Wyatt Johnston, and Morrel Paul Bachynski. *The particle kinetics of plasmas*. Reading, Mass.: Addison-Wesley Publishing Company, 1966. 55

[119] M. G. Haines. Laser-Plasma Interactions 4. In *Proceedings of the Scottish Universities Summer School*, 1979. 56

[120] Guang S He. *Nonlinear optics and photonics*. OUP Oxford, 2014. 60, 88, 93, 94

[121] William L. Kruer. Interaction of plasmas with intense lasers. *Physics of Plasmas*, 7(6):2270, 2000. 61, 63, 65

[122] James F Drake, Predhiman K Kaw, Yee-Chun Lee, G Schmid, Chuan S Liu, and Marshall N Rosenbluth. Parametric instabilities of electromagnetic waves in plasmas. *The Physics of Fluids*, 17(4):778–785, 1974. 63

[123] D W Forslund, J M Kindel, and E L Lindman. Theory of stimulated scattering processes in laser-irradiated plasmas. *The Physics of Fluids*, 18(8):1002–1016, 1975. 63

[124] William H Press, Saul a Teukolsky, William T Vetterling, and Brian P Flannery. *Numerical Recipes 3rd Edition: The Art of Scientific Computing*. 2007. 68, 69, 70, 77

[125] D. A. Knoll and David E. Keyes. Jacobian-free Newton-Krylov methods: A survey of approaches and applications. *Journal of Computational Physics*, 193(2):357–397, 2004. 69

[126] Satish Balay, Shrirang Abhyankar, Mark F. Adams, Jed Brown, Peter Brune, Kris Buschelman, Lisandro Dalcin, Victor Eijkhout, William D. Gropp, Dinesh Kaushik, Matthew G. Knepley, Lois Curfman McInnes, Karl Rupp, Barry F. Smith, Stefano Zampini, Hong Zhang, and Hong Zhang. {PETS}c Users Manual. Technical Report ANL-95/11 - Revision 3.7, Argonne National Laboratory, 2016. 70, 75

[127] Kristopher McGlinchey. *Radiation Hydrodynamic Simulations of the Impact of Instabilities and Asymmetries on Inertial Confinement Fusion*. PhD thesis, Imperial College London, 2017. 79

[128] T H Stix. *Waves in Plasmas*. Springer Science & Business Media, 1992. 80

[129] Steven A. Orszag and Cha-Mei Tang. Small-scale structure of two-dimensional magnetohydrodynamic turbulence. *Journal of Fluid Mechanics*, 90(01):129, 1 1979. 82

[130] D. H. Froula, J. S. Ross, B. B. Pollock, P. Davis, A. N. James, L. Divol, M. J. Edwards, A. A. Offenberger, D. Price, R. P.J. Town, G. R. Tynan, and S. H. Glenzer. Quenching of the nonlocal electron heat transport by large external magnetic fields in a laser-produced plasma measured with imaging Thomson scattering. *Physical Review Letters*, 98(13):135001, 2007. 91, 138

[131] P L Kelley. Self-focusing of optical beams. *Physical Review Letters*, 15(26):1005, 1965. 92

[132] H A Baldis, D S Montgomery, J D Moody, C Labaune, S H Batha, K G Estabrook, R L Berger, and W L Kruer. Parametric instabilities in large nonuniform laser plasmas. *Plasma Physics and Controlled Fusion*, 34(13):2077–2081, 12 1992. 92

[133] A. V. Brantov, V. Yu. Bychenkov, W. Rozmus, and C. E. Capjack. Kinetic Susceptibility and Transport Theory of Collisional Plasmas. *Physical Review Letters*, 93(12):125002, 9 2004. 119

[134] E. M. Epperlein. Effect of electron collisions on ion-acoustic waves and heat flow. *Physics of Plasmas*, 1(1):109–115, 1 1994. 119

[135] Donald Gary Swanson. *Plasma kinetic theory*. CRC Press, 2008. 120

[136] E M Epperlein. The accuracy of Braginskii's transport coefficients for a Lorentz plasma. *J. Phys. D: Appl. Phys.*, 17(17):1823–1827, 1986. 120, 127, 133

[137] S. Brunner, E. Valeo, and J. A. Krommes. Linear delta- f simulations of nonlocal electron heat transport. *Physics of Plasmas*, 7(7):2810–2823, 7 2000. 128

[138] A V Brantov, V Yu Bychenkov, V T Tikhonchuk, and W Rozmus. Nonlocal plasma electron hydrodynamics. Technical Report 96, 1996. 138

SPRINGER NATURE LICENSE TERMS AND CONDITIONS

Jul 11, 2019

This Agreement between Imperial College London -- HENRY WATKINS ("You") and Springer Nature ("Springer Nature") consists of your license details and the terms and conditions provided by Springer Nature and Copyright Clearance Center.

License Number	4625980028969
License date	Jul 11, 2019
Licensed Content Publisher	Springer Nature
Licensed Content Publication	Nature Physics
Licensed Content Title	Inertial-confinement fusion with lasers
Licensed Content Author	R. Betti, O. A. Hurricane
Licensed Content Date	May 3, 2016
Licensed Content Volume	12
Licensed Content Issue	5
Type of Use	Thesis/Dissertation
Requestor type	academic/university or research institute
Format	print and electronic
Portion	figures/tables/illustrations
Number of figures/tables/illustrations	1
High-res required	no
Will you be translating?	no
Circulation/distribution	<501
Author of this Springer Nature content	no
Title	Studies of Magnetised and Non-local Transport in Laser-Plasma Interactions
Institution name	n/a
Expected presentation date	Jul 2019
Portions	Illustration of direct and indirect inertial confinement fusion targets
Requestor Location	Imperial College London Accounts Payable Level 3, Sherfield Building Exhibition Road London, other SW7 2AZ United Kingdom Attn: Imperial College London
Total	0.00 GBP

Terms and Conditions

Springer Nature Customer Service Centre GmbH Terms and Conditions

This agreement sets out the terms and conditions of the licence (the **Licence**) between you and **Springer Nature Customer Service Centre GmbH** (the **Licensor**). By clicking 'accept' and completing the transaction for the material (**Licensed Material**), you also confirm your acceptance of these terms and conditions.

1. Grant of License

1. 1. The Licensor grants you a personal, non-exclusive, non-transferable, world-wide licence to reproduce the Licensed Material for the purpose specified in your order only. Licences are granted for the specific use requested in the order and for no other use, subject to the conditions below.

1. 2. The Licensor warrants that it has, to the best of its knowledge, the rights to license reuse of the Licensed Material. However, you should ensure that the material you are requesting is original to the Licensor and does not carry the copyright of another entity (as credited in the published version).

1. 3. If the credit line on any part of the material you have requested indicates that it was reprinted or adapted with permission from another source, then you should also seek permission from that source to reuse the material.

2. Scope of Licence

2. 1. You may only use the Licensed Content in the manner and to the extent permitted by these Ts&Cs and any applicable laws.

2. 2. A separate licence may be required for any additional use of the Licensed Material, e.g. where a licence has been purchased for print only use, separate permission must be obtained for electronic re-use. Similarly, a licence is only valid in the language selected and does not apply for editions in other languages unless additional translation rights have been granted separately in the licence. Any content owned by third parties are expressly excluded from the licence.

2. 3. Similarly, rights for additional components such as custom editions and derivatives require additional permission and may be subject to an additional fee. Please apply to Journalpermissions@springernature.com/bookpermissions@springernature.com for these rights.

2. 4. Where permission has been granted **free of charge** for material in print, permission may also be granted for any electronic version of that work, provided that the material is incidental to your work as a whole and that the electronic version is essentially equivalent to, or substitutes for, the print version.

2. 5. An alternative scope of licence may apply to signatories of the STM Permissions Guidelines, as amended from time to time.

3. Duration of Licence

3. 1. A licence for is valid from the date of purchase ('Licence Date') at the end of the relevant period in the below table:

Scope of Licence	Duration of Licence
Post on a website	12 months
Presentations	12 months
Books and journals	Lifetime of the edition in the language purchased

4. Acknowledgement

4. 1. The Licensor's permission must be acknowledged next to the Licenced Material in print. In electronic form, this acknowledgement must be visible at the same time as the

figures/tables/illustrations or abstract, and must be hyperlinked to the journal/book's homepage. Our required acknowledgement format is in the Appendix below.

5. Restrictions on use

5. 1. Use of the Licensed Material may be permitted for incidental promotional use and minor editing privileges e.g. minor adaptations of single figures, changes of format, colour and/or style where the adaptation is credited as set out in Appendix 1 below. Any other changes including but not limited to, cropping, adapting, omitting material that affect the meaning, intention or moral rights of the author are strictly prohibited.

5. 2. You must not use any Licensed Material as part of any design or trademark.

5. 3. Licensed Material may be used in Open Access Publications (OAP) before publication by Springer Nature, but any Licensed Material must be removed from OAP sites prior to final publication.

6. Ownership of Rights

6. 1. Licensed Material remains the property of either Licensor or the relevant third party and any rights not explicitly granted herein are expressly reserved.

7. Warranty

IN NO EVENT SHALL LICENSOR BE LIABLE TO YOU OR ANY OTHER PARTY OR ANY OTHER PERSON OR FOR ANY SPECIAL, CONSEQUENTIAL, INCIDENTAL OR INDIRECT DAMAGES, HOWEVER CAUSED, ARISING OUT OF OR IN CONNECTION WITH THE DOWNLOADING, VIEWING OR USE OF THE MATERIALS REGARDLESS OF THE FORM OF ACTION, WHETHER FOR BREACH OF CONTRACT, BREACH OF WARRANTY, TORT, NEGLIGENCE, INFRINGEMENT OR OTHERWISE (INCLUDING, WITHOUT LIMITATION, DAMAGES BASED ON LOSS OF PROFITS, DATA, FILES, USE, BUSINESS OPPORTUNITY OR CLAIMS OF THIRD PARTIES), AND
WHETHER OR NOT THE PARTY HAS BEEN ADVISED OF THE POSSIBILITY OF SUCH DAMAGES. THIS LIMITATION SHALL APPLY NOTWITHSTANDING ANY FAILURE OF ESSENTIAL PURPOSE OF ANY LIMITED REMEDY PROVIDED HEREIN.

8. Limitations

8. 1. ***BOOKS ONLY:***Where **'reuse in a dissertation/thesis'** has been selected the following terms apply: Print rights of the final author's accepted manuscript (for clarity, NOT the published version) for up to 100 copies, electronic rights for use only on a personal website or institutional repository as defined by the Sherpa guideline (www.sherpa.ac.uk/romeo/).

9. Termination and Cancellation

9. 1. Licences will expire after the period shown in Clause 3 (above).

9. 2. Licensee reserves the right to terminate the Licence in the event that payment is not received in full or if there has been a breach of this agreement by you.

Appendix 1 — Acknowledgements:

For Journal Content:
Reprinted by permission from [**the Licensor**]: [**Journal Publisher** (e.g. Nature/Springer/Palgrave)] [**JOURNAL NAME**] [**REFERENCE CITATION** (Article name, Author(s) Name), [**COPYRIGHT**] (year of publication)

For **Advance Online Publication papers:**
Reprinted by permission from [**the Licensor**]: [**Journal Publisher** (e.g. Nature/Springer/Palgrave)] [**JOURNAL NAME**] [**REFERENCE CITATION** (Article name, Author(s) Name), [**COPYRIGHT**] (year of publication), advance online publication, day month year (doi: 10.1038/sj.[JOURNAL ACRONYM].)

For Adaptations/Translations:
Adapted/Translated by permission from [**the Licensor**]: [**Journal Publisher** (e.g. Nature/Springer/Palgrave)] [**JOURNAL NAME**] [**REFERENCE CITATION** (Article name, Author(s) Name), [**COPYRIGHT**] (year of publication)

Note: For any republication from the British Journal of Cancer, the following credit line style applies:

Reprinted/adapted/translated by permission from [**the Licensor**]: on behalf of Cancer Research UK: : [**Journal Publisher** (e.g. Nature/Springer/Palgrave)] [**JOURNAL NAME**] [**REFERENCE CITATION** (Article name, Author(s) Name), [**COPYRIGHT]** (year of publication)

For **Advance Online Publication** papers:
Reprinted by permission from The [**the Licensor**]: on behalf of Cancer Research UK: [**Journal Publisher** (e.g. Nature/Springer/Palgrave)] [**JOURNAL NAME**] [**REFERENCE CITATION** (Article name, Author(s) Name), [**COPYRIGHT**] (year of publication), advance online publication, day month year (doi: 10.1038/sj.[JOURNAL ACRONYM])

For Book content:
Reprinted/adapted by permission from [**the Licensor**]: [**Book Publisher** (e.g. Palgrave Macmillan, Springer etc) [**Book Title**] by [**Book author**(s)] [**COPYRIGHT**] (year of publication)

Other Conditions:

Version 1.2

AIP PUBLISHING LICENSE TERMS AND CONDITIONS

Jul 11, 2019

This Agreement between Imperial College London -- HENRY WATKINS ("You") and AIP Publishing ("AIP Publishing") consists of your license details and the terms and conditions provided by AIP Publishing and Copyright Clearance Center.

License Number	4625970985932
License date	Jul 11, 2019
Licensed Content Publisher	AIP Publishing
Licensed Content Publication	Physics of Plasmas
Licensed Content Title	Kinetic simulations of laser filamentation in plasmas
Licensed Content Author	E. M. Epperlein
Licensed Content Date	Nov 1, 1991
Licensed Content Volume	3
Licensed Content Issue	11
Type of Use	Thesis/Dissertation
Requestor type	Student
Format	Print and electronic
Portion	Figure/Table
Number of figures/tables	1
Title of your thesis / dissertation	Studies of Magnetised and Non-local Transport in Laser-Plasma Interactions
Expected completion date	Jul 2019
Estimated size (number of pages)	150
Requestor Location	Imperial College London Accounts Payable Level 3, Sherfield Building Exhibition Road London, other SW7 2AZ United Kingdom Attn: Imperial College London
Total	0.00 GBP

Terms and Conditions

AIP Publishing -- Terms and Conditions: Permissions Uses

AIP Publishing hereby grants to you the non-exclusive right and license to use and/or distribute the Material according to the use specified in your order, on a one-time basis, for the specified term, with a maximum distribution equal to the number that you have ordered. Any links or other content accompanying the Material are not the subject of this license.

1. You agree to include the following copyright and permission notice with the reproduction of the Material:"Reprinted from [FULL CITATION], with the permission of AIP Publishing." For an article, the credit line and permission notice must be printed on the first page of the article or book chapter. For photographs, covers, or tables, the notice may appear with the Material, in a footnote, or in the reference list.
2. If you have licensed reuse of a figure, photograph, cover, or table, it is your responsibility to ensure that the material is original to AIP Publishing and does not contain the copyright of another entity, and that the copyright notice of the figure, photograph, cover, or table does not indicate that it was reprinted by AIP Publishing, with permission, from another source. Under no circumstances does AIP Publishing purport or intend to grant permission

to reuse material to which it does not hold appropriate rights.
You may not alter or modify the Material in any manner. You may translate the Material into another language only if you have licensed translation rights. You may not use the Material for promotional purposes.

3. The foregoing license shall not take effect unless and until AIP Publishing or its agent, Copyright Clearance Center, receives the Payment in accordance with Copyright Clearance Center Billing and Payment Terms and Conditions, which are incorporated herein by reference.
4. AIP Publishing or Copyright Clearance Center may, within two business days of granting this license, revoke the license for any reason whatsoever, with a full refund payable to you. Should you violate the terms of this license at any time, AIP Publishing, or Copyright Clearance Center may revoke the license with no refund to you. Notice of such revocation will be made using the contact information provided by you. Failure to receive such notice will not nullify the revocation.
5. AIP Publishing makes no representations or warranties with respect to the Material. You agree to indemnify and hold harmless AIP Publishing, and their officers, directors, employees or agents from and against any and all claims arising out of your use of the Material other than as specifically authorized herein.
6. The permission granted herein is personal to you and is not transferable or assignable without the prior written permission of AIP Publishing. This license may not be amended except in a writing signed by the party to be charged.
7. If purchase orders, acknowledgments or check endorsements are issued on any forms containing terms and conditions which are inconsistent with these provisions, such inconsistent terms and conditions shall be of no force and effect. This document, including the CCC Billing and Payment Terms and Conditions, shall be the entire agreement between the parties relating to the subject matter hereof.

This Agreement shall be governed by and construed in accordance with the laws of the State of New York. Both parties hereby submit to the jurisdiction of the courts of New York County for purposes of resolving any disputes that may arise hereunder.

V1.2

Questions? customercare@copyright.com or +1-855-239-3415 (toll free in the US) or +1-978-646-2777.

AIP PUBLISHING LICENSE TERMS AND CONDITIONS

Jul 11, 2019

This Agreement between Imperial College London -- HENRY WATKINS ("You") and AIP Publishing ("AIP Publishing") consists of your license details and the terms and conditions provided by AIP Publishing and Copyright Clearance Center.

License Number	4625970918141
License date	Jul 11, 2019
Licensed Content Publisher	AIP Publishing
Licensed Content Publication	Physics of Plasmas
Licensed Content Title	Linear theory of nonlocal transport in a magnetized plasma
Licensed Content Author	A. V. Brantov, V. Yu. Bychenkov, W. Rozmus, et al
Licensed Content Date	Dec 1, 2003
Licensed Content Volume	10
Licensed Content Issue	12
Type of Use	Thesis/Dissertation
Requestor type	Student
Format	Print and electronic
Portion	Figure/Table
Number of figures/tables	1
Title of your thesis / dissertation	Studies of Magnetised and Non-local Transport in Laser-Plasma Interactions
Expected completion date	Jul 2019
Estimated size (number of pages)	150
Requestor Location	Imperial College London Accounts Payable Level 3, Sherfield Building Exhibition Road London, other SW7 2AZ United Kingdom Attn: Imperial College London
Total	0.00 GBP

Terms and Conditions

AIP Publishing -- Terms and Conditions: Permissions Uses

AIP Publishing hereby grants to you the non-exclusive right and license to use and/or distribute the Material according to the use specified in your order, on a one-time basis, for the specified term, with a maximum distribution equal to the number that you have ordered. Any links or other content accompanying the Material are not the subject of this license.

1. You agree to include the following copyright and permission notice with the reproduction of the Material:"Reprinted from [FULL CITATION], with the permission of AIP Publishing." For an article, the credit line and permission notice must be printed on the first page of the article or book chapter. For photographs, covers, or tables, the notice may appear with the Material, in a footnote, or in the reference list.
2. If you have licensed reuse of a figure, photograph, cover, or table, it is your responsibility to ensure that the material is original to AIP Publishing and does not contain the copyright of another entity, and that the copyright notice of the figure, photograph, cover, or table does not indicate that it was reprinted by AIP Publishing, with permission, from another source. Under no circumstances does AIP Publishing purport or intend to grant permission

to reuse material to which it does not hold appropriate rights.
You may not alter or modify the Material in any manner. You may translate the Material into another language only if you have licensed translation rights. You may not use the Material for promotional purposes.

3. The foregoing license shall not take effect unless and until AIP Publishing or its agent, Copyright Clearance Center, receives the Payment in accordance with Copyright Clearance Center Billing and Payment Terms and Conditions, which are incorporated herein by reference.
4. AIP Publishing or Copyright Clearance Center may, within two business days of granting this license, revoke the license for any reason whatsoever, with a full refund payable to you. Should you violate the terms of this license at any time, AIP Publishing, or Copyright Clearance Center may revoke the license with no refund to you. Notice of such revocation will be made using the contact information provided by you. Failure to receive such notice will not nullify the revocation.
5. AIP Publishing makes no representations or warranties with respect to the Material. You agree to indemnify and hold harmless AIP Publishing, and their officers, directors, employees or agents from and against any and all claims arising out of your use of the Material other than as specifically authorized herein.
6. The permission granted herein is personal to you and is not transferable or assignable without the prior written permission of AIP Publishing. This license may not be amended except in a writing signed by the party to be charged.
7. If purchase orders, acknowledgments or check endorsements are issued on any forms containing terms and conditions which are inconsistent with these provisions, such inconsistent terms and conditions shall be of no force and effect. This document, including the CCC Billing and Payment Terms and Conditions, shall be the entire agreement between the parties relating to the subject matter hereof.

This Agreement shall be governed by and construed in accordance with the laws of the State of New York. Both parties hereby submit to the jurisdiction of the courts of New York County for purposes of resolving any disputes that may arise hereunder.

V1.2

Questions? customercare@copyright.com or +1-855-239-3415 (toll free in the US) or +1-978-646-2777.

AIP PUBLISHING LICENSE TERMS AND CONDITIONS

Jul 11, 2019

This Agreement between Imperial College London -- HENRY WATKINS ("You") and AIP Publishing ("AIP Publishing") consists of your license details and the terms and conditions provided by AIP Publishing and Copyright Clearance Center.

License Number	4625970850501
License date	Jul 11, 2019
Licensed Content Publisher	AIP Publishing
Licensed Content Publication	Physics of Plasmas
Licensed Content Title	The potential of imposed magnetic fields for enhancing ignition probability and fusion energy yield in indirect-drive inertial confinement fusion
Licensed Content Author	L. J. Perkins, D. D.-M Ho, B. G. Logan, et al
Licensed Content Date	Jun 1, 2017
Licensed Content Volume	24
Licensed Content Issue	6
Type of Use	Thesis/Dissertation
Requestor type	Student
Format	Print and electronic
Portion	Figure/Table
Number of figures/tables	1
Title of your thesis / dissertation	Studies of Magnetised and Non-local Transport in Laser-Plasma Interactions
Expected completion date	Jul 2019
Estimated size (number of pages)	150
Requestor Location	Imperial College London Accounts Payable Level 3, Sherfield Building Exhibition Road London, other SW7 2AZ United Kingdom Attn: Imperial College London
Total	0.00 GBP

Terms and Conditions

AIP Publishing -- Terms and Conditions: Permissions Uses

AIP Publishing hereby grants to you the non-exclusive right and license to use and/or distribute the Material according to the use specified in your order, on a one-time basis, for the specified term, with a maximum distribution equal to the number that you have ordered. Any links or other content accompanying the Material are not the subject of this license.

1. You agree to include the following copyright and permission notice with the reproduction of the Material:"Reprinted from [FULL CITATION], with the permission of AIP Publishing." For an article, the credit line and permission notice must be printed on the first page of the article or book chapter. For photographs, covers, or tables, the notice may appear with the Material, in a footnote, or in the reference list.
2. If you have licensed reuse of a figure, photograph, cover, or table, it is your responsibility to ensure that the material is original to AIP Publishing and does not contain the copyright of another entity, and that the copyright notice of the figure, photograph, cover, or table

does not indicate that it was reprinted by AIP Publishing, with permission, from another source. Under no circumstances does AIP Publishing purport or intend to grant permission to reuse material to which it does not hold appropriate rights.
You may not alter or modify the Material in any manner. You may translate the Material into another language only if you have licensed translation rights. You may not use the Material for promotional purposes.

3. The foregoing license shall not take effect unless and until AIP Publishing or its agent, Copyright Clearance Center, receives the Payment in accordance with Copyright Clearance Center Billing and Payment Terms and Conditions, which are incorporated herein by reference.
4. AIP Publishing or Copyright Clearance Center may, within two business days of granting this license, revoke the license for any reason whatsoever, with a full refund payable to you. Should you violate the terms of this license at any time, AIP Publishing, or Copyright Clearance Center may revoke the license with no refund to you. Notice of such revocation will be made using the contact information provided by you. Failure to receive such notice will not nullify the revocation.
5. AIP Publishing makes no representations or warranties with respect to the Material. You agree to indemnify and hold harmless AIP Publishing, and their officers, directors, employees or agents from and against any and all claims arising out of your use of the Material other than as specifically authorized herein.
6. The permission granted herein is personal to you and is not transferable or assignable without the prior written permission of AIP Publishing. This license may not be amended except in a writing signed by the party to be charged.
7. If purchase orders, acknowledgments or check endorsements are issued on any forms containing terms and conditions which are inconsistent with these provisions, such inconsistent terms and conditions shall be of no force and effect. This document, including the CCC Billing and Payment Terms and Conditions, shall be the entire agreement between the parties relating to the subject matter hereof.

This Agreement shall be governed by and construed in accordance with the laws of the State of New York. Both parties hereby submit to the jurisdiction of the courts of New York County for purposes of resolving any disputes that may arise hereunder.

V1.2

Questions? customercare@copyright.com or +1-855-239-3415 (toll free in the US) or +1-978-646-2777.

AIP PUBLISHING LICENSE TERMS AND CONDITIONS

Jul 11, 2019

This Agreement between Imperial College London -- HENRY WATKINS ("You") and AIP Publishing ("AIP Publishing") consists of your license details and the terms and conditions provided by AIP Publishing and Copyright Clearance Center.

License Number	4625970524184
License date	Jul 11, 2019
Licensed Content Publisher	AIP Publishing
Licensed Content Publication	Physics of Plasmas
Licensed Content Title	Inertial confinement fusion implosions with imposed magnetic field compression using the OMEGA Laser
Licensed Content Author	M. Hohenberger, P.-Y. Chang, G. Fiksel, et al
Licensed Content Date	May 1, 2012
Licensed Content Volume	19
Licensed Content Issue	5
Type of Use	Thesis/Dissertation
Requestor type	Student
Format	Print and electronic
Portion	Figure/Table
Number of figures/tables	1
Title of your thesis / dissertation	Studies of Magnetised and Non-local Transport in Laser-Plasma Interactions
Expected completion date	Jul 2019
Estimated size (number of pages)	150
Requestor Location	Imperial College London Accounts Payable Level 3, Sherfield Building Exhibition Road London, other SW7 2AZ United Kingdom Attn: Imperial College London
Total	0.00 GBP

Terms and Conditions

AIP Publishing -- Terms and Conditions: Permissions Uses

AIP Publishing hereby grants to you the non-exclusive right and license to use and/or distribute the Material according to the use specified in your order, on a one-time basis, for the specified term, with a maximum distribution equal to the number that you have ordered. Any links or other content accompanying the Material are not the subject of this license.

1. You agree to include the following copyright and permission notice with the reproduction of the Material:"Reprinted from [FULL CITATION], with the permission of AIP Publishing." For an article, the credit line and permission notice must be printed on the first page of the article or book chapter. For photographs, covers, or tables, the notice may appear with the Material, in a footnote, or in the reference list.
2. If you have licensed reuse of a figure, photograph, cover, or table, it is your responsibility to ensure that the material is original to AIP Publishing and does not contain the copyright of another entity, and that the copyright notice of the figure, photograph, cover, or table does not indicate that it was reprinted by AIP Publishing, with permission, from another

source. Under no circumstances does AIP Publishing purport or intend to grant permission to reuse material to which it does not hold appropriate rights.
You may not alter or modify the Material in any manner. You may translate the Material into another language only if you have licensed translation rights. You may not use the Material for promotional purposes.

3. The foregoing license shall not take effect unless and until AIP Publishing or its agent, Copyright Clearance Center, receives the Payment in accordance with Copyright Clearance Center Billing and Payment Terms and Conditions, which are incorporated herein by reference.
4. AIP Publishing or Copyright Clearance Center may, within two business days of granting this license, revoke the license for any reason whatsoever, with a full refund payable to you. Should you violate the terms of this license at any time, AIP Publishing, or Copyright Clearance Center may revoke the license with no refund to you. Notice of such revocation will be made using the contact information provided by you. Failure to receive such notice will not nullify the revocation.
5. AIP Publishing makes no representations or warranties with respect to the Material. You agree to indemnify and hold harmless AIP Publishing, and their officers, directors, employees or agents from and against any and all claims arising out of your use of the Material other than as specifically authorized herein.
6. The permission granted herein is personal to you and is not transferable or assignable without the prior written permission of AIP Publishing. This license may not be amended except in a writing signed by the party to be charged.
7. If purchase orders, acknowledgments or check endorsements are issued on any forms containing terms and conditions which are inconsistent with these provisions, such inconsistent terms and conditions shall be of no force and effect. This document, including the CCC Billing and Payment Terms and Conditions, shall be the entire agreement between the parties relating to the subject matter hereof.

This Agreement shall be governed by and construed in accordance with the laws of the State of New York. Both parties hereby submit to the jurisdiction of the courts of New York County for purposes of resolving any disputes that may arise hereunder.

V1.2

Questions? customercare@copyright.com or +1-855-239-3415 (toll free in the US) or +1-978-646-2777.

American Physical Society
Reuse and Permissions License

11-Jul-2019

This license agreement between the American Physical Society ("APS") and Henry Watkins ("You") consists of your license details and the terms and conditions provided by the American Physical Society and SciPris.

Licensed Content Information

License Number:	**RNP/19/JUL/016578**
License date:	11-Jul-2019
DOI:	10.1103/PhysRevLett.69.1765
Title:	Damping of ion-acoustic waves in the presence of electron-ion collisions
Author:	E. M. Epperlein, R. W. Short, and A. Simon
Publication:	Physical Review Letters
Publisher:	American Physical Society
Cost:	USD $ 0.00

Request Details

Does your reuse require significant modifications: No

Specify intended distribution locations:	UK & Commonwealth (excluding Canada)
Reuse Category:	Reuse in a thesis/dissertation
Requestor Type:	Student
Items for Reuse:	Figures/Tables
Number of Figure/Tables:	1
Figure/Tables Details:	Plot of thermal conductivity
Format for Reuse:	Electronic and Print
Total number of print copies:	Up to 1000

Information about New Publication:

University/Publisher:	Imperial College London
Title of dissertation/thesis:	Studies of Magnetised and Non-local Transport in Laser-Plasma Interactions
Author(s):	Henry Watkins
Expected completion date:	Jul. 2019

License Requestor Information

Name:	Henry Watkins
Affiliation:	Individual
Email Id:	h.watkins15@imperial.ac.uk
Country:	United Kingdom

American Physical Society
Reuse and Permissions License

TERMS AND CONDITIONS

The American Physical Society (APS) is pleased to grant the Requestor of this license a non-exclusive, non-transferable permission, limited to Electronic and Print format, provided all criteria outlined below are followed.

1. You must also obtain permission from at least one of the lead authors for each separate work, if you haven't done so already. The author's name and affiliation can be found on the first page of the published Article.
2. For electronic format permissions, Requestor agrees to provide a hyperlink from the reprinted APS material using the source material's DOI on the web page where the work appears. The hyperlink should use the standard DOI resolution URL, http://dx.doi.org/{DOI}. The hyperlink may be embedded in the copyright credit line.
3. For print format permissions, Requestor agrees to print the required copyright credit line on the first page where the material appears: "Reprinted (abstract/excerpt/figure) with permission from [(FULL REFERENCE CITATION) as follows: Author's Names, APS Journal Title, Volume Number, Page Number and Year of Publication.] Copyright (YEAR) by the American Physical Society."
4. Permission granted in this license is for a one-time use and does not include permission for any future editions, updates, databases, formats or other matters. Permission must be sought for any additional use.
5. Use of the material does not and must not imply any endorsement by APS.
6. APS does not imply, purport or intend to grant permission to reuse materials to which it does not hold copyright. It is the requestor's sole responsibility to ensure the licensed material is original to APS and does not contain the copyright of another entity, and that the copyright notice of the figure, photograph, cover or table does not indicate it was reprinted by APS with permission from another source.
7. The permission granted herein is personal to the Requestor for the use specified and is not transferable or assignable without express written permission of APS. This license may not be amended except in writing by APS.
8. You may not alter, edit or modify the material in any manner.
9. You may translate the materials only when translation rights have been granted.
10. APS is not responsible for any errors or omissions due to translation.
11. You may not use the material for promotional, sales, advertising or marketing purposes.
12. The foregoing license shall not take effect unless and until APS or its agent, Aptara, receives payment in full in accordance with Aptara Billing and Payment Terms and Conditions, which are incorporated herein by reference.
13. Should the terms of this license be violated at any time, APS or Aptara may revoke the license with no refund to you and seek relief to the fullest extent of the laws of the USA. Official written notice will be made using the contact information provided with the permission request. Failure to receive such notice will not nullify revocation of the permission.
14. APS reserves all rights not specifically granted herein.
15. This document, including the Aptara Billing and Payment Terms and Conditions, shall be the entire agreement between the parties relating to the subject matter hereof.